THÈSE PRÉSENTÉE

POUR OBTENIR LE GRADE DE

DOCTEUR DE

L'UNIVERSITÉ DE BORDEAUX

ÉCOLE DOCTORALE DES SCIENCES CHIMIQUES

SPÉCIALITÉ : PHYSICO-CHIMIE DE LA MATIERE CONDENSEE

Par Céline TANG

EXFOLIATION ET REEMPILEMENT D'OXYDES LAMELLAIRES A BASE DE MANGANESE ET DE COBALT POUR ELECTRODES DE SUPERCONDENSATEURS

Sous la direction de : Liliane GUERLOU-DEMOURGUES
(co-directeur : Domitille GIAUME)

Soutenue le 01/12/2017

Membres du jury :

Mme S. CASSAIGNON	Professeur – UPMC, Paris	Rapporteur
M. F. LEROUX	Directeur de Recherche – ICCF, Clermont-Ferrand	Rapporteur
M. M. MAGLIONE	Directeur de Recherche – ICMCB, Bordeaux	Président, Examinateur
M. P.-L. TABERNA	Chargé de Recherche – CIRIMAT, Toulouse	Examinateur
M. P. BERNARD	Ingénieur – SAFT, Bordeaux	Examinateur
Mme D. GIAUME	Maître de Conférences – IRCP, Paris	Examinateur
Mme L. GUERLOU-DEMOURGUES	Professeur – INP, Bordeaux	Examinateur

Exfoliation et réempilements d'oxydes lamellaires à base de manganèse et de cobalt pour électrodes de supercondensateurs

Résumé : La forte progression démographique mondiale induit une demande d'énergie toujours en hausse. Ceci se traduit par un fort développement de nouvelles énergies renouvelables qui nécessitent, de par leur nature intermittente, des dispositifs de stockage de l'énergie. Parmi eux les supercondensateurs permettent un stockage électrostatique de charges (supercondensateurs à base de carbones activés), mais certains systèmes, dits pseudocapacitifs, font en outre intervenir des réactions redox rapides de surface. L'association des deux systèmes permettent d'accéder à des propriétés intéressantes, en particulier pour le système MnO_2/carbone activé. Cependant, les oxydes de manganèse sont d'excellents matériaux pseudocapacitifs mais assez peu conducteurs électroniques. L'objectif de ce travail est d'améliorer cette conductivité en les associant avec des oxydes de cobalt conducteurs. Pour cela, une approche « architecturale » de synthèse de matériaux a été choisie. En partant d'oxydes de Mn et de Co lamellaires, ceux-ci sont exfoliés pour obtenir des nanofeuillets de nature différente. S'ensuit une étape de réempilement pour aboutir à un matériau lamellaire alterné. L'analyse structurale et morphologique des matériaux prouve que des nanocomposites très finement divisés sont obtenus. Les propriétés électrochimiques obtenues pour ces nanocomposites s'avèrent meilleures que celles des matériaux initiaux, tant en densité d'énergie qu'en puissance. Cette stratégie originale est prometteuse et ouvre la voie à des réempilements de différente nature, notamment le graphène.

Mots clés : [matériaux d'électrode] [exfoliation/réempilement] [oxydes de manganese] [oxyhydroxides de cobalt] [point isoélectrique] [charge de surface]

Exfoliation and restacking of manganese and cobalt based lamellar oxides for supercapacitor electrodes

Abstract : The ever increasing demand of renewable energies imposes, due to their intermittent nature, the development of performant energy storage devices. Supercapacitors are reliable devices that offer a high power density and numerous investigations are focusing on increasing their energy densities. In particular, asymmetric "metal oxides / activated carbons" supercapacitors are possible candidates. **T**he MnO_2/carbon system is the most investigated system, due to its capability to work in aqueous medium at potentials up to 2 V, as well as to the low cost and environmental friendliness of manganese. Nevertheless, this system suffers from the poor electronic conductivity of manganese. This work reports an original strategy for novel electrode materials involving exfoliation and restacking processes of lamellar "building blocks": lamellar manganese oxides for their pseudocapacitive properties and lamellar cobalt oxyhydroxides for their high electronic conductivity. The material engineering strategy focuses on the exfoliation of the lamellar materials into oligolamellae. The obtained suspensions are then restacked through various strategies and new well defined mixed oxides are obtained. After structural and morphological characterization, it is clear that these nanocomposites present an intimate mix of the two initial phases. The electrochemical responses are hereby enhanced, proving the intertwined relationship between structure, morphology and properties. Furthermore, this architectural approach of building novel electrode materials is original and efficient and can easily be transposed to other "building blocks", including graphene.

Keywords : [electrode material] [exfoliation/restacking] [manganese oxide] [cobalt oxyhydroxide] [isoelectric point] [surface charge]

Remerciements

A l'issu de ces trois années de recherche, je suis convaincue que la thèse est loin d'être un travail solitaire. Je n'aurais jamais pu réaliser ce travail doctoral sans le soutien d'un grand nombre de personnes dont le savoir-faire, la générosité, la bonne humeur et l'intérêt manifestés à l'égard de ma recherche m'ont permis de progresser dans cette phase délicate de "l'apprenti-chercheur".

Tout d'abord, j'aimerai remercier mes deux encadrantes de thèse, à commencer par ma directrice de thèse Mme Liliane Guerlou-Demourgues, Professeure à l'Institut Polytechnique de Bordeaux (IPB). Exigeante et rigoureuse, elle a su me former avec une grande pédagogie en m'apprenant à toujours me remettre en question. En parallèle, sa disponibilité et son enthousiasme pour ce travail m'ont permis d'apprendre à avoir confiance en moi et mes résultats. Au cours de ces trois années, j'ai pu apprécier ses qualités humaines grâce à son soutien, sa bienveillance et sa gentillesse. Je la remercie d'avoir toujours été à l'écoute et d'avoir su me comprendre, malgré mes instants "rebelles", qu'elle a su géré avec parcimonie. Grâce à elle, j'ai énormément appris tant en compétences scientifiques qu'en développement personnel, et je lui en suis très reconnaissante.

Sur le même plan, je tiens à remercier ma co-encadrante de thèse, Mme Domitille Giaume, Maitre de Conférences à l'Institut de Recherche de Chimie Paristech (IRCP) à Paris. Durant toute la première année de thèse, nous avons exploré une voie qui certes n'a pas abouti, mais qui m'a grandement transformée. Elle m'a transmis sa curiosité sans limites, et surtout sa définition d'une "recherche où on s'amuse", en chimie des matériaux, cela se traduit par la synthèse de l'imaginaire. Son esprit critique et sa culture scientifique ont amplement contribué à la qualité de ce travail, ainsi que ses conseils avisés et sa bonne humeur. Malgré la distance Paris-Bordeaux, elle a toujours été disponible et d'un enthousiasme sans faille. Je la remercie pour sa sensibilité, ainsi que sa gentillesse infinie car elle a su me repêcher dans mes instants de doute profond. Je lui adresse toute ma reconnaissance pour sa confiance et mon amitié sincère.

Je souhaiterais remercier Mme Sophie Cassaignon, Professeure à l'Université de Pierre et Marie Curie (UPMC) à Paris ainsi que M. Fabrice Leroux, Directeur de Recherche à l'Institut de Chimie de Clermont Ferrand (ICCF) pour m'avoir fait l'honneur de juger ce travail en tant que rapporteurs. Je les remercie notamment pour leurs nombreuses remarques pertinentes et pour l'intérêt qu'ils ont porté à ce travail.

J'adresse aussi ma reconnaissance à M. Mario Maglione, Directeur de Recherche à l'Institut de Chimie de la Matière Condensée de Bordeaux (ICMCB), pour l'accueil au sein du laboratoire ainsi que pour avoir accepté de présider le jury de thèse. Mes remerciements vont également à M. Patrick Bernard, Ingénieur de Recherche à SAFT Bordeaux pour sa participation en tant qu'examinateur.

Ce travail a été réalisé dans le cadre du RS2E en collaboration avec le Centre Interuniversitaire de Recherche de d'Ingénierie des Matériaux (CIRIMAT) à Toulouse. Je tiens à remercier tout particulièrement M. Pierre-Louis Taberna, Chargé de Recherche au CNRS, qui a très largement contribué aux résultats présentés, d'avoir participé au jury de thèse en tant qu'examinateur. Je le remercie de m'avoir formé à l'électrochimie des supercondensateurs, au monde de la spectroscopie d'impédance complexe, ainsi que d'avoir assuré le SAV par téléphone pour m'aider à résoudre les problèmes techniques que je rencontrais à Bordeaux. Je le remercie notamment pour sa constante bonne humeur, son humour (qui permet de relativiser sur les résultats), ainsi que son accueil chaleureux.

Ce mémoire est l'aboutissement de trois années de collaboration entre l'ICMCB et l'IRCP au sein de deux équipes remarquables. Je tiens tout d'abord à remercier chaleureusement M. Philippe Barboux, Professeur à Chimie Paristech (IRCP) et responsable du groupe Ressources et Matériaux pour un Monde Durable (RM2D). C'est grâce à lui que j'ai pu réaliser cette thèse et je le remercie pour sa confiance et son soutien depuis ces six dernières années. Je le remercie d'avoir été ma “bonne fée” et de m'avoir inspiré depuis l'école. J'aimerai aussi remercier Mme Laurence Croguennec, Directrice de Recherche au CNRS et responsable du groupe “Energies : matériaux et batteries” à l'ICMCB à Bordeaux pour m'avoir accueillie dans son groupe avec générosité.

Ce travail n'aurait pu être possible sans la contribution précieuse de nombreux collaborateurs venant de tous horizons, qui ont activement participé aux résultats de ces recherches.

Je tiens particulièrement à remercier M. Hassan Saddaoui (Centre de Recherche Paul Pascal) pour sa patience et sa persévérance, qui m'ont permis d'obtenir des images AFM d'une grande qualité. Nos conversations dynamiques et intéressantes permettaient d'écourter les longues séances aux horaires tardives.

Je remercie vivement M. Grégory Lefèvre (IRCP), de m'avoir introduite à la physicochimie de surface des oxydes, d'avoir pris le temps de m'expliquer (et ré-expliquer) les rouages du Modèle MUSIC, et surtout, de m'avoir fait goûter aux mirabelles de son jardin. J'ai beaucoup apprécié nos échanges au cours de ces trois dernières années, ainsi que son partage des connaissances.

Je remercie chaleureusement Mme Marie-Anne Dourges (ISM) pour les mesures (pas toujours évidentes) de surface spécifique des matériaux. L'intérêt qu'elle a porté pour mon sujet (et mes paillettes) m'a appris à persévérer et mieux appréhender mes résultat.

Je serais éternellement reconnaissante de M. Lénaïc Madec (IPREM), rencontre miraculeuse au détour d'une réunion RS2E, qui m'a sauvé de ma détresse lorsque j'étais au fond de gouffre de l'analyse d'XPS. Je tiens à le remercier pour sa générosité, son soutien et sa disponibilité qui me sont exemplaires. De même pour Mme Antonella Iadecola (SOLEIL) qui a eu l'extrême gentillesse de passer mes échantillons de façon exceptionnelle sur la ligne du synchrotron. Grâce à elle, j'ai pu obtenir des résultats précis sur l'influence de l'exfoliation sur le degré d'oxydation des matériaux. Je la remercie pour sa réactivité incroyable ainsi que son soutien constant.

Mes plus sincères remerciements à Jean-Claude Badot (IRCP) pour son aide concernant les mesures ainsi que les analyses (obscures) de BDS. Son expertise a été primordiale pour mieux comprendre les phénomènes de conduction des matériaux réempilé. Nos journées à Orsay étaient une pause ensoleillée dans mon hiver rédactionnel. Je le remercie pour sa patience infinie.

J'aimerais encenser le trio François Weill, Philippe Legros et Marion Gayot du PLACAMAT. Nous avons passés énormément de temps ensemble dans des salles de microscopies froides et sombres, mais qui baignaient dans la lumière de votre bonne humeur. Chaque séance était un réel plaisir, pour la grande qualité des images, mais surtout pour la chaleur humaine et j'en garde de merveilleux souvenirs.

Je remercie aussi l'ensemble des membres de l'équipe "Revêtements et Traitements de Surface" du CIRIMAT pour leur aide précieuse lors de mes séjours à Toulouse, et notamment Patrice Simon, Barbara Daffos, Léo Nègre, Kévin Brousse, Liu Yinghui, Lin Zifeng...

Mes remerciements s'adressent également à l'ensemble du personnel de l'ICMCB et en particulier ceux avec qui j'ai pu travailler. Eric Lebraud et Stanislas Pechev pour la diffraction des rayons X, Laetitia Etienne pour l'analyse chimique, Rodolphe Decourt pour les mesures électriques, Lydie Bourgeois pour les analyses Raman, Christine Labrugère pour l'XPS, Sandrine Quillateau pour son sourire, Fabien Palencia pour avoir sauvé ma rédaction, ainsi qu'Abder Salhi pour m'avoir tant de fois pardonné de mon manque d'organisation. Une mention spéciale à Nicolas Penin, qui m'a aidé dès mon arrivée à l'institut, et ce jusqu'à l'aboutissement final le jour de la soutenance ! Je tiens à remercier les membres du groupe 2, en particulier Cathy Denage (notre sauveuse) et Elodie Guérin (merci pour les rigolades !). Ainsi que Sabine Goma, Philippe Dagault, Dany Carlier ...

Ces trois années de thèse entre Paris et Bordeaux m'ont aussi permis de rencontrer des collègues qui sont aujourd'hui devenus des ami-e-s. Je tiens tout d'abord à citer les deux parisiennes : maman Réka, avec ses manucures parfaites, son discours conservateur et son amour pour les ragots (et les McDo), ainsi que Jaja pour son entrain, sa spontanéité et sa bonne humeur contagieuse. Puis les rencontres bordelaises, dont Louisiane, mon âme sœur de bureau, je tiens à la remercier pour sa délicatesse, sa douceur, et tous ces moments de détresse et de joie partagés ensemble, j'ai adoré découvrir et apprendre Bordeaux en sa compagnie, et l'aventure n'est pas finie, en avant Philadelphie ! Je tiens à citer Aimery, qui a réussi, après 28 ans de rejet, à me faire boire du café et à me faire aimer ça ! Il m'a aussi sauvé dans mes instants les plus sombres en faisant le pitre, car il ne connait le ridicule. Enfin, j'aimerai citer Cyril, Romain, Anthony, Baptiste et Mathias, autrement dit "Les Pelos" pour les rigolades (ou odeurs) quotidiennes, les sorties à la plage (surtout pendant la rédaction), les quiz du mercredi soir, les soirées de danse endiablées (à la Guinguette ou pas) et les binges improvisées...

Je n'aurais pu autant apprécier ma vie bordelaise (hors labo) sans les ami-e-s que j'y ai rencontré. Je tiens à nommer les Hélènes pour ces déjeuners hebdomadaires qui m'ont sorti de ma bulle quotidienne. Je les admire énormément pour ce qu'elles sont et regrette déjà ces repas-relâche. Un grand merci à Bhargav pour les restaurants morfales et les aventures dansantes. Une mention spéciale à Raquel (habibi coloc styley) qui sait toujours me faire sourire et Hortense (BANG BANG), je les remercie pour leur joie de vivre et leur soutien sans faille. Merci d'avoir été là pendant mes instants les plus sombres, et d'avoir partagé ma renaissance. Je remercie aussi Arthur, arrivé comme un cheveu sur la soupe en plein début de rédaction, qui a largement contribué à mon bien-être tout au long de cette étape cruciale. Je remercie surtout son sens inné du rythme, ses compétences culinaires et son talent de rappeur.

Je ne pourrais oublier les amis d'avant la thèse qui me soutiennent depuis bien plus longtemps et qui contribuent à mon bonheur quotidien. 2017 sonne la fin de la thèse, mais aussi mes 10 ans en France. Je pense à mes premières rencontres : Elsa et William (eh non, on n'est plus si jeunes!) qui "ont un vrai boulot" depuis longtemps déjà et qui reprennent tous les deux les études quand (enfin) je termine les miennes! Je souligne mes amies de cœur Gomar et Lilice (sans vous je ne serais rien), ainsi que Mamie Lola et Papi Alex. Je n'oublie surtout pas les laotiens (Ju, Alice, Alex, Hector...) qui ont toujours été ma pause salvatrice dans ce monde scientifique. Mention spéciale à Karim, coloc de la vie, plus qu'un an et à nous le monde!

Pour finir, une pensée de particulière pour ma famille. Je tiens à remercier Marc et Lydia, ainsi qu'Alio, Nico et Caro pour m'avoir toujours accueillie à bras ouvert. Je me suis toujours sentie chez moi en arrivant à Bourg-La-Reine, et plus forte en repartant.

Enfin, je ne serais qui je suis aujourd'hui sans l'amour inconditionnel que m'ont porté mes parents, et leur soutien sans faille. Vous avez toujours cru en moi, très souvent aveuglément, ce qui a largement contribué à la réussite de cette thèse. Last but not least, merci Cécile, petite sœur en or, qui, avec son petit rire enjoué et ses yeux pétillants illumine mes journées.

Contents

3. Synthesis and exfoliation of layered metal oxides 47

4. Restacking 91

Introduction

In the 21st century, the topic of energy is one of the most important technological issues that must be addressed. Currently, our planet faces huge energy challenges as our reserve of fossil fuels become more and more limited. Furthermore, the burning of fossil fuels results in significant environmental harm, such as global warming and climate change. Consequently, there is an urgent need for efficient, clean, and sustainable sources of energy such as solar energy, or wind energy... However, due to the intermittent character of renewable energies, reliable energy storage systems are required for adapting these technologies to the demand in electricity.

Energy storage is the capture of energy produced at one time for use at a later time. It involves converting energy from forms that are difficult to store to more conveniently storable forms. A wide range of technological approaches is available [1], as energy comes in multiple forms including chemical, kinetic, potential, heat... For example a hydroelectric dam stores energy in a reservoir as potential energy.

With the development of electric vehicles and portable devices, energy storage systems need to meet high capacity and high power to satisfy the requirements for autonomy and speed. Among the various solutions, energy can in particular be stored electrochemically in batteries and supercapacitors [2]. Although batteries currently present much higher energy density, their relatively low power density and poor cycle life limit their use in high power demanding applications such as regenerative braking and load leveling systems [3]. By contrast, supercapacitors store larger amounts of energy than the traditional dielectric capacitors and provide energy far faster than batteries, resulting in a much higher power density [4]. Therefore, they are particularly adapted for applications requiring energy pulses in short periods of time, e.g., seconds or tens of seconds.

Although supercapacitors are now commercially available, they still require improvements, especially for enhancing their energy density. It requires a fundamental understanding of their properties in addition to improving electrode materials, electrolytes and integration in systems. The energy density of supercapacitors can be enhanced by increasing the voltage and/or the capacitance. For reaching these objectives, various strategies have been proposed in the literature, involving the development of new materials, new geometries and new electrolytes [5, 6, 7]. However, the performance and the cost of the supercapacitor devices are the main parameters that guide the choices of industry.

For these reasons, most of the supercapacitors presently available on the market are symmetric EDLC (electric double layer capacitance) devices. EDLCs are based on an electrostatic charge storage. The EDLC electrode can be fabricated using diverse carbon-based materials such as activated carbon (AC) [8], carbon nanotubes (CNTs), graphene or their composites [9, 10]. These materials should have high specific surface area for accommodation of more ion adsorption/desorption on its surface during charge and discharge. The main advantages of EDLCs are related to their high versatility of structure/texture, low cost and highly developed surface area. More important, their high electrical conductivity allows the realization of high power systems. Although environmentally unfriendly, due to the use of acetonitrile as solvent, the organic electrolytes are preferred by industry to the aqueous ones because of their high stability window, e.g. 2.7 – 2.8 V, allowing high energy densities to be reached.

It is possible to enhance energy density by using pseudocapacitive electrodes. Pseudocapacitance is caused by surface redox reaction at electrodes in a faradaic process. They are based on transitional metal oxides such as MnO_2, RuO_2 or polymers [11, 12, 13]. Charge and discharge process involves redox reaction between various valence states of specific elements in these oxides. Due to this faradaic charge storage mechanism, pseudocapacitors possess relatively higher energy density than EDLCs, but a significantly lower power density. This is especially true for MnO_2-based electrodes, which show excellent pseudo-capacitance [14]. However, their electronic conductivity is very low, which increases the charge transfer resistance and thus decreases the power density and the rate capability. It is therefore logical to develop a novel electrode containing both manganese oxide and another conductive material (most commonly carbon-based material).

Another way to satisfy the requirements for high energy as well as high power density, is to develop hybrid supercapacitors [15, 16, 17]. By combining an EDLC electrode with a pseudocapacitive electrode, a hybrid device exhibits both double-layer as well as pseudocapacitive properties, where it compensates the drawbacks of lower power density for batteries, or lower energy density for symmetric capacitors. The voltage window of hybrid supercapacitors can be broadened from 0.9 V to 1.8 V due to over potential in aqueous environment. Thus energy and power density can be greatly increased.

Finding new materials is a crucial task for improving the energy and power density of materials. In this context, the aim of this work is to design novel materials via an original strategy synthesis. Based on 2D materials, the strategy focuses on preserving properties of each starting material - considered as “building blocks” - while expecting an additional synergistic effect between them. In this framework, layered cobalt oxyhydroxides with enhanced electronic conductivity (that have already been developed in the laboratory [18, 19]) are used as conductivity enhancer for layered manganese oxides. Both layered transition metal oxides have been synthesized, and then exfoliated to obtain nano-objects considered as “building blocks”. Then, various restacking techniques are applied in order to obtain novel materials with enhanced properties.

Thus, the goal of this work is to study the rational design of novel 2D layered mixed Mn-Co materials, as positive electrodes for asymmetric supercapacitors. Three objectives were defined to answer this : (i) synthesize the Mn oxide and Co oxyhydroxides “building blocks” through exfoliation of layered metal oxides, (ii) restack them accordingly and evaluate their electrochemical performances as electrode material and (iii) assemble a chosen restacked material as positive electrode into a full asymmetric supercapacitor using activated carbon as a negative electrode.

This work is funded by the RS2E (French Network for Electrochemical Energy Storage) through the CNRS, and is a collaborative research project between two laboratories : ICMCB in Bordeaux, under the direction of Liliane Guerlou-Demourgues, and IRCP in

Paris under the direction of Domitille Giaume. The electrochemical tests and full cell assembly were supervised by Pierre-Louis Taberna from CIRIMAT, in Toulouse, through the RS2E network.

In the first chapter, a brief introduction on various electrochemical devices will be given. They will be classified according to the charge storage mechanism of the electrodes and the various devices that can be made, resulting in different performances.

Chapter 2 presents a literature review showing the state of the art on manganese-based and cobalt-based supercapacitors. The charge storage mechanism will be explained as well as their advantages and drawbacks. Then, various strategies used to enhance their electrochemical performances will be reviewed, resulting in the presentation of electrode materials combining both manganese and cobalt oxides. This will lead to the justification of our strategy : preserving the properties of each material and achieving a synergistic effect between them, through an exfoliation/restacking process of layered materials.

Chapter 3 is dedicated to the synthesis of the initial layered materials as “building blocks”. First, the synthesis of initial pristine materials is described, followed by their structural and morphological characterizations, and by electronic conductivity measurements. Then, the manganese oxides as well as cobalt oxyhydroxides are exfoliated to obtain “building blocks”. This process is delicate and the obtained “building blocks” will be thoroughly characterized.

Chapter 4 presents the various restacking techniques used to assemble Mn and Co “building blocks”. For this, the isoelectric point of the particles is experimentally determined and modeled using MUSIC (Multi-site Complexation). Then, the restacking processes are described and the resulting restacked mixed Mn-Co materials are characterized. A number of morphological differences are observed, according to the restacking process that was used.

The last chapter compares the electrochemical performances of restacked materials according to their morphology and Mn:Co ratio, with the initial pristine materials. Then, the best material is chosen in order to be assembled as a positive electrode in an aqueous full cell, versus a negative activated carbon electrode.

1. Context

1.1. Historical background : the development of capacitors and supercapacitors

Although the first idea of electricity dates from ancient Egyptians (people were aware of shocks from electric fish), humans have spent thousands of years trying to understand its mechanism.

Thales de Millet (600 BC) is the first to describe the static electricity. By rubbing a rod of amber to fur, he noticed it could attract dust [20]. He believed this friction was due to a magnetic phenomenon. Electricity remained a mystery until English scientist William Gilbert (1600) distinguished magnetism from static electricity [20]. He invented the word *electricus* from elektron, the Greek word for "amber", which made its first appearance in print in 1646 thanks to Thomas Browne [21]. Fast forward one century, Charles du Fay discovered positive and negative charges (1733) and differentiated conductive materials to insulators. In 1750, Benjamin Franklin conducted extensive research on the behavior of the Leyden jar (Figure 1.1) as a device for storing large amounts of electrical charge and concluded that it was stored in the glass [22]. Thus the notion of capacitors was invented and Franklin improved the design of the Leyden jar to flat capacitor. This substantially reduced volume and increased convenience and reliability. Along came Volta (1782) and later Faraday (1831) stating the basic principle of a two-plate capacitor : if a voltage is applied between two metallic plates, a charge of +Q on positive plate and a charge of -Q on the negative plate are accumulated, resulting in the stored energy $E = \frac{1}{2}CV^2$, where C is the capacitance of the capacitor and V the applied voltage [23].

In 1853, the concept of double-layer capacitance was first described by German physicist von Helmholtz [24] who conducted theoretical investigation of the Electric Double Layer, paving the way for the development of supercapacitors.

A century later, in 1957, the first patent on double-layer capacitance was granted to Becker [25] at General Electric Corporation. For the first time, porous carbon with high specific surface area was used as electrode material for an electrochemical capacitor. A decade later, scientists at Standard Oil of Ohio (SOHIO) [26] developed a similar technology and sold it to NEC (Nippon Electric Company) who introduced its first commercial application in 1971 with the name “supercapacitor”.

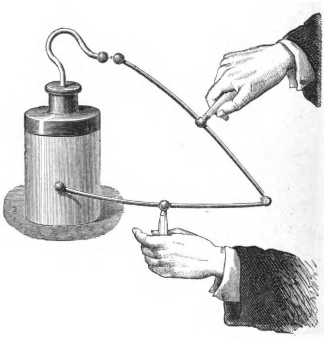

Figure 1.1.: Leyden jar being discharged, from a 1878 science text. A Leyden jar consists of a glass jar with metal foil cemented to the inner and outer surfaces. The hook on top is in contact with the inner foil. The jar is charged with electricity by grounding the outside foil to the terminal of an electrostatic machine. To discharge the jar, the hook is connected to the outer foil and charge neutralization ensures [27].

Among the electrochemical supercapacitors, a different type was originated in 1975 by Conway : pseudocapacitors [28]. Here, the capacitance arises from reversible redox reactions that occur at/near the surface of a material in contact with an electrolyte, or when these reactions are not limited by solid-state ion diffusion.

Recently, supercapacitors based on various material electrodes and association of technologies have been manufactured around the world : Gold Capacitor (Panasonic), K2 Ultracapacitor (Maxwell), Super-Capacitor (NEC), Ultracap (Epcos), Dynacap (ELNA), Aerogel Capacitor (Cooper), BestCap (AVX)... Japan, USA and Russia are pioneers in the development of commercial supercapacitors, widely used as power sources for communication devices, digital cameras, electric vehicles, electric tools and storage of the energy generated by renewable sources...

1.2. Components of an electrochemical device

Depending on the charge storage mechanism of electrode materials, a wide range of electrochemical devices can be assembled, each presenting their own distinctive characteristics.

Power density P (W) and energy density E (J) are the two main attributes of an electrochemical device and they are defined as following :

$$E(J) = \frac{1}{2}CU^2$$

$$P(W) = U \times I$$

where C is the capacity (F), I the current delivered (A) and U the working voltage of the device (V).

A full electrochemical storage device is composed of two working electrodes, an electrolyte, current collectors and a separator (Figure 1.2).

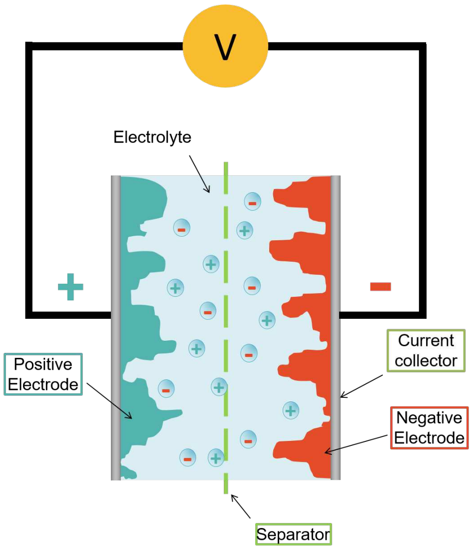

Figure 1.2.: Scheme of an electrochemical energy storage device.

Each component is essential for the proper functioning of a device. In this section, each component will be shortly described. Then a focus will be made on the electrodes and the various charge storage mechanisms possible (faradaic mechanism and capacitive mechanism). Finally, a third charge storage mechanism will be explained : pseudocapacitance.

1.2.1. Electrolyte

Electrolytes are an essential element in electrochemical devices since the positive and negative electrodes are interconnected by it. The electrolyte determines the charge transport during the charge/discharge process. There are liquid electrolytes (aqueous, organic and ionic liquids [29, 30]) or solid ones (polymers, ceramic glasses...) [31]. Electrochemical stability and ionic conductivity are the two main criteria for selecting an electrolyte. Electrochemical stability determines the voltage window and hence has great influence on energy and power density. Ionic conductivity, on the other hand, affects the internal resistance and greatly influences the power density.

Aqueous electrolytes include acid (e.g. H_2SO_4, HCl), alkali (e.g. KOH, NaOH), and neutral pH solutions (e.g. Na_2SO_4, K_2SO_4). They are widely used for their high ionic conductivity (up to ~ 1 S cm^{-1}) and smaller solvated ions which could promote high conductivity and power delivery. However, water has an electrochemical stability window of 1.23 V, which results in a narrow voltage window, usually less than 1 V, and hence low energy density.

To solve this, organic electrolytes are used, presenting a much larger electrochemical stability voltage window (up to ~ 3 V), resulting in high energy density. However, this comes at the expense of ionic conductivity, thus leading to poor power density. Among organic electrolytes, acetonitrile and propylene carbonate (PC) are the most commonly used solvents. Moreover, the use of organic electrolytes generate environmental concerns, as well as safety issues.

A further increase in the voltage window can be achieved by using ionic liquids as promising electrolytes. Ionic liquids correspond to salts with a melting point below 100°C. Advantages include low vapor pressure, broad electrochemical stability window, and good thermal property [32]. Nonetheless, they have a limited ionic conductivity, high viscosity and poor wettability, especially at room temperature, which substantially reduces the power performance.

For our application, in order to obtain high power and develop environmentally friendly and safe devices, aqueous electrolytes will be preferred.

1.2.2. Separator

The separator is a critical component of electrochemical devices. It is a porous membrane placed between the two electrodes to prevent the physical contact between them while allowing ion diffusion across it. Its role is to prevent short circuit between working electrodes, which can trigger the conversion of chemical energy to heat and cause irreversible damage to the device.

An separator should present good permeability in order to allow the diffusion of ions and electrolyte molecules while being insulating to electrons. Furthermore, a good ability to absorb electrolyte is necessary to reduce internal resistance. Finally, they should have a good chemical stability (in different electrolytes) and cycling stability under high potential.

Based on these requirements, separators are usually made from membranes or thin and highly porous films. The most commonly used separator materials are cellulose, polymer membranes and glass fibers. Commercially, the most used are Celgard® membranes made of porous polypropylene. Their high porosity (55%) allows the ions to flow easily from one electrode to another.

Commonly dismissed, separators are directly linked to the safety of electrochemical devices. This is why recent research focuses on advanced separators with high structural stability under working conditions. Functionalization or hybrid inorganic material/polymer are strategies developed to improve their properties [33].

1.2.3. Current collectors

The current collector is essential to the device as it ensures electrical contact between the electrode material and the circuit. Most current collectors are metallic as they are highly conductive. They should present a good interface contact with the active electrodes. This way, the degree of utilization of the active material can be maximized and the internal resistance of the device is minimized. Grids, surface treatment or nanostructuration are developed in order to achieve this.

Another important feature is the chemical stability of the current collector versus the electrolyte, because it can strongly affect the lifetime and performance of the device. When a strong acid electrolyte is used, due to its high corrosive nature, some corrosion-resistant metallic materials (e.g. Au) are traditionally used. To reduce the cost, carbon-based materials can be promising. For alkaline electrolytes, nickel current collectors are commonly used due to their relatively low cost, good chemical and electrochemical stability (under such conditions). To increase the active surface area of the material, nickel foam is often used. Due to their less corrosive nature, neutral aqueous electrolytes can give more choice for current collectors. A wide variety of materials have been used, including stainless steel, ITO (indium tin oxide), carbon-based materials...

In the case of organic electrolytes, the majority of devices use Al as current collectors. They have a relatively low density, and can be stable in a large potential window (up to 3 V). However, they can not be used in aqueous media nor in presence of oxygen because of a spontaneous passivation of the surface, leading to an insulating layer of Al_2O_3.

By designing novel current collectors with suitable hierarchical systems of macropores, mesopores and micropores, a balance of efficient transport of electrolyte, ions and electrons can be achieved. In addition, unconventional current collectors such as carbon fiber papers, conductive cotton textiles and carbon cloths, sponges, paper, etc. offer new designs for various applications .

1.2.4. Electrodes

Electrochemical storage of energy implies the conversion of electric energy to and from chemical energy, both conveyed by electrons and ions. The storage is performed by active materials which constitute the electrodes, through various charge storage mechanisms detailed below.

1.2.4.1. Faradaic charge storage

Faradaic processes convert electrical energy to chemical energy through an electrochemical reaction. It relies on redox reactions between two electrodes. When charging, the positive electrode is oxidized (loss of electrons) while the negative electrode is reduced (gain of electrons). To modify the oxidative state of the solid electrodes, transfer of charges (ions, electrons) is necessary. The charge/discharge capacity is defined by the quantity of ions exchanged per quantity of electroactive materials.

1.2.4.2. Capacitive charge storage

Capacitive charge storage mechanism is based on the electrostatic accumulation of charges (electrons, ions...) on the surface of electrodes, without any chemical nor electrochemical transformation. The total charge density Q (C/g) is directly linked to the specific surface area S (m^2/g) and the surface charge density σ (C/m^2) of the electrodes according to equation 1.1.

$$Q \propto \sigma \times S \tag{1.1}$$

1.2.4.3. Example : Dielectric capacitance

A dielectric capacitor is composed of two metallic plates separated by a dielectric medium (as shown in Figure 1.3). When the two conductors experience a potential difference, an electric field develops across the dielectric, causing a net positive charge on one plate and a net negative charge on the other plate.

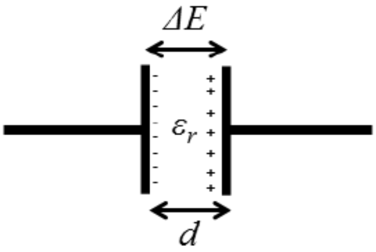

Figure 1.3.: Classic dielectric condensator.

This electronic transfer is extremely fast and reversible, leading to high response rate and high power densities, along with quasi-infinite cyclability. The quantity of charges (Q in Coulombs) stored is proportional to the applied voltage (ΔE in Volts) through equation 1.2 :

$$Q = C \times \Delta E \tag{1.2}$$

The capacitance C (in Farad) depends on the relative permittivity (ε_r) of the dielectric medium, the surface of the metallic plates (S in m^2) and the distance between the two electrodes (d in m) according to equation 1.3 :

$$C = \frac{\varepsilon_0 \varepsilon_r S}{d} \tag{1.3}$$

ε_0 is the electric constant of free space (F$\cdot m^{-1}$) and ε_r is the relative permittivity of the insulating material between the electrodes.

In order to increase C, different insulating materials have been developed. A few examples are shown in Table 1.1, along with their relative permittivity. However, the surface limitation and high distance between the electrodes induce a low quantity of energy obtained, and require the development of other electrode materials.

Insulating material	ε_r
PTFE (Teflon)	2.1
Polypropylene	2.2-2.36
Glass	3.7-10
Mica (ruby)	5.4
Strontium titanate	310
Barium titanate	1250 -10 000 (depending on temperature)

Table 1.1.: List of materials commonly used in capacitors, along with their values of ε_r at the frequency of 1kHz at room temperature.

1.2.4.4. Pseudocapacitive charge storage

The term pseudocapacitance was first introduced by B. E. Conway in 1970 to characterize the behavior of RuO_2. RuO_2 presents a wide potential window, high conductivity and highly reversible redox reactions involving three distinct oxidation states [34, 28, 35].

Pseudocapacitive charge storage arises from fast and reversible electrochemical reactions occurring on the electrode surfaces. The energy storage mechanism is based on a redox reaction not limited by ion diffusion, but presents a capacitive response signature : a linear dependence of the charge stored with changing potential within the window of interest. Like capacitive electrodes, a pseudocapacitance C_p can be defined by the following equation 1.4 :

$$C_p = \frac{\delta Q}{\delta V} \tag{1.4}$$

where δQ is the amount of charge stored, which is proportional to the potential difference (δV).

1.3. Different types of full devices

A full working device is the combination of two working electrodes, an electrolyte, a separator and current collectors. According to the nature and charge storage mechanism of the working electrodes, devices can be divided in categories that will be described below.

1.3.1. Batteries

A battery is a device with two electrodes that store energy through a faradaic charge storage mechanism (see section 1.2.4.1). When charged, the positive electrode is oxidized (electron loss) and the negative electrode is reduced (electron gain). When discharged, the positive electrode is reduced and the negative one is oxidized.

Primary batteries are used once and discarded : the structure of the active materials in the electrodes is irreversibly changed during discharge. Common examples are the alkaline batteries, for example Zn/KOH/MnO_2batteries. Secondary (rechargeable) batteries can be discharged and recharged several times using main power from a plug : the original composition of the electrodes can be restored by reverse current. The oldest form of rechargeable battery is the lead-acid battery. To increase the energy density and particularly the operating voltage of the battery, other devices have been developed, including nickel-cadmium (Ni-Cd), nickel metal hydride (NiMH) and lithium-based cells (lithium-metal, lithium-ion, lithium-polymer...). A comparison of the different battery technologies is shown in Figure 1.4.

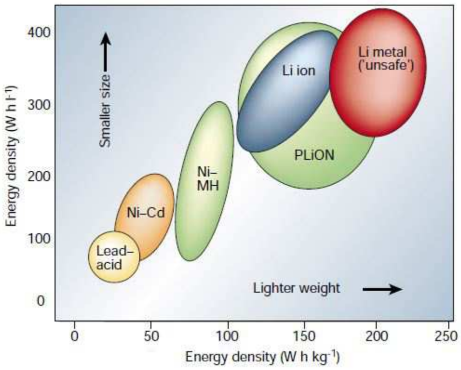

Figure 1.4.: Comparison of the different battery technologies in term of volumetric and gravimetric energy density [3].

Lithium-based cells were born to answer to the energy density issue as negative electrodes were based on metallic lithium (most reducing couple known $Li^+/Li_{(s)}$). However, due to safety reasons, other technologies had to be developed, lithium-ion and lithium-polymer batteries. Nowadays, lithium-ion batteries are most common in home electronics. They are one of the most popular types of rechargeable batteries for portable electronics, with a high energy density, tiny memory effect and low self-discharge. This is why we will focus on describing the Li-ion batteries. In Li-ion batteries, lithium ions move from the positive electrode to the negative electrode during charge and back when discharging. Li-ion batteries use intercalated lithium compounds as electrode materials.The characteristics found in a commercial battery are given in Table 1.2.

	Nokia 3310 mobile battery
Specific energy	100 - 265 Wh / kg
Specific power	250-340 W / kg
Charge / discharge efficiency	80-90 %
Energy / consumer price	2.5 Wh / US$
Cycle durability	400-1200 cycles

Table 1.2.: Example of Li-ion battery (Used in a Nokia 3310 mobile phone) [36].

A schematic representation and operating principles of Li-ion batteries are shown in Figure 1.5.

The positive electrode of a Li-ion battery can be constituted by various materials, for example $LiCoO_2$. $LiCoO_2$ develops a pseudo tetrahedral structure that allows for two-dimensional lithium ion diffusion. These electrodes are ideal due to their high volumetric capacity, low self-discharge, high discharge voltage, and good cycling performance. Limitations include the high cost of the material, slight toxicity, and low thermal stability.

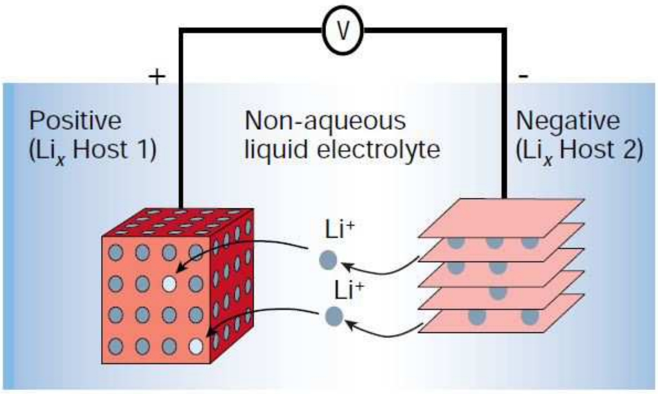

Figure 1.5.: Schematic representation and operating principles of Li-ion battery [3].

The negative electrode is usually made of graphite or other carbon materials which can insert Li^+ at low potential. These materials are used because they are abundant, electrically conducting and function as a lithium sponge, reversibly absorbing and releasing lithium ions in the intercalation process [37].

During charge-discharge processes, these redox reactions occur :

At the positive electrode : $Li_{1-x}CoO_2 + xLi^+ + xe^- \rightleftharpoons LiCoO_2$

At the negative electrode : $Li_xC_6 \rightleftharpoons xLi^+ + xe^- + C_6$

Organic liquid electrolytes are used for Li-ion batteries, they consist of lithium salts such as $LiPF_6$, $LiBF_4$ or $LiClO_4$ in anhydrous organic solvents, such as ethylene carbonate, dimethyl carbonate and diethyl carbonate [38]. The advantage of using those is that they can hold a high potential window (up to 4.2 V) leading to high energy densities. However, due to the chemical nature of faradaic processes, ion diffusion limits the power density of these devices. Furthermore, their cyclability is limited, with a lifespan of around 1000 cycles. Also, even if metallic lithium is not present, these can be dangerous and pose a safety hazard since they contain flammable electrolyte and are kept pressurized.

As the bulk of the material takes part in the process, great energy density can be achieved. However, due to the kinetics of these reactions (limited by the diffusion of charges), the charge-discharge rate of the electrodes is restricted. As shown in Figure 1.6, a typical cyclic voltammogram for battery electrode presents distinct oxidation and reduction peaks. In theory, these peaks should mirror each other, but the hysteresis in oxidation and reducing potentials shows the importance of ion diffusion in the electrode material. Furthermore, their cyclability and lifespan are limited : energetic yield of redox reactions seldom reach 100% while the repetitive charge-discharge cycles induce a structural/composition modification of the electrodes.

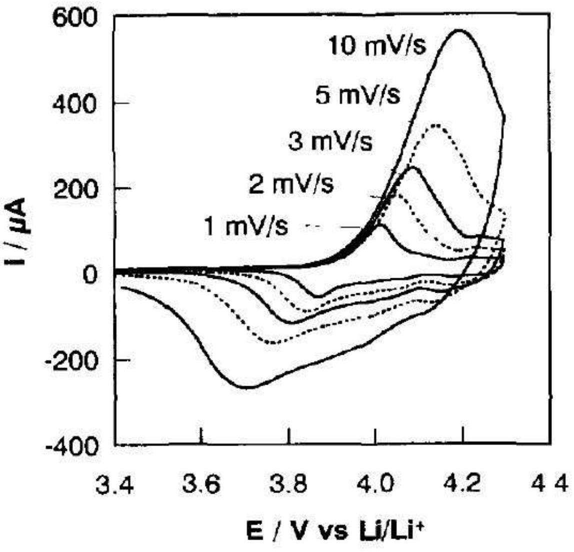

Figure 1.6.: Cyclic voltammogram for thin-film in $LiCoO_2/LiClO_4/PC$ at different scan rates [39].

1.3.2. Supercapacitors

In this category of devices, working electrodes present a capacitive charge storage mechanism (see section 1.2.4.2). If both working electrodes are of same nature with double layer capacitance, the device is called an *Electric Double Layer Capacitor* (EDLC). It is a symmetrical device, in which the charge storage mechanism is based on the electrostatic adsorption of charges at the interfaces of the electrodes and electrolyte (as seen in 1.2.4.3). Most of the commercially available EDLCs are composed of two highly porous carbon electrodes.

1.3.2.1. Electrodes for Double Layer Capacitance (EDLC)

EDLC present a much higher surface area than those for dielectric capacitors (seen in section 1.2.4.3). The insulating material is replaced by an electrolytic solution, decreasing the distance between the electrodes and involving the electrostatic accumulation of ions (and no more electrons) on the electrode surface.

The double layer was first described and modeled by Von Helmholtz in the 19th century [24, 40]. The Helmholtz double layer model (Figure 1.7.a) states that two layers of opposite charge form at the electrode/electrolyte interface and are separated by an atomic distance. This model was improved by Gouy and Chapman (Figure 1.7.b), considering the interface as a diffuse layer. Later, Stern combined both models into two layers : some ions adhere to the electrode as suggested by Helmholtz (called the Stern layer) while other solvated ions stay in the diffuse layer. Grahame [41] modified it by further proposing that some ionic or uncharged species can penetrate the Stern layer, although the closest approach to the electrode is normally occupied by solvent molecules. This model proposes the existence of three regions. First the inner Helmholtz plane (IHP) where the solvent ions are specifically adsorbed. A second region is the outer Helmholtz plane (OHP) in which solvated ions pass close to the electrode. Finally, the diffuse layer is the region beyond the OHP (Figure 1.7.c).

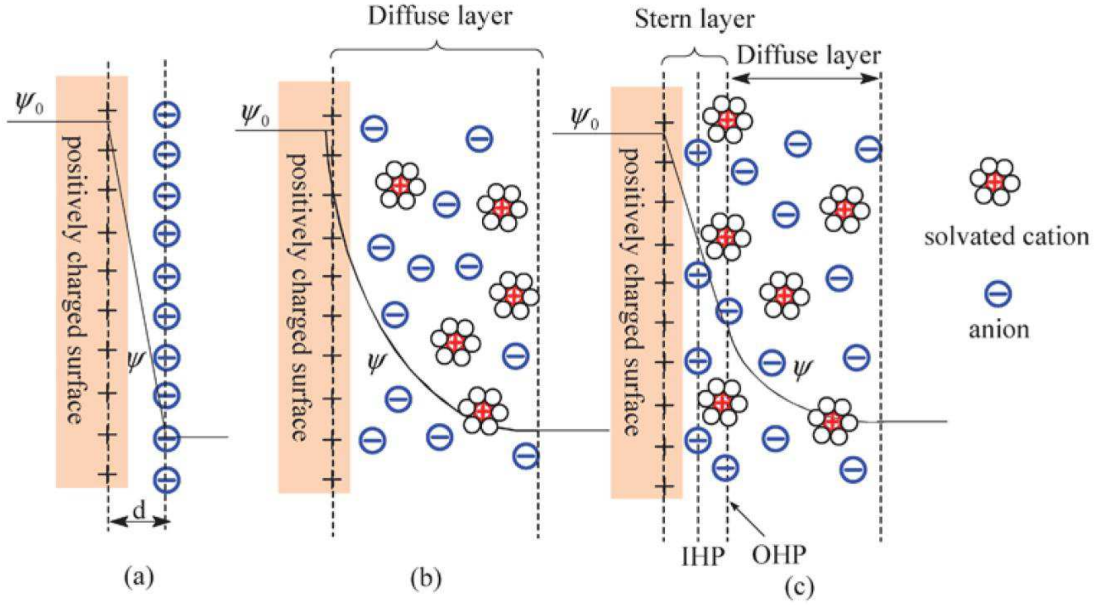

Figure 1.7.: Models of the electrical double layer at a positively charged surface (a) the Helmholtz model, (b) the Gouy-Chapman model, (c) the Grahame model showing the Stern layer divided into an internal Helmholtz plane (IHP) and an outer one (OHP) [41].

The mechanism of charge generation includes surface dissociation as well as ion adsorption between the electrodes and electrolyte. During the process of charging, the electrons travel from the positive electrode to the negative electrode through an external circuit. In the electrolyte, cations move towards the negative electrode while anions move towards the positive electrode. During discharge, the reverse processes take place.

By increasing the specific surface area, the quantity of charges stored increases. Therefore high power density can be reached, with fast charge-discharge rates. Most typical EDLC electrodes are made of high surface-area materials such as porous carbon in order to maximize the surface area of the double-layer. The advantages of carbon materials include abundance, low cost, easy processing, non-toxicity, high specific surface area (up to 2000 m^2/g) and a wide temperature range [8, 42, 43, 44]. It exists in various micro-textures (powder, fiber, foam, fabric...) and dimensions (0 to 3D) (Figure 1.8). So far, the most used are activated carbons (AC) [45, 46, 8], carbon aerogels [47], carbon nanotubes (CNT) [48, 49], carbon fibers and graphene [50, 51, 52].

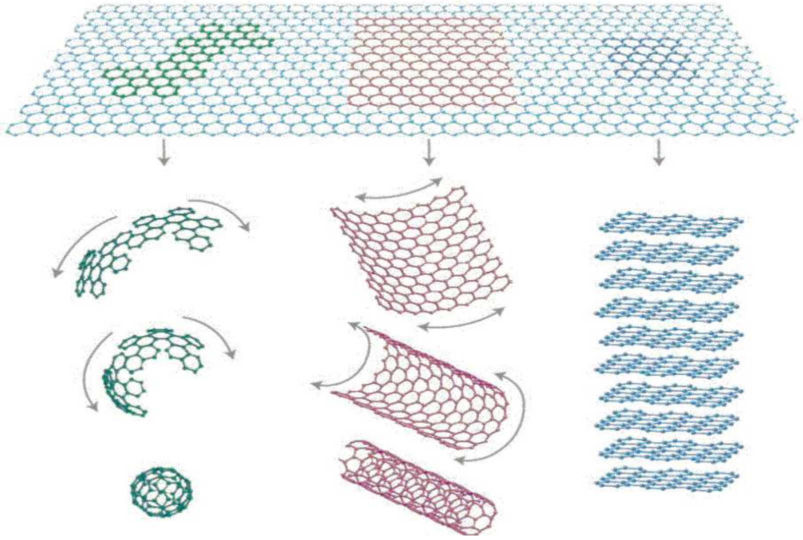

Figure 1.8.: Schematic of carbon family in 0-dimensional fullerene, 1-dimensional carbon nanotube, 2-dimensional graphene, 3-dimensional graphite [53].

Since the charge storage is electrostatic, the stored charge depends linearly on the voltage applied. As shown in Figure 1.9, the cyclic voltammetry curves of carbon materials have good rectangular shapes, typical of a capacitive behavior. However, since the surface charge density of carbon electrodes is limited, the specific energy is kept low. With equation 1.1 in mind, another way to increase the charge capacity would be to study materials with a higher surface charge density or higher specific surface.

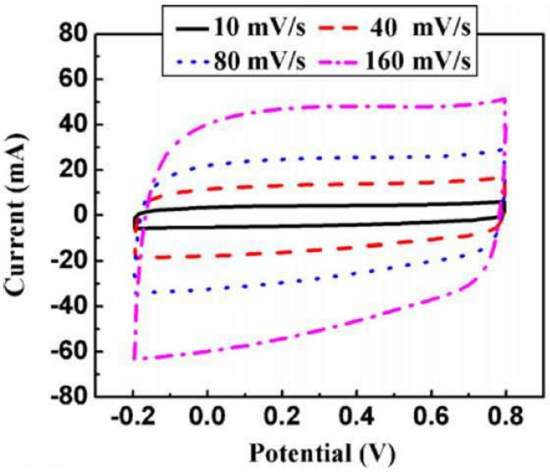

Figure 1.9.: Cyclic voltammetry curves of an activated carbon microbeads / carbon nanotube compound electrode at different scan rates (10, 40, 80 and 160 mV/s) [54].

1.3.2.2. Pseudocapacitors

The search for materials with higher charge density than EDLCs motivated research on metal oxides and led to the discovery of pseudocapacitance. These can combine the advantages of both faradaic electrodes (high energy density) and capacitive electrodes (high power density). Two main types of materials that can present pseudocapacitance : reversible redox reaction of transition metal oxides and reversible electrochemical doping-dedoping in conductive polymer based electrodes.

Pseudocapacitors are symmetrical devices with two electrodes fabricated from identical pseudocapacitive materials : either the same conducting polymer (p-type or n-type) [55, 56] or transition metals [57].

Conducting polymer-based electrodes

Conducting polymers exhibit many advantages that make them suitable electrode materials, such as low cost, low environmental impact, easy fabrication and flexibility [58, 59, 60]. The most studied polymers for pseudocapacitive electrodes are polypyrrole [61], polyaniline [62, 55] and derivatives of polythiophenes [63, 64, 65] (Figure 1.10).

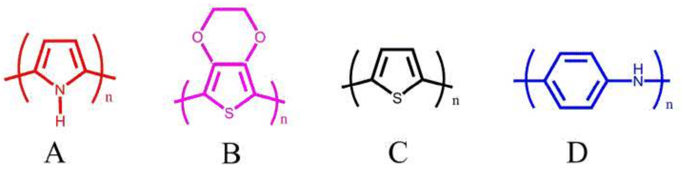

Figure 1.10.: Various conducting polymer structures. A. Polypyrrole (PPy), B, poly(3,4-ethylenedioxythiophene)(PEDOT). C. polythiophene (PTh). D. polyaniline (PANI).

Charges are stored by redox reaction in a doping process. In the case of PANI and PPy, the conductivity arises from p-doping (also known as oxidative doping) where the removal of π-electrons from the conjugation leads to a net positive charge. A schematic description of the charge storage mechanism for PANI is provided in Figure 1.11 as an illustration : emeraldine salt, obtained by partial oxidation and acid doping from leuco-emeraldine is the only conductive form of PANI.

The redox reactions occur in its entire bulk and not only at the surface. A typical cyclic voltammogram can be seen in Figure 1.12, where nearly rectangular curves are obtained and a high specific capacitance of 260 F/g is found.

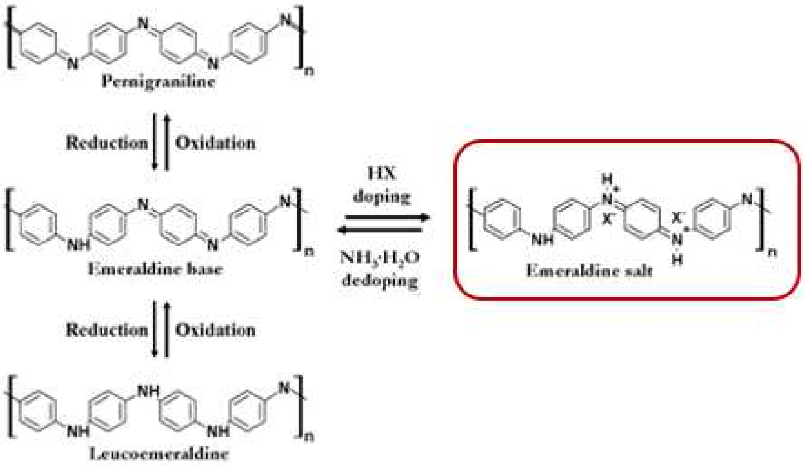

Figure 1.11.: Schematic visualization of the conduction mechanism of PANI. Emeraldine salt is the only conductive form of PANI.

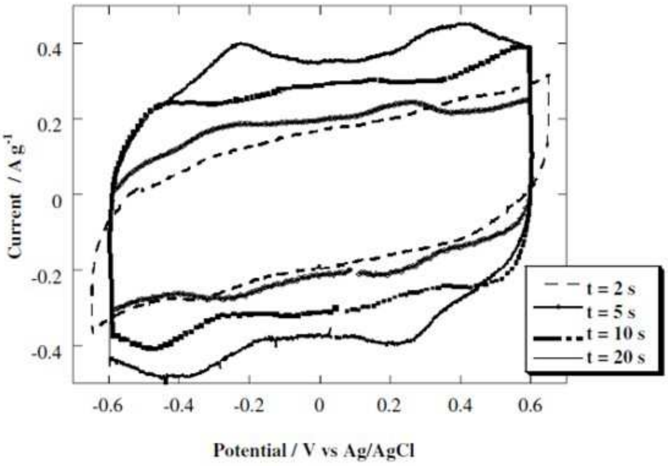

Figure 1.12.: Cyclic voltammograms recorded in 2-symmetrical supercapacitor cell based on PANI electrodes obtained for different deposition times. (Scan rate 10 mV/s). Medium: 1 M H_2SO_4. [66].

Unfortunately, swelling and shrinking may occur during the intercalation/deintercalation process. This leads to mechanical degradation of the electrode and fading of electrochemical performance during cycling, which compromises their application.

Transition metal oxide-based electrodes

In general, metal oxides can provide better electrochemical stability than polymer materials and higher energy density than conventional carbon materials.

The pseudocapacitance of transition metal oxide-based electrodes refers to the electrochemical adsorption of ions onto or near the surface of an electrode [34], leading to charge transfer. The fundamental requirements of metal oxides for application as supercapacitive electrodes are:

- good electronic conductivity
- multiple oxidation states that coexist over a continuous range, with no phase change involving irreversible structural modifications (for cyclability)
- protons that can freely intercalate into the oxide lattice on reduction (or deintercalate from the lattice on oxidation)

RuO_2 was the first electrode material thoroughly studied for pseudocapacitance. The pseudocapacitive behaviors of ruthenium oxides in acidic and alkaline electrolytes involve different reactions. In Figure 1.13, the oxide film develops a remarkably reversible cyclic voltammogram resembling the ideal rectangular shape characteristic of a capacitance that is independent of potential (i.e. EDLC cyclic voltammogram shown in Figure 1.9).

It is proved that the capacitive behavior arises on account of several overlapping redox processes involving proton and electron injection (or removal) that remain highly reversible because no phase change arises. This behavior is emphasized in poorly crystalline RuO_2, as proton diffusion is facilitated when it is hydrated [34].

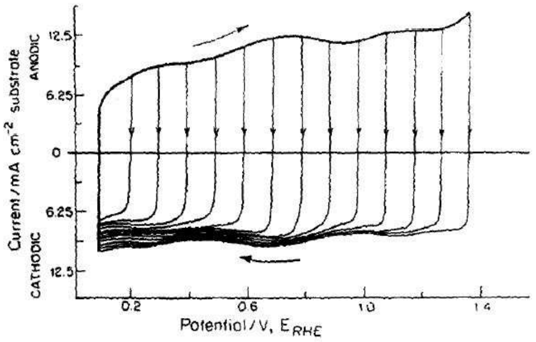

Figure 1.13.: Reversible cycling voltammetry for a RuO_2 film in aqueous H_2SO_4 [34].

However, the limited commercial availability of RuO_2 due to its high cost and high toxicity motivated research on several other metal oxides as pseudocapacitive electrodes. Other oxides such as MnO_2 [67], IrO_2 [68] and NiO [69] are considered potential candidates due to their low cost and environmental compatibility [12]. In this work, focus was made on MnO_2-based electrodes for their low toxicity and excellent pseudocapacitive properties. This will be discussed in more details in section 2.1.

1.3.3. Strategies to enhance electrochemical performances of devices

In order to enhance the electrochemical performances of devices, i.e. increase their power density and energy density, various strategies can be used. On a device scale, it is possible to vary the assemblies in order to make asymmetric devices or hybrid devices. On an electrode scale, it is possible to synthesize novel composite materials.

1.3.3.1. On the scale of the device

Asymmetric devices

In order to achieve higher energy density using supercapacitive electrodes, one strategy consists in increasing the voltage operating window. Unlike symmetric supercapacitors (or pseudocapacitors) described above, both double-layer capacitance and pseudocapacitance can be assembled in a single device to form an *asymmetric* system. This way, better energy and power performance is achievable, with extra benefits such as cycling stability. These cover a wide range of electrode combinations enabling improvements in the overall performance of the device.

The coupling of carbon based material electrodes with pseudocapacitor electrodes has gained significance due to substantial enhancement in total capacitance of the device [70, 71, 72]. For example Arbizzani et al. have developed a new asymmetric supercapacitor using a p-doped polymer as the positive electrode and AC as the negative electrode. Another example is the combination of a transition metal oxide electrode with an EDLC electrode [15, 73, 74, 16, 17]. These supercapacitors showed good specific power and significantly higher specific energy by utilizing both faradaic and non-faradaic processes to store energy. Asymmetric supercapacitors have a better cycling stability than pseudocapacitors along with higher energy and power densities than EDLCs.

A summary of the performances of various symmetric or asymmetric devices are given in Table 1.3. The examples were chosen so as to give a general idea of the energy and power densities that can be reached.

Electrode material	Electrolyte (mol/L)	C (F/g)	E_{max} (Wh/kg)	P_{max} (kW/kg)	Cycle stability	Charge retention
μC * [75]	H_2SO_4 (1)	264	20	10	10000	89
MPC * [76]	KOH (6)	225	63	32	700	100
SWCNT * [77]	$TEABF_4$	160	94	210	1000	95
RGO * [78]	$[BMIm]BF_4$	166	20	75	10000	97
RGO/RuO_2 * [79]	H_2SO_4 (1)	570	20	10	1000	98
MnO_2 || AC [80]	K_2SO_4 (0.1)	-	17	19	5000	87
MnO_2 || PANI [74]	KNO_3 (2)	-	14	120	500	80

Table 1.3.: Summary of the performances of various symmetric (*) or asymmetric devices. μC = Microporous Carbon. MPC = Mesoporous carbon. SWCNT = Single walled carbon nanotube. RGO = Reduced Graphene oxide. PANI = polyaniline. AC = Activated Carbon.

Hybrid devices : “supercapatteries”

Another strategy to enhance electrochemical performances is to associate a battery electrode with a supercapacitive electrode (EDLC or pseudocapacitive)[81, 82, 83, 84]. Batteries show higher energy densities than supercapacitors, while the power densities of supercapacitors are higher. This type of hybrids, recently proposed as supercapattery (= *supercapa*citor + ba*ttery* [84]) has a big potential to fill the gap between the normal supercapacitors and batteries. They can combine the higher energy density of batteries and specific power, short charge time, cycle life as well as reversibility of supercapacitors. They can be made EDLC electrode with battery electrode [85] or pseudocapacitive electrode with battery electrode [86, 87, 88].

To have a clearer picture of the energy and power densities achievable, a Ragone plot is presented in Figure 1.14. On this Ragone plot, it is quite obvious that conventional internal combustion devices (G, H) have the highest specific energy and power. In the electrochemical devices, fuel cells (F) and Li-ion batteries (E) present high specific energy densities to the detriment of specific power. High specific power is instead achieved by conventional capacitors (A) and supercapacitors (B). It is interesting to see the position of asymmetric supercapatteries in aqueous (I) and organic (J) electrolyte, thus proving the beneficial effect of assembling different electrodes and the enhanced electrochemical performances of supercapatteries.

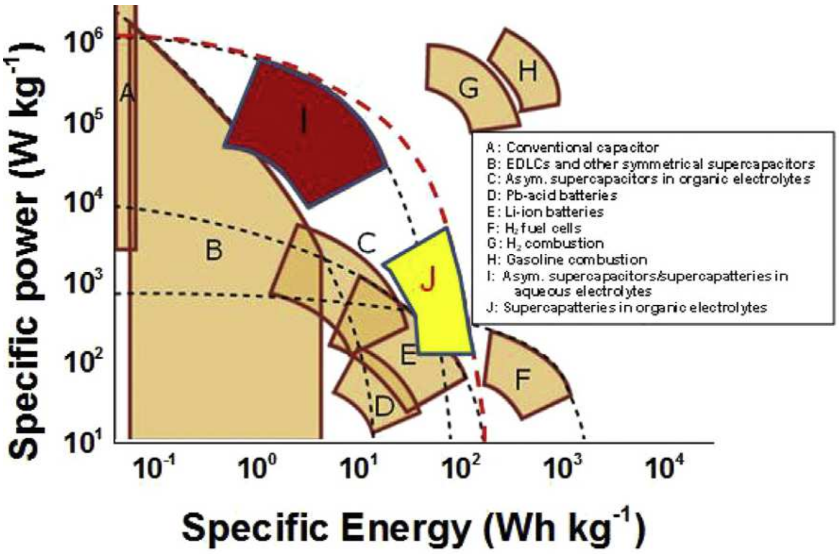

Figure 1.14.: Ragone plot of various electrochemical and internal combustion power devices [84].

1.3.3.2. On the scale of electrodes

Instead of working on the device, in which various electrodes with different charge storage mechanisms can be assembled, another strategy is to focus on the electrodes to enhance electrochemical performance. It is possible to combine the features of double layer capacitance (fast charge-discharge rate) and pseudocapacitance (high energy density). Composite electrodes integrating high surface carbon material with either metal oxides or conducting polymers have been extensively studied [89, 90, 91, 92].

For most transition metal oxides, poor conductivity is a major problem, thus limiting their performance and greatly decreasing their energy conversion efficiency as well as capacitance retention at high voltage scan rate. Consequently, composite pseudocapacitive electrodes combining conducting polymers and transition metal oxides are interesting to study. For example, Inzelt et al. have prepared RuO_2-polyaniline composites by a novel method based on the use of the chemical oxidation of aniline by ruthenium oxide [93]. By doing so, they reached capacitance of 540 F/g at 20 mV/s on 0.95 V. An infinite number of combinations can be made this way. For instance, Fauvarque et al. reported the synthesis of nanohybrid polypyrrole/Fe_2O_3 materials [94]. By optimizing the synthesis conditions, they have modified the morphology of the composite, thus improving the charge storage capacity (as shown in Figure 1.15). Indeed, the nanoparticles act as a support to the polymerization process of pyrrole and lead to a more porous structure with a higher specific surface area, which increases the accessibility of the conducting polymer sites during the electrochemical process.

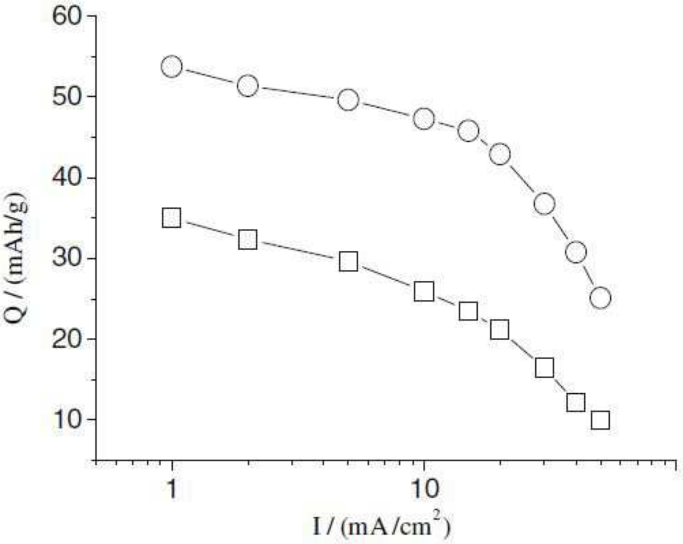

Figure 1.15.: Evolution of the capacity vs discharge current for PPy/Fe_2O_3 composite (○) and PPy (□) [94].

For most of pseudocapacitive materials (e.g. conducting polymer, transition metals etc.), poor specific surface area is a major problem. Consequently, double layer capacitive materials with high surface area (e.g. carbon-based) are used for enhancing conductivity and boosting power density of the electrode. Porous carbon materials can provide a high surface area backbone to enhance the contact between the metal oxides or conducting polymer materials and the electrolyte. The metal oxides or conducting polymer materials will further increase the capacitance by faradaic reactions.

For example, In et al have synthesized RuO_2/carbon nanotube (CNT) composite electrodes, enhancing the capacitance of CNT from 27 F/g to 295 F/g [95]. Thanks to the high specific surface area and conductivity of carbon nanotubes, the capacitance of RuO_2 could be fully exploited. Similarly, Ghosh et al. have electrodeposited V_2O_5 on a carbon-nanofiber paper and obtained capacitances of 214 F/g (at 2 mV/s on 1 V) [96]. Instead of two-dimensional carbon structures, one dimensional nanoporous carbon has also been used, along with spinel cobalt Co_3O_4 [97]. Müllen et al. have reported in situ fabrication of Co_3O_4 incorporated in nanoporous carbons via an organometallic precursor-controlled thermolysis approach. The calculated specific capacitance of these composites at a current rate of 3 A/g reaches 382 F/g.

Not only metal oxides can be incorporated in carbon structures : conducting polymers are also an alternative. Jang et al have experimented it by coating carbon nanofiber with polyaniline in a one-step vapor deposition polymerization technique. They showed that the specific capacitance exhibited a maximum value of 264 F/g when the thickness of polyaniline layer was approximately 20 nm. Another study was conducted by Liu et al. on flexible single-walled carbon nanotube. Again, owing to the high specific surface and high conductivity of carbon nanotubes, an increase of capacitance of approximately 40% was attributed to more available charge-transfer channels. Other widely studied composite electrodes are MnO_2/CNTs [98, 99], MnO_2/graphene (or reduced graphene oxides) [100], polypyrrole/CNTs [101]...

In all these examples, the enhancement of specific surface area, electronic conductivity and electrochemical activity lead to fast responses, thus making electrodes that exhibit high power and energy densities.

1.4. Conclusion

In this first chapter, a rapid introduction of all the different electrochemical storage devices was made. According to the nature of the electrodes, their charge storage mechanism will greatly influence their power and energy densities. Moreover, by assembling one to another in various conformations, greater electrochemical performances can be achieved. However, it is important to stress out that according to the application intended, not all devices would be suitable. Indeed, supercapacitors were not invented to substitute batteries in the market, but as a complementary for batteries to provide continuous power supply. Thanks to its charging mechanism, the power delivery of supercapacitors is much faster than that of a battery, which enables them to supply large amount of energy in a very short time without side effects such as heating and reducing lifetime. Another advantage is its extremely long cycle life under fast charge discharge rate. This is why supercapacitors are used when high power delivery and long cycle life are needed, such as power buffers and energy recovery systems.

Pseudocapacitors are particularly interesting for their greater energy densities, and in order to obtain higher power densities, various strategies on different scales can be considered. As seen in this chapter, on the device scale, the assembly of faradaic and supercapacitive electrodes can be very efficient. The electrodes used in symmetrical supercapacitors can be assembled in asymmetric devices, so higher energy and power densities can be achieved. On the electrode scale, the design of novel composite materials or hybrid electrodes made up of materials with different charge storage mechanisms are a route to explore. All the same, enhancing the intrinsic physico-chemical properties of the electrode materials (i.e. higher electronic conductivity, higher surface area...) can be an efficient alternative. Indeed, the active material is the key point of the electrode : by various nanostructuration, nano-architecture methods it is possible to improve their capacitance. This work focuses on this last point : the elaboration of new composite materials with enhanced intrinsic properties.

In order to do so, manganese dioxide was chosen as a starting material for its highly interesting pseudocapacitive properties, high abundance and low toxicity. In the following chapter, the advantages and limitations of manganese oxide based materials will be presented. To face the manganese oxide drawbacks, cobalt oxyhydroxides will be introduced by comparing their electrochemical properties and charge storage mechanisms. Finally, a review will be made on manganese and cobalt based composite electrodes, in order to justify the original strategy proposed for the synthesis of new electrodes.

2. State of the art on Mn and Co electrodes

Transition metal oxides are the most studied class of inorganic pseudocapacitive materials due to the easy synthesis and the electrochemical reduction of materials with high oxidation states [11].

One successful example is the application of RuO_2 pseudocapacitors in the military field due to its high specific capacitance of up to 720 F/g [35]. However, the high cost and toxicity issues of RuO_2 limit its widespread application. Therefore, tremendous efforts have been devoted to developing inexpensive and non-toxic transition metal oxides such as manganese oxides, iron oxides, nickel oxides and cobalt oxides. Among them, manganese oxides are the most investigated thanks to their environmental abundance, low cost and high capacitance (normally ranged 20-400 F/g over 1V). However, their poor cycling stability and low conductivity associated with low high-rate capability remain to be improved. Being widely used in electrocatalysts and secondary batteries, cobalt-based compounds have also been studied as pseudocapacitive electrode materials. They exhibit excellent reversible redox behavior, large surface area and high electronic conductivity.

In this chapter, the first part will present manganese-based electrodes for supercapacitors, with their charge storage mechanism and both advantages and drawbacks. A second part will describe cobalt-based electrodes and their attributes and shortcomings. Finally, the last part will review the different strategies that are likely to enhance the electrochemical performances of the electrode by combining both manganese and cobalt oxides, and present the strategy chosen for the next chapters.

2.1. Manganese-based electrodes for supercapacitors

Manganese oxides (MnO_x) exhibit relatively low cost, low toxicity, and environmental safety, as well as high theoretical capacities (1370 F/g when considering one electron per manganese atom) [102].

2.1.1. A large variety of crystal structures

The pioneering studies on the capacitive behavior of MnO_2 are focused on amorphous MnO_2, with the belief that a porous morphology can enhance the ion accessibility [103]. However, poorly crystallized MnO_2 contains inter-growths of different tunnel structures, leading to more difficult cation diffusion and resulting in higher resistance [104]. Therefore, many attempts have been made to explore the capacitance of crystallized MnO_2.

Crystallized MnO_2 materials exhibit several crystalline structures, including cryptomelane (α), pyrolusite (β), ramsdellite (γ) and birnessite (δ). The first three structures, which are schematized in Figure 2.1, have a tunnel structure : 2 x 2 octahedral units for α-MnO_2, which is the phase with the largest tunnels, 1 x 2 octahedral units for γ-MnO_2 and 1 x 1 octahedral units for β-MnO_2, the most compact and dense phase. δ-MnO_2 has a relatively open layered structure.

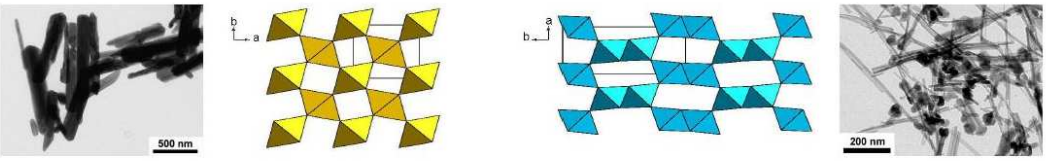

Pyrolusite, β-MnO_2. Ramsdellite, γ -MnO_2.

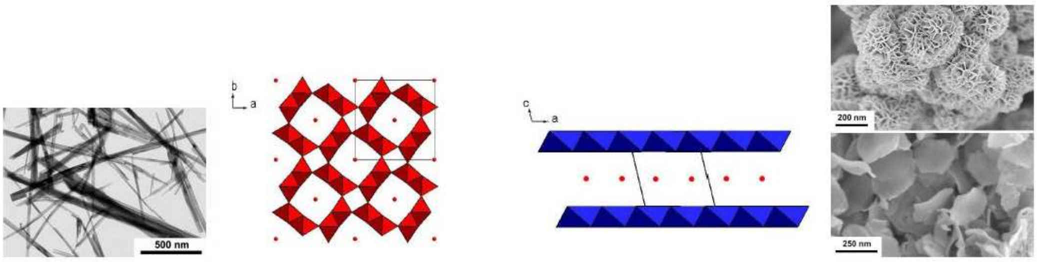

Cryptomélane, α-MnO_2 (TMO). Birnessite, δ-MnO_2 (LMO).

Figure 2.1.: Different manganese dioxide crystalline structures [105].

It has been shown that different preparation conditions result in different MnO_2 structures, as illustrated in Figure 2.2 from [106]. For example, modifying the acidity of starting aqueous medium for permanganate decomposition can lead to the synthesis of layered δ-MnO_2, or α-MnO_2, with large tunnels, or to a more compact and dense β-MnO_2. It has been shown that in a NaOH or KOH solution, the δ-MnO_2 phase is preferentially obtained. These structural changes in MnO_2 give rise to significant changes in electronic and ionic conductivity, affecting the pseudocapacitive behavior of the material.

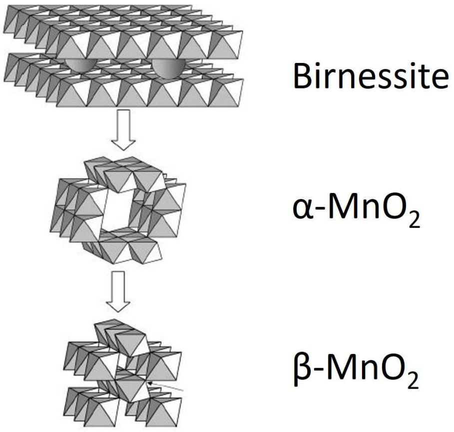

Figure 2.2.: Structural transitions induced during material synthesis of manganese dioxide [106].

On one hand, although high crystallinity can give rise to higher conductivity, loss of surface area occurs simultaneously. On the other hand, although lower crystallinity can result in a highly porous microstructure, the electrical conductivity of the resulting oxide will be low. Consequently, there should be a trade-off between electrical conductivity in the solid phase and ionic transport in the pore.

2.1.2. Comparison of electrochemical performances

Since there are many types of manganese dioxides, different physical (specific surface area, morphology...) as well as chemical (reactivity, structure) properties are expected. This will induce electrodes with different capacitive properties, as reported by Brousse et al. [104] and Munichandraiah et al. [107]. All four crystalline compounds with various structures were synthesized and tested as active material electrodes for supercapacitors. The results revealed that the capacitance is closely associated with the tunnel size of crystalline MnO_2 : as the tunnel size increases, the specific capacitance is larger. More specifically, the tunnel sizes of 1D α-MnO_2 (4.6 Å) and 2D δ-MnO_2 (7 Å) are suitable for fast insertion of hydrated K^+ cations (3 Å). However, β-MnO_2 and γ-MnO_2, with 1D tunnel sizes that are smaller than the hydrated cations, limit the diffusion process. This suggests that the tunnel space should be sufficiently large to accommodate a high rate insertion/extraction of the electrolyte ions for charge storage. Clearly the 2D structure of birnessite materials present the highest capacitance values (80-110 F/g) while 1D tunnel structures provide only up to 30 F/g. In order to fully understand the role of cations and of specific surface area as well as of pore size distribution of the MnO_2 samples, the charge storage mechanism will be discussed in the following paragraph.

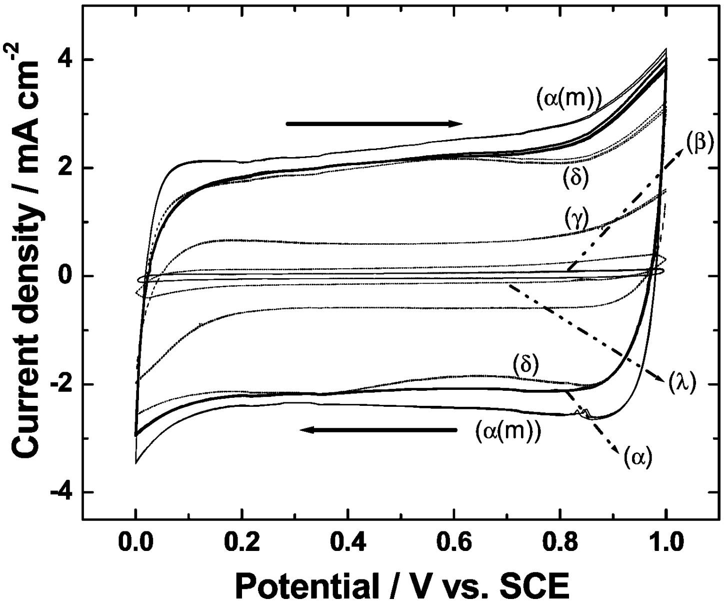

Figure 2.3.: Cyclic voltammograms of α-, β-, γ-, δ-, and λ-MnO_2 recorded between 0 and 1.0 V vs SCE in aqueous 0.1 M Na_2SO_4 at a sweep rate of 20 mV·s^{-1} [107].

2.1.3. Charge storage mechanism of birnessite-based electrodes

The capacitive charge storage mechanism of MnO_2 was first described by Pang et al. [108] as a redox process involving the surface reversible insertion and extraction of protons into/from the material, accompanied by a variation of Mn valence between Mn^{3+} and Mn^{4+}(according to Equation 2.1) :

$$MnO_x(OH)_y + \delta H^+ + \delta e^- \rightleftharpoons MnO_{x-\delta}(OH)_{y-\delta} \tag{2.1}$$

This mechanism suggests that the protons play an exclusive and crucial role in the charge storage process. However, Wen et al. soon found that the capacitance value of MnO_2 depends on the nature and concentrations of the alkali metal cations (Li^+, Na^+, K^+), regardless of pH value [109]. Furthermore, protons are likely to give rise to the formation of inert materials such as $Mn(OH)_2$ and MnOOH, which would contradict the relatively good cycling stability of MnO_2. These findings indicate that Equation 2.1 may not be the sole mechanism and cannot fully explain the behavior of MnO_2. This is why they proposed a mechanism based on the chemisorption of alkali metal cations on the surface of MnO_2 (Equation 2.2) :

$$(MnO_2)_{surface} + M^+ + e^- \rightleftharpoons (MnOOM)_{surface} \tag{2.2}$$

where M^+ represents the alkali metal cations including Li^+, Na^+ and K^+. According to Eq. 2.2, the specific capacitance appears to be proportional to the specific surface area of MnO_2. Nevertheless, in some cases, MnO_2 with smaller specific surface area exhibits a larger specific capacitance, which demonstrates that the mechanism is not as simple as described in Eq. 2.2 (see Figure 2.4).

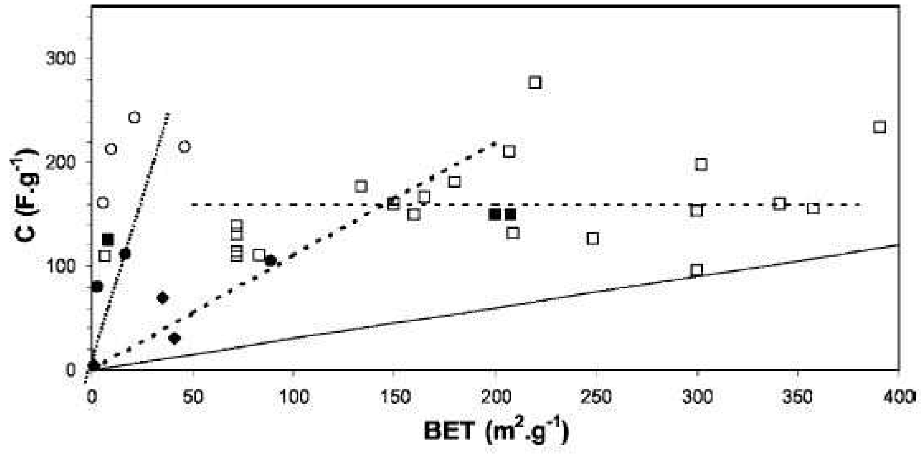

Figure 2.4.: Capacitance vs BET surface area for (●,◆) crystallized and (■) amorphous MnO_2 synthesized compared to the literature data on (○) crystallized and (□) amorphous MnO_2. Open circles correspond to the layered MnO_2 compounds. The horizontal dashed line is added as a guide to the eye to indicate the average capacitance value of amorphous MnO_2 (Reproduced from [104]).

This led to the study of Bélanger et al. who proposed a redox-based mechanism based on purely faradaic charge-transfer process limited to surface Mn atoms, as demonstrated in Equation 2.3 [102] :

$$MnO_2 + M^+ + e^- \rightleftharpoons MnOOM \tag{2.3}$$

This was confirmed by XPS, XANES and in-situ synchrotron X-ray diffraction studies where the valence change of Mn was shown to be highly reversible [110, 111]. The charge transfer upon reduction/oxidation of MnO_2 is balanced by the bulk insertion/extraction of the cations into/from the oxide structure, causing a reversible expansion and shrinkage of the lattice spacing. This has been clearly observed in the layered structure birnessite because the inter-layer distance increased from 0.71 to 0.72 nm upon oxidation, which indicates the insertion of alkali cations (Na^+) into the 2D tunnels [112]. Ghodbane et al. [113] put the “breathing” of structures upon charging/discharging in evidence by in situ synchrotron XRD measurements. Having studied the four allotropes of MnO_2, they showed clear distinct charge storage mechanisms due to their structural arrangement. For the layered structure as birnessite, the structural breathing in the c-axis direction comes from the modulation of the electrostatic interaction between negatively charged layers and intercalated hydrated cations from the electrolyte. Whereas for the 1D channel structures, charge compensation proceeds by intercalation of cations driven by size/steric considerations [114].

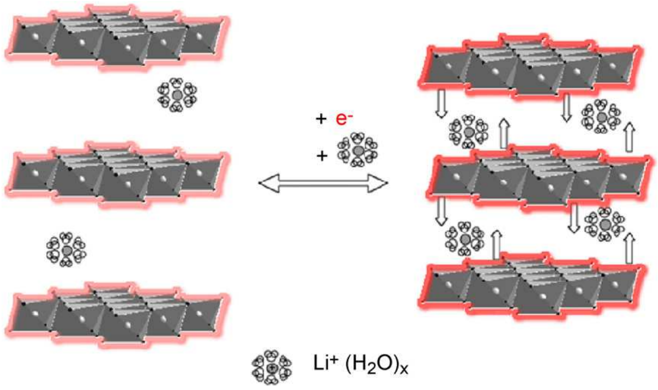

Figure 2.5.: Schematics showing the electrostatic effect of intercalated/deintercalated hydrated cations between MnO_2 layers in birnessite [113].

Overall, the charge storage mechanism of MnO_2 involves three processes :

- surface charge storage by faradaic reaction : adsorption/desorption of cations at the surface sites of electrodes (which depends on the cation size, the mobility of cations and their hydration/dehydration rate)
- bulk pseudocapacitive reaction : electrolyte cation insertion/extraction into/from the MnO_2 thin subsurface
- cation transport in the electrolyte

Therefore, the final electrochemical performances of the manganese oxides and the capacitance reached are clearly dependent on the crystallographic structure, but they are also greatly affected by other factors, such as the specific surface area of the active electrode material, as well as the electronic and ionic conductivities.

2.1.4. Limitations

Although MnO_2 presents very promising pseudocapacitive properties, the active manganese sites are limited to a thin subsurface layer of active material of a few hundred nanometers in thickness [102]. This is due to the poor electrical conductivity (10^{-5} to 10^{-6} S cm^{-1}) and slow proton and cation diffusivity in the solid MnO_2 phase.

In order to increase the specific capacitance of MnO_2-based electrodes, synthesis of nanostructured MnO_2 with novel morphologies, hierarchical porous structures, large pore volume and high specific surface area has been explored by various methods. For example, a large surface area can be achieved by introducing multilayered film electrodes containing transition-metal composite materials [115]. In this way, the formed Mn oxides have high electrochemical activities, leading to excellent electrochemical capacitance and long cycling durability. Besides, this method, introducing small amounts of other metals into MnO_2, is a proven effective way to increase the surface area. In a nanostructured nickel–manganese oxide composite, the presence of nickel oxide increases the total surface area by about 46% and the specific capacitance by 37% (Figure 2.6 [116]).

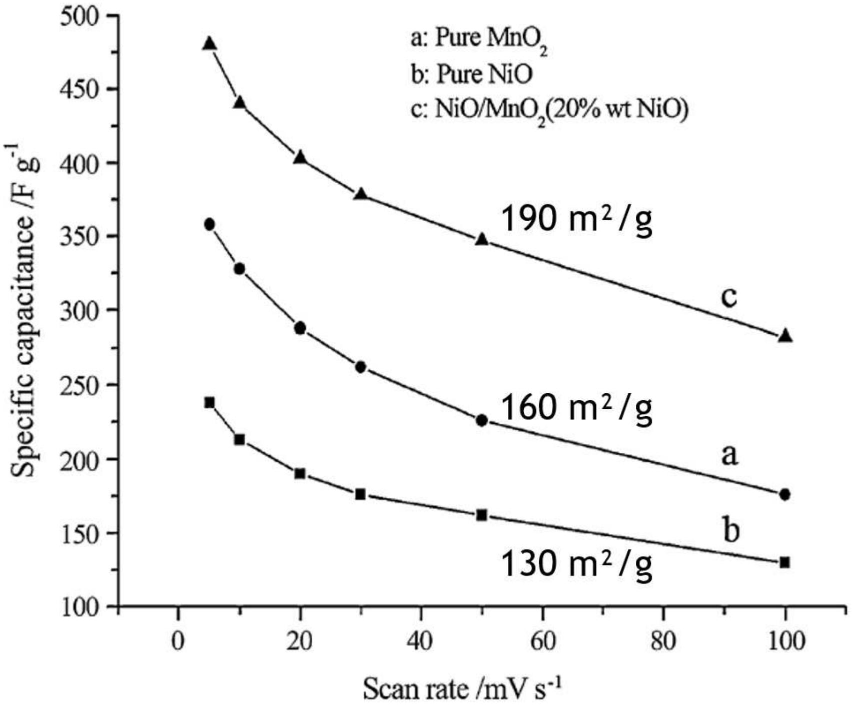

Figure 2.6.: Enhancement of specific capacitance with addition of nickel oxide to amorphous MnO_2 [116].

To address the issue of enhancing the poor electronic conductivity of manganese dioxides, adding highly conductive supports such as porous metal substrates, conducting polymers [117, 118, 119], carbon nanotubes/nanofibers/spheres [99, 120, 98], and graphene [121, 122] can be promising solutions. The presence of conductive supports not only improves the electrical conductivity of MnO_2 but also increases its active surface area. Indeed using a supporting strategy, MnO_2 can be dispersed over a large area, preventing its further growth by agglomeration and ensuring high utilization of the active materials in addition to providing double-layer capacitance. The most important feature of the supporting strategy is that these conductive supports can form a three-dimensional porous conducting network to effectively assist electron transfer and ion transport within MnO_2.

Another way to boost the electronic conductivity of manganese dioxides is to add other electronically conductive metallic elements (Ni [123], Co [124], Zn [125]...). In particular, cobalt oxyhydroxides, which were successfully used as conductive additives at the positive electrode of alkaline batteries [126], also show suitable properties for electrochemical supercapacitors. Indeed, they exhibit enhanced electronic conductivity.

2.2. Cobalt-based electrodes for supercapacitors

Being widely used in electrocatalysts and secondary batteries, cobalt-based compounds are interesting for their high theoretical capacitance value (up to 3000 F/g) [127]. The electrochemical reactions and the formation of different cobalt phases in the lower potential range involve the Co^{2+}/Co^{3+} couple (from -0.192 to 0.222 V vs Hg/HgO, measured by Behl et al. [128]). At higher potential preceding the oxygen evolution reaction (OER), the Co^{3+}/Co^{4+} couple should predominate (from 0.195 to 0.562 V vs Hg/HgO, [128]). Cobalt oxyhydroxides are electronically conductive and a lot of studies focus on their conductivity enhancement [19, 129, 126]. This will be developed in Chapter 3.

2.2.1. Spinel structure Co_3O_4

The spinel structure Co_3O_4 offers a robust crystalline architecture with three dimensional diffusion pathways. Co_3O_4 crystallizes in a normal spinel structure (space group $Fd\bar{3}m$), which can be described as a three-dimensional $[Co_2O_4]$ framework of Co^{3+} ions in edge-sharing octahedral sites (16d), with empty channels in the three space directions. Co^{2+} ions are located in tetrahedral sites (8a), at the intersection of the channels, and share only corners with the octahedra. It can exhibit battery-type behavior due to the formation of oxyhydroxides during the charge storage process in an alkaline electrolyte. The mechanism involves two reversible redox processes (equations 2.4 and 2.5) :

$$Co_3O_4 + H_2O + OH^- \rightleftharpoons 3CoOOH + e^- \tag{2.4}$$

$$CoOOH + OH \rightleftharpoons CoO_2 + H_2O + e^- \tag{2.5}$$

In the cyclic voltammogram of such materials (Figure 2.7 from [130]), the presence of several sets of broad redox peaks can be observed. This electrochemical signature combines pseudocapacitive and faradaic contributions and a maximum specific capacitance of 355 F/g was obtained at 5 mV/s. In order to enhance the performances of such materials, Guerlou-Demourgues et al. prepared non-ideal spinel phases with improved conductivity, due to the presence of Co^{4+} ions allowing an electronic delocalization in the octahedral network [19, 131]. The maximum specific capacitance of 380 F/g was obtained at 5 mV/s.

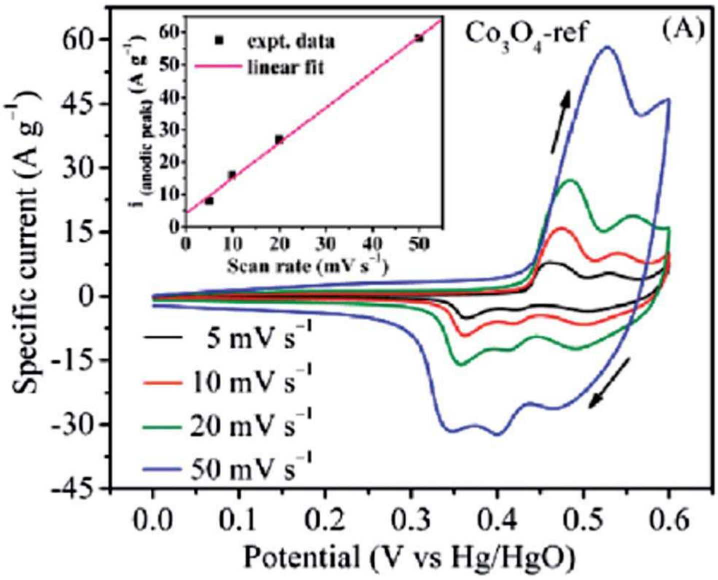

Figure 2.7.: Cyclic voltammogram for a composite electrode consisting of Co_3O_4 nanowires in 1M KOH from 5 to 50 mV/s [130].

2.2.2. Layered cobalt hydroxide $Co(OH)_2$

$Co(OH)_2$-based materials are attractive due to their layered structure and large interlayer spacing, which promises high active surface area and fast ion insertion/de-insertion. The most plausible reaction that occurs is described in equation 2.6 :

$$Co(OH)_2 + OH^- \rightleftharpoons CoOOH + H_2O + e^- \tag{2.6}$$

Most experimental studies report of $Co(OH)_2$ in alkaline electrolytes, where the material exhibits faradaic properties in a limited potential window, which in turn limits the energy and power density of their devices. Munichandraiah et al. used electrolytes based on NaOH, varying its concentration in order to evaluate best capacitance performance of electrodeposited cobalt hydroxide (see Figure 2.8 from [132]). However, alkaline solutions are corrosive and environmentally unfriendly. This is why Gebert et al. investigated the performance of cobalt hydroxides in a 1M Na_2SO_4 solution, and high values of 141 F/g were reached at a scan rate of 8 mV/s [133].

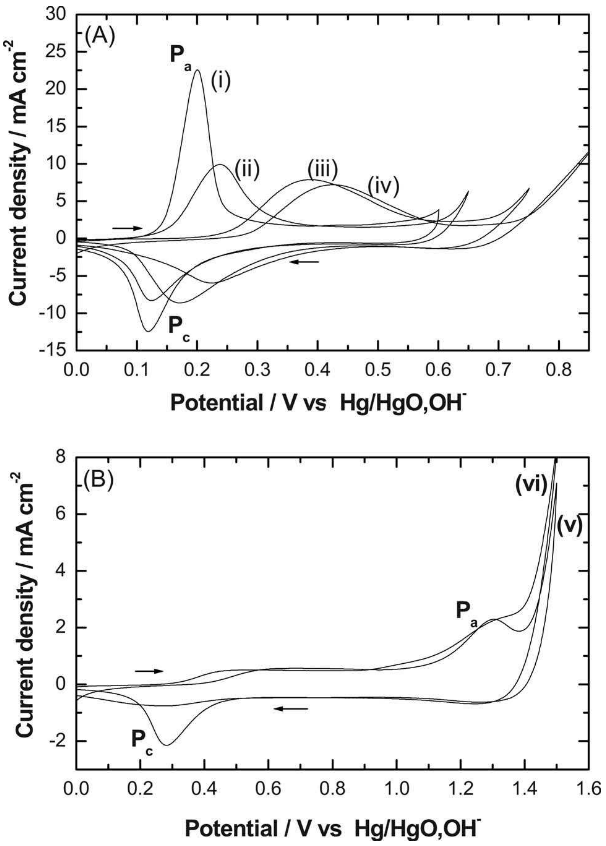

Figure 2.8.: Cyclic voltammograms of $Co(OH)_2$ electrodes at 10 mV/s sweep rate in (i) 1.0 M NaOH (ii) 0.5 M NaOH, (iii) 0.1 M NaOH (iv) 0.05 M NaOH (v) 1.0 M Na_2SO_4 and (vi) 0.1 M Na_2SO_4 [132].

2.2.3. Layered cobalt oxyhydroxide

CoOOH is well-known as a highly conductive material, with a conductivity of 5 S/cm, and a highly electroactive material. Hosono et al. have prepared layered hydroxide cobalt acetate (LHCA) nanosheets by a chemical bath deposition procedure, which were then converted to CoOOH by alkaline treatment [134]. These CoOOH nanoflakes exhibit a surface area of about 100 m^2/g and a porosity of 65%. This ensures high specific capacitance of up to 200 F/g at 10 mV/s, which is maintained at 79.1% and 63.6% of the initial value when the scan rate increases to 250 and 500 mV/s, respectively. The excellent rate capability is due to the high conductivity of CoOOH as well as to the micro/nanometer scaled morphology (Figure 2.9).

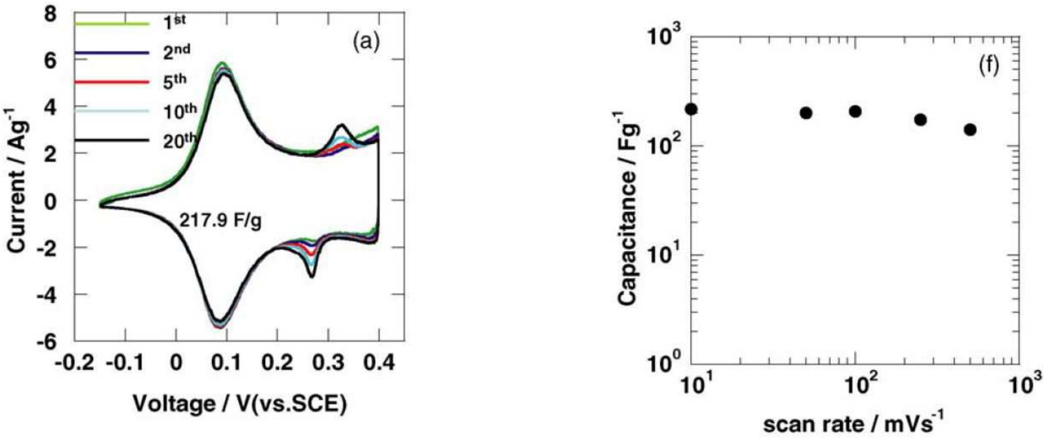

(a) (b)

Figure 2.9.: (a) CV curve of CoOOH films at 10mV/s. (b) Relationship between capacitance and scan rate [134].

The importance of surface morphology and substrate stability is essential. Jagadale et al. reported an electrodeposition method to prepare CoOOH nanoflake thin films on stainless steel and achieved a specific capacitance of 449 F/g [135]. However, a capacitance loss of 44% is observed after 10 000 cycles due to surface contamination or loss of active material from the substrate (Figure 2.10).

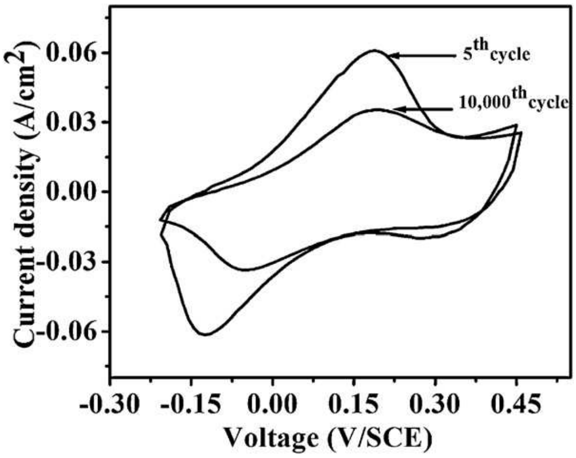

Figure 2.10.: CV curves of CoOOH thin films at 5th and 10000th cycle at 100 mV/s [135].

2.3. Strategies to improve electrochemical performances of MnO_2 electrodes

In recent years, some intensive studies have been carried out in order to enhance the electrochemical performances of pseudocapacitive metal oxide materials. In order to do so, two main strategies can be considered and will be outlined below.

2.3.1. Nanostructuration : enhancing specific surface area

The first strategy consists in increasing the specific surface area through nanostructuration. Indeed, a higher surface area means higher surface activity and thus more electroactive sites, leading to high utilization of the electrode materials.

Nanostructured electrode materials have received extensive interest due to their potential in improving the performance of supercapacitors [10, 136]. As demonstrated above, performances do not depend only on the micro-structure but also on the morphology of the active material. Hence, control over the dimensions and morphology of electrode materials is very important for monitoring their electrochemical properties. Nanostructured materials have several advantages over their bulk counterparts :

1. nanostructuration enables the design of materials with a high specific surface area, thus leading to an enhanced specific capacitance ;
2. extremely small particles can be reached, significantly shortening the path length of ion transfer and drastically enhancing the charge/discharge rate. Additionally, the small size could release stress produced from the expansion and contraction of crystalline electrodes during the charge/discharge process, and therefore improve the cycle stability ;
3. nanostructured materials can be designed to be structurally uniform, leading to untortuous channels for an easier transport of electrolyte ions

The most promising and extensively used method for achieving novel structures is the self-assembly process.

The self-assembly process can be template-assisted. In particular, a hard template can be used as scaffold for the deposition and define the shape of the desired nanomaterials. It can also act as a chemical reagent. By coupling the hard template with solvothermal/hydrothermal methods, various nanostructures can be obtained. For example, Tang et al. synthesized hierarchical hollow MnO_2 nanospheres by a template-assisted hydrothermal process [137]. In this work, SiO_2 spheres were used as the template to obtain SiO_2@MnO_2 core–shell nanospheres, and then hollow MnO_2 nanospheres were obtained after etching away the SiO_2 core in a NaOH solution (as seen in Figure 2.11.a and b). The as-prepared hollow MnO_2 nanospheres exhibited good capacitive behavior (299 F/g) and cycling stability (97.6% retention after 1000 charge/discharge cycles) in a neutral electrolyte system.

Soft templates, such as surfactants, flexible organic molecules, micro-emulsions can also act as structure-directing agents in the formation of MnO_2. Compared to the hard template method, the soft-template method has advantages such as a simple process and relatively low cost. During the self-assembly process in the synthesis of MnO_2 nanostructures, the surface tension can be largely reduced by surface adsorption of an amphiphilic surfactant. Triblock co-polymer P123 is a symmetric triblock co-polymer constituted of poly(ethylene oxide)(PEO) and poly(propylene oxide) (PPO). It is a popular structure-directing agent thanks to the unique characteristic of PPO block exhibiting hydrophobicity at temperatures above 288 K and solubility in water at temperatures below 288 K. When Mn^{2+} ions are added into the P123 solution, Mn^{2+} first coordinates with the polymer to form the Mn^{2+}–P123 complex and then MnO_2 particles grow along the polymer chains as Mn^{2+} is oxidized by $KMnO_4$, forming nanorods that pile up to secondary particles.

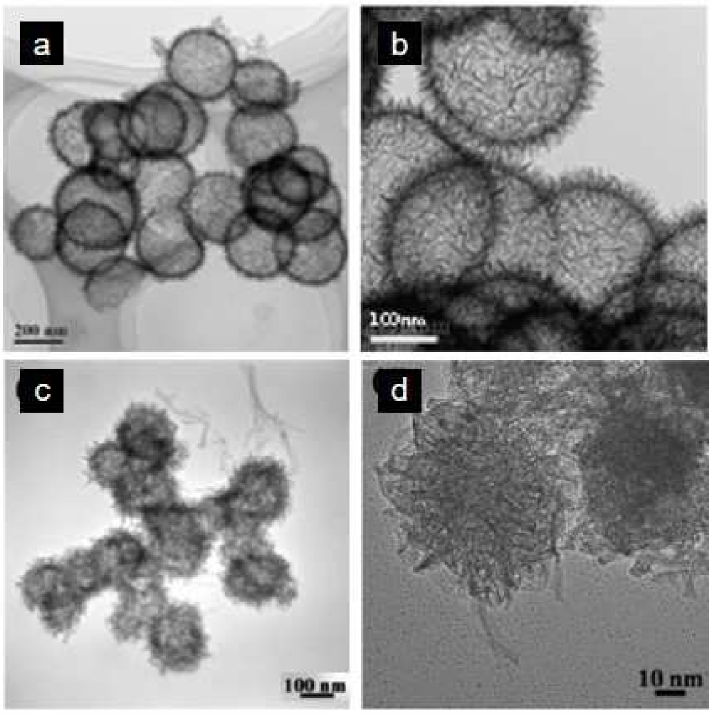

Figure 2.11.: (a) and (b) TEM images of hollow MnO_2 nanosphere synthesized with hard template and hydrothermal method [137]. (c) and (d) TEM images of MnO_2 nanostructures synthesized by self-assembly process [138].

Wang et al. synthesized porous MnO_2 via an ultrasound-microwave-intensified precipitation method with this template P123 [138]. As seen in the TEM images shown in Figure 2.11.c and d, the MnO_2 particles showed a loose sphere-network structure with tiny pores (4–5 nm in diameter) inside the spheres, and architectural mesopores and macropores among the secondary particles. The specific capacitance of the as-prepared MnO_2 was as high as 214 F/g and the capacitance reduction was less than 10% after 5000 cycles.

However, although nanostructured electrodes exhibit higher specific capacitance, they show lower cyclability than non nanostructured ones. Furthermore,their performances are still limited by the poor electronic conductivity of manganese oxides. To solve this problem, a second strategy is employed.

2.3.2. Enhancing electronic conductivity

The introduction of other materials can improve the electronic conductivity of MnO_2 and guarantee a thorough use of MnO_2. As a result, the composite electrodes can display higher specific capacitances and thus higher power densities.

Forming MnO_2-based hybrid structures with highly conductive carbons is one of the most adopted methods to improve the capacitance performance of MnO_2 electrodes. Carbon materials (carbon nanotubes, graphene, porous carbon, carbon nanofibers, carbon spheres, carbon nanofoam/aerogel) are promising candidates for such coupling with MnO_2 nanostructures. Indeed, they show good electrical conductivity, excellent mechanical, electrochemical stability and interesting supercapacitive properties when high surface area is reached.

For example, carbon nanotubes with one dimensional tubular structure exhibit high electrical conductivity, high mechanical strength, high chemical stability and high activated surface areas. Huang et al. prepared three-dimensional carbon nanotubes@MnO_2 core–shell nanostructures grown on Ni foam for binder-free capacitor electrodes, by a chemical vapor deposition and hydrothermal process [139]. Ultrathin layered MnO_2 nanosheets were uniformly coated on the surface of the carbon nanotubes (CNTs), directly grown on Ni foam. This binder-free electrode exhibits a high specific capacitance (325.5 F/g at a current density of 0.3 A/g), good rate capability (71% retention), and excellent cycling stability (91% capacitance retention per 5000 cycles).

Conducting polymers, such as polyaniline (PANI), poly(3,4-ethylenedioxythiophene) (PEDOT), and polypyrrole (PPy), are also considered as a category of promising materials to be coupled with MnO_2 for advanced electrochemical energy storage. The advantages of conducting polymers mainly include good conductivity, controllable synthesis, feasibility of forming uniform and porous structures, and good pseudocapacitive properties.

Guo and coworkers proposed a facile and scalable one-step strategy for patterning ultrathin MnO_2 nanorods (3 nm in diameter) on the surfaces of PANI nanofibers, by using polymer nanofibers and $KMnO_4$ as raw materials [140]. The loading amount and patterning of MnO_2 nanorods on the surface of PANI nanofibers was controlled by simply altering the $KMnO_4$ concentration. In comparison with the pristine PANI nanofibers, the specific capacitance of MnO_2-PANI composites has substantially increased by almost four-fold, with values as high as 417 F/g achieved.

However, the largely enhanced specific capacitance of MnO_2-carbon composite is due to relatively low mass loading of MnO_2, resulting in low energy density of the overall supercapacitor cell. Additionally, conducting polymers swell and contract substantially on charge/discharge. Consequently, they show low cycle life (typically a few thousand cycles) [60].

Another effective way to improve electrical conductivity and to boost electrochemical performance is to synthesize MnO_2-conductive metal composites. Noble metal (Au [141], Ag [142]...) as well as transition metals (Cu , Ni [143, 144]...) can be used. This study will focus on composite Mn-Co electrodes, which are presented below.

2.4. Composite manganese - cobalt electrodes

As seen previously, incorporation of different metal oxide/hydroxides with MnO_2 to fabricate MnO_2-based composite is one of the most effective ways to improve their electrochemical properties. Through optimizing the preparation parameters, generated synergistic effects may enlarge the specific surface area, facilitate electron and ion transport, add active sites or improve cycling stability. In this section, a focus will be put on reporting various works on manganese and cobalt composite electrodes.

In order to synthesize electrode materials with both elements, two distinct strategies can be considered. The first strategy consists in synthesizing one single phase of binary oxide, while the other strategy tries to combine two distinct phases in order to make a composite electrode.

2.4.1. Binary Mn - Co oxides

Mixed Mn-Co phases have been developed in all kinds of morphologies with 1D, 2D or 3D structures. A great variety of strategies are employed, from electrodeposition to solvothermal synthesis. A few examples are cited below.

Bhagwan et al. have obtained one-dimension structures (see Figure 2.12.a). They have demonstrated a simple cost effective and potentially scalable way to synthesize binary Mn-Co oxides [145]. By an electrospinning process followed by a heat treatment, a well crystallized spinel structure was obtained. The material presents a high value of 320 F/g at a current density of 1 A/g and a cyclability of 10000 cycles is obtained. The excellent performance is attributed to the high specific area of the nanofibers, their unique morphology consisting of interconnected particles with suitable space in between, which impose minimum inter-particle resistance to the electron/ion transport. Also, these voids work as extra intercalation/deintercalation sites for extra storage performance.

Another technique to obtain one-dimensional morphologies is by hydrothermal synthesis. Co-Mn nanocomposites were synthesized by Kim et al. by a hydrothermal method [146]. The samples are composed of multiphase MnO_2 with dominating ramsdellite structure. SEM images showed the obtention of nanowires of around 10-20 nm. Co increases the conductivity and electrochemical properties of the electrode. Among the various concentrations, 5 mol% of Co addition showed the highest specific capacitance (415 F/g at 0.2 A/g) and a cycling stability of 5000 cycles, with 97% of capacity retention. The variation of specific capacitance and the enhanced cycle life are shown in Figure 2.13.

Two dimensional Co-Mn binary oxides porous nanosheets can also be obtained. They were synthesized via a simple liquid phase precipitation method by Zhang et al. [147]. A pure binary $Co_{1.5}Mn_{1.5}O_4$ tetragonal spinel structure was obtained, rather than a mechanical mixture of two kinds of metal oxides (Co_3O_4 and Mn_3O_4). The SEM images shown in Figure 2.12.b display irregular nanosheets with large amounts of piled pores between the nanosheets. This nanosheet structure can shorten the electrolyte ion diffusion distance. The abundant mesopores also provide more electrochemical active sites, and facilitates ion diffusion while reducing the volume expansion in the charge/discharge cycling process. Furthermore, there is a synergistic effect on the electrochemical reaction. Owing to its high electrical conductivity, cobalt phase can decrease the impedance and increase charge transfer rate. Specific capacitance as high as 472 F/g at 0.5 A/g was reached, with 1000 cycles of almost 100% capacity retention.

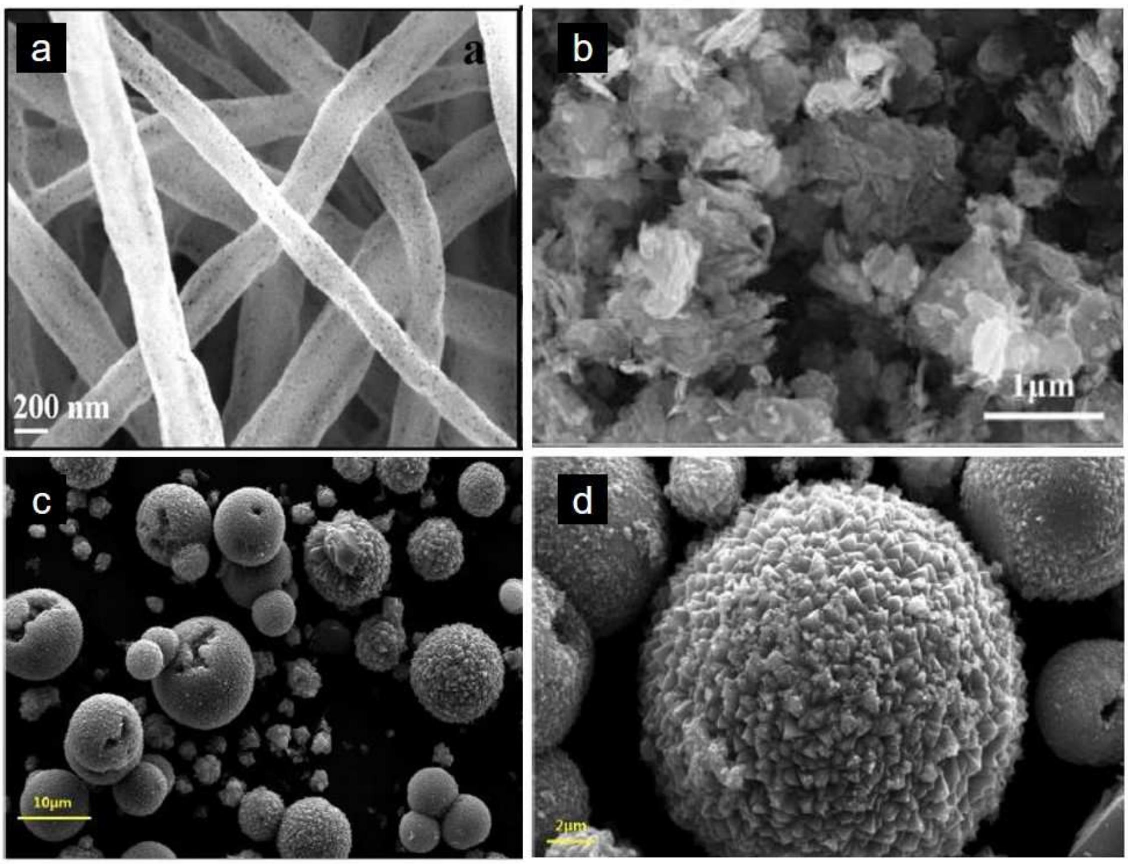

Figure 2.12.: (a) SEM image of sintered nanofibers showing morphological voids (small black points refer to porosity) [145]. (b) SEM images of $Co_{1.5}Mn_{1.5}O_4$ from [147] (c) and (d) SEM images of binary Mn-Co microspheres obtained by solvothermal synthesis [148].

Finally, three-dimensional microspheres could be obtained by solvothermal method, using urea as precipitation agent, cobalt acetate and manganese acetate as raw materials [148]. The obtained oxide shows relatively broad XRD peaks meaning they are poorly crystallized. SEM images reveal a morphology of microsphere shaped particles (see Figure 2.12.c and d) and tiny trigonal planar particles scattered onto the surface like sea urchins. It was shown that a Co:Mn ratio of 1:2 leads to the highest specific capacitance (290 F/g at a current density of 1 A/g) and 59% of initial capacitance was maintained after 500 cycles.

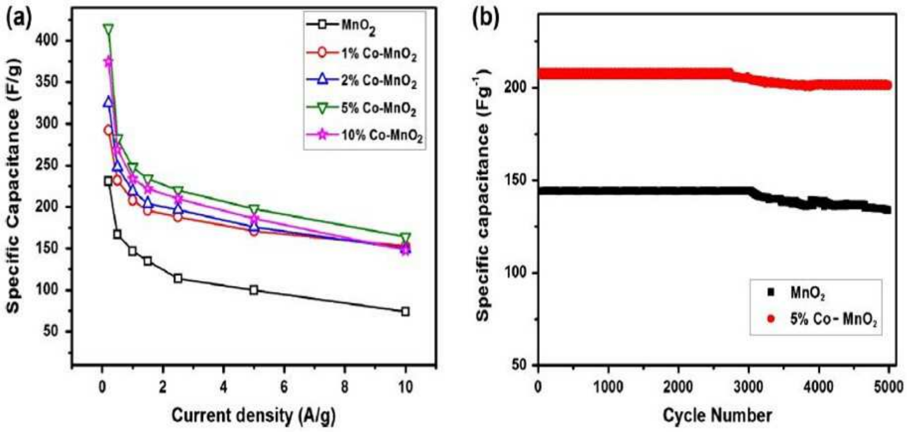

Figure 2.13.: (a) Variation of specific capacitance with discharge current density for bare MnO_2 and Co-MnO_2 electrodes presenting various Co ratios. (b) Cycle life of the MnO_2 and 5% Co-MnO_2 electrodes at current density of 5 A/g [146].

In all these syntheses, the aim is to synthesize binary oxides containing both Mn and Co in the same structure. Co acts as an additive to enhance electrochemical performances. However, it is also possible to directly synthesize composite electrodes of manganese oxides and cobalt oxyhydroxides. This will not only maintain the properties of each material but most importantly create a synergistic effect between them.

2.4.2. Mn dioxide - Co (oxyhydr)oxide composites

Instead of making binary oxides with manganese and cobalt, another strategy is to synthesize biphasic mixtures of manganese oxides and cobalt oxides. Among the various phases of cobalt oxyhydroxides, Co_3O_4 is extensively studied, as this phase exhibits promising conductivity properties. By tuning the synthesis strategy, very interesting morphologies can be obtained.

For example, Che et al. have synthesized three dimensional flower-like Co_3O_4@MnO_2 core-shell microspheres by a controllable two-step reaction [149]. First, Co_3O_4 nanosheets were self-assembled into microsphere cores. Then birnessite MnO_2 nanosheet shells were grown through the hydrothermal decomposition of $KMnO_4$. The SEM images of these core-shell structures are shown in Figure 2.14.a. Flower-like Co_3O_4 microspheres of 4-6 µm display homogeneously wrapped MnO_2 nanosheets. These MnO_2 nanosheets increase the electrochemical active sites and allow faster redox reaction kinetics. As seen in Figure 2.15.a and b, an enhanced specific capacitance of 671 F/g was achieved at 1 A/g, as well as improved rate capability. These good properties can be attributed to synergistic effects generated by both the MnO_2 nanosheets and the flower-like Co_3O_4 microspheres.

Co_3O_4 can also be grown as nanowire array on nickel foam [150] or on a steel substrate [151]. The cobalt-based nanowire array then acts as a core, as MnO_2 nanosheets are grown by reaction between $KMnO_4$ and graphitic carbon [150]. A highly ordered three-dimensional Co_3O_4@MnO_2 hierarchical porous nanoneedle array is therefore fabricated. SEM images are presented in Figure 2.14.b. The as-prepared materials exhibit high specific capacitances of 933 F/g at a scan rate of 10 mV/s, as well as long-term cycling stability (see Figure 2.15.c and d). This proves that each metal oxide contributes to the performance enhancement. Moreover, the 3D Ni foam substrate can increase the surface area of the active electrode materials, and thus help to further improve the overall energy density.

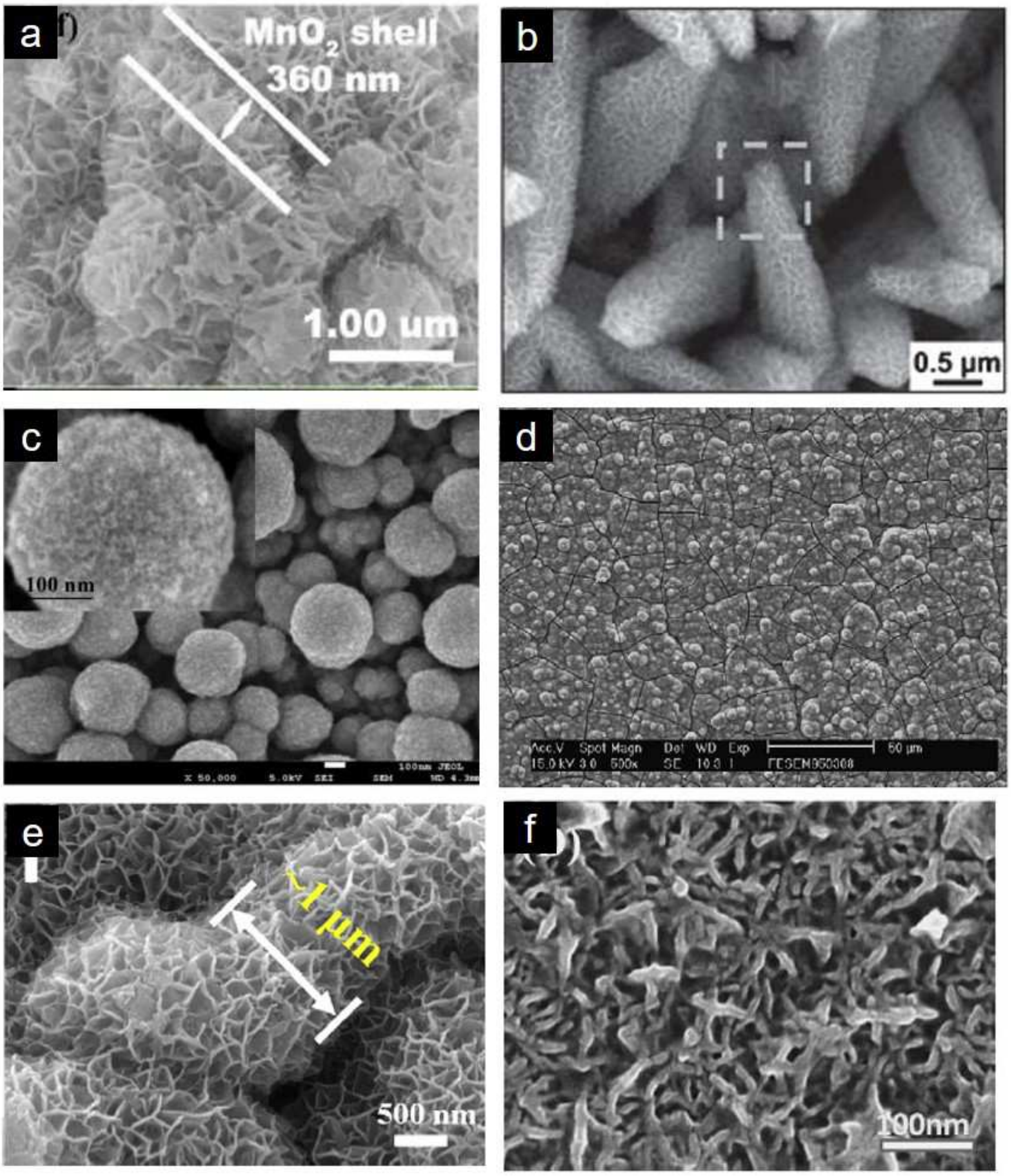

Figure 2.14.: SEM images of (a) Flower-like Co_3O_4@MnO_2 core shell microspheres [149]. (b) Co_3O_4@MnO_2 nanowire array [150]. (c) Spherical Co_3O_4 particles electrodeposited on layer of MnO_2 [152]. (d) Composite Mn-Co oxide electrode obtained by anodic deposition [153]. (e) Hierarchical porous CoO nanosheet@ultrathin MnO_2nanosheet core-shell arrays [154]. (f) Multilayered films deposited on ITO glass substrate obtained by electrostatic deposition of MnO_2 on the surface of CoOOH nanowire layers [115].

Another suitable technique to synthesize core-shell composite structures is by electrodeposition [152, 155]. Rusi et al. explored this strategy by first depositing a layer of MnO_2, followed by the ex situ electrodeposition of a second layer containing mixed metal hydroxide (cobalt or nickel) by chronopotentiometry [152]. The SEM image presented in Figure 2.14.c. shows spherical particles with a size range of 100 - 400 nm. The surface of the particles exhibits a nanoflake-like structure, which is influenced by the nucleation process of the second electrodeposited layer. The first layer of MnO_2 was confirmed to be cryptomelane while the cobalt layer crystallized in the nanosized spinel structure of Co_3O_4. The composite electrode exhibits a specific capacitance of 285 F/g at current density of 1.85 A/g. Gobal et al. also did electrodeposition of layers of cobalt and manganese oxides on top of each other on a steel substrate, without reaching the same capacitance [155].

Other composite structures can be obtained by electrodeposition and be used as a coating of a substrate. Chang et al. synthesized Mn-Co oxides by anodic deposition on graphite substrate [153]. By controlling the composition of the plating solution, the Co content ratio could be adjusted from 1 to 4.5 % (atomic). Instead of obtaining a binary oxide, the Mn oxide is nanocrystalline and its crystal structure is ramsdellite (γ-MnO_2), while the added Co exists in three different forms (Co_2O_3, CoOOH and $Co(OH)_2$). This composite oxide was examined by SEM (shown in Figure 2.14.d) and a granular surface morphology is observed as well as a uniformly distribution of Co in the deposit. The Co addition could suppress the anodic dissolution of Mn during charge-discharge cycling, and therefore greatly improved the electrochemical stability of the oxide electrode. However, it should be limited since it can cause a significant reduction in the specific capacitance of the oxide.

Other cobalt oxyhydroxides were also studied as core for three-dimensional core-shell structures. Wang et al. studied two different morphologies of CoO [154, 156] by tuning the first step of CoO synthesis. CoO is extensively used as an additive to create blue-colored in the ceramics industry [157]. However, it is also often used as a conductive agent to decrease the inner resistance of the Ni-MH battery in KOH electrolyte and improve the performance of nickel-hydroxide electrodes [158, 159]. In the first step, a CoO nanosheet array or nanowire array is grown on nickel foam through a solvothermal process. Then MnO_2 nanosheets are directly grown by a hydrothermal reaction, followed by annealing in Ar gas. It is interesting to note that the one layer thick MnO_2 nanosheet covering the CoO core forms a dense core-shell, without any modification of the structure, while enhancing the porosity and therefore the active surface area. The image is shown in Figure 2.14.e. As for electrochemical performances, shown in Figure 2.15.e, a specific area capacitance of 2.40 F/cm^2 is obtained, which is significantly higher than that obtained for a single CoO nanosheet array, with only 0.33 F/cm^2 at current density of 2 mA/cm^2. These improved performance of CoO@MnO_2 can be attributed to its unique structure. First, the highly conductive porous CoO core does not act only as a great electron collector, but also offers a high capacitance and mechanical strength. Second, ultrathin MnO_2 sheets grown on the surface of the porous CoO form a porous layer with interconnected MnO_2 walls, facilitating the penetration of electrolyte into the inner MnO_2 and CoO core.

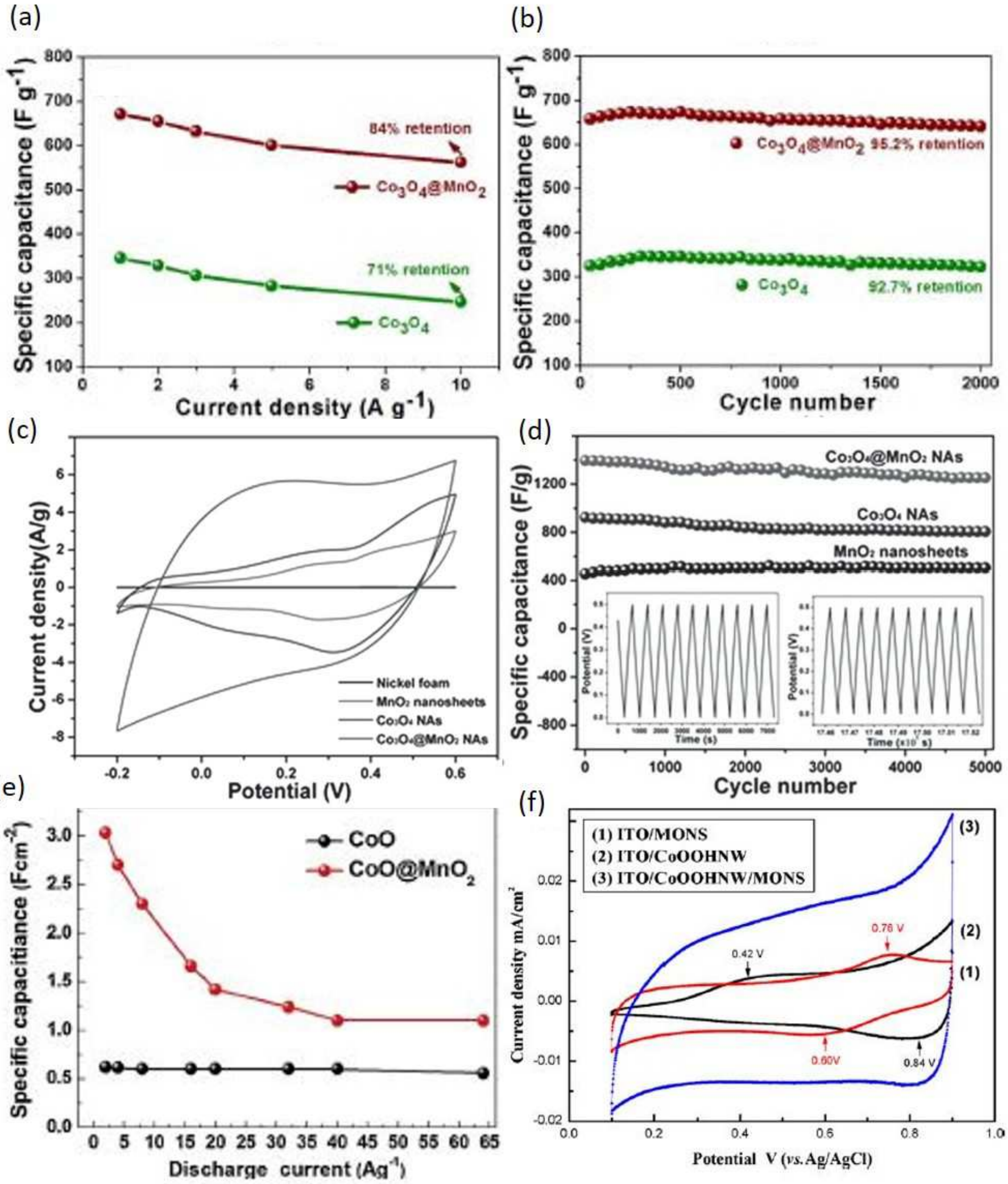

Figure 2.15.: (a) Specific capacitances at different current densities of 1-10 A/g of flower-like Co_3O_4@MnO_2 core shell microspheres [149]. (b) Cycling performance after 2000 cycles at 1 A/g of flower-like Co_3O_4@MnO_2 core shell microspheres [149]. (c) Cyclic voltammogram curves for Ni foam, MnO_2 nanosheets, Co_3O_4 nanoarrays (NAs) and Co_3O_4@MnO_2 NAs, recorded at a scan of 10 mV/s [150]. (d) Cycling performance of previous Co_3O_4@MnO_2 nanoarray [150]. (e) Specific capacitances at different current densities of CoO@MnO_2 nanowire array [156]. (f) Cyclic voltammogram of multilayered film at scan rate of 10 mV/s. MONS = Manganese oxide nanosheets. CoOOH-NW = Cobalt oxyhydroxide nanowires [115].

Bi-layered films of cobalt oxyhydroxide nanowires and exfoliated manganese oxide nanosheet are fabricated by potentiostatic deposition and electrostatic self-assembly on indium-tin oxide coated glass substrates [115]. First, an array of of cobalt oxyhydroxide nanowires is electrodeposited on an ITO substrate. Then the sample is dipped in a poly(diallyldimethylammonium) chloride solution and placed into a well-dispersed manganese oxide nanosheet suspension. The morphology and chemical composition of these films are characterized by SEM and show an irregularly distributed network of interconnected nanowires packed on the surface (see Figure 2.14.f.). As shown in Figure 2.15.f, these multilayered film electrodes exhibit excellent electrochemical capacitance properties, including high specific capacitance (507 F/g) and long cycling durability (less than 2% capacity lost after 5000 charge/discharge cycles). This indicates, once again, the advantage of using 2D layers with higher surface area to improve electrochemical stability.

All these examples of composite Mn-Co oxide materials show that combining manganese oxides with cobalt (oxyhydr)oxides improves systematically the electrochemical performances. However, they are not assembled in an ordered alternating manner. This is why an original strategy was developed to synthesize well-ordered composites at a finer scale.

2.4.3. Our strategy : exfoliation / restacking starting from lamellar manganese oxides and cobalt oxyhydroxides

After having considered various strategies to synthesize mixed manganese cobalt oxides as electrode material, an original synthesis strategy was chosen for this work. The aim is to create a synergistic effect between lamellar cobalt oxyhydroxides, which exhibit high electronic conductivity and interesting faradaic properties, and lamellar manganese oxides (birnessite-type), which are known for their excellent pseudocapacitive properties, by combining both existing materials. The synthesis of such composite materials, rather than binary oxides, is likely to truly preserve the properties of initial materials. Birnessite layered manganese oxide was chosen as starting material for this work because it exhibits the best specific capacitance, as shown in Figure 2.3). Layered cobalt oxyhydroxides were of interest for the extensive studies on their enhanced electronic conductivity (developed in details in Chapter 3).

A schematic representation of the strategy chosen for this work is presented in Figure 2.16. It consists first in synthesizing the starting layered materials chosen for their excellent complementary properties.

The layered materials can be considered as a stacking of monolayers, which are intended to be exfoliated in order to obtain “building blocks” of cobalt and manganese oxides.

Then, these bricks can be restacked upon each other by various methods. Numerous techniques have been developed to control precisely how the “building blocks” are restacked together. The goal is to finely tune the order of Mn and Co layered oxides in a large scale in order to obtain an inter-stratification of different metal oxide slabs.

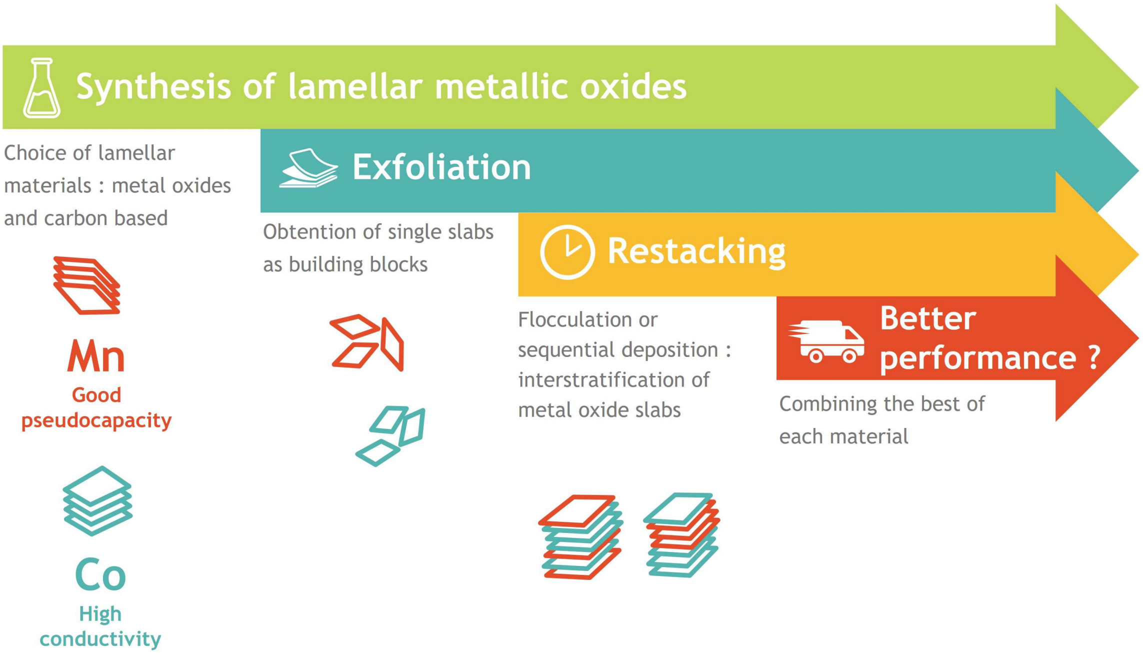

Figure 2.16.: Schematic representation of strategy synthesis chosen in this work

It is a “nano-architectural” approach of material synthesis, preserving the layered structure, whereby a synergistic effect could be achieved. The desired combination of excellent pseudocapacitive properties of manganese oxide as well as high electronic conductivity of cobalt oxyhydroxides would clearly improve the global electrochemical performances of the material. It is interesting to note that for the targeted energy storage applications, to preserve the properties of the initial materials, “building blocks” of a few layers are expected to be more interesting than monolayers. Indeed, ionic conductivity happens in the inter-layer space of manganese oxides, while electronic conductivity should be more efficient in objects containing several cobalt nanosheets.

In the following chapter (chapter 3), the synthesis of initial layered materials and their exfoliation process will be described. Various restacking methods will be detailed in the subsequent chapter (chapter 4), as well as the main characterizations and morphologies obtained. Finally, the last chapter will be dedicated to the electrochemical performances of the restacked materials.

3. Synthesis and exfoliation of layered metal oxides

Transition metal oxides have received considerable attention as electrode active materials thanks to their pseudocapacitive behavior [6, 11, 12]. Mainly employing fast reversible faradaic redox reactions, electrode materials such as $Ni(OH)_2$ [69], MnO_2 [73, 104] and Co_3O_4 [19, 160, 161] often exhibit very high specific capacitance.

However, pseudocapacitive storage sites are only limited to the surface/near-surface, excluding the bulk of materials, causing very low active material utilization and therefore low energy density. Furthermore, the kinetics of faradaic redox reactions is relatively slow : they cannot ensure a good rate capability and induce a low power density.

In order to improve those points, the alternative is to explore novel pseudocapacitive materials, where high capacitance is retained at fast charge-discharge rates without any capacity decay, thanks to high active material utilization and favorable reaction kinetics.

Recently, 2D nanomaterials, such as graphene and inorganic nanosheets, have attracted attention due to their promising physical and chemical properties for their potential applications. Indeed, 2D nanomaterials can provide short ion and electron diffusion paths, accessible electrochemical active sites, extended electrode-electrolyte interface and improved structural stability versus intercalation/deintercalation.

The best way to obtain 2D nanomaterials in large quantities is to exfoliate or delaminate layered materials [162, 163]. Such materials can be sheared parallel to the in-plane direction according to different techniques. As seen in chapter 2, we have chosen to focus our research on manganese and cobalt-based electrode materials for their complementary properties leading to promising supercapacitors. In this chapter, we will first briefly describe the layered oxide structures. In a second part, we will detail the synthesis of the layered Mn and Co oxides as precursors and give a description of their chemical and physical properties. Finally, we will explain how the precursors are exfoliated into two dimensional nanosheets.

3.1. A brief description of the manganese and cobalt lamellar oxide structures

Layered materials are defined as solids with strong in-plane chemical bonds but weak out-of-plane bonds. In particular, A_xMeO_2 layered metal oxides (A=Na, Li, H and Me= transition metal) can be described as densely packed MeO_2 slabs composed of edge-sharing MeO_6 octahedra. The MeO_2 sheets are the strong backbone of the structure in between which the alkali ions or protons are inserted. These ions can stabilize the structure by counterbalancing the electrostatic repulsion between adjacent oxygen layers. These structures can be described according to the environment of the inter-layer ion (trigonal T, prismatic P or octahedral O) and the number of slabs per unit cell (T1, T2, O2, O3, O6, P2, P3...) [164].

3.1.1. Birnessite

Birnessite is a hydrous layered manganese oxide (phyllomanganate). Its layers consist of edge-sharing MnO_6 octahedra and can be non-stoichiometric, due to the presence of vacant sites or coexistence of heterovalent Mn cations in the octahedral layer. This induces a positive charge deficiency within the layers, compensated by the insertion of cations (K^+, Na^+, Li^+, Mg^{2+}) [165, 166, 167] or ammonium-based species ($NH_4{}^+$, primary, secondary and tertiary ammoniums...) [168]. The cohesion of the structure results from electrostatic attraction between the intercalated cations and the negatively charged manganese-based slabs, as well as from a strong hydrogen bond network that is established between the oxygen atoms of the slab and the intercalated protons and water molecules. These interactions can be modified until complete delamination of the metal oxide slabs [169, 170, 171].

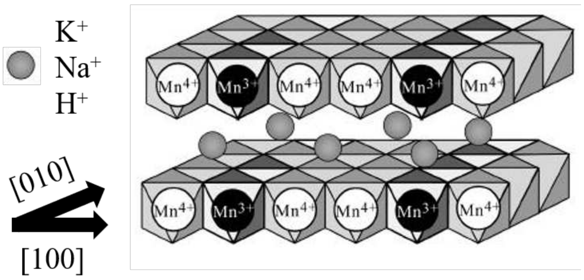

Figure 3.1.: Structure of birnessite.

Birnessite can be synthesized under a variety of physico-chemical conditions, from 0 to 1000°C, which will greatly influence the presence of vacancies, their organization and the stacking of the slabs [172, 173, 174, 175, 176, 177]. Overall, two main synthesis strategies can be considered : precipitation by the oxidation of Mn^{II} (from manganese salts) and/or the reduction of Mn^{VII} (permanganate ion MnO_4^-). Various oxidants and reductors can be used and the synthesis medium is most commonly strongly alkaline. The following table gives few examples of synthesis strategies and methods that have been developed : hydrothermal reactions (170°C in an autoclave); reduction of Mn^{VII} at high pressures, thermal decomposition at very high temperature (600-1000°C) or "chimie douce" (oxidation, reduction or sol-gel) at room temperature with optional aging (at RT or 100°C).

Chemical reaction	Reactant	Media	Reference
Oxidation at ambient temperature	$MnCl_2$, $MnSO_4$ or $Mn(NO_3)_2$	NaOH	[174, 178, 179]
Reduction and aging	Na/$KMnO_4$	Na/KOH	[180, 181]
Hydrothermal reaction	Na/$KMnO_4$	Na/KOH	[167, 173, 182, 183]
Thermal decomposition	$KMnO_4$	Dry air	[175]
Sol-gel	$KMnO_4$ + sugar or organic acid	Na/KOH	[176, 177, 184]

Table 3.1.: Synthesis conditions for birnessite (non exhaustive).

In addition birnessite is, as a rule, poorly crystallized and its complex structure may contain stacking faults and/or consist of interstratified layer types corresponding to different birnessite polytypes [178, 179, 184, 185]. Four polytypes of birnessite can be distinguished according to the symmetry of the manganese oxide slab and their stacking mode [186]. The details of each polytype will not be described in the manuscript. However, a brief description of the synthesized birnessite (from a chosen route) will be given later.

3.1.2. Lamellar cobalt (oxyhydr)oxides

Cobalt oxyhydroxides are also layered structures composed of CoO_2 slabs, consisting of edge-sharing CoO_6 octahedra. Depending on the stacking of the slabs and the nature of inter-lamellar ions, different phases exist. Three phases were especially used in the present work, their crystalline structures and cell parameters are schematically presented in Figure 3.2.

3.1.2.1. β3-CoOOH phase

The β3-CoOOH phase crystallizes in the rhombohedral system (space group $R\bar{3}m$). Due to the complexity of the rhombohedral symmetry, the structure is usually described in a triple hexagonal cell. The stacking of oxygen atoms is P3-type (AB BC CA) and the inter-layer space is composed of edge-sharing triangular-based prisms. Each prism shares one side with an octahedron of one slab and three edges with three octahedra from the adjacent slab. Inter-layer protons are located along the edges of the prisms, aligned between two oxygen atoms. In the ideal β3 phase, the cobalt oxidation state is 3.

However, it has been shown that the mean oxidation state of cobalt can increase (thanks to the presence of the Co^{4+}), which is correlated with a change of the stoechiometry of hydrogen element from 1. In these conditions, the cobalt oxyhydroxide will become more electronically conductive [18], as reminded at the end of paragraph (see section 3.1.2.3).

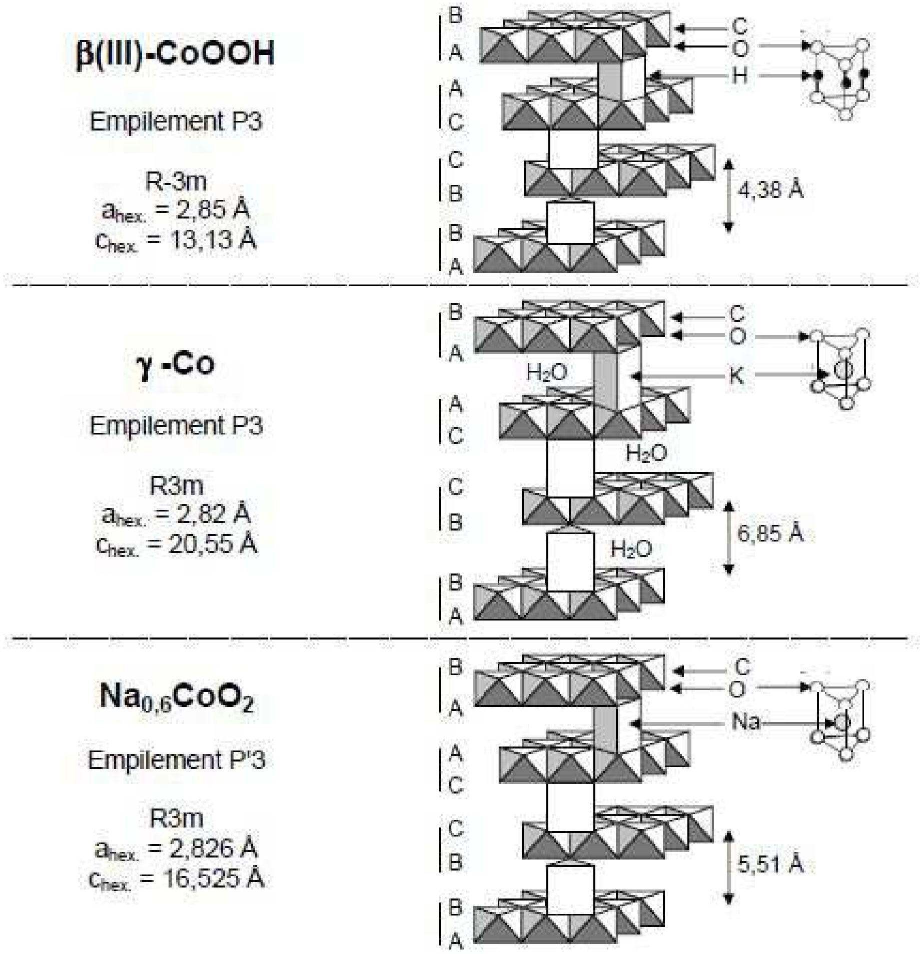

Figure 3.2.: Structures of layered cobalt oxyhydroxides from [187]: β3-CoOOH, γ-Cobalt and $Na_{0.6}CoO_2$.

3.1.2.2. γ-$A_xH_y(H_2O)_zCoO_2$ phase

The γ-$A_xH_y(H_2O)_zCoO_2$ phase (denoted as γ-Co) crystallizes also in the rhombohedral system (space group R3m), with a P3-type oxygen packing. The difference between the γ phase and the β3 phase results from the presence of alkaline ions (located in the prismatic sites) and water molecules in the interslab space, in addition to protons. The general formula is $\underbrace{A_xH_y(H_2O)_z}_{interslab-space}\underbrace{CoO_2}_{slab}$ (where A=Na^+, Li^+, K^+). The insertion of water molecules between the CoO_2 slabs induces an increase of the inter-layer spacing and therefore of the c_{hex} parameter. As values of $(x+y)$ are generally lower than 1, the mean oxidation state of cobalt is higher than 3 and can vary in the range of 3.4 to 3.7.

3.1.2.3. $Na_{0.6}CoO_2$ phase

The structure of the $Na_{0.6}CoO_2$ phase consists also of a P3-type stacking of CoO_2 slabs, but with the intercalation of sodium ions only. The structure can be roughly described with a triple hexagonal cell, but a slight monoclinic distortion can be observed : this is why the stacking is usually called P'3 and not P3. The sodium ion occupies a triangular-based prism, sharing one side with an octahedron from one CoO_2 slab, and three edges with three octahedra from the adjacent slab. As in the γ-Co phase, alkaline ions are not stoichiometrically present, thus leading to a mean cobalt oxidation state of around 3.4.

These previous three phases exhibit parent electronic conductivity behaviors. Indeed, an electronic transfer can occur over the common edges of the CoO_6 octahedra through t_{2g}-t_{2g} transfer as soon as mixed oxidation state is present. Co^{3+} has a $3d^6$ low spin configuration, with full t_{2g} orbitals ($t_{2g}^6e_g^0$). When only Co^{3+} ions are present, which is the case of ideal β3-CoOOH, no electronic transfer is possible. This leads to a semi-conductor behavior with low electronic conductivity. However, by inserting Co^{4+} ions ($t_{2g}^5e_g^0$) in the slab, the t_{2g} band is only partially filled, so that an electronic delocalization becomes possible within the CoO_2 slab, leading to metallic-like conductivity and higher electronic conductivities. From a general point of view, in the considered phases, the conductivity will increase with the Co^{4+} amount : values up to 10 $S\cdot cm^{-1}$ can be reached in the case of the γ phase. As far as the β3 phase is concerned, depending on the synthesis route (precursors, temperature, oxidation agent...), the amount of Co^{4+} ions will differ, and a wide range of electronic conductivities can be obtained.

3.2. Synthesis and characterization of layered metal oxides

In view of exfoliation, layered manganese and cobalt oxides have to be synthesized. First, we will describe the various synthesis strategies and their experimental implementation. These materials will then be characterized and their properties will be explained.

3.2.1. Experimental

3.2.1.1. Birnessite

Numerous synthesis routes are possible to obtain birnessite. In the following work, the most “classic” route has been chosen for practicality, low environmental impact (room temperature and pressure) and high yield : the method developed by Ching [188]. The overall synthesis process is schematized in Figure 3.3.

First, Na-birnessite (K-birnessite) is synthesized, corresponding to manganese oxide layers with sodium (respectively potassium) ions intercalated in between. To achieve this, $MnSO_4$ is dissolved in water, followed by the addition of a strong alkaline solution (NaOH or KOH 6M). There is a spontaneous precipitation of a tan colored slurry of $Mn(OH)_2$ (pyrochroite). It is then oxidized by $K_2S_2O_8$ (slowly added in the powder form) in order to obtain Na-birnessite or K-birnessite (respectively noted Na-birn and K-birn). The reaction between $Mn(OH)_2$ and $K_2S_2O_8$ must proceed very slowly to prevent the formation of a by-product of layered manganese oxide (Mn_3O_4) called haussmanite. The resulting brown-black slurry is stirred for an additional 30 minutes, before being centrifuged and washed three times with water. The brown-gray solid corresponding to Na-birnessite (K-birnessite) is then dried at 70°C in air.

Once Na-birnessite (K-birnessite) is prepared, the alkaline ions must be exchanged with protons, to facilitate the subsequent exfoliation step (as explained in section 3.3.1.1). This topotactic ion-exchange reaction, during which the MnO_2 slabs are preserved (except for the possible formation of manganese vacancy), takes place in acidic medium (mainly HCl 0.1M). The powder is stirred in HCl (0.1 M) for a certain duration, then it is recovered by centrifugation and washing with water. The dark brown solid is then dried at 70°C in air. The influence of the stay of the powder in acidic medium was carefully studied. The experiments show that the reaction duration does not affect the structure of the final protonated phase, but after ten days of stirring, the yield of protonation changes drastically : it decreases from 80 % after one day of protonation down to 60 %. In order to maximize the amount of protonated birnessite recovered, the reaction was completed for one day only. The phases obtained after the acidic treatment of Na-Birnessite and K-Birnessite will be denoted as H_{Na}-birn and H_K-birn respectively.

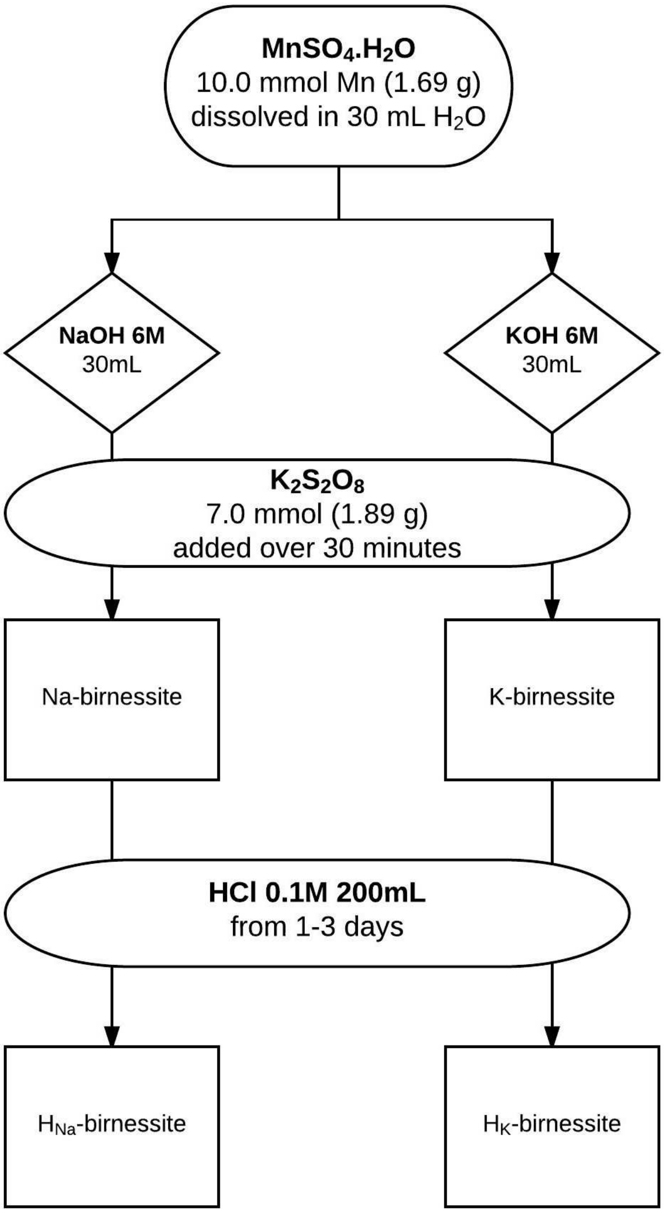

Figure 3.3.: Schematic representation of synthesis process of birnessite.

3.2.1.2. Cobalt oxyhydroxide

It is of our best interest to synthesize nanoparticles of layered cobalt oxyhydroxide with the highest amount of tetravalent cobalt as possible (see section 3.1.2.3), in order to obtain the highest electronic conductivity [18]. According to the work developed in the laboratory by M. Butel [189], layered H_xCoO_2 cobalt oxyhydroxides can be synthesized via two strategies. Both have been explored in order to study their impact on the structure, morphology, oxidation state and properties of the obtained materials. For a clearer idea, a schematic overview of the different strategies carried out to obtain the desired nanometric layered cobalt oxyhydroxide phases is presented hereafter in Figure 3.4.

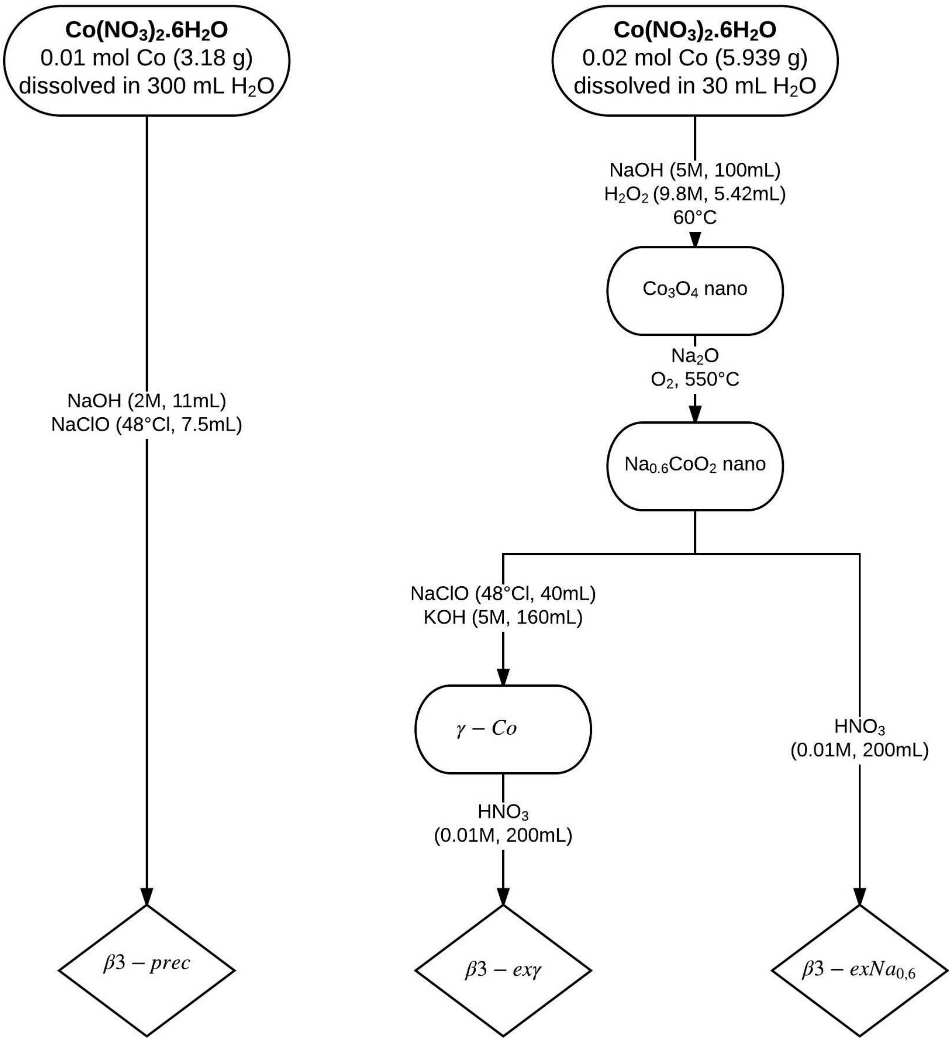

Figure 3.4.: Schematic representation of synthesis strategies for cobalt oxyhydroxides.

The first route, similar to the synthesis of birnessite, consists in a precipitation in an alkaline oxidizing medium, starting from Co(II) solutions. It can be divided in two steps : precipitation and aging. First, a cobalt salt, (Cobalt(II) nitrate hexahydrate, $Co(NO_3)_2.6H_2O$) is dissolved in water before being added drop-wise to NaOH. This leads to the formation of a blue precipitate corresponding to the hydrated phase α-$Co(OH)_2{\cdot}zH_2O$. Being highly unstable, it is immediately converted into a non hydrated pink-colored β-$Co(OH)_2$ phase. Secondly, due to the presence of atmospheric oxygen, this phase is spontaneously oxidized into a $\beta3$-H_xCoO_2 cobalt oxyhydroxide (denoted as $\beta3$-prec). Since this oxidation by air is slow at room temperature, a strong oxidizing agent is added (NaClO, 48° Cl i.e. 4M) in order to shorten the duration of the reaction, which must be particularly controlled to obtain nanosized particles. After centrifugation, the material is dried overnight at 70°C.

Another strategy to obtain target oxyhydroxides is to carry out reactions at low temperature, from lamellar nanometric $Na_{0.6}CoO_2$ precursor phases [18]. First and foremost, these starting phases are prepared by heating a nanometric spinel cobalt oxide phase, synthesized following the protocol developed previously by the group [160], in presence of Na_2O at 400°C for 1 hour (according to the following reaction 3.1) :

$$\frac{1}{3}Co_3O_4 + 0.3Na_2O + \frac{1}{15}O_2 \rightarrow Na_{0.6}CoO_2 \tag{3.1}$$

The subsequent reactions involve redox and exchange reactions. Since they are carried out at room temperature, the cobalt oxide slab is preserved, while the content of the interslab space can be modified depending on the reaction conditions. From the $Na_{0.6}CoO_2$ precursor phase, two distinct routes have been explored, both leading to β3-H_xCoO_2 phases. In the first route, the $Na_{0.6}CoO_2$ precursor is directly introduced into an oxidizing acid, HNO_3 (10^{-2}M) stirred for 15 hours. After centrifugation, the material is dried overnight at 70°C. The phase thus obtained is denoted as β3-ex$Na_{0.6}$. In the second route, the $Na_{0.6}CoO_2$ precursor phase is introduced into an oxidizing alkaline solution (4M KOH, 0.8M NaClO), leading to a γ intermediate phase (denoted as γ-Co), which is in turn hydrolyzed in the presence of HNO_3(10^{-2}M), to give a β3-H_xCoO_2 type phase after centrifugation and drying at 70°C overnight. The latter is denoted as β3-exγ.

3.2.2. Structure

3.2.2.1. Birnessite structures

The X-Ray diffraction patterns of the manganese-based materials (pristine and protonated phases) are shown in Figure 3.5. It should be noticed that the purpose of the present work was not to perform an accurate study of the structure of the materials. The diagrams were therefore only indexed on the basis of a profile matching. The indexation results are gathered in Table 3.2.

Phase	Symmetry	Space group	Parameters (Å)	$d_{interslab}$ (Å)
Na-birn	Monoclinic	C2/m	a = 5.1728(4) b = 2.8491(2) c = 7.3233(6) β = 103.178(8)°	7.127
K-birn	Hexagonal	P6	a = 2.934(1) c = 7.076(2)	7.076
H_{Na}-birn	Hexagonal	P-3m1	a = 2.8426(6) c = 7.278(2)	7.278
H_K-birn	Hexagonal	P-3m1	a = 2.8231(6) c = 7.262(4)	7.262

Table 3.2.: Symmetry, space group and lattice parameters (Å) of layered manganese oxides synthesized in this study.

Except for the diagram of Na-birn that is indexed with a monoclinic cell, the other diagrams are all indexed with a hexagonal cell, which is in accordance with various data reported in the literature [166, 177]. In all cases, the inter-reticular distance of the lowest angle peak (001) corresponds to the spacing measured between the midpoints of adjacent manganese oxide sheets. In the diagrams indexed with an hexagonal cell, the inter-reticular distance of the (110) line represents half the distance between two adjacent Mn atoms within the hexagonal slab, and is therefore closely linked to the average oxidation state of manganese within the slabs. When relevant, the sizes of the coherent domains were calculated by the Debye Scherrer method on the basis of the integral width of the (001) and (110) lines (see Annex A.1). They are reported in Table 3.3. The sizes along (001) and (110) respectively can be correlated to the thickness and the width of the coherent domains.

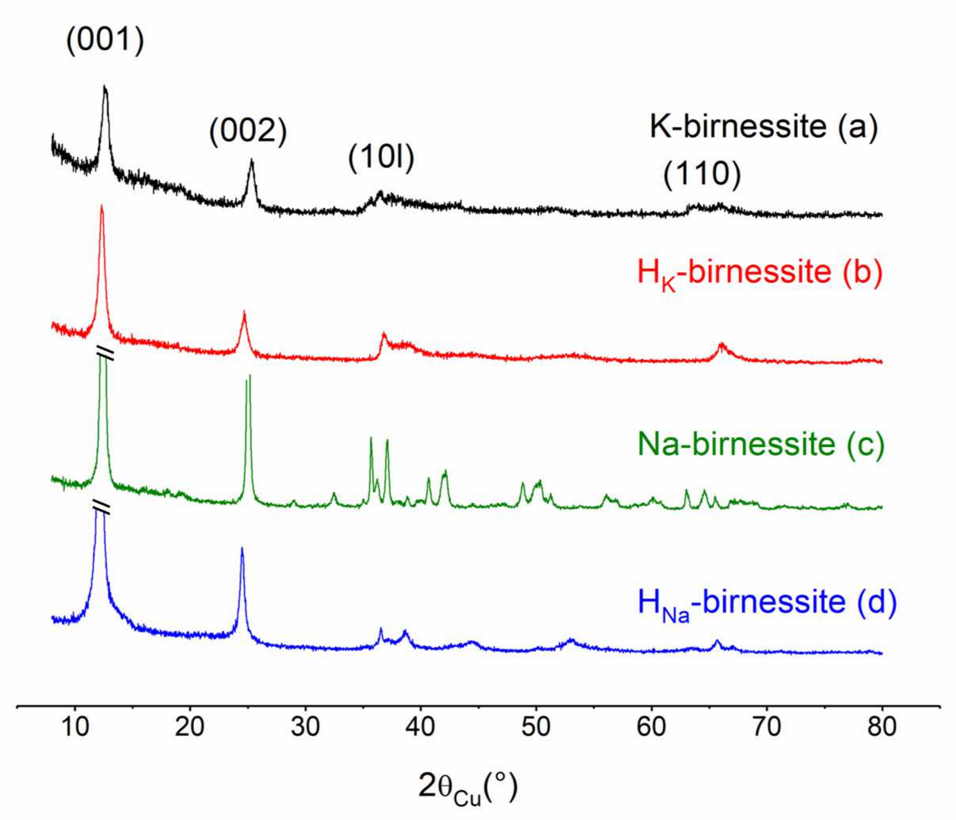

Figure 3.5.: Powder X-Ray diffraction patterns of the layered manganese oxide phases synthesized. (a) K-birnessite. (b) Protonated K-birnessite : H_K-birnessite. (c) Na-birnessite. (d) Protonated Na-birnessite : H_{Na}-birnessite.

Influence of alkaline counter-ion on birnessite structure (Figure 3.5.a and c)

Although very similar in their general shape, the X-ray diffraction patterns of initial materials show various differences. First and foremost, the diagram of K-birn exhibits wider and less well-defined lines than Na-birn. This can be first correlated to the fact that, for K-birn, the coherent domains are significantly smaller, as shown in Table 3.3. This behavior will be correlated to the morphology of the materials, presented in section 3.2.4.1. Moreover, the structure of K-birn is very disordered, with wide (10l) and (11l) “bands”, which are significant of turbostratic stacking of the slabs and/or presence of several stacking polytypes, as commonly observed in birnessites.

Furthermore, as shown in Table 3.2, the interslab distance in K-birn is slightly shorter than in Na-birn. This is at first sight counter intuitive because, in size, potassium ions are much bigger than sodium ions : their ionic radius is 1.51 Å, compared to 0.99 Å for sodium [190]. This has to do with the higher amount of interlamellar sodium, as will be shown in the analysis section (see section 3.2.3), and also with the hydration of the cations : according to the nature of the cation, the radius and hydration state are different. Since the charge/size ratio is larger for Na^+ than for K^+, the polarizing effect is higher for Na^+ and thus, leads to a larger hydration shell for Na^+, which tends to increase the interslab space.

Coherent domain	Na-birn	H_{Na}-birn	K-birn	H_K-birn
Thickness	43	17	10	11
Width	51	15	8	6

Table 3.3.: Average coherent domain sizes (nm) of the various synthesized birnessite phases. The domains are considered as platelets. The thickness is evaluated from the (001) line. The width is evaluated from the (200) line for monoclinic symmetry and the (110) line for hexagonal symmetry.

Effect of protonation on birnessite structure (Figure 3.5.b and d)

The general shape of the X-ray diffraction patterns is preserved after protonation step, which suggests that the acidic hydrolysis of birnessite is in fact a topotactic reaction : the lamellar structure of the material is maintained, while the size of coherent domains is barely modified. Only inter-layer Na^+ and K^+ cations are exchanged for protons, which has to be correlated with the increase of the inter-layer distance (0.15 Å starting from Na-birn and 0.19 Å starting from K-birn, from Table 3.2).

This behavior, in addition to the fact that the protonated phases exhibit an hexagonal symmetry, is in full agreement with data reported by several authors [178, 186, 191, 192]. It is indeed well-known that, in our synthesis conditions (low temperature, oxidation of a divalent manganese solution), the metallic slabs of the pristine Na-birn and K-birn phases are composed of Mn^{3+} and Mn^{4+} ions, with very few metal vacancies. Nevertheless, when these phases are treated at low pH, several authors have shown that a number of Mn^{3+} go through a disproportionation reaction ($2\ Mn^{3+} \rightleftharpoons Mn^{4+} + Mn^{2+}$). The resulting Mn^{2+} are removed from the material, thus leading to vacancies in the slabs.

Concerning Mn^{3+} that did not go through disproportionation, some Mn^{3+} ions will tend to migrate into the interslab space, leaving some vacancies within the slabs, so that the symmetry is maintained (in the case of K-birn) or turns (in the case of Na-birn) to hexagonal. This “redistribution” of manganese induces an increase of the average oxidation state of manganese within the slabs, therefore a contraction of the slabs which, due to antagonistic bond effect, leads to an increase of the interslab distance, as experimentally observed. This is fully consistent with the chemical analysis results, presented afterwards, which show the increase of the manganese oxidation state. This tendency is also confirmed by the fact that, as an example in the case of K-birn, after protonation, a strong decrease of the a_{hex} parameter (corresponding to the Mn-Mn distance) has to be noticed (see Table 3.2); it is also illustrated by the shift of the (110) line in Figure 3.5. This is due to lower ionic radius of Mn^{4+} compared to Mn^{3+} one.

3.2.2.2. Cobalt oxyhydroxides

Figure 3.6 presents the X-ray diffraction patterns of the pristine $Na_{0.6}CoO_2$ and γ phases and of the three final $\beta3$ cobalt oxyhydroxides (for exfoliation purpose), synthesized according to the processes summarized in Figure 3.4. As described in the introduction part, the X-ray diagrams of these phases can be indexed with a triple P3-type hexagonal cell. The cell parameters (determined from profile fitting), as well as the sizes of the coherent domains in the (001) and (110) directions (calculated by the Scherrer method) are gathered in Table 3.4. The interslab distances, equal to $c_{hex}/3$, are also reported in the table. The sizes along (001) and (110) can be respectively correlated to the thickness and the width of the coherent X-Ray domain.

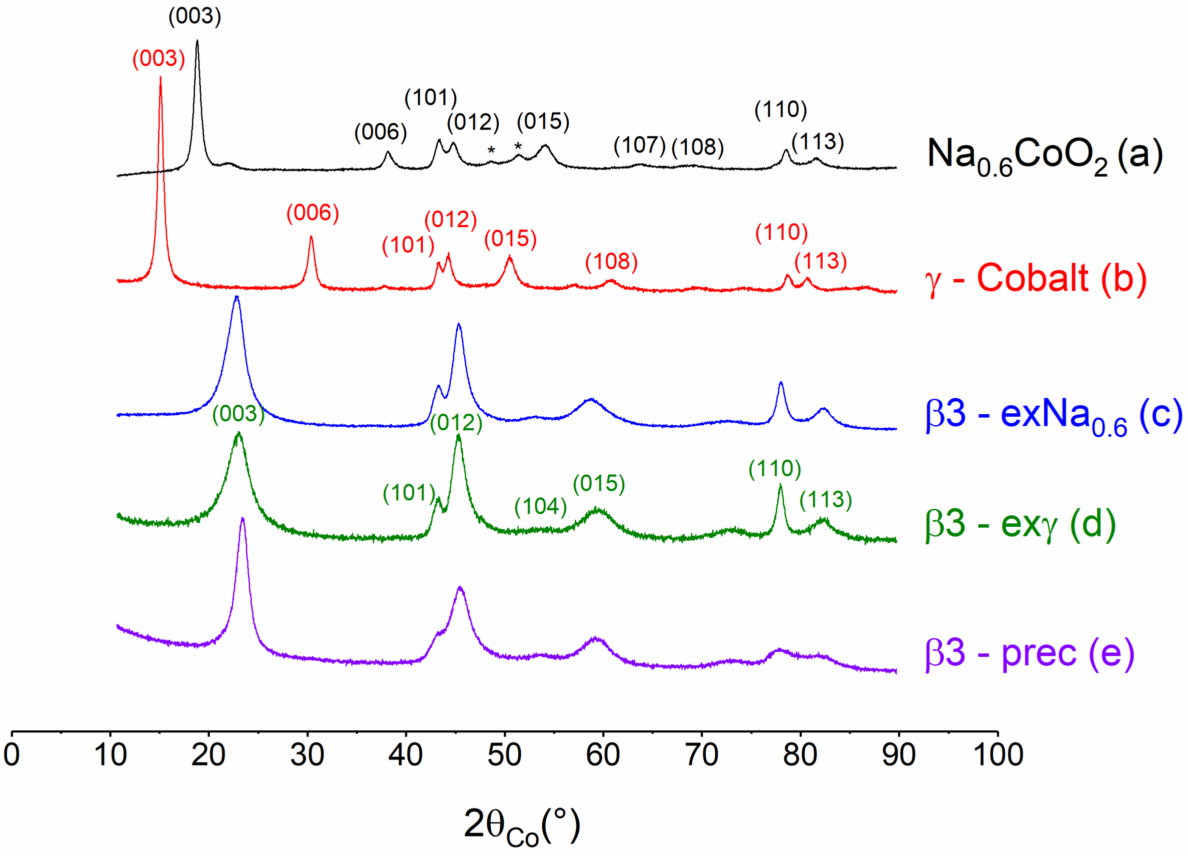

Figure 3.6.: Powder X-Ray diffraction patterns of the layered cobalt oxyhydroxide phases synthesized. (a) $Na_{0.6}CoO_2$. (b) γ-Co, synthesized by ion-exchange from $Na_{0.6}CoO_2$. (c) $\beta3$-exγ, synthesized from acidic hydrolysis of γ-Co. (d) $\beta3$-ex$Na_{0.6}$, synthesized by acidic hydrolysis of $Na_{0.6}CoO_2$. (e) $\beta3$-prec, synthesized by precipitation of cobalt salts in alkaline oxidizing media. The lines with * correspond to impurities of $NaHCO_3$ (which pass into solution during the subsequent steps).

Influence of the synthesis route on the $\beta3$-Co structures

The different synthesis routes described above lead to three different $\beta3$-Cobalt phases : $\beta3$-exγ, $\beta3$-ex$Na_{0.6}$ and $\beta3$-prec. These materials exhibit cell parameters which are close to each other. As we can see in Figure 3.6 (c, d and e), the β3-exγ and β3-exNa$_{0.6}$ phases, prepared by topotactic exchange from the two pristine phases, exhibit X-ray diagrams with similar shapes and line widths. Their coherent domains, very close in size, are very thin (2 - 5 nm) with a width around 9 - 11 nm. The diagram of the β3-prec phase, which is directly prepared by oxidizing precipitation, is a little bit different from the other two ones. First, it exhibits a narrower (003) line, which is a sign of a slight increase of the thickness. As a matter of fact, as was previously shown by Butel [18], the β3-exγ and β3-exNa$_{0.6}$ phases are characterized by a slight inter-stratification, which corresponds to the stacking, among major β3 domains, of slab domains with γ or $Na_{0.6}CoO_2$ type. The interslab distance being higher in these latter domains than in β3 domains, the presence of these defects explains why the c$_{hex}$ parameter (or the interslab distance) is a little bit higher in the these β3-exγ and β3-exNa$_{0.6}$ phases than in the β3-prec phase. Second, the diagram of the β3-prec phase shows much wider (10l) and (110) lines than the other two cases, revealing higher crystal disorder within the slabs.

It is a direct consequence of the synthesis routes, since β3-exγ and β3-exNa$_{0.6}$ are both issued from $Na_{0.6}CoO_2$ synthesized at high temperature, which is more ordered than the precipitated β3-prec phase. The extended formulas of these phases are presented later, in Table 3.5.

Phase	a$_{hex}$ (Å)	c$_{hex}$ (Å)	d$_{interslab}$ (Å)	Size (nm) along (001) (thickness)	Size (nm) along (110) (width)
$Na_{0.6}CoO_2$	2.8308(2)	13.414(1)	5.47	10	11
γ-Co	2.8257(2)	20.584(3)	6.86	11	13
β3-exγ	2.8481(2)	13.500(4)	4.50	2	11
β3-exNa$_{0.6}$	2.8465(1)	13.640(2)	4.54	3	9
β3-prec	2.8511(2)	13.257(1)	4.42	5	2

Table 3.4.: Hexagonal cell parameters and average size of coherent domains along (001) and (110), determined by the Scherrer formula, for the various cobalt oxyhydroxide phases prepared. The profiles of the X-ray diagrams were fitted with the $R\bar{3}m$ space group for $Na_{0.6}CoO_2$ and γ phases and the R-3m space group for the β3 phases (triple hexagonal cell).

3.2.3. Chemical analysis

In order to study the influence of synthesis routes on their composition, both birnessite phases and cobalt oxyhydroxides have been analyzed by ICP (elements Co, Mn, Na, K), CHNS (element H) and iodometric titration, to evaluate the oxidation state of cobalt and manganese. All these analytical techniques are described in the Annex A.2. On the basis of these measurements, the chemical formulae of the materials were determined in the following way (see more details in Annex A.2.4). Starting from the MeO_2 slab (Me=Co, Mn), the -IV charge of the two oxygen atoms is balanced by the mean oxidation state of the metal ion determined by iodometric titration and by the necessary amount of monovalent alkaline cations (K^+, Na^+), determined by ICP. The quantity of protons H^+ is deduced by taking into account the total charge neutrality. Then the amount of water is determined with the CHNS data. The results are reported in Table 3.5.

In the case of the manganese birnessite phases (Table 3.5.a), during the protonation reaction, the Na(K)/Mn ratio drops while the H/Mn ratio increases. This composition evolution as well as the structural study of the previous paragraph confirm that HCl solution is very efficient for extracting Na^+ and K^+ ions from Na or K-birnessite without a significant change in morphology and crystallinity. The change in the average oxidation state of manganese during protonation has to be noticed. It increases from 3.52 to 3.63 in the case of Na and from 3.53 to 3.56 in the case of K. This behavior was already observed by several authors and was previously explained in section 3.2.2.1. It results from the partial disproportionation of Mn^{3+} to Mn^{4+} and Mn^{2+}. The latter Mn^{2+} ions, unstable for steric reasons, are then removed from the material to the solution, which tends to globally increase the average oxidation state of the metal in the oxide.

Concerning the $\beta3$-cobalt oxyhydroxide phases, the chemical composition and formulae are consistent with a $\beta3$ structure consisting of CoO_2 slabs, with protons and Na^+ ions (coming from the reaction media and/or from the pristine phases) intercalated within the interslab space. The water molecules reported in the chemical formula may be mainly adsorbed on the nanosized particles. As far as the average cobalt oxidation state is concerned, it ranges from 3.08, for $\beta3$-prec to 3.18 for $\beta3$-exNa$_{0.6}$ and 3.30 for $\beta3$-exγ, which confirms the presence of Co^{4+} ions, in a slightly different amount, in the three phases. Nevertheless, it is interesting to note that the highest oxidation state of Co is obtained for $\beta3$-exγ. This is due to the high oxidation state of Co in γ-Cobalt precursor phase (3.58), as well as to the use of HNO_3 as a strong oxidizing hydrolysis agent. The presence of Co^{4+} ions in the $\beta3$ type phases is particularly promising in terms of electronic conductivity, as will be shown later.

3.2.4. Morphology and surface properties

If XRD analysis can give information on the coherent domain sizes of primary particles, it does not allow to make assumption on the global morphology of the objects obtained, neither on their global size. Microscopy and gas adsorption studies are key techniques to reveal these information.

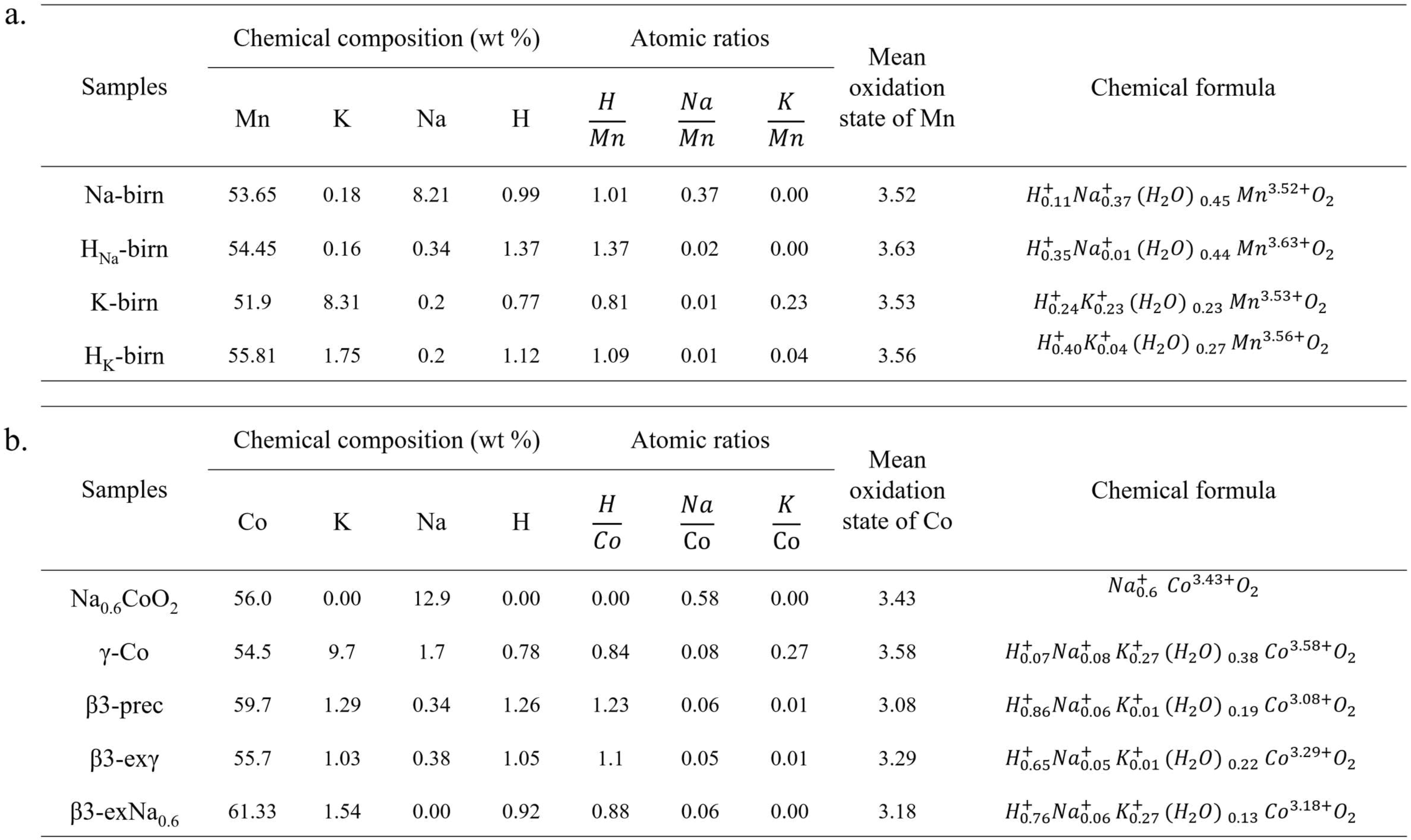

a.

Samples	Chemical composition (wt %)				Atomic ratios			Mean oxidation state of Mn	Chemical formula
	Mn	K	Na	H	$\frac{H}{Mn}$	$\frac{Na}{Mn}$	$\frac{K}{Mn}$		
Na-birn	53.65	0.18	8.21	0.99	1.01	0.37	0.00	3.52	$H^+_{0.11}Na^+_{0.37}(H_2O)_{0.45}Mn^{3.52+}O_2$
H_{Na}-birn	54.45	0.16	0.34	1.37	1.37	0.02	0.00	3.63	$H^+_{0.35}Na^+_{0.01}(H_2O)_{0.44}Mn^{3.63+}O_2$
K-birn	51.9	8.31	0.2	0.77	0.81	0.01	0.23	3.53	$H^+_{0.24}K^+_{0.23}(H_2O)_{0.23}Mn^{3.53+}O_2$
H_K-birn	55.81	1.75	0.2	1.12	1.09	0.01	0.04	3.56	$H^+_{0.40}K^+_{0.04}(H_2O)_{0.27}Mn^{3.56+}O_2$

b.

Samples	Chemical composition (wt %)				Atomic ratios			Mean oxidation state of Co	Chemical formula
	Co	K	Na	H	$\frac{H}{Co}$	$\frac{Na}{Co}$	$\frac{K}{Co}$		
$Na_{0.6}CoO_2$	56.0	0.00	12.9	0.00	0.00	0.58	0.00	3.43	$Na^+_{0.6}\ Co^{3.43+}O_2$
γ-Co	54.5	9.7	1.7	0.78	0.84	0.08	0.27	3.58	$H^+_{0.07}Na^+_{0.08}K^+_{0.27}(H_2O)_{0.38}Co^{3.58+}O_2$
β3-prec	59.7	1.29	0.34	1.26	1.23	0.06	0.01	3.08	$H^+_{0.86}Na^+_{0.06}K^+_{0.01}(H_2O)_{0.19}Co^{3.08+}O_2$
β3-exγ	55.7	1.03	0.38	1.05	1.1	0.05	0.01	3.29	$H^+_{0.65}Na^+_{0.05}K^+_{0.01}(H_2O)_{0.22}Co^{3.29+}O_2$
β3-exNa$_{0.6}$	61.33	1.54	0.00	0.92	0.88	0.06	0.00	3.18	$H^+_{0.76}Na^+_{0.06}K^+_{0.27}(H_2O)_{0.13}Co^{3.18+}O_2$

Table 3.5.: (a) Chemical composition and formulae of synthesized birnessites. (b) Chemical composition and formulae of synthesized cobalt oxyhydroxides.

3.2.4.1. Birnessites

SEM and TEM images of the pristine and protonated birnessites are presented in Figure 3.7 and 3.8. Although they follow similar synthesis processes, the morphologies of Na-birn and K-birn are very different.

Morphology comparison of Na-birn and K-birn (Figure 3.7)

The sodium-based samples present plate-like shapes. The fragmented platelets are irregular in size and their observed lengths are mainly in the micronic range. The thickness of the different platelets is rather uniform, which is estimated by the larger magnification SEM images (Figure 3.7.a and b) to be approximately 50 nm. Na-birn appears as characteristic “hard” platelets, whereas K-birnessite particles are wrinkled, and more veil-like. In the case of K-birn, the particles shown in Figure 3.7.c and d are thinner and smaller. Also, particles do not appear as single objects, but are rather aggregated which renders the size difficult to determine.

The morphology and microsructure of the samples were further examined by transmission electron microscopy. These images (Figure 3.7.e and g) confirm rigid platelets of Na-birn and veil-like morphology of K-birn. Some thin platelets could be distinguished from the edge region of the aggregates, supporting the lamellar structure.

The electronic diffraction patterns of the samples are also different. The sodium birnessites give a series of well-defined diffraction spots (Figure 3.7.f) whereas the potassium birnessites give rise to a set of diffraction rings (Figure 3.7.h). The indices and spacing for diffraction spots and rings, annotated on the images, are consistent with the XRD data. Indeed, if spot diffraction patterns are observed, it means that a single crystal or very few nanocrystals are observed by the TEM aperture. However, if ring diffraction patterns are observed, it either means that a polycrystalline sample is observed, consisting in numerous, nanocrystals or that the veil-like particle is not flat. Indeed, each ring corresponds to a possible randomly-orientated diffracting plane. In other words, the Na-birn have larger coherent domains than K-birn. This is in accordance with the X-ray diffraction patterns discussed in section 3.2.2.1, which show, for K-birn, wider peaks than those of Na-birn, indicating smaller coherent domains and turbostraticity (as seen in Table 3.3). It is also consistent with the difference of rigidity observed.

Morphology of protonated phases (Figure 3.8)

No drastic difference can be observed in the morphologies of H_{Na}-birn (Figure 3.8.a, b and e) and its precursor Na-birn (Figure 3.7.a, b and e). The global layered structure is preserved, proving that protonation is a topotactic reaction and does not alter the lamellae. However, it can be noted that the platelets of H_{Na}-birn exhibit slightly more eroded edges, probably because the acidic medium dissolves the edges of the particles, which is coherent with a slight Mn^{2+} dissolution in the acidic medium. In the same way, no major difference is observed between H_K-birn (Figure 3.8.c, d and g) and its precursor K-birn (Figure 3.7.c, d and g). Since K-birn particles are smaller and different in shape from platelets, no significant change can be observed after protonation.

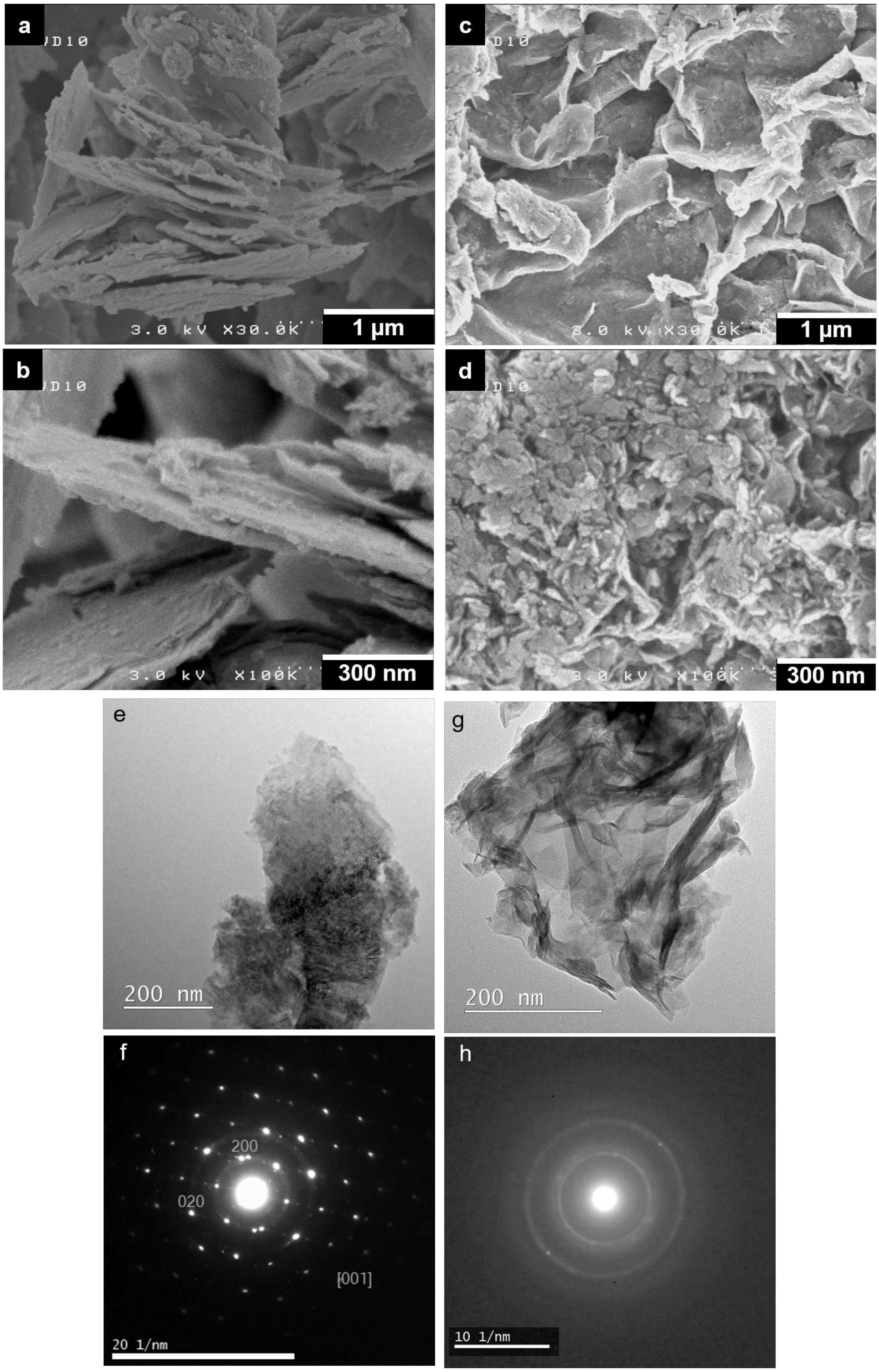

Figure 3.7.: Images of pristine birnessites. (a) and (b) SEM images, (e) TEM image and (f) electron diffraction pattern of Na-birn. (c) and (d) SEM images, (g) TEM image and (h) electron diffraction pattern of K-birnessite.

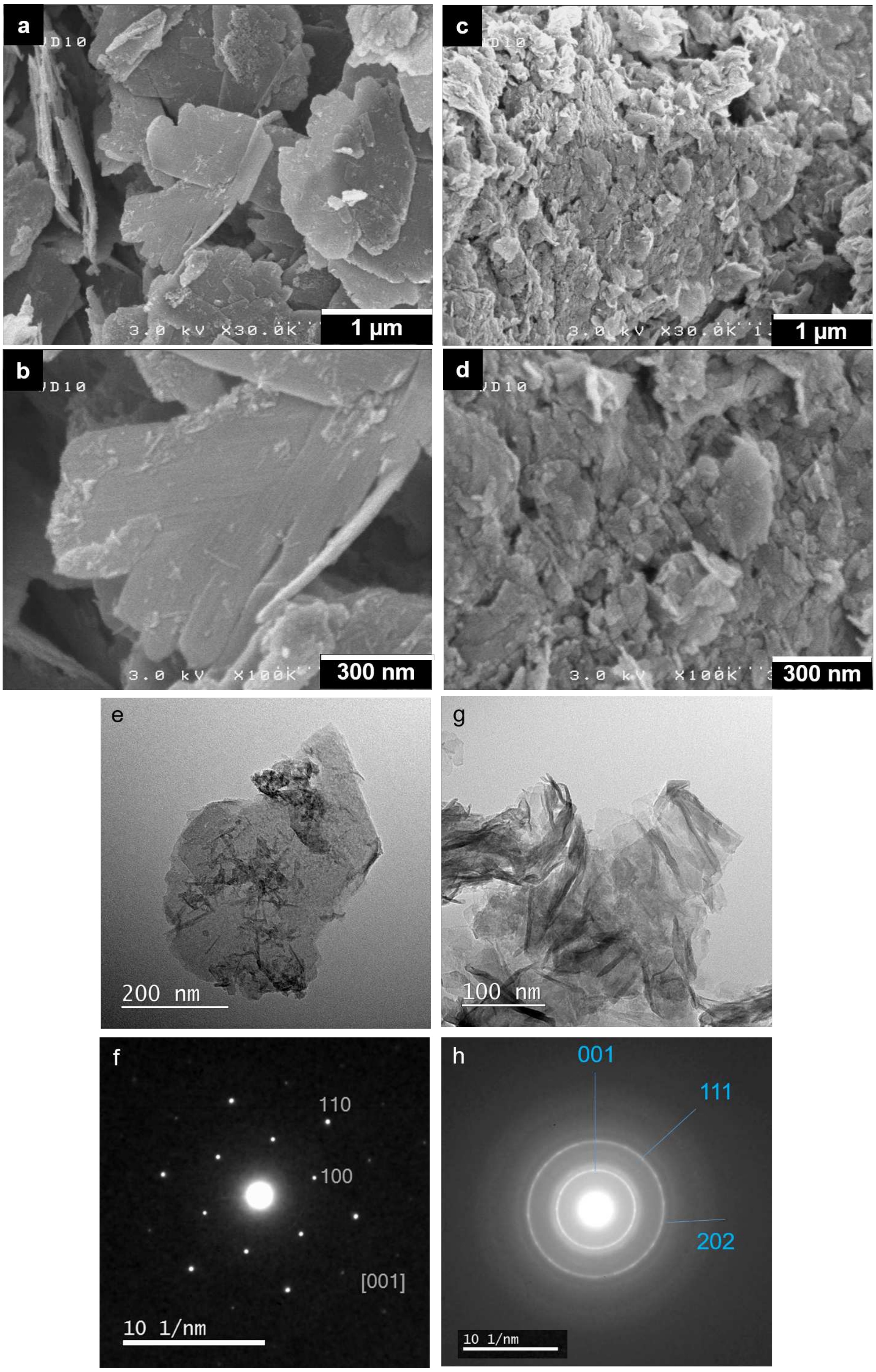

Figure 3.8.: Images of protonated birnessites. (a) and (b) SEM images, (e) TEM image and (f) electron diffraction pattern of H_{Na}-birn. (c) and (d) SEM images, (g) TEM image and (h) electron diffraction pattern of H_K-birn.

Surface properties

Figure 3.9 presents the N_2 adsorption/desorption isotherms obtained for protonated manganese oxides (H_K-birn and H_{Na}-birn). For clarity reasons, only the curves of protonated birnessites are shown. According to the classification established by Sing et al. [193], these isotherm curves could be classified in type IV category, which would correspond to mesoporous materials (pore size from 2 to 50 nm). Their characteristic features are their hysteresis loop, which is associated with capillary condensation taking place in mesopores. At low P/P° ($0.05<P/P°<0.3$), the isotherm is attributed to monolayer-multilayer adsorption. From these curves, the specific surface of each material can be determined with the BET method. The values are presented in Table 3.6.

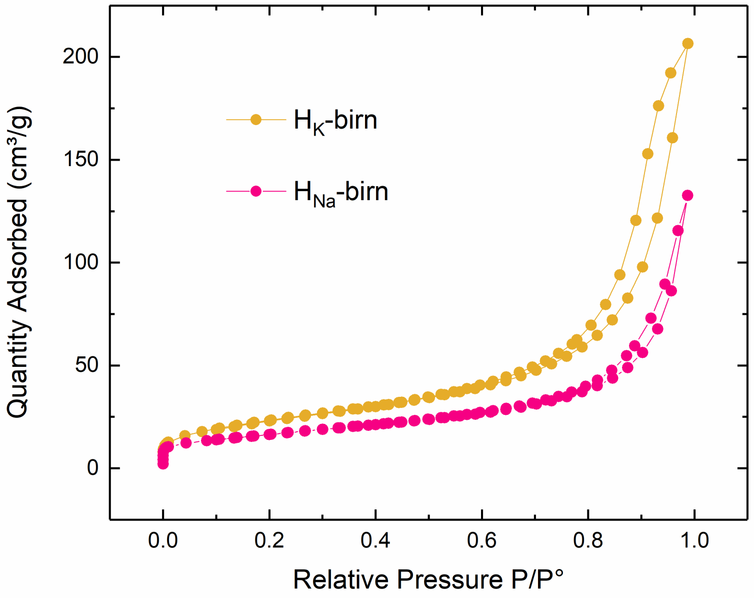

Figure 3.9.: N_2 adsorption/desorption isotherms at 77K for protonated birnessite : H_K-birn (—●—) and H_{Na}-birn (—●—).

Judging from the morphology of the particles, it could correspond to an H_3-type of hysteresis, as it does not exhibit any limiting adsorption at high P/P°, which is usually observed with aggregates of plate-like particles that give rise to slit-shaped pores [193].

Materials	Specific BET surface (m^2/g)
Na-birn	35
K-birn	45
H_{Na}-birn	60
H_K-birn	85

Table 3.6.: Specific surface area of pristine manganese birnessites and protonated birnessites.

The specific surface area of K-birn is higher than the specific surface area of Na-birn, which is in accordance with their different morphologies (as observed in section 3.2.4.1). Also, the specific surface areas of protonated birnessites are nearly twice the values of their precursors, which shows that the protonation reaction increases porosity. This is due to the ion-exchange reaction of sodium ions for protons, which induces a slight increase of the interlayer spacing, and therefore partial delamination of the particles. It also reveals the effect of an acidic medium, which tends to "nibble" the surface of the particles and therefore to increase the surface.

3.2.4.2. Cobalt oxyhydroxides

The three types of $\beta 3$-cobalt oxyhydroxide phases synthesized by different routes as well as the pristine $Na_{0.6}CoO_2$ and γ phases have been characterized by TEM and SEM.

Morphology of $Na_{0.6}CoO_2$ and γ-Co precursor phases (Figure 3.10 and 3.11)

The images of the $Na_{0.6}CoO_2$ and γ phases pristine phases before exchange, are shown in Figure 3.10 and 3.11. Pristine $Na_{0.6}CoO_2$ is constituted of aggregates of well defined hexagonal platelets (SEM images in Figure 3.10.a and b, TEM images in Figure 3.11.a and b), which appear to be around 10-20 nm thick and several tens nm wide. Comparison of these values with XRD coherent domains (determined with Scherrer formula, see Table 3.4) suggests that these platelets may consist of a few coherent domains. For γ-Co, which is prepared from pristine $Na_{0.6}CoO_2$, the morphology exhibits similarities with the previous one, but the objects are smaller and their shape is less defined (see SEM images in Figure 3.10.c and d, TEM images in Figure 3.11.c and d). This modification results from the strains induced by the exchange reactions, which tend to break the initial particles.

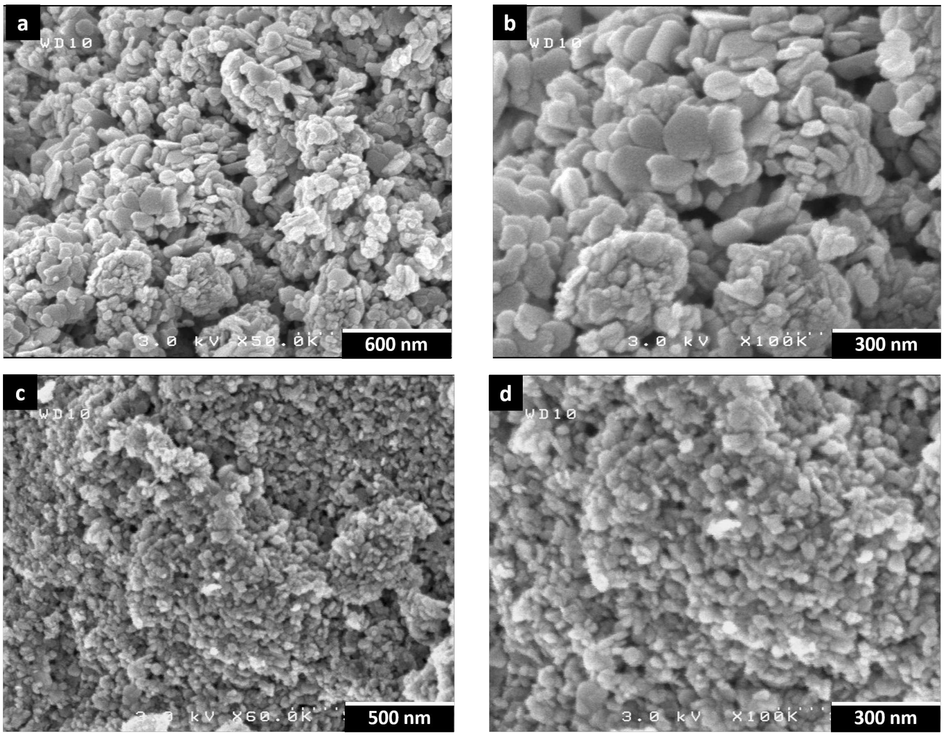

Figure 3.10.: SEM images of synthesized cobalt oxyhydroxides. (a) and (b) $Na_{0.6}CoO_2$, (c) and (d) γ-Cobalt.

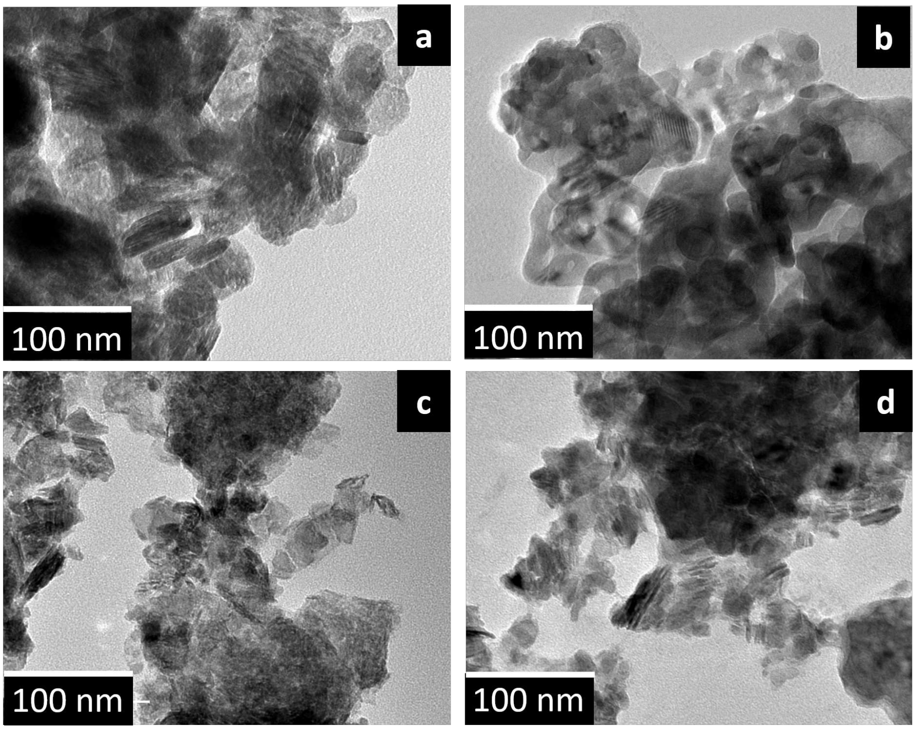

Figure 3.11.: TEM images of synthesized cobalt oxyhydroxides. (a) and (b) $Na_{0.6}CoO_2$, (c) and (d) γ-Cobalt.

Morphology of β3 phases (Figure 3.12 and 3.13)

Concerning the β3 phases, as expected from the XRD patterns, there is a clear disparity in the morphologies of the particles. The SEM images are shown in Figure 3.12 and TEM images are shown in Figure 3.13.

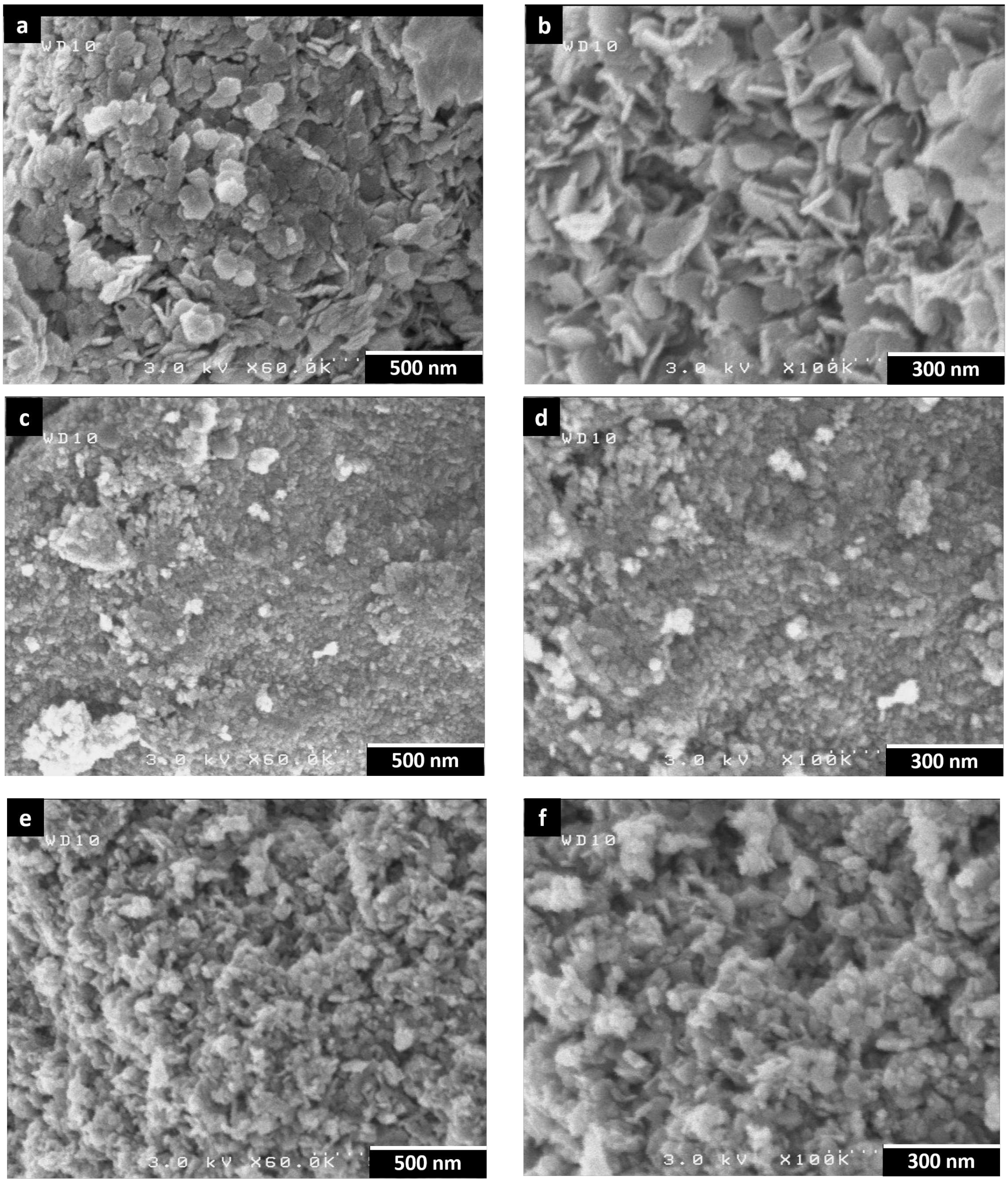

Figure 3.12.: SEM images of synthesized cobalt oxyhydroxides. (a) and (b) β3-prec, (c) and (d) β3-exNa$_{0.6}$, (e) and (f) β3-exγ.

On one hand, the compound β3-prec exists as flat hexagonal platelets with clearly distinct edges. In the SEM (Figure 3.12.a and b) and TEM images (Figure 3.13.a and b), these platelets are very well defined and an average size can be determined : the platelets are around 60 nm wide and 10 nm thick. These values are significantly higher than the

Scherrer value (Table 3.4) which suggests that the SEM and TEM images correspond to aggregates made up in the plane of several disordered nanocrystallites. This is illustrated in Figure 3.14 which shows a high resolution TEM image of β3-prec particles. The particles are aggregated into hexagonal thin platelets with clear edge and regular angles of 120°. The nanocrystalline domains are distinguishable as they have different orientations and distinct contrast.

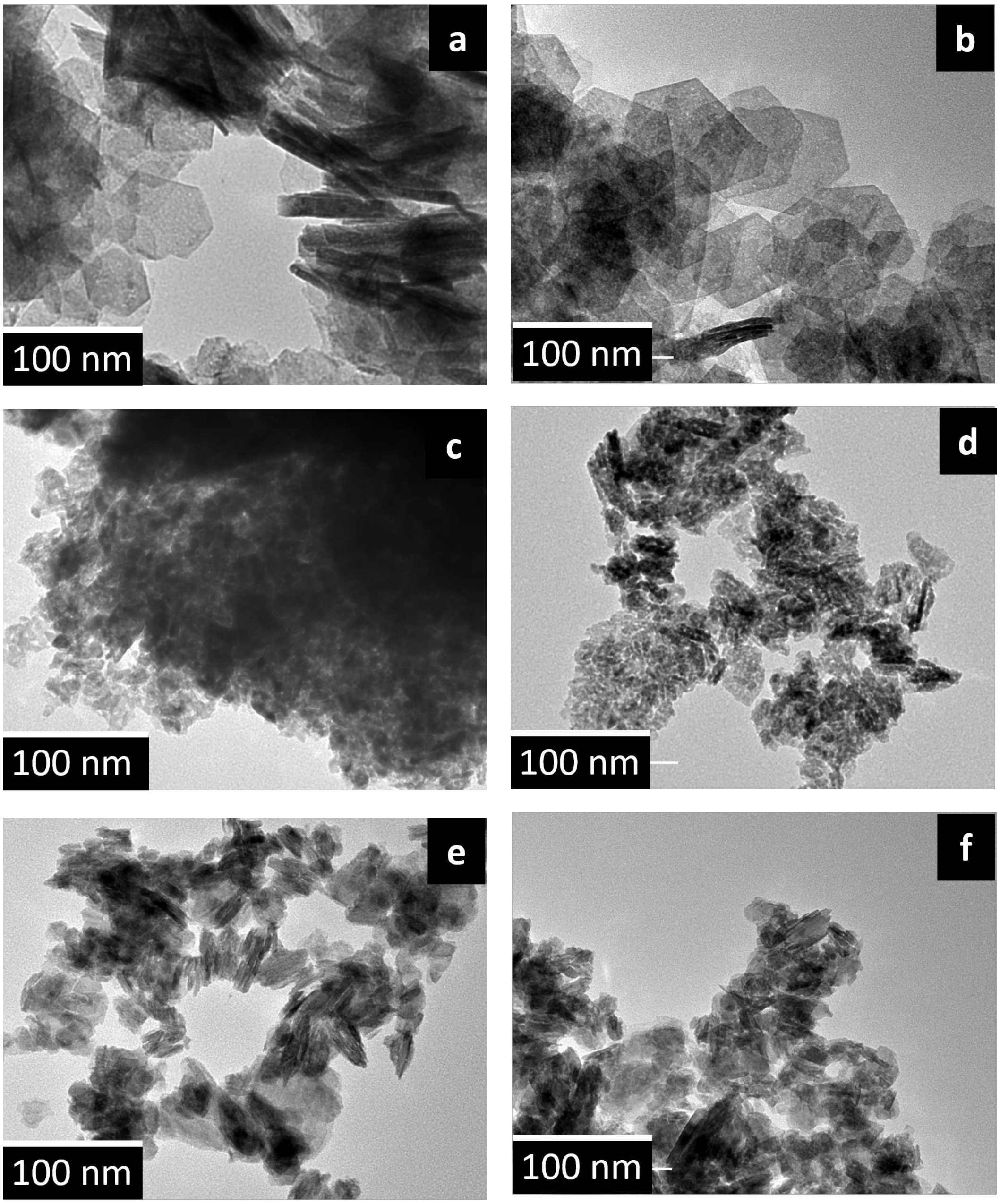

Figure 3.13.: TEM images of synthesized cobalt oxyhydroxides. (a) and (b) β3-prec, (c) and (d) β3-exNa$_{0.6}$, (e) and (f) β3-exγ.

On the other hand, the particles of β3-exNa$_{0.6}$ (SEM in Figure 3.12.c and d, TEM in Figure 3.13.c and d) and β3-exγ (SEM in Figure 3.12.e and f, TEM in Figure 3.13.e and f) are drastically different from the hexagonal platelets of β3-prec. According to the XRD data, the crystallites are better defined along (110) (compared to β3-prec), which suggests a different size of the crystallite. This impacts the morphologies of the final particles. Very small objects of approximately 30 nm wide and 5-6 nm thick can be observed. They pack together into larger objects.

The difference is mainly due to the synthesis route chosen. Indeed, the precipitated phase is obtained by dissolution of a cobalt salt in alkaline medium through the formation of $Co(OH)_2$ phase. This phase is spontaneously oxidized into β3-prec through a isomorphic reaction [194]. In this case, the hexagonal shape is preserved. In contrast, β3-ex$Na_{0.6}$ and β3-exγ are obtained by topotactic reaction from $Na_{0.6}CoO_2$. The β3-exγ particles are very similar to the γ-Co phase. However, the β3-ex$Na_{0.6}$ particles show the biggest difference with their $Na_{0.6}CoO_2$ precursors. With the deintercalation of sodium ions, replaced by protons, the inter-layer space can generate extended structural defects. As a consequence, densely packed micro-crystallites make the particles observed.

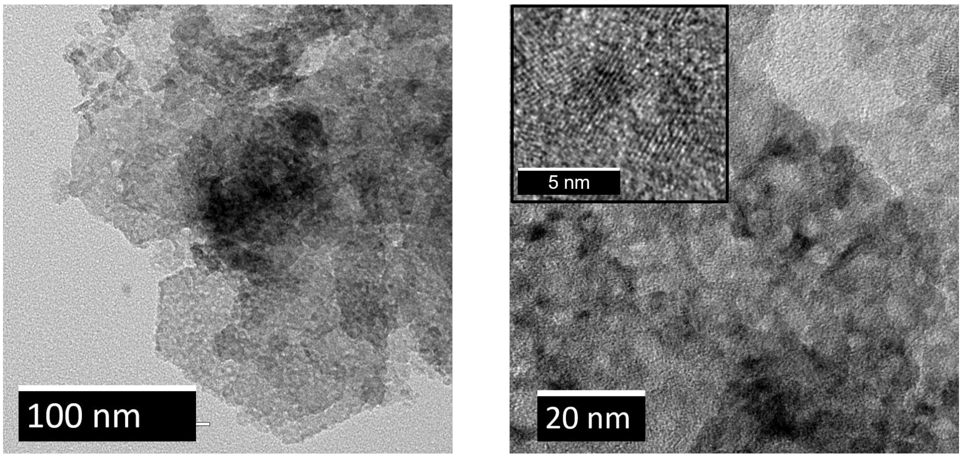

Figure 3.14.: High-Resolution TEM images of synthesized cobalt oxyhydroxide β3-prec.

Surface properties of β3 phases

Figure 3.15 presents the N_2 adsorption/desorption isotherms obtained for cobalt oxyhydroxides (β3-prec, β3-ex$Na_{0.6}$ and β3-exγ). The precursors are not shown for clarity reasons. Similarly to the isotherms of manganese oxides (see section 3.2.4.1), the isotherm curves can be classified in type IV category according to the classification established by Sing et al. However, the three β3 phases show different hysteresis loops. Both β3-ex$Na_{0.6}$ and β3-exγ phases present a hysteresis that could be H_4 type, as the two branches remain nearly parallel over a wide range of P/P°. Similarly to H_3 type, as it does not exhibit any limiting adsorption at high P/P°, this type of hysteresis is often associated with aggregates of plate-like particles giving rise to narrow slit-like pores. The β3-prec phase stands out as its hysteresis can be identified as more of a H_2 type, which suggests the presence of a porous interconnected network of agglomerates. The differently shaped hysteresis may be linked to the difference of morphology of the particles : as the particles of β3-prec are an assembly of hexagonal platelets, the shape and sizes of pores will be different from the similarly shaped β3-ex$Na_{0.6}$ and β3-exγ phases (see Figure 3.12).

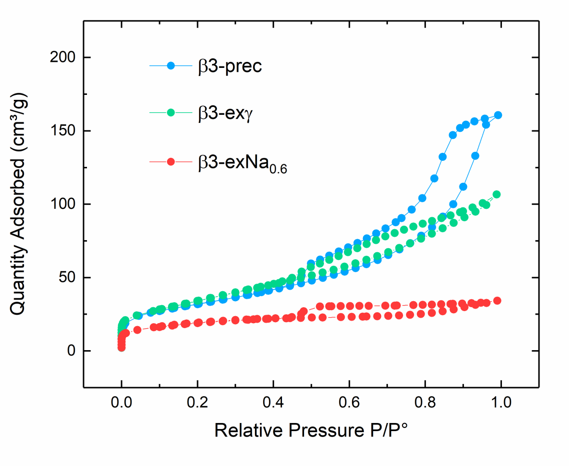

Figure 3.15.: N_2 adsorption/desorption isotherms at 77K for $\beta 3$ phases.

The specific surface area of each material determined with the BET method are presented in Table 4.5.

Materials	Specific BET surface (m^2/g)
$\beta 3$-prec	110
$\beta 3$-exγ	120
$\beta 3$-ex $Na_{0.6}$	70

Table 3.7.: Specific surface area of $\beta 3$ phases.

According to the synthesis strategy of the cobalt oxyhydroxides, very different morphologies are obtained (as seen in previous section). However, surprisingly, no significant change in the surface area is observed from the well-defined hexagonal platelets of $\beta 3$-prec and the more divided morphology observed for $\beta 3$-exγ. A significant decrease is observed for $\beta 3$-ex $Na_{0.6}$.

3.2.5. Electronic conductivity

After having compared the various morphologies and specific surface properties of initial materials, their electronic conductivities have been measured and compared. The variations of the electronic conductivity versus reciprocal temperature of the pristine and protonated birnessites as well as of the various cobalt oxyhydroxides are displayed in Figure 3.16 (experimental conditions are in Annex A.3.1). Several experiments on various pellets have been done and only typical average results are presented. Therefore, the changes in conductivity between the various materials can be considered as significant. The values of activation energy, conductivity at room temperature and average metal oxidation state, for discussion purpose, are presented in Table 3.8. From a general point of view, except for $Na_{0.6}CoO_2$ and γ-Co that exhibit a pseudo-metallic behavior (the activation energy is lower than 0.01 eV), the other materials are semi-conductors.

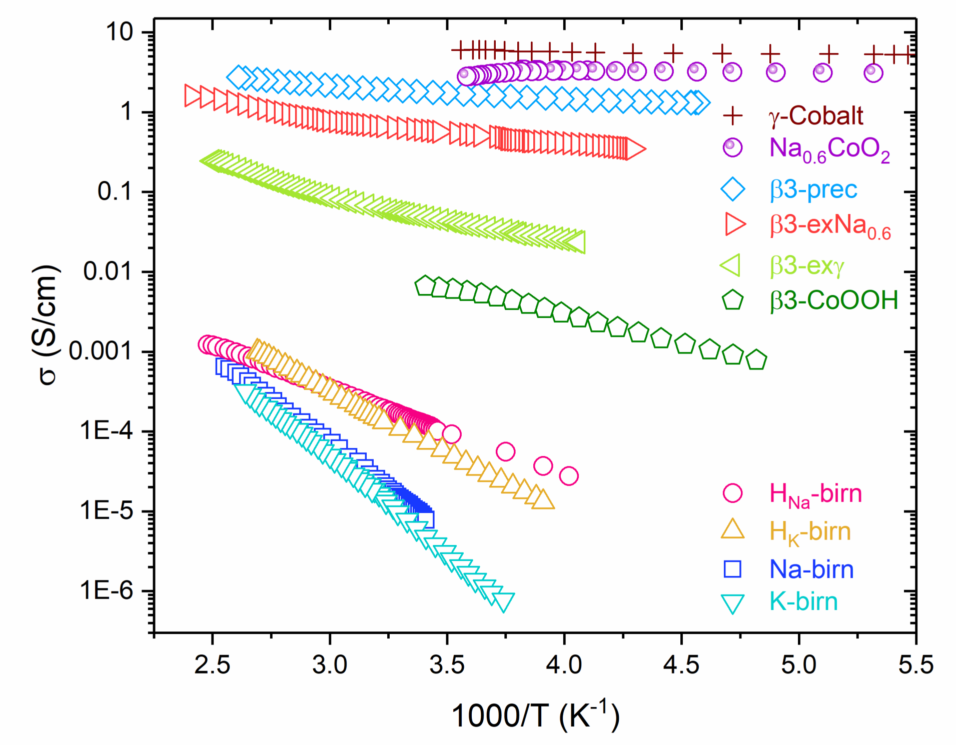

Figure 3.16.: Thermal variation of electronic conductivity for the as-prepared samples.

For the β3-cobalt oxyhydroxides, the activation energy is quite low (<0.1 eV), and the conductivity values at room temperature are high, close to those of the metallic phases. These results confirm the very interesting conductivity properties of the cobalt oxyhydroxides, already reported in the laboratory, which justifies their utilization as electronic conductor additives within the positive electrode of alkaline batteries [187]. According to previous works, the conductivity values are normally related to the Co^{3+}/Co^{4+} ratio within the slabs. As the average oxidation state of Co increases, the conductivity should increase, following the mechanism described in section 3.1.2.3. This tendency is confirmed when two β3-prec phases of different cobalt oxidation states are compared (Figure 3.16). To do so, a β3-CoOOH with a mean cobalt oxidation state of 2.95 was synthesized by precipitation without a strong oxidizing medium. The resulting phase presents a much lower conductivity ($6.6 \cdot 10^{-3}$ S/cm) than β3-prec (1.8 S/cm). However, this tendency is not fully confirmed for the other β3 phases, because the values and curves collected for the β3 phases do not vary in the right order. This anomaly can be related to the fact that the electrodes are not sintered, as a result of the thermal instability of the oxyhydroxides, so that the absolute conductivity values can vary over one order of magnitude for the same material. This induces that, for materials in which the average cobalt oxidation states are very close to each other, which is the case of our β3 phases, the order of the curves can be inverted.

In comparison to the cobalt phases, the manganese oxide phases exhibit much lower conductivities (10^{-6} S/cm) with much higher activation energies (~0.1-0.2 eV). It is interesting to note that, in the protonated phases, the conductivity values are higher and the activation energies are lower than in the pristine birnessite phases. This slight improvement of the conductivity properties can be linked to the increase of the average oxidation state of manganese in the protonated phase, as reported Table 3.5.

The big discrepancy in the conductivity properties observed here between the manganese and the cobalt materials justifies the strategy of the present work : seek synergy effects between manganese phases, characterized by poor conductivity and good pseudocapacitive properties and cobalt phases, characterized by good conductivity (at least one order of magnitude higher) and good faradaic properties.

Materials	E_a(eV)	σ(290K) (S/cm)	Mean oxidation state
γ-Co	<0.01	6.5	3.58
$Na_{0.6}CoO_2$	<0.01	3.4	3.43
β3-prec	0.02	1.8	3.08
β3-ex$Na_{0.6}$	0.03	$5.8 \cdot 10^{-1}$	3.18
β3-exγ	0.05	$4.6 \cdot 10^{-2}$	3.29
β3-CoOOH	0.04	$6.6 \cdot 10^{-3}$	2.95
Na-birn	0.19	$8.7 \cdot 10^{-6}$	3.52
K-birn	0.21	$4.8 \cdot 10^{-6}$	3.63
H_{Na}-birn	0.10	$1.2 \cdot 10^{-4}$	3.53
H_K-birn	0.13	$7.2 \cdot 10^{-5}$	3.56

Table 3.8.: Activation energy, conductivity at room temperature and mean oxidation state of metal for birnessites and cobalt oxyhydroxides obtained by precipitation and chimie douce reactions.

3.3. Exfoliation

Over the last decade, the study of 2D materials has evolved into one of the most popular areas of nanomaterials science, based on the observation that many 2D materials have very exciting physical and chemical properties [163, 195, 196]. This rapid growth was greatly driven by research on graphene, a 2D material with interesting properties and high application potential [197]. As research about graphene deepened, the field began to broaden to other 2D materials such as metal chalcogenides [198], metal phosphates and phosphonates, as well as layered metal oxides [195, 199].

In order to produce and use 2D materials, various methods can be applied. In the early days, graphene 2D nanosheets were produced by mechanical exfoliation (thin single atomic layers of graphene were obtained by exfoliation with thin transparent adhesive tape [42]). However, as the field progressed, the need for more scalable techniques became necessary. In general, modern production techniques can be divided in two classes :

- chemical vapor deposition [200], which produces high quality, extended monolayer films on substrates
- liquid exfoliation methodologies, which transform layered crystals into large quantities of small nanosheets [163]

The first class of techniques remains the source of the highest quality nanosheets obtained and has resulted in some major advances. However, it suffers from low yield and a production rate that is technologically non scalable. This is why the second class of liquid exfoliation methods is preferred, as they give large quantities of dispersed nanosheets. There are three main liquid exfoliation techniques for layered materials :

1. ion intercalation : appropriate ions are intercalated between the layers in a liquid environment, swelling the crystal and weakening the inter-layer attraction. Additional energy (such as shear, ultrasonication or thermal) can completely separate the layers, resulting in a dispersion of exfoliated objects [201]
2. ion exchange : some layered compounds contain ions between the layers to compensate their surface charge. These ions can be exchanged in a liquid environment for other, often larger ions. Vigorous stirring results in an exfoliated dispersion [202, 203]
3. sonication-assisted exfoliation : the layered crystal is sonicated in a solvent, resulting in its exfoliation and nanosheet formation. The nanosheet dispersion is stabilized either in solvents with appropriate surface energy or by using surfactants. Otherwise, re-aggregation and sedimentation will occur [162, 204]

In general, liquid exfoliation can be considered as a three step process. First, as explained above, the weak inter-layer attractions between adjacent sheets need to be overcome by additional energy during the actual exfoliation process. Second, nanosheets need to be stabilized against re-aggregation by suitable solvents or surfactants. The last one play a dual role as they minimize the net energy cost of the exfoliation while also adsorbing to the nanosheet surface, shielding them from restacking in the liquid. Third, because the as-produced dispersion is highly polydisperse, containing nanosheets with a range of sizes and thicknesses, size-selection is required.

In the following, a brief state of the art about exfoliation of layered manganese oxides and layered cobalt oxyhydroxides will be given. Then, protocols of exfoliation will be detailed, along with methods for selecting nanosheets according to their size. Finally, the characterization of the nanosheets will be presented.

3.3.1. State of the art

3.3.1.1. Exfoliation of manganese oxides

As previously seen, manganese oxides are of considerable interest due to their versatile range of applications. Their synthesis, structures and physico-chemical properties have been largely reported. The study of swelling, delamination and exfoliation of birnessite-type layered manganese oxides has thus attracted a lot of attention [168, 169, 205, 206, 207, 208].

This exfoliation can be performed starting from various layered MnO_2 precursors [169, 209, 171]...). Indeed, Liu et al. [168] used a highly crystalline sodium-manganese oxide precipitated in hydrothermal conditions because it was necessary to have highly regular manganese oxide nanosheets for precursors of new functional devices. The nature of the inter-layer alkaline ion can differ, as Omomo et al. [169] chose to work on potassium-based birnessite, obtained by high temperature calcination of Mn_2O_3.

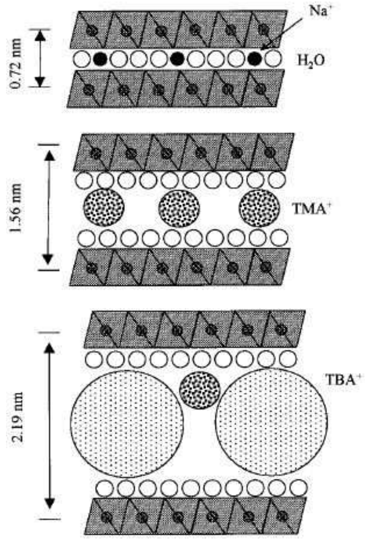

Figure 3.17.: Schematic diagram of cation-intercalated birnessite at the molecular level [168].

In all cases, the birnessite phases are placed in acid for nearly complete removal of inter-layer K^+ or Na^+ ions, which are exchanged for protons. The resulting proton intercalated phase is then treated with tetralkylammonium ions (for exfoliation in aqueous medium), for an ion intercalation process that results in the swelling of the structure [210]. This swelling originates from the modification of attractive and repulsive forces between the slabs, induced by the intercalation of ions that will alter the electrostatic interaction.

Because of this, the hydration state of inter-layer cations is modified, and the inter-layer hydrogen bond is weakened, leading to subsequent delamination.

The nature and concentration of tetralkylammonium ions can alter the process. Liu et al. have extensively studied the swelling behavior due to the intercalation of tetramethylammonium cations (TMA^+) with different concentrations. Schematic diagrams of intercalated manganese oxides at the molecular level can be described as in Figure 3.17. It seems that the expansion of the inter-layer is not observed when the concentration of TMA^+ is too low : when $TMA^+/H^+<1$ (TMA^+ is the amount of TMAOH in the solution, and H^+ is the number of inter-layer protons within the material), no significant structural change is observed. However, as the concentration increases, a detailed structure analysis revealed the formation of layers of water molecules in addition to the TMA^+ intercalation. The intercalation of one TMA^+ ion drives one intercalated proton out of the inter-layer space to the solution, so that it can neutralize one OH^- present in the solution. pH titration indicates that the intercalation process is an ion-echange mechanism.

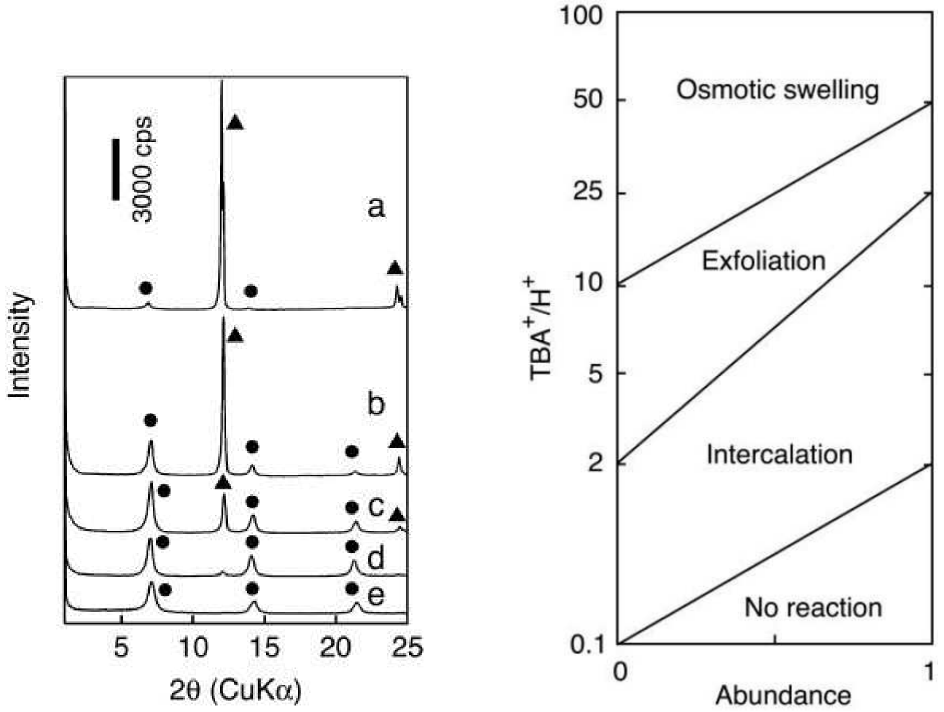

(a) (b)

Figure 3.18.: a. X-ray diffraction patterns for a solid centrifuged from an aqueous mixture of $H_{0.13}MnO_2(H_2O)_{0.7}$ and TBAOH. The molar ratios of TBA^+/H^+ are (a) 0.1, (b) 0.3, (c) 0.5, (d) 1, and (e) 2. Triangles and circles denote the basal reflections from $H_{0.13}MnO_2(H_2O)_{0.7}$ (0.73 nm) and the TBA^+ intercalated phase (1.25 nm), respectively. b. Reaction diagram for a system of $H_{0.13}MnO_2(H_2O)_{0.7}$ and TBAOH [169]

Omomo et al. have chosen to focused on the obtention of single-lamellar nanosheets [169]. To do so, they have extensively studied the swelling behavior of layered MnO_2

through treatment with aqueous solutions of tetrabutylammonium hydroxide (TBAOH) at various concentrations. At lower amount of TBA^+ ($TBA^+/H^+<2$), layered manganese oxide undergoes intercalation, resulting in the presence of a layer of TBA^+ in the interlayer. The intercalation process is observed by X-ray diffraction, as the interlamellar space of the starting material increases from 0.73 nm to 1.25 nm (presented in Figure 3.18.a). However, at high TBA^+ concentration ($TBA^+/H^+>25$), a series of diffraction peaks with large intersheet expansions (from 0.35 to 0.72 nm). This cannot result from the simple accommodation of TBA^+ ions (size range 0.84-1.05 nm) but can be ascribed to a large volume of electrolyte ions introduced in the inter-layer space of the layered host, called osmotic swelling. It differs from the normal intercalation reaction as electric double layers are formed on both sides of the negatively charged nanosheets. This way, charge neutrality of the total system is achieved. For intermediate TBA^+ amounts, exfoliation into single MnO_2 sheets is promoted. The ranges in which these reactions undergo (intercalation, exfoliation and osmotic swelling) overlap with each other and largely depend on the layered materials. A summary of this behavior is shown in a reaction diagram in Figure 3.18.b. However complete and concise these studies may be, none report the yield of nanosheets obtained, meaning that although single layered nanosheets can be obtained, the quantity is probably very scarce.

Exfoliation is a time consuming process. On average, colloidal suspension of manganese nanosheets are obtained after at least a week of vigorous agitation, and high concentration of the swelling agent is required. In order to fasten this, Cui et al. [211] have reported a new simple approach which can be carried out by 20 minutes of ultrasonic treatment, which drastically speeds up the delamination process.

3.3.1.2. Exfoliation of cobalt oxides

The exfoliation of cobalt oxides is much less studied than the manganese oxides.

A handful of studies has been published concerning the exfoliation of cobalt hydroxides in organic [212, 213] or aqueous [214, 215] media. Ma et al. [213] have successfully delaminated cobalt layered double hydroxides in formamide. Due to the positively charged layers of the initial material, anionic exchanges can be carried out. First, the LDH phase is put in the presence of bromine to intercalate Br^- ions. Then, another anionic exchange can begin with the addition of $NaClO_4$. After ultrasonically dispersing as-exchanged ClO_4^--LDH in formamide, the delamination is achieved, as proven by the Tyndall scattering effect illustrated in Figure 3.19 and single-lamellar oxides are observed.

Another route can be used to exfoliate cobalt hydroxides, using bigger anions such as sodium dodecylsulphate (SDS ($NaC_{12}H_{25}OSO_3$)) for the ionic exchange. Liu et al. [214] were the first to succeed in the anionic exchange : after synthesizing highly crystalline cobalt hydroxide phases by hydrolysis in HMT (hexamethylenetetramine), they have intercalated inorganic (NO_3^-) and organic anions to modify the inter-layer space. The reaction was performed at 90°C and during 48 hours under stirring. The phase and size control of the materials were achieved by controlling the concentrations of salts added. Although very polydisperse suspensions are obtained, the highly crystalline and hexagonal plate-like morphology was preserved.

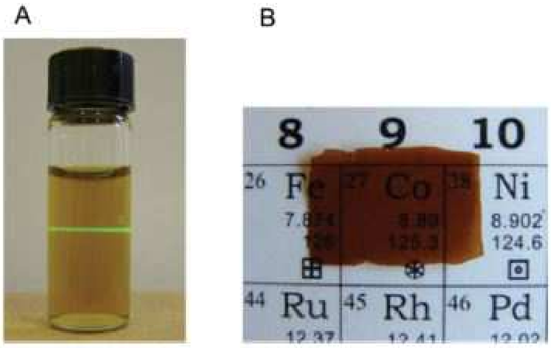

Figure 3.19.: Delamination of cobalt hydroxides : A. Dispersion of the cobalt hydroxide nanosheets documented by the Tyndall scattering of green laser light; B. Self-standing film prepared from a slow evaporation of water from the dispersions on a polypropylene tray [215]

Schneiderova et al. went even further [215] and succeeded in complete delamination of the particles. In order to do so, they have directly synthesized SDS-intercalated cobalt hydroxides in HMT. After a supplementary step of topotactic anion-exchange with lactates, a colloidal suspension of cobalt oxides can be obtained by subsequent washing in water (Figure 3.19.A.). The delamination is immediate, and self-standing films can be prepared for further characterization (Figure 3.19.B.).

As far as cobalt oxides are concerned, only three publications can be found [216, 217, 218]. An attempt was made to exfoliate the layered lattice of $Na_{0.7}Co^{3.3+}O_2$ through the intercalation of neutral ethylamine. However, this trial only led to a modification of the initial phase into a structure with reduced mean Co oxidation state [216]. The observed decrease of cobalt oxidation state can be attributed to the Lewis basicity of the neutral amine used. In fact, the difficulty for exfoliating the layered cobalt oxide contrasts with the easy preparation of exfoliated manganese oxide nanosheets, although both compounds exhibit close lamellar structures. From the viewpoint of electronic structure, this phenomenon can be attributed to the instability of the tetravalent cobalt oxidation state in the phase.

Hwang et al [218] have successfully synthesized colloidal suspensions of layered cobalt oxide nanosheets through the intercalation of quaternary ammonium cations into the layered $LiCoO_2$ lattice. First, a proton exchange reaction was performed by dispersing the $LiCoO_2$ powder in HCl. Exfoliation is then achieved by reacting the protonated cobalt oxide in TMAOH for ten days. Different concentrations of TMAOH were tested (TMA^+/H^+=0.15-75) in order to obtain single layers. The negative surface charge of the exfoliated $[CoO_2]$ monolayers makes it possible to apply them as “building blocks” for hybrid materials.

Compton et al. also have reported successful delamination of cobalt oxides in the presence of TBAOH in water [217]. They first proceeded by direct synthesis of $HCoO_2$ by oxidation of β-$Co(OH)_2$. Then the $HCoO_2$ phase was put into TBAOH (25 g of 40% mixture) and shaken and sonicated. Exfoliation was promoted by vigorously stirring the sonicated mixture at 75°C for four days. To characterize the exfoliated nanosheets, they were isolated from the colloidal suspension via ultra-centrifugation and subjected to five cycles of re-suspension and centrifugation to remove residual TBA^+ from solution. The isolated nanosheets were redispersed in water, where they are stable and self-supporting films were made by micro filtration under vacuum.

With these studies in mind, and in order to maximize the yield of obtained nanosheets (for "building blocks" as new supercapacitor materials), we performed the following exfoliation experiments with the aid of ultrasonication and long stirring duration.

3.3.2. Intercalation and exfoliation protocols

A schematic overview of the intercalation and exfoliation process used in this present work is presented in Figure 3.20. Exfoliation of the layered H-birnessite into single layered manganese oxide nanosheets was carried out using a method described by Sasaki et al. [169]. A weighted amount of starting material was suspended in 200 mL of an aqueous TBAOH solution for at least 10 days at 298 K. The amount of TBAOH applied with respect to the amount of exchangeable protons in the H_K-birn material, that is, the molar ratio of TBA^+/H^+ was fixed to 10 after optimization of the concentration of TBA^+. The resulting dark brown suspension was continuously stirred for one week at room temperature, and a coffee-colored stable colloidal suspension was obtained. For cobalt oxyhydroxides, exfoliation was achieved with a molar ratio of TBA^+/H^+ fixed to 2, with respect to the amount of exchangeable protons in $H_xCoO_2(0.60<H<0.86)$.

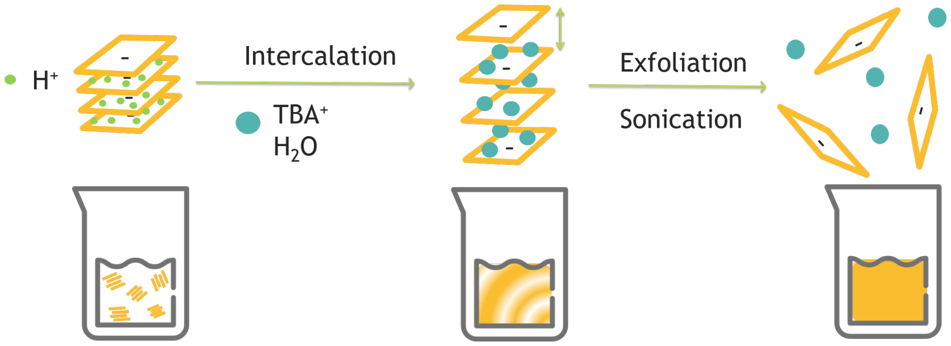

Figure 3.20.: Schematic overview of exfoliation process.

At the very beginning, TBA^+ ions are intercalated into the interlayer space. This is due to an ion-exchange reaction during which the hydroxyl groups of TBAOH will interact with interlayer protons, leading to intercalation of TBA^+ and formation of water molecules in the solution. X-ray diffraction patterns registered at various steps of the intercalation process are gathered in Figure 3.21. The X-ray diagram of the intermediate material obtained after 2 hours of suspension in TBAOH shows the coexistence of initial H_K-birn and of an intercalated material, which exhibits an interlayer spacing of 12.3 Å, consistent with the successful intercalation of TBA^+ ions that have an ionic radius of 0.84 nm [169].

In order to increase production rates of exfoliated material, tip sonication is commonly used to apply ultrasonic energy to the sample. The shock waves generate local shear stresses, large enough to weaken the out-of-plane bounds and delaminate the layered materials. The process must be carefully monitored as heat is generated during sonication. This is largely due to energy losses of the acoustic waves, due to viscous frictional losses as well as to thermal conduction from areas of high pressure to low pressure areas. This means that break and cooling steps must be alternated, particularly for higher power sonication.

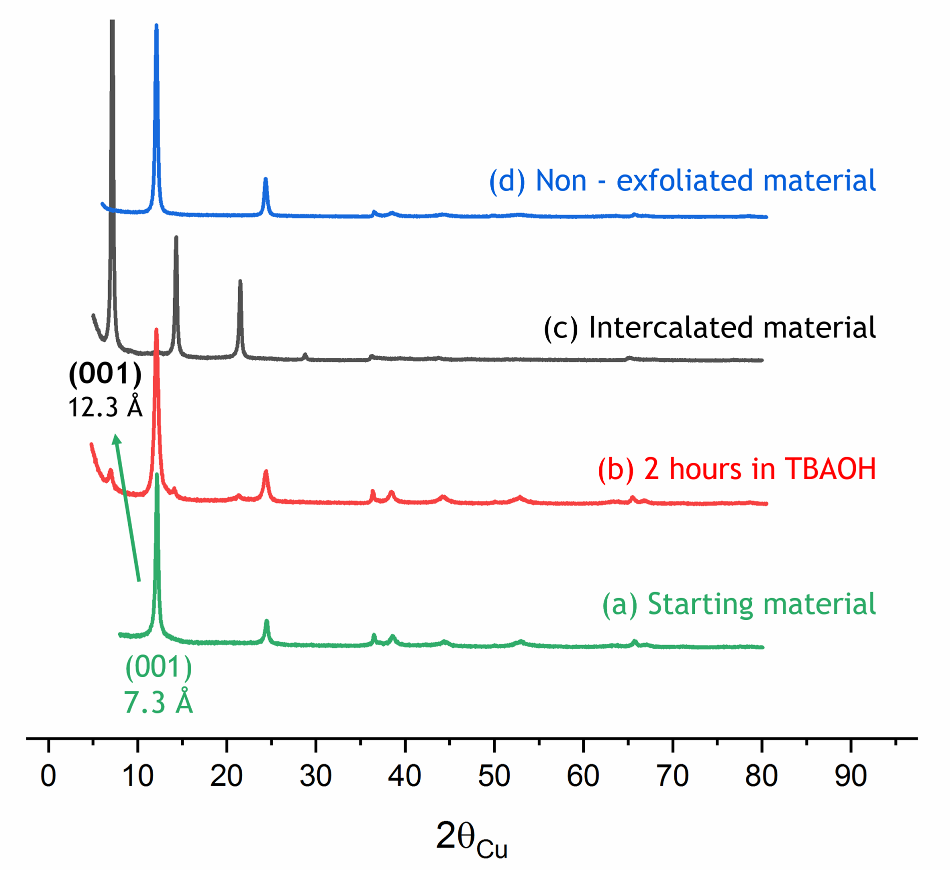

Figure 3.21.: X-ray diffraction patterns of: (a) Initial protonated H_K-birn. (b) The material after 2 hours stay of H_K-birn in the presence of TBAOH. (c) Intercalated birnessite in $TBA^+/H^+=10$. (d) Non-exfoliated H_K-birn recovered as sediment after centrifugation at 4000 rpm.

In general, after being stirred for 15 hours, the suspension is subjected to a 20 kHz ultrasonication for approximately 3 hours, alternating pulses of 0.5 second of ultrasonication and of 0.5 second pause, at a 100 % amplitude. Every hour, the ultrasonication is stopped to allow the suspension to cool down. As a result, a stable brown colloidal suspension is obtained. After the sonication treatment, the suspension is stirred for approximately 2 more weeks.

The unexfoliated component is separated from the colloidal suspension by slow centrifugation at 4000 rpm. The colloidal suspension is identified as the exfoliated manganese oxide or cobalt oxide nanosheets, which will be the precursors of restacked materials. The manganese based colloidal suspensions are very stable and can be kept for up to

6 months in a fridge without any alteration. However, the cobalt based colloidal suspensions are only stable for one month. This discrepancy is consistent with the higher stability of manganese oxide nanosheets.

3.3.3. Size selection

A major problem with this type of exfoliation is the limited control over the size polydispersity. The samples contain broad distributions of nanosheet size and thickness. The colloidal suspensions produced using sonication still contain large amounts of unexfoliated and unstable dispersed material. Usually, such samples do not fulfill the requirements needed to perform studies on fundamental properties. Hence, in order to study and characterize the produced nanosheets, they must first be separated from the bulk material and unstable phases, and size-selection is required.

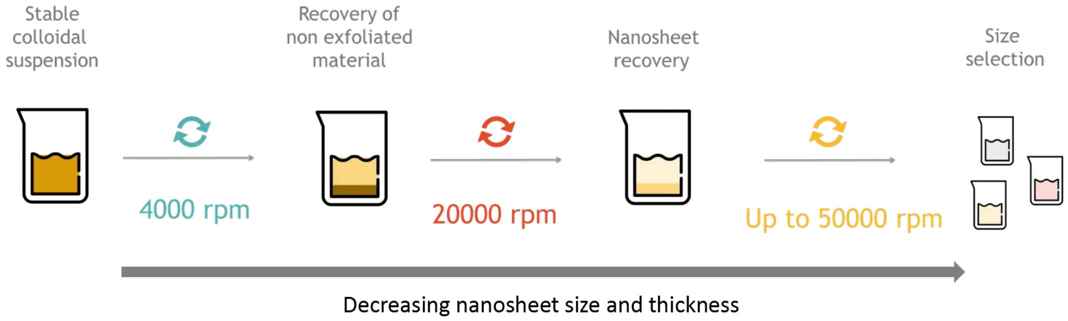

Figure 3.22.: Schematic overview of the size selection process. The suspension is subjected to liquid cascade centrifugations. After each step, size-selected nanosheets are collected as sediments while the supernatant is subjected to another centrifugation at higher rotation speed.

A procedure to do so is liquid cascade centrifugation, which consists in a multi-step process where various centrifugations at increasing speeds are carried out. To illustrate this process, a schematic overview of a general cascade is presented in Figure 3.22. During centrifugation, the particles are separated on the basis of weight. First, the colloidal suspension is centrifuged at 4000 rpm in order to recover the non exfoliated material in the bottom of the flask. The X-Ray diffraction pattern of the collected sediment, presented in Figure 3.21.d, confirms that the powder recovered after this step is indeed the same as the precursor. By accurately weighting the non-exfoliated powder, the yield of the exfoliation can be evaluated : about 40 % of Mn oxides have been successfully exfoliated, against only 30-35 % of Co oxyhydroxides. Thus, the global colloidal suspension has a rough concentration of maximum 2 g/L. After this first step, the supernatant is collected and subject to a series of other centrifugation cycles with increasing speed (up until 50000 rpm -214000 g). In order to achieve such high speeds, ultracentrifugation is required. After each centrifugation, the sediment recovered contains nanosheets in a given size range, which have been trapped between two centrifugation speeds.

To achieve efficient size selection, it is critical to completely remove the supernatant from the sediment. This means that the centrifugation time has to be long enough to allow the majority of the nanosheets to sediment to the bottom of the vial. Also, the volumetric capacity of ultracentifugation tubes being relatively small (up to 10 mL), the amount of nanosheets collected is very limited. This way, only very small amounts (approximately 10 mg) of nanosheets can be recovered. Although very small, this amount is enough for further characterizations that will be described below.

3.3.4. Characterization of nanosheets obtained

While the stability of the colloidal suspension is an excellent proof of exfoliation, the delamination of the layered materials into individual nanosheets, not just oligolayer aggregates, has to be confirmed. First, size determination of the suspended objects has been attempted by dynamic light scattering. However, as the objects are 2D layers, their hydrodynamic size might be difficult to estimate. Different microscopies such as high resolution transmission electron microscopy and atomic force microscopy have been used to visualize them.

3.3.4.1. Size of suspended nanosheets

Dynamic Light Scattering has been used to determine the hydrodynamic radius of the particles in suspension. The measurements have been conducted on the supernatant obtained after each centrifugation (with increasing speed) and average size (Z average) are presented in Figure 3.23.

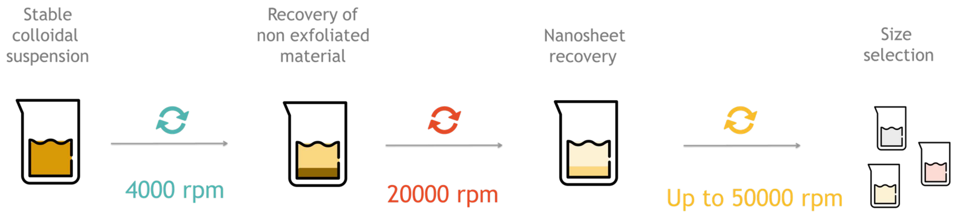

Z (d.nm)	745	260	130	66
PdI	0.68	0.53	0.38	0.35

Figure 3.23.: Average size and polydispersity index (PdI) of supernatant suspensions after each centrifugation cycle for the exfoliation of H_K-birn.

Before any centrifugation, the average particle diameter measured is 745 nm. This size gradually decreases as the centrifugation speed increases, and reaches 66 nm after 50 000 rpm. Overall, there is a net decrease of particle size as the centrifugation speed is increased, which means that the size-selection process is efficient. The major shortcoming is that the average size measured does not represent the reality, as the calculations are based on a spherical particle model. Indeed, in the algorithms used, there is a shape factor that has to be taken into consideration. As the particles present in our colloidal suspensions are anisotropic platelets, the exact size determination by DLS is impossible. Furthermore, the polydispersity index indicates the width of the distribution and ranges from 0 to 1. Values greater than 1 indicate that the distribution is so polydisperse that the sample is not suitable for measurement. Here, all supernatants have a PdI lower than 1. However, as PdI values are higher than 0.08 (characteristic of a mono-disperse sample), this means that the suspensions are polydisperse. Therefore, due to the anisotropy of the studied suspended particles, it is not possible to conclude exactly on the size and thickness of obtained particles. This is why other characterization methods have been used for a precise size determination.

3.3.4.2. TEM morphology

Transmission electron microscopy (TEM) is ideal for the analysis of the shape and width of the nanosheets. It provides higher resolution compared to scanning electron microscopy and more global overview of the objects distribution than atomic force microscopy.

The images of exfoliated H_{Na}- birn are presented in Figure 3.24. They show nanosheets with faint but uniform contrast, which reveals their ultrathin nature. The morphology of MnO_2 nanosheets can be distinguished in two categories. In Figure 3.24.a and b, micrometric sheets constituted by few layers can be observed, especially with the folding of the edges that reveal substantial exfoliation. The nanosheets observed have a basal size ranging from 200 nm to 1 µm. The fact that the grid membrane is visible through the particles is an additional proof that thin layers are synthesized. Another category of particles observed is presented in Figure 3.24.c. These look like nanopieces of “exploded” micrometric lamellae after exfoliation. Their presence is most probably due to the ultrasonication step : upon exfoliation, the lamellae are thinner and more fragile than the precursors. Under high frequency energy input, the thin layers are broken apart, and tend to roll on themselves to form a mix of nanopieces and nanoneedles.

In the case of cobalt based materials, the TEM images of single β3-prec nanosheets (Figure 3.25) show hexagonal platelet shapes of approximately 60-70 nm, in good accordance with the morphology observed for the starting β3-prec phase before exfoliation. In this case again, the grid membrane can be distinguished through the particles. In Figure 3.25.c, the particles observed are nearly transparent, with just a slight contrast difference, revealing the very thin nature of the observed particles.

Unfortunately, the TEM images show very fine cobalt oxyhydroxide objects that are very similar to pristine β3-prec. It seems that TEM is not well suited to prove the success of exfoliation, nor for the determination of nanosheet thickness, as the lamellae deposited on the grid lay flat on their basal face. Thus, even if the contrast can give some idea on the platelet thinness, it is not possible to fully quantify it. Indeed, whereas TEM microscopy is very precise for in-plane dimension, this is not the case for measurement of the depth of the material (along the z-axis).

On the contrary, and despite being more challenging and time-consuming, local probes can give a precise measure of the thickness of objects. AFM was therefore used to evaluate the thickness of the exfoliated nanosheets and estimate the number of oxide layers along the z-axis.

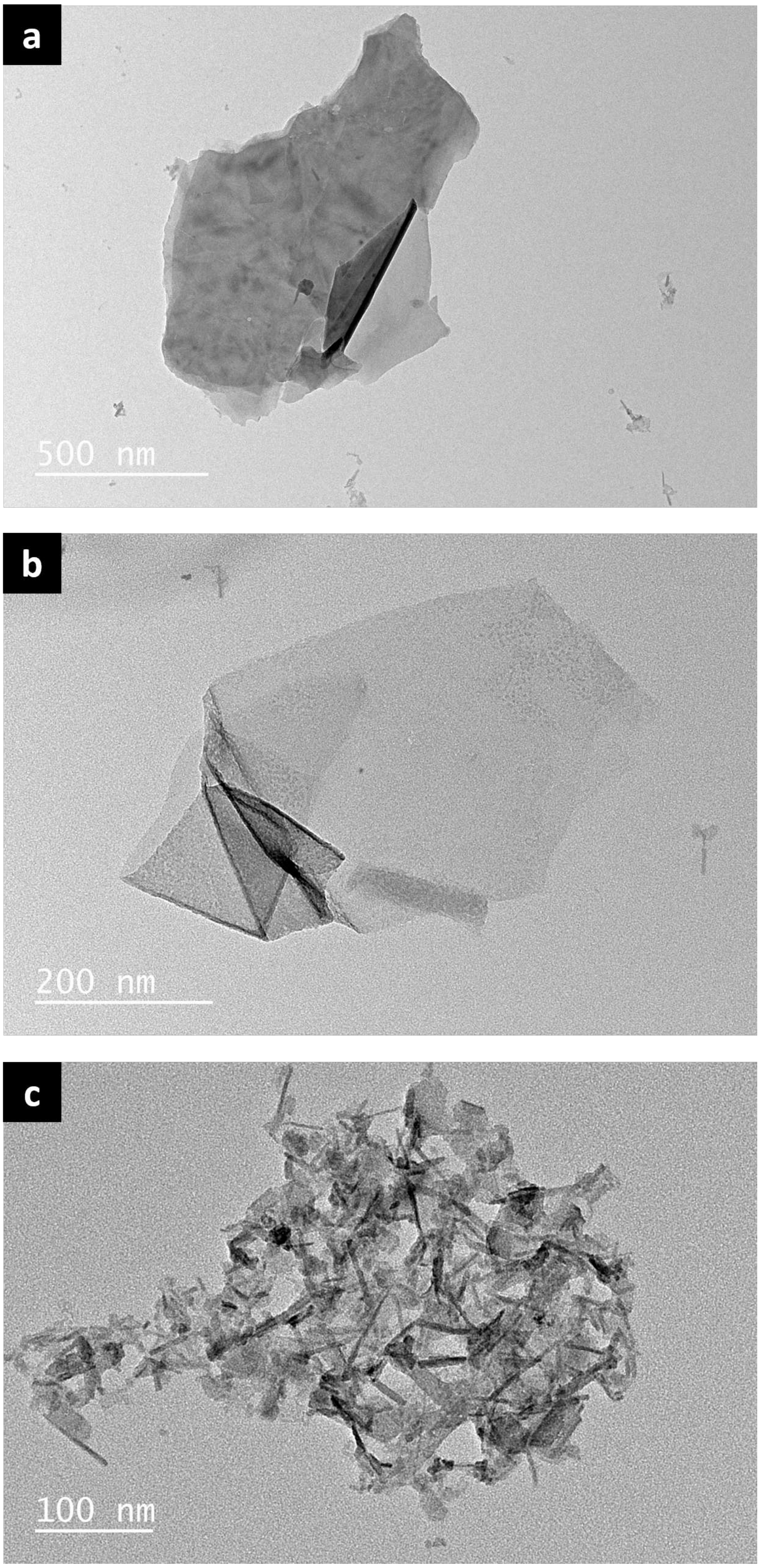

Figure 3.24.: TEM images of exfoliated H_{Na}- birn.

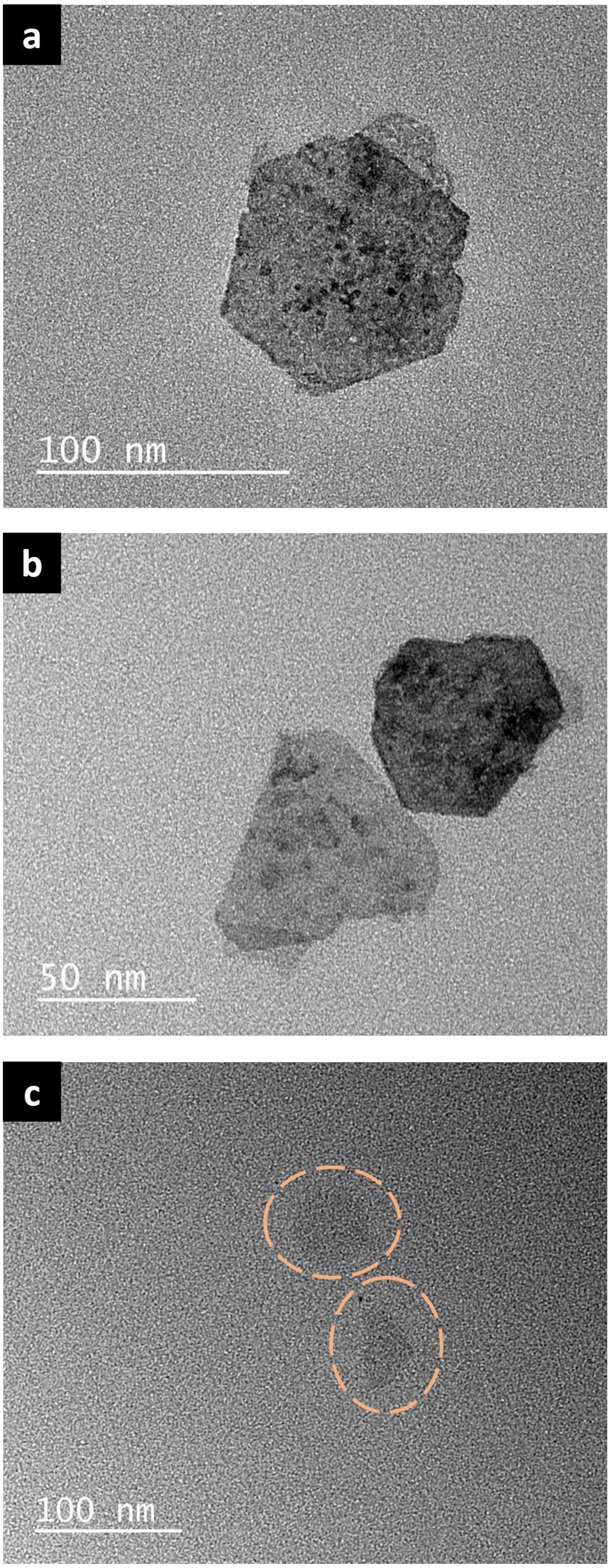

Figure 3.25.: TEM images of exfoliated β3-prec.

3.3.4.3. AFM local probe

Three tapping-mode AFM images of MnO_2 nanosheets are presented in Figure 3.27. The images and height profiles presented in Figure 3.27.a, b and c, correspond to nanosheets that were collected in the supernatant after centrifugation of the suspension at 4000 rpm, 20 000 rpm and 50 000 rpm respectively. The results reveal 2D flat objects with similar lateral dimensions as those detected by TEM observations (between 200 nm to 400 nm as seen in Figure 3.24.a). Small fragments of “exploded” nanosheets are not observed since the scale of observation is very large. The height profiles indicate that the terrace of the objects is fairly flat and their thickness can be determined on the basis of steps between the nanosheet and the substrate surface. The height detection threshold is around the angstrom, making this technique very accurate.

It is interesting to note the efficiency of the size-selection process. The average crystallite thickness in the colloidal suspension after removal of unexfoliated material is 60 ± 20 nm. After 20 000 rpm, the particle thickness only reaches 10 ± 5 nm, and at 50 000 rpm, thin objects of 3 ± 2 nm can be obtained. The thickness of one MnO_2 monolayer is evaluated to be 0.38 nm based on its atomic architecture, so that the thinnest objects may be constituted by a few oxide layers (as modeled in Figure 3.26.a). After centrifugation at 50 000 rpm, it is possible to detect particles that show a minimum thickness of 1.5 nm. It should be noticed that measured AFM heights obtained for exfoliated materials in liquids are known to be commonly overestimated due to the presence of residual solvent (water in our case). The discrepancy between the theoretical thickness of one layer (0.38 nm, represented in Figure 3.26.a) and the experimentally obtained value (1.5 nm) is due to the hydration of the nanosheets. Indeed, as shown in Figure 3.26.b, the size of a water molecule can reach up to approximately 0.12 nm. It can therefore be assumed that the height profile measured in Figure 3.27.c (green) corresponds to two or three layers of manganese oxide. The height profile measured in Figure 3.27.c in red would correspond to six layers, and in blue to eight or nine layers.

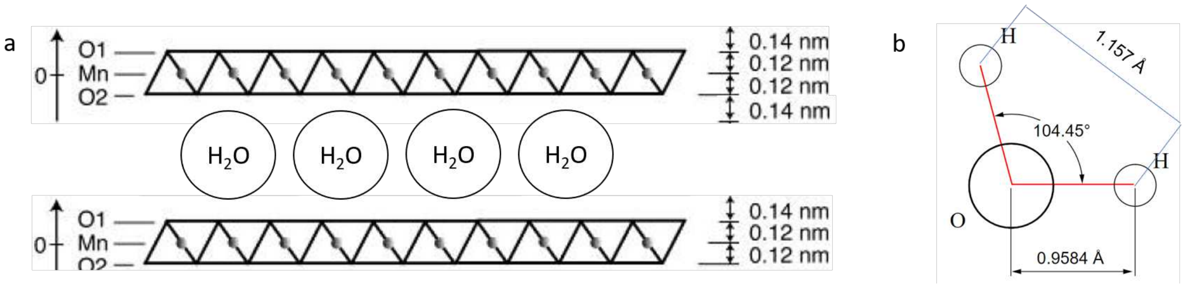

Figure 3.26.: (a) Schematic representation of a monolayer of MnO_2 (inspired from [169], (b) Water molecule dimensions (from Wikipedia).

In the case of $\beta3$-prec cobalt precipitated phases, height profiles reveal the presence of 15 ± 5 nm thick particles in the supernatant after centrifugation at 4000 rpm, corresponding to multilayer (several dozens) aggregates. The thickness decreases down to 8 ± 2 nm nm after centrifugation at 20 000 rpm and to 4 ± 1 nm at 50 000 rpm. From the crystal structure, the thickness of a CoO_2 monolayer is 0.48 nm, thus revealing that considering the hydration of nanosheets, bi or tri-layer exfoliated materials might have been isolated.

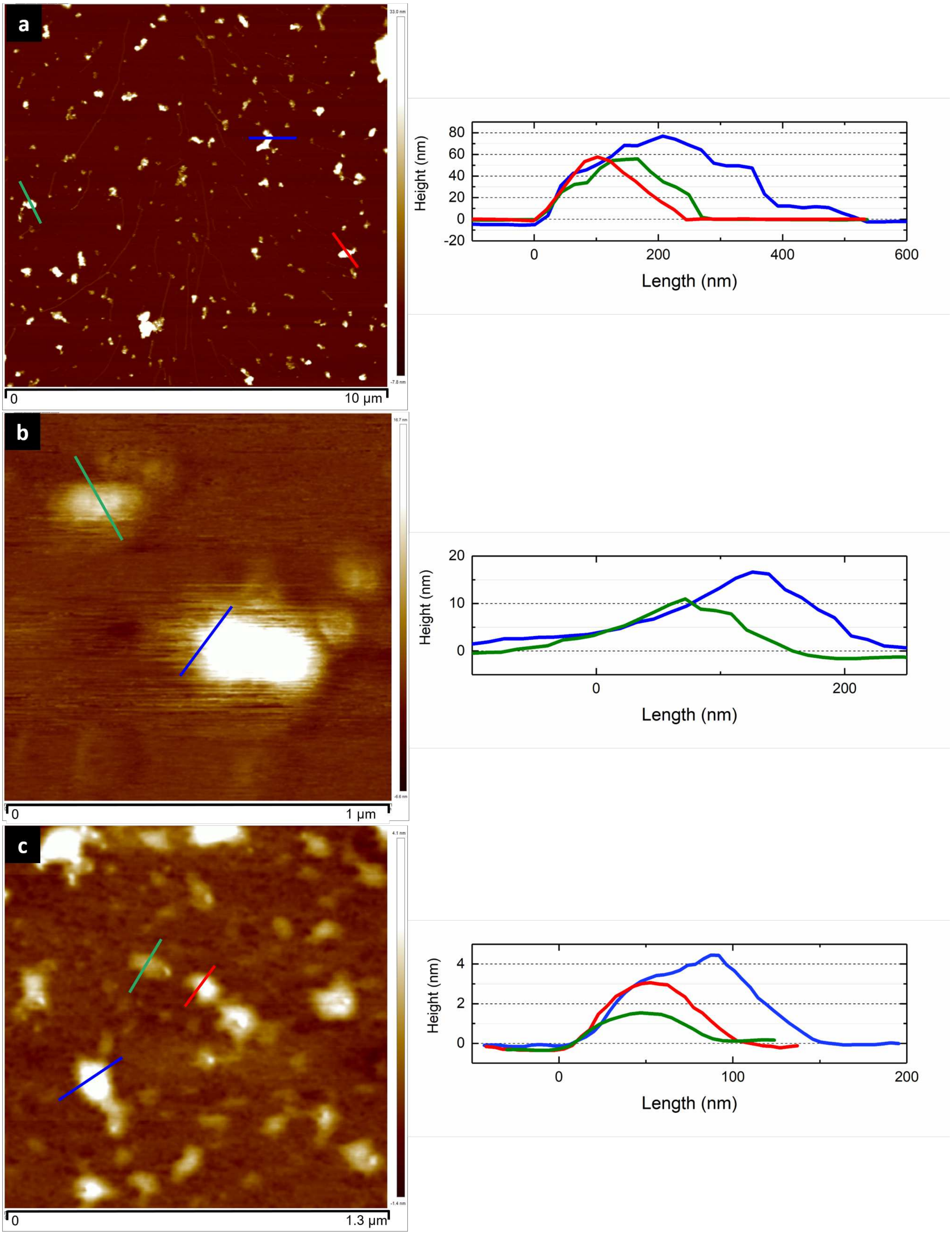

Figure 3.27.: Tapping-mode AFM image and height profiles of MnO_2 nanosheets obtained in the supernatant after centrifugation at : (a) 4000 rpm. (b) 20 000 rpm. (c) 50 000 rpm.

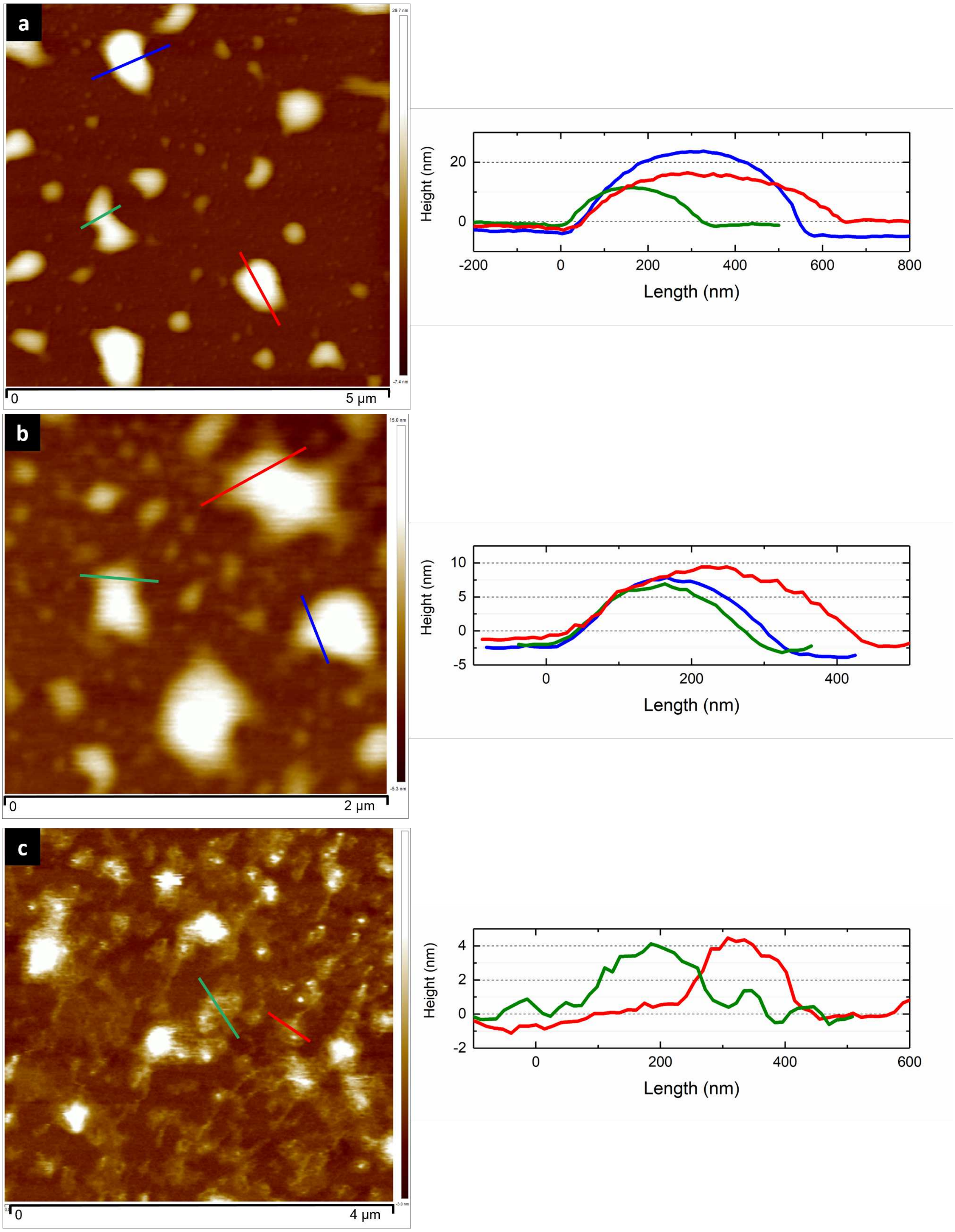

Figure 3.28.: Tapping-mode AFM image and height profiles of CoO_2 nanosheets obtained in the supernatant after centrifugation at : (a) 4000 rpm. (b) 20 000 rpm. (c) 50 000 rpm.

3.4. Conclusion

In this chapter, we reported how colloidal suspensions of manganese oxides and cobalt oxyhydroxides oligolayers were successfully obtained, starting from lamellar protonated materials first synthesized by precipitation and “chimie douce” reactions. Manganese birnessite phases, pre-intercalated with sodium or potassium, were subjected to a protonation through an acidic ion-exchange reaction, in order to facilitate the subsequent exfoliation using TBAOH. According to the synthesis method, different morphologies were achieved : from rigid platelets to veil-like slabs, from clear distinct hexagonal aggregates to nanometric particles. In addition to differences in the morphology and the size, cobalt oxyhydroxides are much more conductive than manganese oxides.

Ion-exchange process involving the intercalation of TBA^+ species lead to the successful obtention of MnO_2 nanosheets dispersions. Liquid cascade centrifugation enables a size-selection of the particles, and various objects with various thicknesses can be isolated, as proven by TEM and AFM analyses, depending on the centrifugation rate. However, this process is long and tedious, yielding only to a few milligrams of nanosheets each time.

Since our prospect is to ensure restacking between various colloidal suspensions and make thick electrodes, although oligolayers were clearly obtained, all colloidal suspensions used later on in this work have only been subjected to 4000 rpm. This way, a maximum quantity of exfoliated material as well as “nanopieces” of material is recovered and can be used as electrode material. Furthermore, for the target applications, it might be more interesting to work with multilayers. Indeed, the pseudocapacitance of manganese oxides rely on the ion mobility in the interlayer space. Also, the conductivity of cobalt oxyhydroxides depends on the mean oxidation state of Co, which can be subject to change if other metal oxide layers are present. Beforehand, these Co and Mn colloidal suspensions have to be restacked together to obtain the synergistic effect wanted. In order to do so, a precise study of their surface charge and restacking properties has to be explored, which will be explained in the following chapter.

4. Restacking

Nanosheets can be considered as charge-bearing lamellar aggregates, dispersed in a colloidal suspension. After having successfully obtained nanosheet suspensions, solution-based techniques can be applied to build a range of functional materials by employing them as “building blocks”. Various methods with precise control at the nanometer scale have been developed in the literature and are schematically illustrated in Figure 4.1 :

- Flocculation : very convenient protocol for preparing micro- and mesoporous lamellar solids or nanocomposites based on nanosheets. Flocculation consists in adding counter-ions to colloidal nanosheets to promote their restacking. It does not affect the 2D morphology of the nanosheets and usually produces a randomly stacked lamellar aggregate

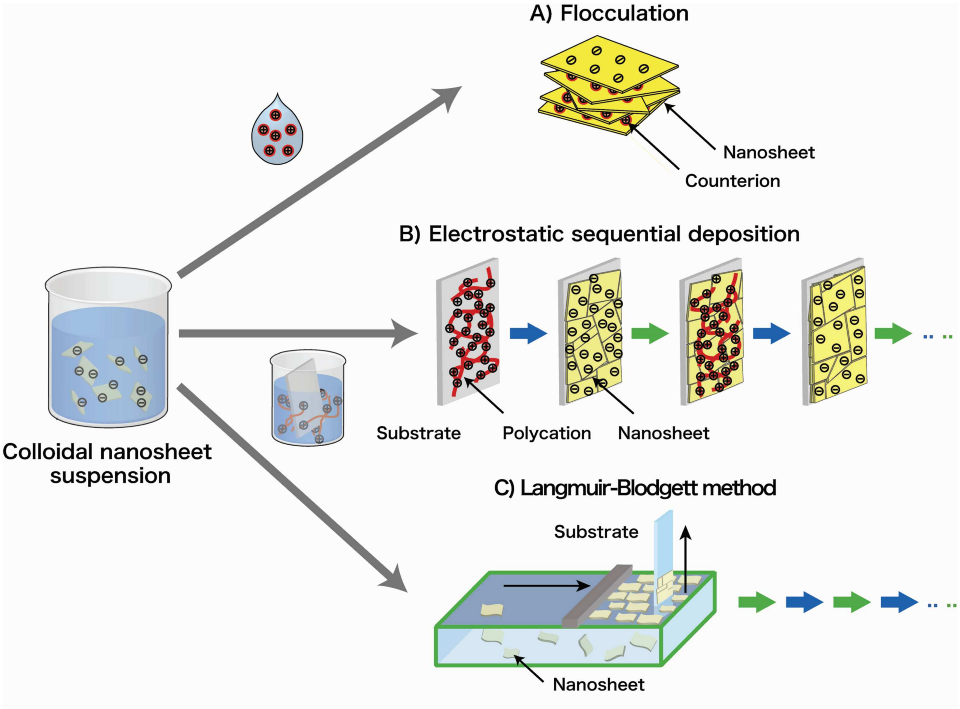

Figure 4.1.: Schematic assembling processes for nanosheets. (A) Flocculation, (B) Electrostatic sequential adsorption, and (C) Langmuir-Blodgett method [219].

- Layer-by-layer assembly : most frequently used to design and build up multilayer nanofilms and core–shell nano-architectures on a planar or curved surface. In principle, a precise control of 1-nm step or nanosheet thickness can be achieved.
  - Electrostatic sequential deposition : since both oxide and hydroxide nanosheets bear charges, a multilayer film can be built up layer-by-layer by repeatedly

dipping a substrate in first a polyelectrolyte solution (polycation or polyanion) and second the colloidal suspension of nanosheets.

- Langmuir-Blodgett Deposition : this procedure is applicable for fabricating highly organized films of nanosheets. It consists in the formation of a floating monolayer on a liquid surface in a Langmuir trough followed by an appropriate level of compression. Through vertical-dipping or lifting, the monolayer is deposited onto a flat surface. Surfactants are used to disperse suspensions of nanosheets on a water surface, and then the floating monolayers are forced to assemble at high density.

The final objective of this work is to obtain electrode material for supercapacitors. Thick electrodes are more interesting than thin film electrodes since they enable a higher energy density. This is why the flocculation technique was chosen to be optimum for the target application. In the case of oxide nanosheets, which are generally negatively charged, flocculation is usually performed by simply mixing the nanosheet suspension with cations. On the contrary, hydroxide nanosheets usually bear a positive charge, so flocculation occurs when anions/polyanions are added to the colloidal suspension. More importantly, direct flocculation of hydroxide nanosheets (positively charged) and oxide nanosheets (negatively charged) is possible, which may be one of the ultimate goals for material synthesis using nanosheets as “building blocks”. Sasaki et al. used this technique to prepare inorganic sandwich layered materials of oxide nanosheets ($Ti_{0.91}O_2$ or $Ca_2Nb_3O_{10}$) and layered double hydroxide (LDH) nanosheets of $Mg_{2/3}Al_{1/3}(OH)_2$ [220].

To successfully assemble the manganese oxide and cobalt oxyhydroxide nanosheets in a controlled, alternate manner requires the precise knowledge of their surface state. This information is easily accessible for initial pristine particles by isoelectric point measurement (pH at which the global particle surface charge is neutral). However, as exfoliation ensues and nanosheets are obtained, experimental IEP determination becomes less straightforward, as it requires a great quantity of starting material and is time-consuming in pH stabilization. Furthermore, as the particles become thinner, their reactivity could be changed and possible interactions might arise.

For a global approach of this problem, the MUSIC model (Multi-site Complexation) was used to evaluated the IEP of initial non-exfoliated materials. Then this model was generalized to colloidal suspensions to predict their theoretical IEPs.The comparison of these model IEP and the experimental ones will lead to a better understanding of the studied nanosheets.

In this section, a first part is dedicated to the application of MUSIC model for the surface charge prediction of the exfoliated materials. Then, actual restacking strategies adopted, based on MUSIC predictions, will be developed. Finally, the obtention of multilayer composites will be verified by various characterization techniques, including X-ray diffraction, scanning and transmission electronic microscopy, and conductivity measurements.

4.1. Surface acidity/basicity of transition metal oxides (Co, Mn)

The contact between the surface of oxide particles and water induces a property modification on both : the solid is strongly solvated and the oxygen atoms on its surface interact with water molecules by exchanging protons. The particle surface acquires an electrostatic charge, when water molecules become strongly polarized by the surface and sees its physico-chemical properties modified on a distance that can reach several nanometers.

4.1.1. Origins of charge surface

The surface charge of oxide particles results from the ionization of the monolayer of hydroxyl groups on the surface of the solid in contact with water [221]. Within the oxide, there is a total compensation of anionic and cationic charges so that the solid can be electrically neutral. If the charge of a cation is equivalently distributed within its bonds with neighboring anions, the *strength of the electrostatic valence bond* υ going to each corner of the polyhedron of anions is defined as :

$$\upsilon = \frac{Z}{CN} \tag{4.1}$$

with Z the electric charge of the cation (or its oxidation state) and CN its coordination number [222]. For the oxygen atoms situated within the solid linked with n_v cations, its partial charge equals :

$$\delta(O)_{volume} = n_v\upsilon - 2 = 0$$

However, for oxygen localized on the surface, approximately half of the cations are missing, and therefore the charges are not fully compensated anymore, and the partial charge is :

$$\delta(O)_{surface} = n_s\upsilon - 2 < 0$$

Consequently, the surfacic oxygen atoms present a basic nature and provoke the dissociation of water molecules in its contact. This leads to the hydroxylation of the surface. For oxides synthesized by precipitation in water, the hydroxyl surfacic groups are naturally present since they originate from the coordination sphere of the last cations incorporated. Consequently, the acidity of a solid surface depends on two main factors :

1. the characteristics of underlying cation (oxidation state and coordination number)
2. the structure of oxygen group

Therefore, oxides present an acid-base behavior in water. They carry an electrostatic charge that depends on the nature, charge of the cation, the structure of oxygen group and the pH. The acidity of an oxide is generally characterized by the *point of zero charge* (PZC) or the *isoelectric point* (IEP). The PZC is defined as the pH value at which the immerse solid oxide has a surface charge equal to zero (obtained by acid-base titration). Whereas the IEP is defined as the pH value at which the electrokinetic potential equals zero [223]. For dispersions of metal oxides in dilute solutions of inert electrolytes, IEP is most often used : at pH < IEP, the oxide bears a positive charge, while at pH > IEP, the oxide is negatively charged. The main factors that impact the IEP are :

1. Coordinence of surfacic groups and their polarization by the metal cation : the basicity of surface ions is set lower if their coordinence if high and the cation polarization is strong
2. Crystalline structure and particle morphology : according to the crystalline structure, the number of multi-coordinated oxygens will differ. Since each group has a different acidity, the morphology will be an important factor for the global acidity of the faces (for example, basal planes and lateral planes will present various groups)

In order to theoretically determine the IEP, the Multisite Complexation model (MUSIC) is applied and will be explained in the following section.

4.1.2. MUltiSIte Complexation model (MUSIC)

Several approaches have tried to correlate IEP/PZC to characteristics of metal oxyhydroxides. Thus, Parks has proposed a formula based on the size and valence of the cation and on the crystal field stabilization energy of the solid for simple (hydr)oxides [221]. Sverjensky and Sahai have developed a model in order to simulate PZC of complex oxides (including clays) using the dielectric constant of the solid, the bond valence v (Equation 4.1) and the metal-oxygen distance [224].

Since the IEP is a particular point of the function describing the evolution of surface charge vs. pH, an indirect possibility to determine its value is to model the whole surface charge curve, i.e. to use a model able to give the characteristics of each acido-basic site present at the surface (site density, charge, acidity constant). This approach has been developed in MUSIC model and is described below [225, 226, 227].

As seen in section 4.1.1, oxygen atoms present on the surface carry a non-compensated charge $\delta(O)_{surface} = n_s v - 2 + p$ (p represent the number of protons). Therefore, on the surface of the oxide, two protonation equilibrium can be considered :

$$Me_n - O^{(n_s v-2)} + H^+ \Longleftrightarrow Me_n - OH^{(n_s v-1)} \qquad K_{n,1} = \frac{[Me_n - O^{(n_s v-2)}][H^+]}{[Me_n - OH^{(n_s v-1)}]}$$

$$Me_n - OH^{(n_s v-1)} + H^+ \Longleftrightarrow Me_n - OH_2^{(n_s v)} \qquad K_{n,2} = \frac{[Me_n - OH^{(n_s v-1)}][H^+]}{[Me_n - OH_2^{(n_s v)}]}$$

n represents the number of cations linked to the oxygen atom and ν represents the electrostatic valence bond. K$_{n,1}$ and K$_{n,2}$ are the dissociation constants. [H$^+$] represents the activity of protons situated in the vicinity of the surface. The MUSIC model provides a simple way of calculating the dissociation constants based on electrostatic and crystallographic considerations. In the model proposed by Hiemstra, the protonation constants are directly proportional to the charge carried by the oxygen atom at the surface, as shown in equation 4.2 :

$$\log K_{n,x} = -A(\Sigma s_j + V) \tag{4.2}$$

where A is a constant (-19.8 at 25°C) obtained by calibration proposed by Hiemstra [225], V is the valence of the oxygen (-2) and s_j represents the bond valence of the surrounding atoms around the oxygen.

The oxygen atom is surrounded by either metal cations, protons or hydrogen bonds. The bond valence will depend on the nature of the surrounding atom :

- for a proton, the carried charge is shared between the oxygen it is attached to (80%) and a surrounding water molecule by hydrogen bond (20%). This means that each oxygen atom receives a +0.8 charge per proton in a OH bond and +0.2 charge through a hydrogen bond,

- the bond valence of the metal can be calculated using Pauling's rule [225] or with the formula proposed by Brown and Altermatt [228] based on the Me-O distance. In this case of a symmetrical distribution of charge in the coordination environment, the bond valence will be determined using Pauling's rule. In our case, metal atoms are in octahedral sites, i.e. their charge is distributed over 6 bonds, s_{Me} = Z / 6 where Z represents the electric charge of the cation

4.1.3. Theoretical determination of IEP of exfoliated MnO_2 and $\beta 3$-Cobalt particles

4.1.3.1. Hypothesis

As described in the previous chapter, the oxides are lamellar structures composed of layers built up of MeO_6 (Me= Co or Mn) octahedra sharing 6 edges with their neighbors. These planar mono-slabs are separated by an inter-lamellar space, in which cations can be inserted. Two main crystal faces represent the surface of the oxides : basal face (00l) with only tri-coordinated oxygen surface groups, and lateral face (hk0) where mono-coordinated and bi-coordinated oxygen sites are found in the same proportion. For better representation, the oxygen sites are shown schematically in Figure 4.2.

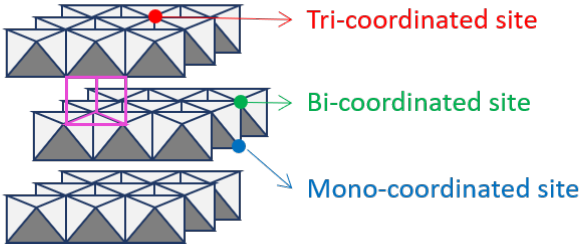

Figure 4.2.: Schematic representation of layered structure. The various oxygen sites are reported as dots. Mono-coordinated oxygen sites are reported as blue dots, bi-coordinated oxygen sites in green and tri-coordinated oxygen sites in red dots. Environment in the interlayer space is schematized in pink.

From a topological point of view, the two oxyhydroxides differ one from the other by the stacking of the slabs, but the close environment of the surface oxygen atoms present do not differ. Therefore, from a MUSIC model perspective, both oxides present the same oxygen surface sites. These oxygen surface sites can be divided into three categories : mono-, bi- or tri-coordinated oxygen sites (respectively noted Me-O, Me_2-O or Me_3-O).

Protonation reactions	Dissociation constant $K_{n.i}$	Metal cations oxidation state			
Tricoordinated oxygen sites (n=3)		$Me^{3+}Me^{3+}Me^{3+}$ (v=3/2)	$Me^{3+}Me^{3+}Me^{4+}$ (v=5/3)	$Me^{3+}Me^{4+}Me^{4+}$ (v=11/6)	$Me^{4+}Me^{4+}Me^{4+}$ (v=2)
$Me_3\text{-}O^{(3v-2)} + H^+ \Leftrightarrow Me_3\text{-}OH^{(3v-1)}$	$K_{3.1}$	5.94	2.64	-0.66	-3.96
$Me_3\text{-}OH^{(3v-1)} + H^+ \Leftrightarrow Me_3\text{-}OH_2^{(3v)}$	$K_{3.2}$	-5.94	-9.24	-12.54	-15.84
Bicoordinated oxygen sites (n=2)		$Me^{3+}Me^{3+}$ (v=1)	$Me^{3+}Me^{4+}$ (v=6/7)	$Me^{4+}Me^{4+}$ (v=4/3)	
$Me_2\text{-}O^{(2v-2)} + H^+ \Leftrightarrow Me_2\text{-}OH^{(2v-1)}$	$K_{2.1}$	15.84	12.54	9.24	
$Me_2\text{-}OH^{(2v-1)} + H^+ \Leftrightarrow Me_2\text{-}OH_2^{(2v)}$	$K_{2.2}$	3.96	0.66	-2.64	
Monocoordinated oxygen sites (n=1)		Me^{3+} (v=1/2)	Me^{4+} (v=4/6)		
$Me\text{-}O^{(v-2)} + H^+ \Leftrightarrow Me\text{-}OH^{(v-1)}$	$K_{1.1}$	21.78	18.48		
$Me\text{-}OH^{(v-1)} + H^+ \Leftrightarrow Me\text{–}OH_2^{(v)}$	$K_{1.2}$	9.9	6.6		

Table 4.1.: Log of dissociation constants of the different protonation reactions determined by the MUSIC model. Three types of oxygen sites are considered, differentiated by the number of metal cation bonds (n = 1, 2 or 3). The oxidation state of neighboring metal cations influences the dissociation constant. $\nu = \frac{Z}{CN}$, where Z is the oxidation state and CN the coordination number (6), is given for each site.

The distinction between hydrous manganese oxides and cobalt oxyhydroxides will be reflected in the bond valence of the metal cation on the surface. Indeed, the mean oxidation state of manganese in hydrated manganese dioxide ranges in between 3 and 4, which means that a variable proportion of Mn^{3+} and Mn^{4+} will be found in the vicinity of surface oxygen atoms. In the case of cobalt oxyhydroxides, when the mean oxidation state is between 2 and 3, a mix of Co^{2+} and Co^{3+} will be present. In our case, since the mean oxidation state of Co is usually higher than 3, a mix of Co^{3+} and Co^{4+} is present.

Considering all these conditions, the dissociation constant $K_{n,1}$ and $K_{n,2}$ defined earlier can be calculated by the MUSIC model and are reported in Table 4.1.

For simplification and because it corresponds to the reality of our materials, Table 4.1 only presents the values obtained for slabs with mixed oxidation state between 3 and 4. Calculations considering mixed oxidation state between 2 and 3 are obtained the same way, according to the same formula, but are not presented here.

4.1.3.2. IEP prediction

Based on the calculated dissociation constants, it is possible to predict the charge surface of the particles. This can be linked to the zeta potential of dispersed particles, which in turn, can lead to the prediction of their isoelectric points. The method used was developed in collaboration with Grégory Lefèvre (IRCP, Chimie Paristech) and is detailed below:

1. The first data required is the mean oxidation state of the metal cation in the oxide of interest, determined by iodometric titration. It is necessary in order to determine the proportion of each type of oxygen site.
2. Keeping the mean oxidation state in mind, a Monte-Carlo simulation is programmed in Excel VBA. This simulation will be programmed in order to generate the proportion of the different sites and to fit closely to the target mean oxidation state. At the end of this, the proportions of all types of oxygen sites is obtained for each mean oxidation state.
3. Based on crystallographic considerations, the Multisite Complexation model (MUSIC) is used to calculate the dissociation constant of each oxygen site [226]
4. PHREEQC is a computer program for simulating chemical reactions and transport processes in water. Surface complexation can be represented by various models [229, 227]. In this work, the Basic Stern Model is used to estimate the composition of the electrical double layer on a surface. Thanks to previously calculated dissociation constants (by MUSIC) and the proportion of oxygen site types, the surface charge density is calculated as a function of pH for each mean oxidation state
5. Strictly speaking, the pH value for which the surface charge density is zero corresponds to the PZC of the particle. However, if no impurities are considered, if the surface charge is zero, then the electrokinetic potential of the particle is zero as well. Thus the IEP can be predicted.

4.1.3.3. Particle thickness

The oxides studied here all show platelet morphologies. According to the thickness of the platelets, the densities and proportion of oxygen sites will be different. Indeed, the basal face (001) only has tri-coordinated oxygen sites, whereas the lateral face (hk0) has a mix of mono- and bi-coordinated oxygen sites.

	Sites on basal face (110)	Sites on lateral face (001)
H_K-birn	14.49	9.76
β3 - prec	14.21	15.56

Table 4.2.: Density of sites/nm^2 on basal and lateral faces of H_K-birn and β3-prec, determined with the crystallographic cell deduced from X-Ray data.

This will certainly have an impact on the IEP. This is why the calculations were performed considering various thicknesses. The thickness of the particles is defined by the basal surface area percentage over total surface area : from 50% for an isotropic grain to 100% for an infinite sheet.

Basal surface area / Site ratio	50%	60%	70%	80%	90%	100%
Me_3-O	14.49	14.49	14.49	14.49	14.49	14.49
Me_2-O	4.88	3.25	2.09	1.22	0.54	0
Me_1-O	4.88	3.25	2.09	1.22	0.54	0

Table 4.3.: Number of tri-coordinated (respectively bi-coordinated and mono-coordinated) oxygen sites for a basal surface of 1 nm^2 and various basal percentages of H_K-birn.

To do the calculation, it is necessary to evaluate the number of tri-coordinated sites (respectively bi-coordinated sites and mono-coordinated sites). For this, the site density is evaluated from the crystallographic cell deduced from X-Ray data. The densities for H_K-birn and β3-prec are shown in Table 4.2. As an example, if the basal surface area is 1 nm^2, the number of sites calculated for H_K-birn for each basal percentage is shown in Table 4.3.

Discussion

All IEP values determined by this method for a mean oxidation state ranging from 2 to 4 are presented in Figure 4.3 with various basal surface area percentages.

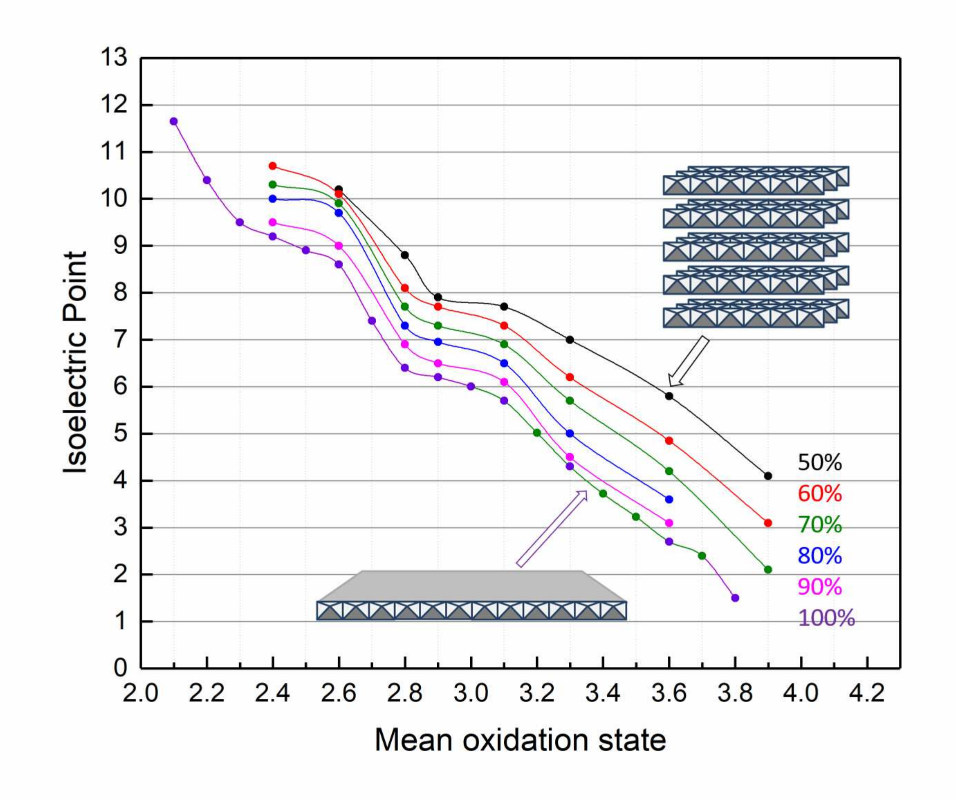

Figure 4.3.: Theoretical IEP calculations depending on the mean oxidation state of the metal ion in lamellar $MeO_x(OH)_y$ materials, for basal surface area percentages over total surface area varying from 50% (isotropic object) to 100% (infinite lamellae).

MUSIC model predicts a major impact of the mean oxidation state of the metal ions on the IEP value, which is a well-known phenomenon. The metal cations are more acidic at higher oxidation state and less acidic at lower oxidation state [230]. This correlation found in solution cations strongly supports the result found in this case. As shown in Figure 4.3, as the mean oxidation state of the metal oxide increases, they become more acidic and therefore show a lower IEP.

In addition, the model also shows an effect of the particle morphology on IEP, with an IEP decrease of approximately 3 pH units when moving from isotropic particles to infinite lamellae. This morphology impact is very important : as the initial platelet particles are exfoliated, if the integrity of the layers is not affected, the proportion of lateral sites will be greatly diminished. Therefore exfoliation imposes a basal surface area percentage close to 100%, which would lead to a decrease of the IEP of the materials.

4.1.4. Experimental determination of IEP

4.1.4.1. Definition of Zeta (ζ) potential

The liquid layer surrounding the particle exists as two parts (double layer) : an inner region (Stern layer) where the ions are strongly bound and an outer (diffuse) region where they are loosely associated to the particle. Within the diffuse layer there is a notional boundary inside which the ions and particles form a stable entity. When a particle moves (e.g. due to gravity), ions within the boundary move. The ions beyond the boundary stay with the bulk dispersant. The potential at this boundary (surface of hydrodynamic shear) is the zeta (ζ) potential. As illustrated in Figure 4.4, ζ potential is not equal to the Stern potential or electric surface potential in the double layer because these are defined at different locations. Such assumptions of equality should be applied with caution. Nevertheless, ζ potential is often the only available path for the characterization of double-layer properties.

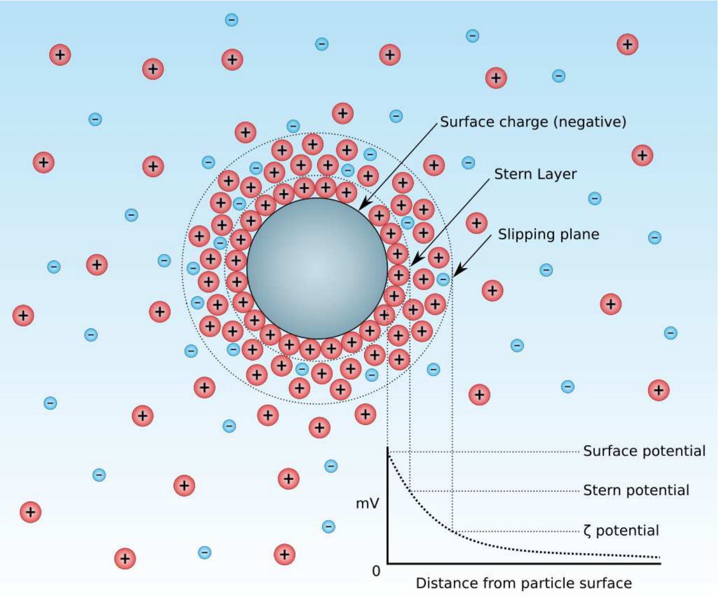

Figure 4.4.: Diagram showing the ionic concentration and potential difference as a function of distance from the charged surface of a particle suspended in a dispersion medium (from Wikipedia).

The magnitude of the ζ potential gives an indication of the potential stability of the colloidal system. The IEP corresponds to the pH value for which $\zeta = 0$. However, calculation of the ζ potential from experimental data can be difficult. But a zero value of directly measured quantities (e.g. electrophoretic mobility) corresponds to $\zeta = 0$, so the IEP can be determined experimentally without any model assumption.

4.1.4.2. Measurement

Zeta potential (ζ) is not directly measurable but it can be experimentally-determined thanks to electrophoretic mobility.

An important consequence of the existence of electrical charges on the surface of particles is that they interact with an applied electric field. These effects are collectively defined as electrokinetic effect. When an electric field is applied across an electrolyte, charged particles suspended in the electrolyte are attracted towards the electrode of opposite charge. Viscous forces acting on the particles tend to oppose this movement. When equilibrium is reached between these two opposing forces, the particles move with constant velocity. The velocity of a particle in an electric field is referred to as its electrophoretic mobility. It is dependent on the strength of electric field or voltage gradient, the dielectric constant of the medium and the viscosity of the medium. Zeta potential is related to the electrophoretic mobility by the Henry equation (equation 4.3) :

$$U_E = \frac{2\varepsilon\zeta f(Ka)}{3\eta} \tag{4.3}$$

where U_E = electrophoretic mobility, ζ = zeta potential, ε = dielectric constant, η = viscosity and $f(Ka)$ = Henry's function. The units of K, termed the inverse Debye length is often taken as a measure of the "thickness" of the electrical double layer. The parameter a refers to the radius of the particle and therefore Ka measures the ratio of the particle radius to electrical double layer thickness. Electrophoretic determination of zeta potential are most commonly made in aqueous media and moderate electrolyte concentration. $f(Ka)$ in this case is 1.5, and this is referred to as the *Smoluchowski* approximation [231]. This approximation is applicable to particles larger than about 0.2 microns dispersed in electrolytes containing more that 10^{-3} molar salt. Therefore calculation of zeta potential from the mobility is straightforward for our system, which globally fits the Smoluchowski model.

In order to measure the zeta potential of initial non-exfoliated oxides, dispersions of 10^{-2} M of initial powders in water were prepared. After sonication, this measurement was conducted on a Malvern Zetasizer. Dispersions are put into a capillary cell with electrode at each end, between which a potential is applied. Charged particles within the dispersion will migrate toward the electrode of opposite charge, with a velocity proportional to the magnitude of the zeta potential. The technique used to measure this velocity in Malvern Zetasizer is Laser Doppler Velocimetry.

4.1.4.3. The relation between zeta potential and surface charge

To experimentally determine the IEP of dispersed particles, the method employed here is to measure the zeta potential of dispersions at different pH. By adding acidic or basic solutions in the media, zeta potential ζ vs pH curves for our materials are obtained.

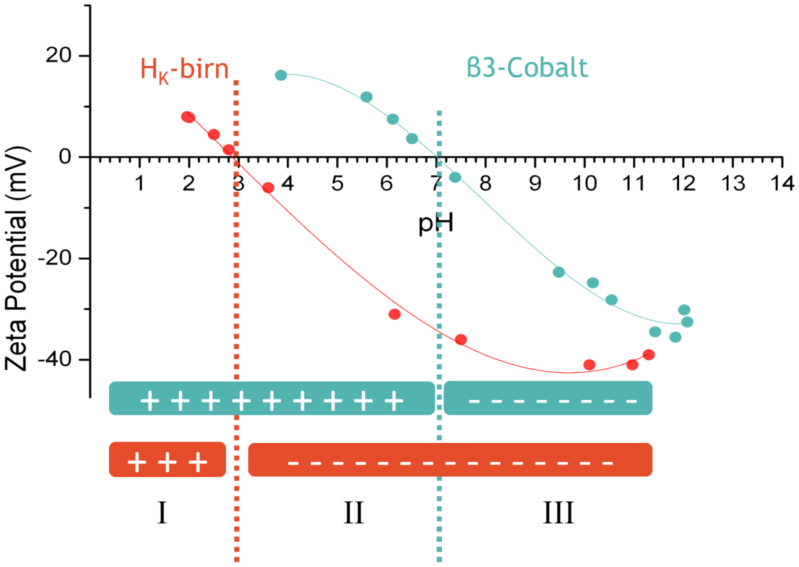

Figure 4.5.: Experimental zeta potential-pH curves of initial protonated birnessite H_K-birn particles (red) and β3-prec cobalt oxyhydroxide particles (blue). (+) and (-) represent the surface charge of the particles. If pH<3, both H_K-birn and β3-prec particles are positively charged. If pH>7, they are negatively charged. If 3<pH<7, H_K-birn particles are negatively charged and β3-prec particles are positively charged.

The IEP corresponds to the pH at which the ζ equals to zero. Two examples are represented on Figure 4.5 : manganese oxide H_K-birn have an IEP of around 2-3, whereas cobalt oxyhydroxides β3-prec have an IEP around 7. These are in accordance with the predicted model. As the mean oxidation state of manganese cations are higher than those of cobalt cations in the $MeO_x(OH)_y$, the IEP value of manganese oxides is lower than that of cobalt oxyhydroxides.

4.1.4.4. Comparison between theoretical IEP predicted by MUSIC model and experimental IEP

In order to validate the use of the MUSIC model to predict IEP, experimental values of IEP have been measured for various oxides and exfoliated layers, with a wide range of mean oxidation states, and compared to theoretical values. The results are presented in Figure 4.6. The dashed area corresponds to basal surface area percentages in the layered materials from 85% to 100% (calculated in previous section) : as initial materials exhibit a strong anisotropy with a platelet morphology, their basal surface area percentage has been estimated from SEM images (see Figure 3.8 and 3.12) around 86% for cobalt oxyhydroxides and 96% for manganese oxides. Exfoliated materials should present ratios close to 100%. Thus, the experimental IEP should fall in the dashed area to fully validate the MUSIC model.

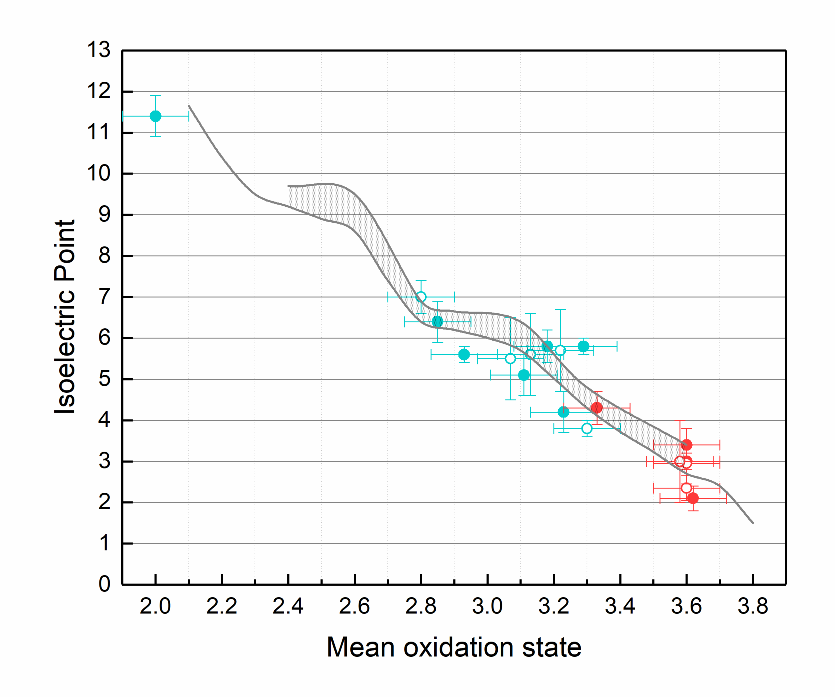

Figure 4.6.: Experimental values of IEP depending on the mean oxidation state of metal ions in the pristine materials (manganese oxides (●), cobalt oxyhydroxides (●)) and exfoliated ones (manganese oxide colloidal suspensions (○), cobalt oxyhydroxide colloidal suspensions (○)). They are compared with calculated IEP values with the basal surface area percentage of 85% (upper black line) and 100% (lower black line) corresponding to the dashed area.

In Figure 4.6, the filled circles represent the IEP values of the pristine materials whereas the empty ones correspond to the exfoliated samples. Experimental values of manganese (oxyhydr)oxides are very close to the values calculated with a basal surface area percentage of 100%. The experimental IEP values of cobalt oxyhydroxides samples follow the same trend. Theoretical IEP values seem to be slightly overestimated. Variations of IEP for a same oxidation state come from variations in initial morphology of the grains. MUSIC model can thus accurately predict the experimental IEP of metal (oxyhydr)oxides, considering only the mean metal oxidation state.

As exfoliation should increase the mean basal surface area percentage to 100%, a decrease of the IEP should be observed (as seen in section 4.1.3.3). However, since the initial basal surface area percentage is already quite high (>85%), the model predicts a very limited impact of the exfoliation on IEP values of less than 0.5. By making the assumption that the mean oxidation state of nanosheets is the same as pristine materials (which will be proved further in section 4.3.2.5), this is what is observed in Figure 4.6, in which the exfoliated materials show IEP values very similar to pristine materials.

It is interesting to compare the experimentally measured IEP values to the theoretical calculated ones for the exfoliated nanosheets. To do this, the experimental thickness of a MnO_2 nanosheet is evaluated by AFM (see section 3.3.4.3). For the thinnest nanosheet obtained, the thickness is approximately 1.5 nm for a width around 90 nm. This leads to a basal surface area percentage of 98.7 %. As the exfoliated suspension has particles with a manganese mean oxidation state of 3.6, the theoretical IEP would be 2.9. Experimentally, we have obtained an IEP of 2.4 for one sample or 3 (concerning another sample). The theoretical value thus falls in the experimental error bar, which is of approximately 17%.

4.1.4.5. pH domains

The measurement of IEP enables a good understanding of the particles dispersed in water. It validates the MUSIC model in which IEPs are predicted only taking into account the mean oxidation state of the metal oxides. Indeed, the experimental IEP values are in good agreement with the calculated ones for initial pristine layered oxides.

Furthermore, as the particles are exfoliated, no significant change of experimental IEP value is observed. This is in accordance with the MUSIC model which predicts a low impact of exfoliation of lamellar materials on IEP values. Therefore, from the mean oxidation state of pristine materials, the surface charge of the exfoliated nanosheets in the colloidal suspensions can be evaluated. Taking all this into account, distinct pH domains can defined, in which the exfoliated particles will behave differently. They are schematically represented in Figure 4.5. In domain I ($\mathrm{pH} < 3$), both oxide particles are positively charged, whereas in domain III ($\mathrm{pH} > 7$), they are both negatively charged. It is only in domain II ($3 < \mathrm{pH} < 7$), that they are oppositely charged.

The aim of this study is to obtain mixed Mn-Co layered oxides organized in a controlled alternating way. By controlling the pH of the colloidal suspensions, the surface charge of the dispersed nanosheets will change considerably. The nanosheets of different nature will then interact differently and their assembly can be finely tuned. Bearing this in mind, various strategies can be considered for the restacking of particles and will be detailed in the following section.

4.2. Restacking methods

The objective of this work is to synthesize novel nanocomposites that will combine the excellent pseudocapacitive properties of manganese dioxide, and the good electronic conductivity of cobalt oxyhydroxides. The idea behind the exfoliation process is to consider the nanosheets as “building blocks” and to restack them together to obtain mixed layered particles.

Thanks to the IEP prediction, the surface charge of the particles of interest, depending on the pH, is clearly known. The identification of pH domains in which the particles are negatively or positively charged help in the choice of counter-ions that will induce flocculation. Depending on the desired restacking nature and order, many strategies can be considered.

The most direct technique is to flocculate the negatively charged nanosheets by adding a counter-ion. Another strategy is to induce flocculation of positively charged nanosheets and negatively charged nanosheets. Since both techniques are based on different interactions between nanosheets, it is expected that they lead to distinct restacked materials (restacking order, strength of bonds, interlayer space...). Both explored techniques will be described in details below.

4.2.1. Flocculation by adding a counter-ion

The addition of counter-ions to colloidal charged nanosheets promotes their restacking, i.e. flocculation. Flocculation does not affect the 2D morphology of the nanosheets and usually produces a randomly restacked lamellar aggregate. Through flocculation, foreign species can be more easily incorporated, with regard to other synthesis methods, to synthesize new nanocomposites, e.g. polymer hybrid composites [232], which would be difficult to obtain through conventional ion-exchange and intercalation reactions.

4.2.1.1. Simple restacking (mono-element)

In order to study the effect of exfoliation/restacking process on the initial materials properties, the colloidal suspensions of cobalt and manganese-based objects were first flocculated separately. This is performed by simply mixing the nanosheet suspension with cations. Indeed, after exfoliation, the colloidal suspensions of Mn or Co-based nanosheets suspensions are strongly basic ($pH \simeq 12$). As seen in Figure 4.5, $pH = 12$ corresponds to pH domain III, where both Mn and Co colloidal suspensions are negatively charged. Figure 4.7 presents a schematic representation of the entire exfoliation/restacking process of the layered oxides. First, the synthesized pristine materials go through an intercalation reaction of TBA^+ ions in presence of TBAOH. Then, the layered materials are exfoliated in order to obtain a colloidal suspension. The stability of the colloidal suspension is verified, meaning that exfoliation was successful (details in section 3.3.2). By adding counter-ions in the stable colloidal suspension, the nanosheets are destabilized and aggregated into larger precipitates.

Experimentally, two colloidal suspensions were subjected to flocculation : one of manganese oxide H_{Na}-birn and the other of cobalt oxyhydroxide β3-prec. In both cases, the stable colloidal suspension obtained after exfoliation is vigorously stirred and a solution of NaCl (200 mL, 1 M) is added drop-wise. Immediately, flocculates appear in the suspension. They are stirred for another 30 minutes before being centrifuged at 4000 rpm. The deposit obtained in the bottom of the centrifugation vial corresponds to the restacked nanosheets, it is dried and then analyzed to better understand the flocculation process.

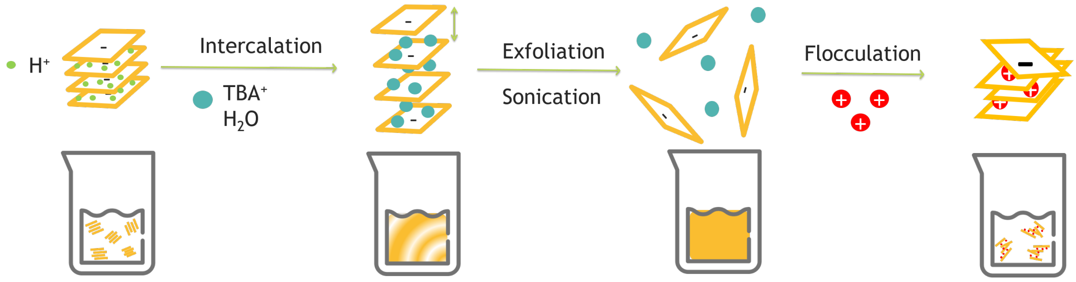

Figure 4.7.: Schematic representation of exfoliation/restacking process of mono-element layered oxides.

4.2.1.2. Mixed manganese-cobalt restacking induced by addition of counter-ion

The desired mixed Mn-Co materials can also be obtained with the same approach, the addition of a counter-ion. According to Figure 4.5, both colloidal suspensions are stabilized at pH=12. A vigorous mixing of both gives one stable colloidal suspension of manganese and cobalt nanosheets at pH=12.

Then, flocculation can be induced by adding a positively charged counter-ion. This positive ion will balance the electrostatic repulsion between the nanosheets and the nanosheets will spontaneously flocculate. This will be called restacking method 1α.

4.2.2. Flocculation between oppositely charged nanosheets

Restacking can be provoked by a change of pH. Indeed, initial suspensions are both negatively charged at pH domain III. By shifting to pH domain II, Mn and Co-based nanosheets are oppositely charged, and attract each other. Thus, an alternate restacking and flocculation can take place. Two different strategies to change the pH can be adopted. A schematic summary of the restacking methods are presented in Figure 4.8.

4.2.2.1. One-pot strategy (method 1)

The one-pot strategy consists in mixing both colloidal suspensions when they are stabilized, i.e. at the exfoliation pH of 12, leading to a mixed stable colloidal suspension at pH 12 (domain III). As seen in Figure 4.5, in pH domain II, manganese nanosheets remain negatively charged. However, cobalt nanosheets become positively charged, since their

IEP value is equal to 7. Therefore, the pH of 4.5 appears to be optimal for restacking as the cobalt and manganese nanosheets are oppositely charged and the zeta potential is superior to 10 mV.

To induce flocculation of the mixed colloidal suspension, the pH is decreased from 12 down to 4.5 by adding nitric acid. The choice of nitric acid is motivated by the fact that it is a strong oxidizing acid, so that reduction of the cobalt cations in the nanosheets will be prevented, which should preserve good electronic conductivity.

It is important that the initial mixed colloidal suspension at pH 12 sees its pH decrease to 4.5 in a very fast way. If not, since the cobalt-based nanosheets become positively charged at pH 7, they will tend to flocculate first, entailing an inhomogeneous restacking.

Thus, the mixed colloidal suspension is vigorously stirred and suddenly added into a concentrated nitric acid solution at pH 1, in order to obtain a final global suspension of pH in domain II. Final pH is adjusted to 4.5 by addition of nitric acid or sodium hydroxide. This restacking method will be denoted as 1β.

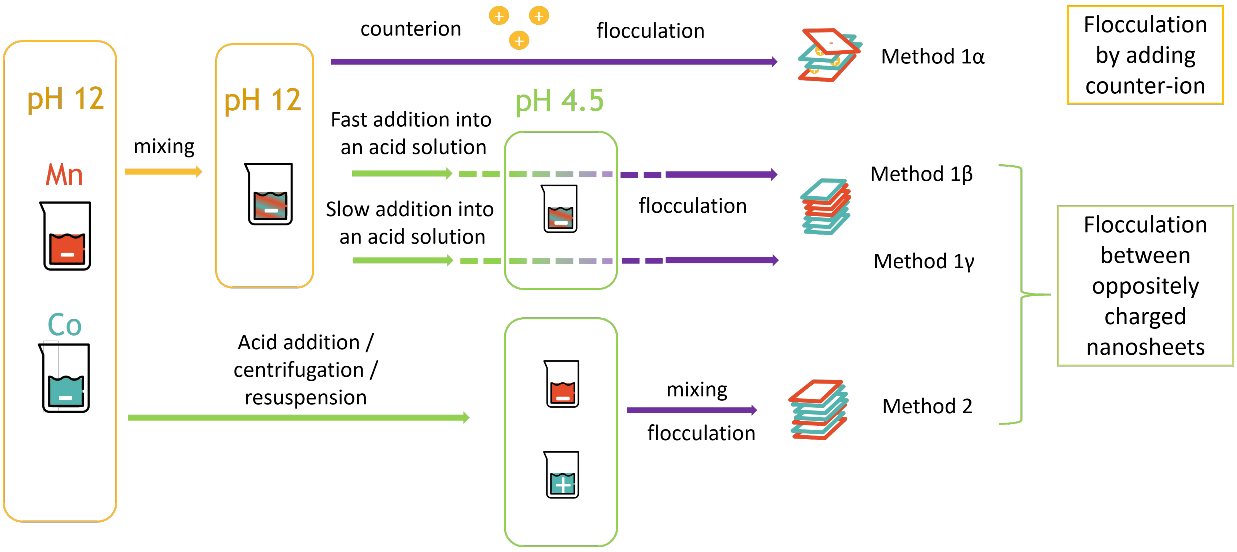

Figure 4.8.: Schematic representation of restacking methods : one pot strategy (method 1) and two-pots-in-one strategy (method 2).

Brutally adding the mixed colloidal suspension to a concentrated acidic solution could lead to partial dissolution. Also, all restacking would be kinetic without any thermodynamic stabilization. To alter this, another strategy is to add drop-wise the initial mixed colloidal suspension to a solution of nitric acid fixed at pH 4.5. The speed of addition is very slow and controlled by a peristaltic pump, which enables a thermodynamic stabilization and consequent flocculation. Because adding an alkaline suspension changes the pH of the acidic solution, the pH is constantly adjusted through a drop-wise addition of HNO_3. This restacking method will be denoted as 1γ.

4.2.2.2. Two-pots-in-one strategy (method 2)

In this strategy, the initial colloidal suspensions are not mixed at pH 12, but instead, they are both brought to the optimum pH 4.5 separately. Then, they are mixed together in a third vessel by carefully controlling the final pH and monitoring the addition speed of the two suspensions. This is likely to allow a finer restacking of negatively charged manganese nanosheets upon positively charged cobalt nanosheets. This method is denoted as method 2.

The main difficulty lies in the fact that initial suspensions must be stabilized at pH 4.5 before mixing. Lowering pH in the two suspensions increases their ionic strength thus destabilizing the nanosheets. Also, as pH decreases to 7, the IEP value of the cobalt nanosheets is reached, which means that these nanosheets are greatly destabilized in the suspension and will inevitably flocculate. This alters completely the nanosheet nature of the particles and a fine restacking is made impossible.

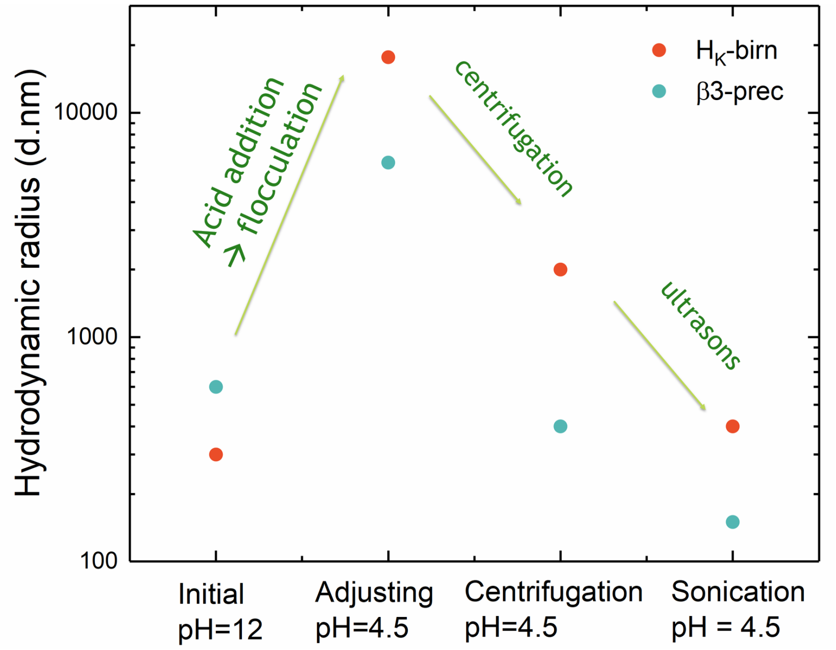

Figure 4.9.: Hydrodynamic radius at different stages of pH adjustment in the restacking method 2 : the colloidal suspensions are both adjusted to pH 4.5 and then mixed into a third vessel.

To counteract this effect, it is necessary to decrease the ionic strength of the suspensions brought to pH 4.5. After pH is decreased, as flocculation is observed, the suspension is centrifuged at 15000 rpm to isolate the nanosheets. The supernatant containing most of TBA^+ ions is discarded and nanosheets are re-suspended by ultrasonication at the corresponding pH. The size of particles present in the colloidal suspension can be monitored on the basis of Dynamic Light Scattering measurements (see in Figure 4.9). This technique can accurately measure the hydrodynamic radius of spherical particles. In the present case, the particles observed are platelets, leading to inaccurate values of the hydrodynamic radius. However, the orders of magnitude of the measured sizes can be compared to each other. As the suspension is adjusted to pH 4.5, the hydrodynamic radius increases drastically, which translates into flocculation of particles. By lowering the ionic strength of the suspension through centrifugation and ultrasonication, the size of particles is brought down to the same order of magnitude as for initial exfoliated materials.

4.2.3. Mechanical grinding of initial powders

At the end of the exfoliation/restacking process, mixed layered metal oxides are obtained. In order to prove the efficiency of this process, for comparison purpose, mixed layered metal oxides are also prepared by simple thorough grinding, in a mortar, of initial pristine powders (before exfoliation) at a given ratio. This method is call MG.

For an even more efficient grinding, a planetary ball-milling has also been used. The idea is that maybe the planetary mill will give enough shear strength to delaminate the initial powders without altering the 2D morphology. The results obtained after those tests will be discussed in the following section.

4.3. Characterization of the restacked materials

The various restacking techniques have been used to obtain novel restacked materials. First, the characterization of the materials obtained after flocculation (see section 4.2.1.1) from the colloidal suspensions of cobalt or manganese oxide objects separately, are presented in order to study the impact of exfoliation on the pristine materials. In a second step, the mixed materials obtained after restacking of the Mn and Co-based objects upon one another from the two colloidal suspensions are characterized, with special focus on the influence of the restacking technique.

4.3.1. Simple restacking

One stable colloidal suspension of each metal oxide has been flocculated in the presence of NaCl salts in order to study the effect of exfoliation/restacking process on the pristine materials. In this section, four samples will be discussed :

- pristine β3-prec
- the exfoliated/restacked β3-prec which will be denoted as RC (Restacked Cobalt oxyhydroxide)
- pristine H_{Na}-birn or Na-birn
- and the exfoliated/restacked H_{Na}-birn which will be denoted as RM (Restacked Manganese oxide)

4.3.1.1. Structure

The X-Ray diffraction patterns of the exfoliated/restacked materials and their parents before exfoliation are shown in Figure 4.10. Since the diffraction patterns of initial materials have been extensively discussed in section 3.2.2, the present section will only focus on the comparison between the non-exfoliated materials and the exfoliated/restacked materials. The line indexation reported for the manganese materials (Figure 4.10.a and b) corresponds to an hexagonal cell (space group $P\bar{3}m1$, one slab per cell). For the cobalt materials, the indexation is performed with 3 slabs per hexagonal cell (space group $R\bar{3}m$). The sizes of the coherent domains, determined by Scherrer method, on the basis of the (001) for manganese or (003) for cobalt lines, and of the (110) lines, are gathered in Table 4.4. Let us remind that they correspond to the thickness and the width of the coherent domains in a platelet morphology.

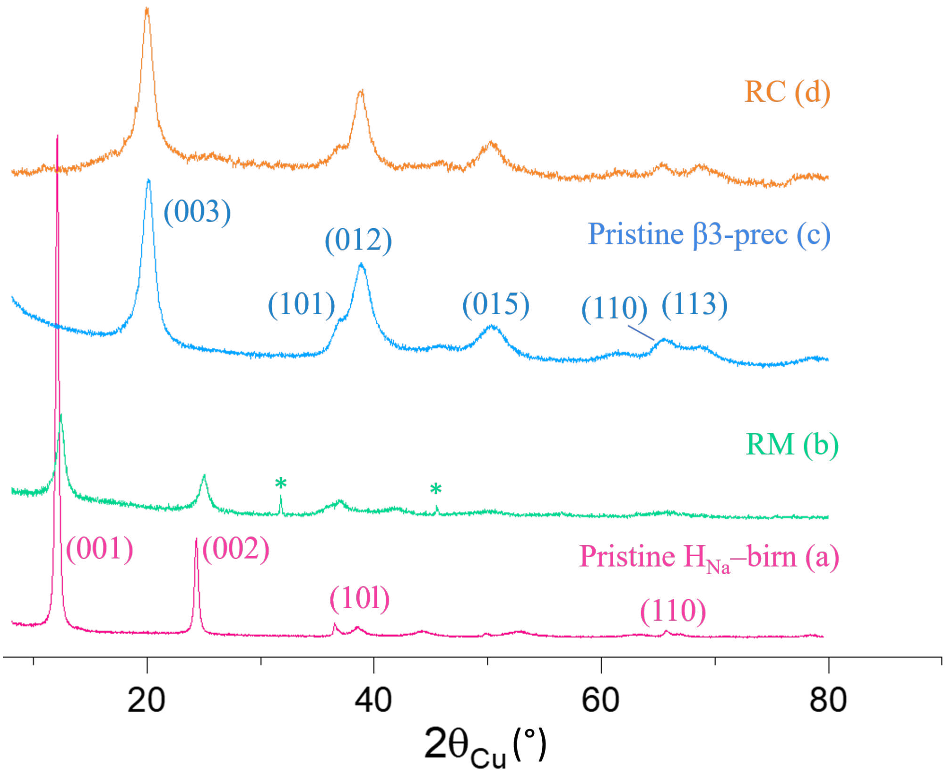

Figure 4.10.: X-Ray diffraction patterns of pristine materials : (a) H_{Na}-birn and (c) β3-prec. Compared to the X-Ray diffraction patterns of exfoliated/restacked materials obtained by flocculation of exfoliated nanosheets in NaCl solution (1 M) : (b) RM and (d) RC (* NaCl impurities).

Pristine H_{Na}-birn (Figure 4.10.a) and RM (Figure 4.10.b) exhibit X-Ray diffraction patterns with close shapes, that are characteristic of birnessite phases. Nevertheless, the lines are significantly broadened in the restacked sample, with a significant decrease of the size of the coherent domains in the two directions, suggesting that the exfoliation/restacking process affects the crystallinity of the sample. A broadening of the (10l) lines, characteristic of turbostraticity, is also observed in the final restacked material, in good accordance with the exfoliation/restacking process. In addition, the inter-reticular distance of the (001) line, which corresponds to the interslab distance, is slightly decreased in the restacked RM sample. As already discussed in chapter 3, this is currently observed when sodium alkaline ions are intercalated in between layers, instead of protons. The Na/Mn ratio is indeed equal to 0.3 in the restacked material, vs 0.01 in the H_{Na}-birn material.

Sample	Size of coherent domain (nm) (001) line (thickness)	 (110) line (width)
RC	4	3
β3-prec	5	2
RM	7	3
H_{Na}–birn	17	15

Table 4.4.: Average coherent domain sizes (nm) of coherent domains along (001) and (110) for pristine materials H_{Na}-birn and β3-prec compared to exfoliated/restacked materials obtained by flocculation of exfoliated nanosheets in NaCl solution (1 M) RM and RC determined by Scherrer method.

In the case of cobalt, the behavior is different since the pristine β3-prec cobalt oxyhydroxide phase (Figure 4.10.c) and its exfoliated/restacked RC derivative (Figure 4.10.d) exhibit quite similar diffraction patterns, with, in particular, no significant change in the size of the coherent domains. This behavior, suggesting that the structure and crystallinity of the cobalt material is restored by the exfoliation/restacking process, will be discussed hereafter in relation with the morphology evolution.

4.3.1.2. Morphology

The morphology of the pristine manganese and cobalt oxide and exfoliated/restacked materials was investigated by electron microscopies. The images are reported in Figure 4.11 for Mn-based materials and in Figure 4.12 in the case of Co-based materials.

As far as manganese is concerned, SEM images of the restacked RM material at two magnifications (Figure 4.11.d and e) can be compared to the images of the initial pristine Na-birn manganese birnessite (Figure 4.11.a and b).

The images of pristine Na-birn (Figure 4.11.a and b) show hexagonal hard platelets that are approximately 1 µm long and 50 nm thick. They are directly compared to images of the restacked RM phase, as it is not possible to obtain SEM images of the exfoliated nanosheets in colloidal suspension. Indeed, the SEM sample preparation requires to put samples under vacuum, while the separated nanosheets are stable only in the exfoliation liquid medium. Nevertheless, a drop of colloidal suspension was casted onto a sample holder and analyzed upon evaporation of liquid medium. However, no concluding images were obtained as the concentration of nanosheets is very low and no clear contrast could be obtained. On the images of RM (Figure 4.11.d and e), a general aspect of jagged platelets can be discerned, with, on their surface, some kinds of “nanopieces” of exfoliated nanosheets, probably produced by the exfoliation process, as the samples are sonicated at high frequencies. With the sodium ions present in the flocculation medium, these nanopieces will tend to flocculate around the big sheets, thus creating packages of material.

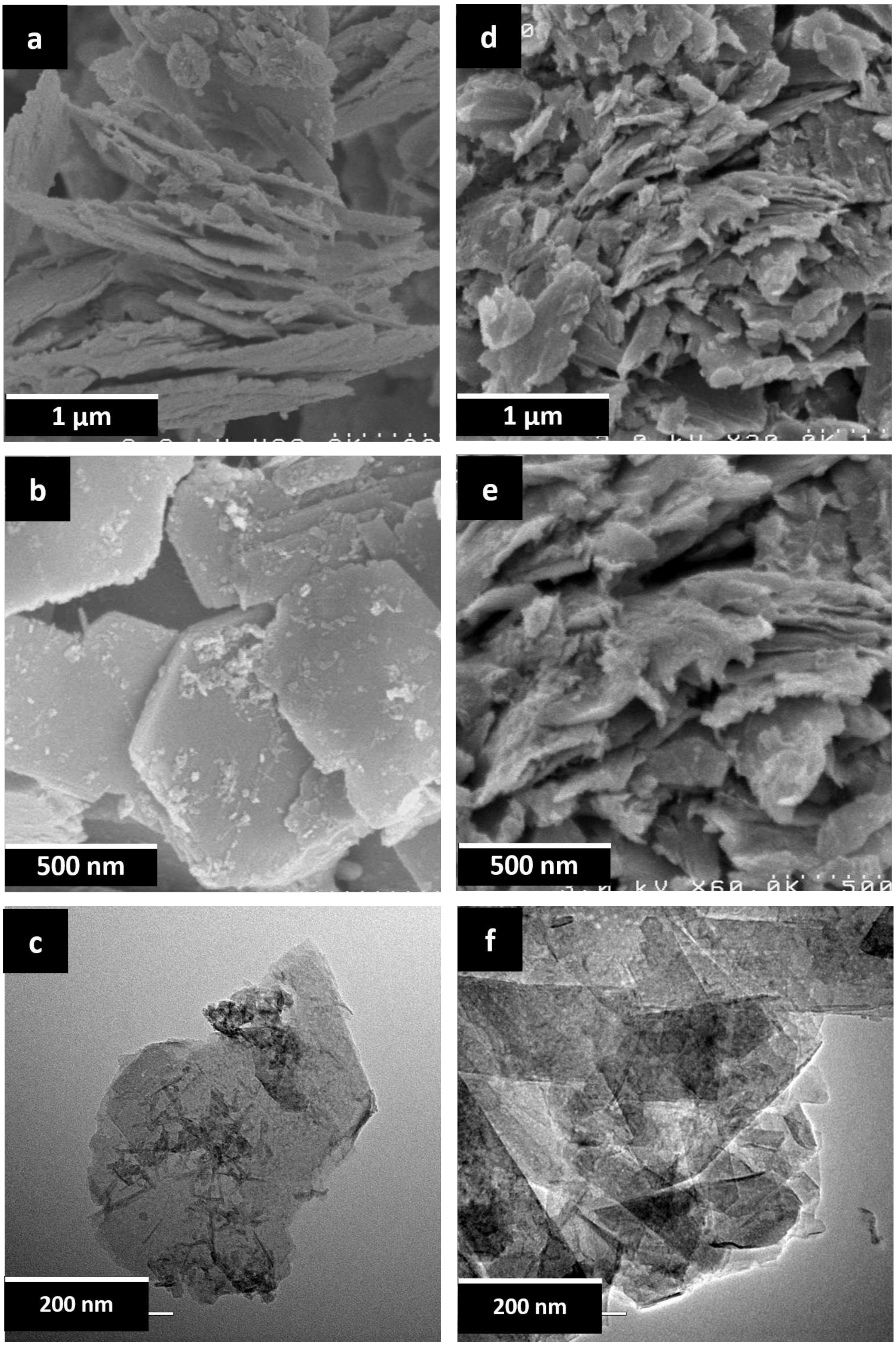

Figure 4.11.: (a) and (b) SEM, and (c) TEM images of Na-birn. (d) and (e) SEM, and (f) TEM images of the restacked material RM obtained by flocculation of exfoliated/restacked H_{Na}-birn in NaCl (1 M).

The morphology and microstructure of the samples were further examined by transmission electron microscopy. The images, presented in Figure 4.11.c and f confirm the aggregated morphology of the exfoliated sample. Indeed, before exfoliation, the images (Figure 4.11.c) show individual particles with a lamellar morphology. During exfoliation, this layered structure is delaminated into thinner layers of nanosheets, as well as nanopieces of exploded nanosheets.

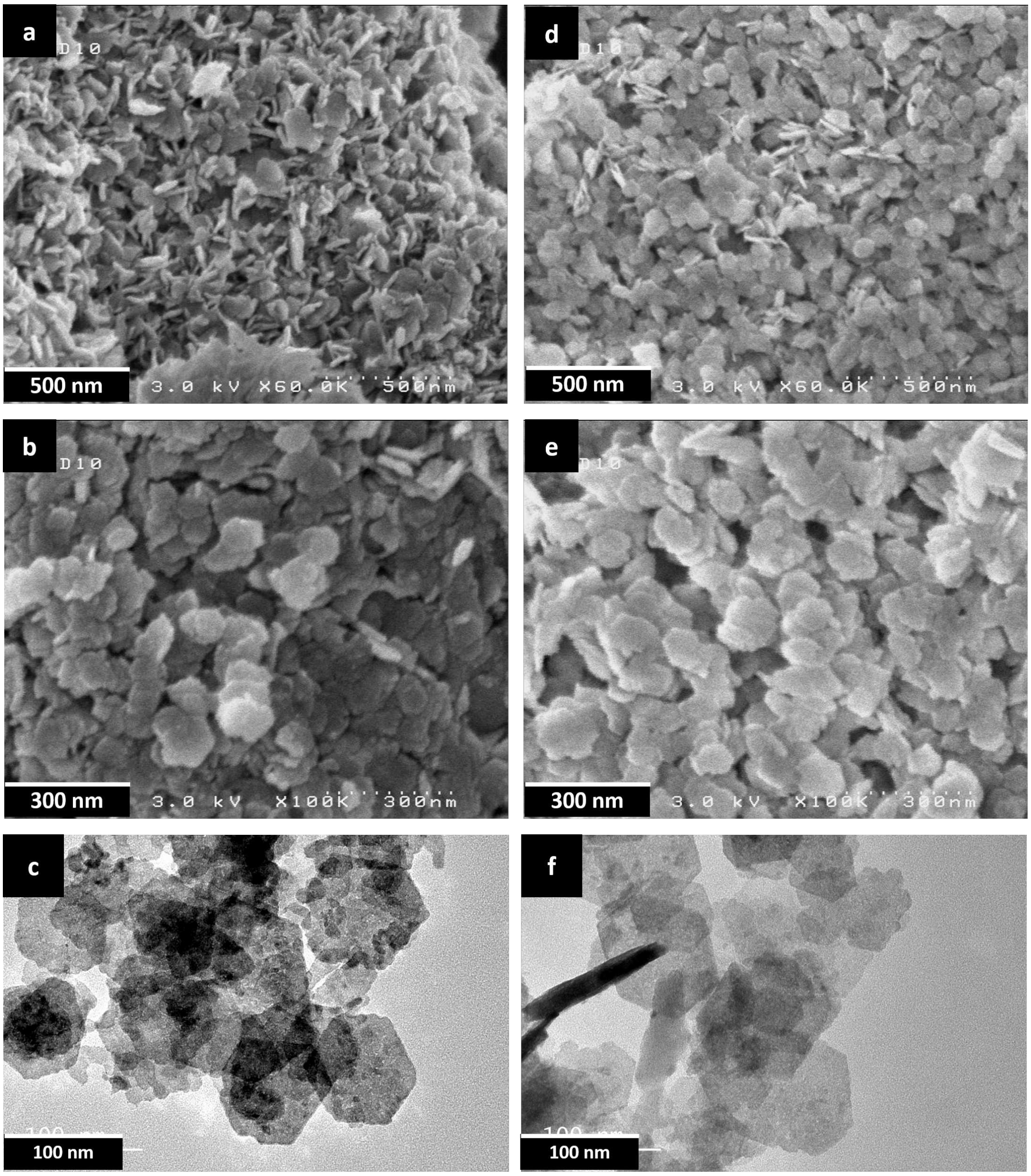

Figure 4.12.: (a) and (b) SEM, and (c) TEM images of β3-prec. (d) and (e) SEM, and (f) TEM of images of restacked material RC obtained by flocculation of exfoliated/restacked β3-prec in NaCl (1 M).

On the images of the restacked material (Figure 4.11.f), various sized nanosheets seem to be randomly superimposed on top of each other in a multitude of directions. This again shows that flocculation is a process leading to restacked materials with high turbostratic character. The shredded appearance, the presence of small nanosheets and the disordered stacking of the objects after restacking are in good accordance with the broadening of the X-Ray diffraction lines described in the previous section.

As far as cobalt is concerned, in the SEM images of initial β3-prec materials (Figure 4.12.a and b), flat hexagonal platelets with clear distinct edges can be observed. The platelets are around 120 nm wide and 20 nm large. The images of the restacked RC material (Figure 4.12.d and e) shows a similar morphology, the width of the platelets is preserved but the thickness is lower for the RC particles (around 10-15 nm as statistically measured by SEM image analysis) than for pristine β3-prec. This obtention of thinner particles after restacking is confirmed on the TEM images (Figure 4.12.c and f) by the fact that the electron density of the particles seems lower (the carbon membrane of the copper grid on which the particles are deposited is much more visible). These observations show that the exfoliation/restacking process leads in the case of cobalt to thinner nanoparticles while their width is maintained. As seen in section 3.2.4.2, the layered cobalt oxyhydroxide particles are constituted of a stacking of several coherent domains (crystallites). Since X-Ray diffraction did not show any structural change (no significant broadening of (110) and (003) lines), it means that the exfoliation/restacking process does not alter the size of the coherent domains. However, the efficient delamination of the particles has been observed in section 3.3.4.3 and is further verified by TEM as the flocculated objects are thinner than initial ones.

The evolution in the structure and the morphology reported above tend to prove that the exfoliation/restacking process is efficient, and leads to a significant decrease of the particle thickness.

4.3.1.3. Specific surface area

In order to further understand the effect of exfoliation on the pristine particles, the specific surface areas of restacked materials have been determined by BET. The N_2 adsorption/desorption isotherms for the initial materials (H_{Na}-birn, β3-prec) and the exfoliated/restacked materials (RM and RC) are presented in Figure 4.13. The specific surfaces areas are presented in Table 4.5.

Concerning the manganese oxides, the general shape of the isotherm curves are quite similar, which is typical of aggregates of plate-like particles with very limited porosity [193]. The calculated specific area of the exfoliated/restacked RM material is 30 m^2/g, which represents half the value of the initial protonated sodium birnessite. However, it is closer to the surface area of the pristine Na-birn, which exhibits a surface area of 35 m^2/g. This is expected as the flocculation was induced by adding Na^+ as a counter-ion, so that the restacked material is in its chemical composition very close to pristine Na-birn.

Concerning the cobalt oxyhydroxides, the isotherm curves (Figure 4.13) are quite different. The isotherm curve of initial β3-prec material could be interpreted as a H_2 type hysteresis loop, which suggests the presence of a porous interconnected network of agglomerates.

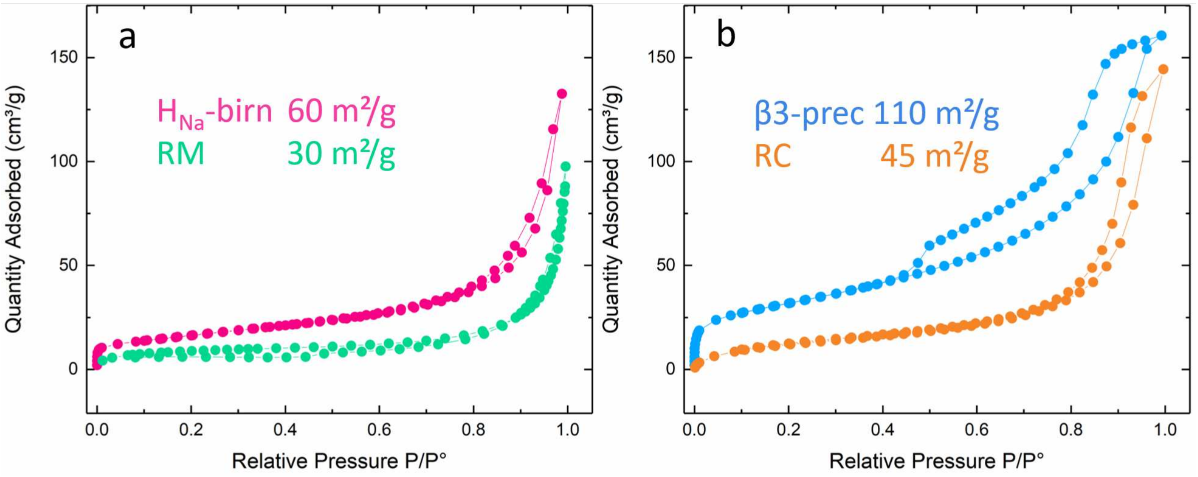

Figure 4.13.: N_2 adsorption/desorption isotherms at 77K of (a) H_{Na}-birn (pink), RM (green), (b) β3-prec (blue) and RC (orange).

However, after exfoliation, the isotherm of the restacked material RC shows hysteresis loop that could be identified as a H_3 type, which means that there has been a clear change of the pore connectivity and size of the material. The specific surface area determined by BET is 45 m^2/g, which is much lower than the initial 110 m^2/g, this can be explained by the restacking process : the addition of salts might block the pores.

Materials	Specific BET surface (m^2/g)
Na-birn	35
H_{Na}-birn	60
RM	30
β3-prec	110
RC	45

Table 4.5.: Specific surface area of manganese birnessites, protonated birnessites and β3-Cobalt oxyhydroxides.

In both cases, the tendency is that the exfoliation/restacking process lowers the specific surface area measured by adsorption/desorption of N_2. Intuitively, it is expected that the surface area should increase after exfoliation. A possibility to explain the decrease is the restacking strategy employed. The restacking process is very random : instead of being well ordered, the nanosheets will have a tendency to restack in arbitrary directions in a more packed manner. Furthermore, since the medium is very concentrated in NaCl salt, there might be an over-saturation of cations in the interlayer space, that will induce some pores to be blocked.

4.3.1.4. Conclusion

The exfoliation/restacking process has induced a significant modification of the particles.

Structurally speaking, the restacked RM manganese material is less well-ordered than the initial material. There has been some turbostraticity induced by the randomly oriented restacking. The morphological observations by SEM and TEM also show a difference, as the RM particles are shaped like platelets with shredded aspect; nanopieces of the initial particles can be observed. However, the specific surface of RM is equivalent to the initial Na-birn.

Concerning the cobalt restacked RC material, no structural modification has been observed by X-Ray diffraction. The images by SEM and TEM indicate that in general, the RC particles are thinner than the initial ones. However, surprisingly, the specific surface area is much lower than the initial particles. This could be due to the restacking method, as an excess of salt is added and might alter the porosity.

Although only partial exfoliation is achieved, there are some net differences between the restacked materials and their initial precursors, especially in terms of thickness decrease. The next section is devoted to the characterization of mixed Mn-Co materials, obtained from the restacking of the nanosheets obtained previously.

4.3.2. Mixed restacking

Various mixed Mn-Co materials are likely to be obtained depending on the restacking techniques. First, the restacked materials are characterized by X-Ray diffraction to study their structural differences. Then, the morphologies are investigated thanks to electron microscopy techniques as well as specific surface measurements. This way, the restacking techniques can be compared, evaluating how it influences the final materials.

Then, the impact of Mn:Co ratio has been studied. By choosing one restacking technique, the amounts of Mn and Co in the starting exfoliated colloidal suspensions have been varied.

Finally, to complete the study of the exfoliation/restacking process, the mean oxidation states of Mn and Co in restacked materials and in the initial materials are measured and compared one to each other. This study will be correlated to the electronic conductivity measurements, in order to evaluate if the addition of conductive cobalt oxyhydroxides to manganese oxides in exfoliated/restacked materials does indeed enhance conductivity or not.

4.3.2.1. Proof of flocculation of metal (oxy)hydroxides

All the restacking techniques rely on the flocculation of charge bearing nanosheets, induced either by adding a counter-ion or by oppositely charged particles. Experimentally, the flocculation is visualized as soon as salts are added or when the oppositely charged suspensions are added into a third vessel. Indeed, from brown stable colloidal suspensions, it is possible to see flocculates that will settle. The supernatant is clear and analyzed by ICP. In all cases, no Mn nor Co phases were found dissolved in the supernatant solution. Therefore, in every method it was possible to obtain restacked materials.

4.3.2.2. Structure of restacked particles

Since there are various restacking techniques, it is interesting to study their impact on the structure of restacked materials. To do so, it is necessary to compare restacked materials with a similar Mn to Co ratio. However, it is difficult to fully control the amount of nanosheets in the exfoliated colloidal solutions, as a result of a very limited exfoliation yield, which strongly depends on experimental conditions. It is possible to estimate the concentration of nanosheets in the following way : as seen in section 3.3.3, the colloidal suspensions are first centrifuged at 4000 rpm in order to remove the non-exfoliated material. By subtracting the weight of non-exfoliated material to the initial amount of powder added, a rough estimation of the concentration of nanosheets can be determined.

Nonetheless, because the exfoliation process is not complete, the thickness and sizes of nanosheets are very variable. This is why it is very difficult to estimate the exact Mn:Co ratio in the restacked compound. Therefore, chemical analysis by ICP is necessary to determine the precise chemical composition of the restacked materials.

Samples with Mn:Co ratio of 1 to 1, as determined by ICP, are obtained using three different restacking processes, all relying on electrostatic attraction of nanosheets, and previously described in section 4.2.2. Using the one-pot strategy, one sample is obtained by suddenly adding the mixed Mn/Co colloidal suspension into an acidic solution (method 1β) and will be denoted as *Restack-1*β. Another sample is obtained by slowly adding the mixed Mn/Co colloidal suspension to a solution with a pH maintained at 4.5 (method 1γ), it will be denoted as *Restack-1*γ. Finally, a last sample is obtained by using the two-pot strategy, in which the initial colloidal suspensions are first adjusted to pH 4.5 before being mixed into one another, it will be denoted as *Restack-2*.

In order to study the effect of exfoliation/restacking process, these restacked samples are compared to mixtures of cobalt oxyhydroxides and manganese oxides, obtained by mechanical grinding (denoted as *MG*), and ball-milling in a planetary mill (denoted as *BM*).

In the three restacked samples described above, the manganese oxide colloidal suspension used is based on the protonated H_K-birn material. However, due to quantity issues, the studies were carried out with different exfoliated cobalt oxyhydroxides (β3-prec and β3-ex$Na_{0.6}$).

The X-ray diffraction patterns of the synthesized samples are shown in Figure 4.14. First, the composite material obtained by ball-milling (Figure 4.14.e) is structurally completely different from the other ones. It contains a spinel-type phase, which results from a chemical reaction between the initial manganese and cobalt oxyhydroxides. This sample will not be further studied, since the exfoliation/restacking strategy put in use in this study aims at designing novel composited by combining layered Mn and Co oxides while preserving the integrity of lamellae.

The X-ray diffraction patterns of the samples prepared by restacking methods 1β, 1γ and 2 (shown on Figure 4.14.b, c and d) exhibit strong similarities with the pattern obtained for the material synthesized by mechanical grinding (Figure 4.14.a). Indeed, the lines are characteristic of a mixture of the initial two phases : cobalt oxyhydroxide and manganese birnessite. This suggests a successful recombination of initial manganese and cobalt bricks through the exfoliation/restacking process.

The width of the (110) peaks is more or less maintained, which means that the size of coherent domains in the plane of the lamellae is not altered.

However, depending on the method used, the width or intensities of the (001) line of birnessite and of the (003) line of the cobalt phase can vary, inducing a different crystalline organization. The intensity ratio between the (001) line of birnessite and the (003) line of cobalt oxyhydroxide is in favor of manganese birnessite when the mixture of the two colloidal suspensions is brutally added to a low pH (method 1β, Figure 4.14.b). On the contrary, when the mixture of the two colloidal suspensions is slowly added to a solution at pH 4.5, under pH control (method 1γ, Figure 4.14.d), or when the two colloidal suspensions are simultaneously and slowly added to a solution under pH control, the most intense peak is the (003) line of cobalt oxyhydroxide.

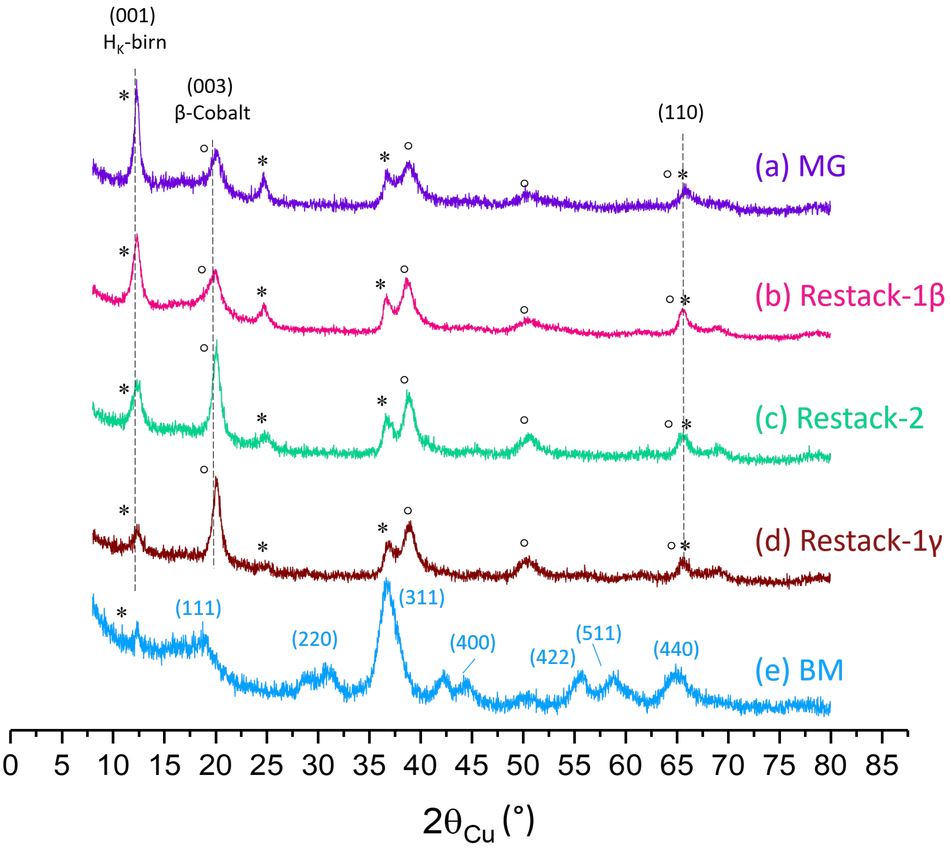

Figure 4.14.: X-Ray diffraction patterns of restacked materials from H_K-birn and various cobalt oxyhydroxides with different methods. (a) MG : Mixed composite obtained by mechanical grinding of H_K-birn and β3-prec. (b) Restack-1β : Restacked composite of H_K-birn and β3-exNa$_{0.6}$ obtained by method 1β. (c) Restack-2 : Restacked composite of H_K-birn and β3-prec obtained by method 2. (d) Restack-1γ : Restacked composite of H_K-birn and β3-exNa$_{0.6}$ obtained by method 1γ. (e) BM : Restacked composite of H_K-birn and β3-prec obtained by ball-milling. (*) correspond to the H_K-birn phase and (°) to the β3 phase.

The average crystallite sizes along the (00l) direction (thickness of platelet-like objects), determined by Scherrer formula, for manganese oxide and cobalt oxyhydroxide are gathered in Table 4.6. The thickness of the manganese-based domains seems to be quite constant (around 6-7 nm), whatever the restacking method, while the thickness of the cobalt-based domains is higher for “slow” restacking of methods 2 and 1γ (6 nm), than for “fast” restacking of method 1β (3 nm). These results suggest that restacking kinetics seems to play a key role on the organization of the final composite, the cobalt oxyhydroxides objects being more inclined to restack one onto another when the suspensions are slowly poured in the acidic medium.

In order to fully understand the organization of the oxides, it is necessary to visualize the morphology and get the detailed composition at a lower scale. Microscopy characterizations have been conducted and are presented below.

Sample	Size of coherent domain (nm)	
	(00l) line of H_K-birn	(003) line of β3-Cobalt
MG	12	3
Restack-1β	7	3
Restack-2	6	6
Restack-1γ	7	6

Table 4.6.: Average coherent domain sizes (nm) along the slab stacking direction for the manganese and cobalt-based phases in the restacked samples determined by Scherrer formula.

4.3.2.3. Morphology of restacked materials

According to the previous section, the various restacking methods lead to composite materials consisting of a mixture of manganese oxide and cobalt oxyhydroxide. They have been studied by SEM-EDS and TEM-EDS (Energy-dispersive X-Ray Spectroscopy) to understand how they are organized at the aggregate scale. The EDS technique coupled with imaging is particularly interesting because it allows a local elemental analysis of the sample so that the organization of the various objects can be deduced.

SEM-EDS

The SEM-EDS images of a composite obtained by mechanical grinding and of the various exfoliated/restacked composites are shown in Figure 4.15.

The SEM images (presented in Figure 4.15.a, c, e and g) images show that, in spite of the same Mn:Co ratio, the topographies of the materials are very different. This is firstly due to the different initial materials used in the restacking : in Figure 4.15.a and e, the hexagonal platelets representative of β3-prec can be easily distinguished, while on 4.15.c and g, the morphology of aggregates is similar to that of the β3-exNa$_{0.6}$ (see Figure 3.12). The Mn oxide particles are much less distinguishable because of their veil-like morphologies (see SEM images of initial particles on Figure 3.8.c and g).

The EDS images of each sample also reveal significant differences. On one side, after mechanical grinding (Figure 4.15.b), a clear distinction can be made between the cobalt oxyhydroxide particles appearing in green and the manganese oxide particles in red. On the other side, the images of the exfoliated/restacked material (4.15.d, f and h) are strikingly different. Instead of a clear difference of color between aggregates, the Mn and Co elements are closely mixed, which is revealed by a yellow color. At this observation scale, this color reveals an intimate mixture of initials materials, and the restacked compounds can be considered as nanocomposites of Mn oxide and Co oxyhydroxide.

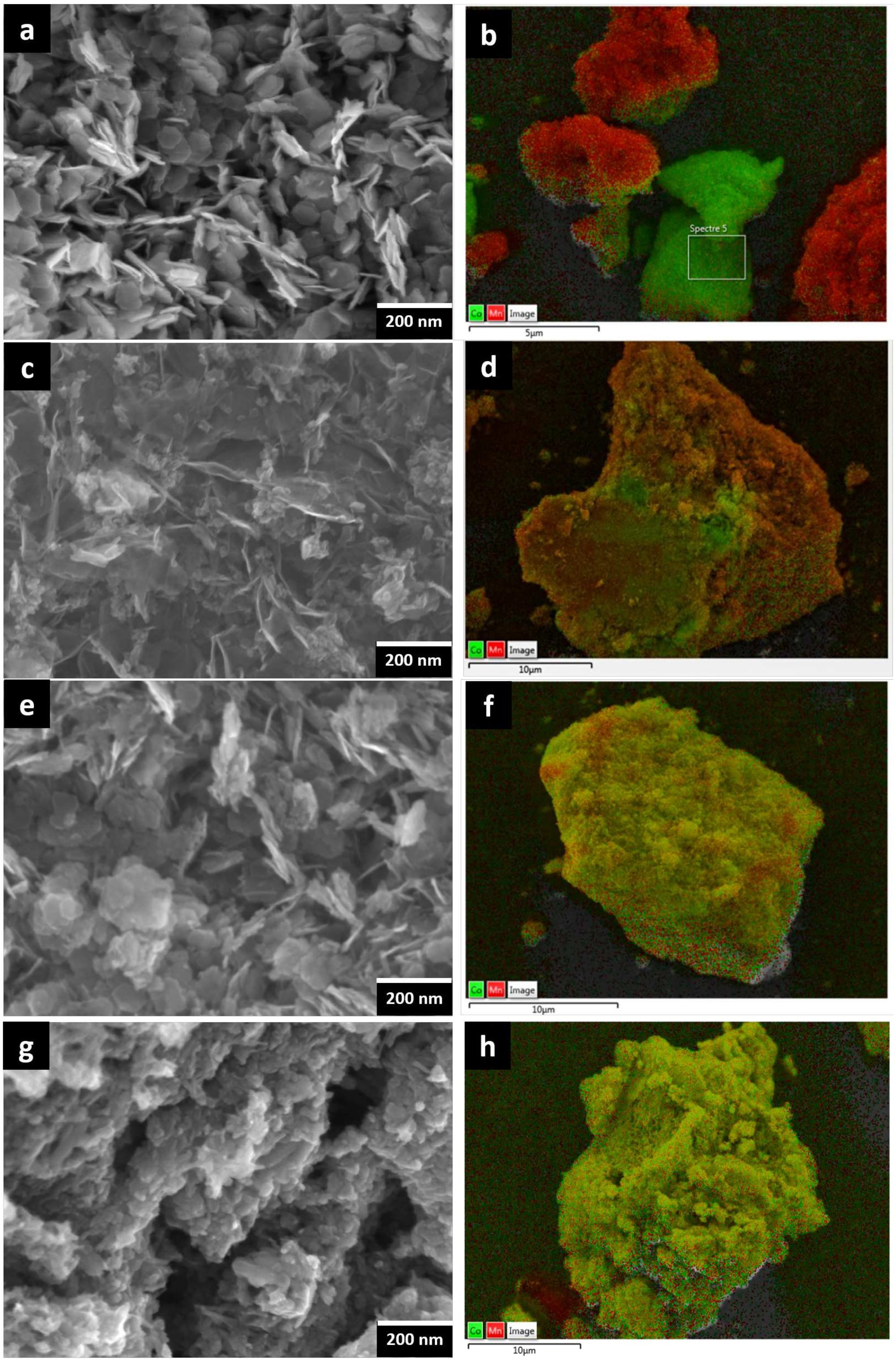

Figure 4.15.: (a) and (b) SEM-EDS images of MG composite (SEM image focused on a Co oxyhydroxide particle) obtained by mechanical grinding of H_K-birn and β3-prec. (c) and (d) SEM-EDS images of Restack-1β : Restacked composite of H_K-birn and β3-exNa$_{0.6}$ obtained by method 1β. (e) and (f) SEM-EDS of Restack-2 : Restacked composite of H_K-birn and β3-prec obtained by method 2. (g) and (h) SEM-EDS images of Restack-1γ : Restacked composite of H_K-birn and β3-exNa$_{0.6}$ obtained by method 1γ. Colors : red = Mn, green = Co.

A close observation of the EDS images of Restack-1β, Restack-1γ and Restack-2 leads to the conclusion that the restacking method affects the homogeneity of the manganese and cobalt mixture. Restack-2 (4.15.f) seems to be the most homogeneous, when Restack-1β (4.15.d) shows more manganese on the surface, the red color being predominant. Alternatively, Restack-1γ (4.15.h) is greener, revealing more Co on the surface. The probing depth of EDS analysis is around 2 µm for Mn and Co elements. Similarly, the probing depth of XRD ranges from one µm to the whole bulk of the sample. Since both probing depth are at the same scale, it is possible to compare both XRD and EDS observations and to establish a coherent correlation between them. In particular, the EDS observations can be linked to the diffraction line intensities of the X-ray diffraction patterns (Figure 4.14). It can also be linked to the thickness of the Mn and Co particles in the composite determined by Scherrer method (see previous paragraph). Indeed, in the case of Restack-1β (4.15.d), the cobalt particles are thinner (3 nm) than the manganese ones (7 nm), which is in accordance with the predominant red color, characteristic of manganese, in the EDS image. On the contrary, in the case of Restack-1γ (4.15.h), the thickness of cobalt particles has increased (6 nm) and the (003) line of cobalt oxyhydroxide is the most intense one, which is in good agreement with the predominating green color, characteristic of cobalt on the EDS image. Restack-2 appears to be intermediate between Restack-1β and Restack-1γ on the basis of EDS images and X-Ray data.

It is interesting to underline that all three restacked materials have the same Mn:Co ratio although their morphologies exhibit differences. This can be reasonably attributed to the restacking technique : the flocculation kinetics are different for Co oxyhydroxides and Mn oxides, depending on the restacking and the pH modification process used.

Furthermore, it seems that method 1β might inhibit the flocculation of cobalt oxyhydroxides and favors the flocculation of Mn oxides. This could be explained by the fact that the mixed Mn-Co colloidal suspension is rapidly added to a strong acid solution at pH 1, which is closer to the IEP of manganese objects than to that of cobalt objects.

In method 1γ, the mixture of colloidal suspensions at an initial pH of 12 is added slowly to a pH solution fixed at 4.5. Since the initial suspension is more alkaline, the resulting pH, when the suspension is added, is closer to the IEP of Co oxyhydroxides. This could explain why, in method 1γ, Co-based objects are flocculated in bigger aggregates than in method 1β, hence being more visible in EDS for the former method than for the latter one.

Finally, the restacking method 2 consists in first bringing the initial suspensions to pH 4.5 separately and then mixing both together in a controlled way. This method is suitable to obtain Mn and Co aggregates with a similar size, as several acidic/centrifugation/ resuspension treatments are conducted. This is the reason why Restack-2 seems to be the most homogeneous sample.

However, although the probing depth is similar in EDS and XRD measurement and could lead to interesting correlation, it is interesting to observe the composites at a local, smaller scale. This is why further studies were conducted with TEM-EDS.

TEM-EDS

Transmission electronic microscopy coupled with EDS is used to go to a lower scale in order to see the intimate stacking. The images are shown in Figure 4.16. The two distinct phases in the MG composite are confirmed in Figure 4.16.a. While, the EDS images of all the restacked samples show that there is an intimate mix of particles, but differences appear. Restack-1β (4.16.b) and Restack-1γ (4.16.d) show clear green and red patches, together with a lot of yellow zones, which are characteristic of domains in which Mn and Co are very close to each other. On the contrary, Restack-2 (4.16.c) has very few yellow pixels. This may be linked to the restacking technique, as, for methods 1β and 1γ, the initial suspensions are mixed before any flocculation, and then vigorously stirred, which might lead to a more intimate mix.

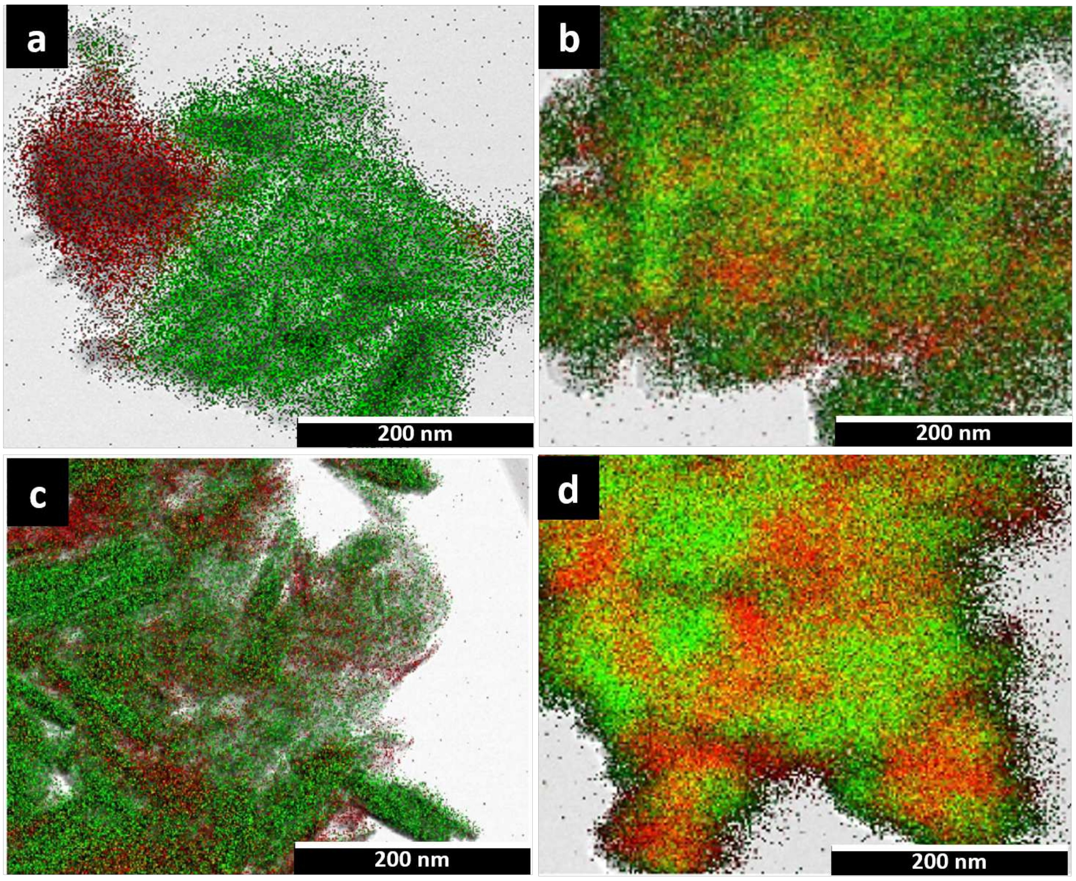

Figure 4.16.: TEM-EDS images of (a) MG : Mixed composite obtained by mechanical grinding of H_K-birn and β3-prec. (b) Restack-1β : Restacked composite of H_K-birn and β3-exNa$_{0.6}$ obtained by method 1β. (c) Restack-2 : Restacked composite of H_K-birn and β3-prec obtained by method 2. (d) Restack-1γ : Restacked composite of H_K-birn and β3-exNa$_{0.6}$ obtained by method 1γ. Colors : red = Mn, green = Co.

However, transmission electronic microscopy probes the entire aggregates of composite particles. The samples observed are crossed by the electron beam and therefore the entire particle is detected (depth of probe is around 2 µm). A superposition of Mn and

Co is naturally observed. This means that this technique is not suitable to conclude definitely on the morphology observations.

Surface properties

To fully understand the impact of restacking method and complement the morphology studies, measurements of specific surface areas were conducted.

Figure 4.17 shows the N_2 adsorption/desorption isotherms for restacked materials compared with MG mechanically grinded sample. The restacked materials all contain the same Mn:Co ratio of 1:1 but are obtained by different restacking techniques : Restack-1β, Restack-2 and Restack-1γ. The specific surface area calculated are presented in Table 4.7.

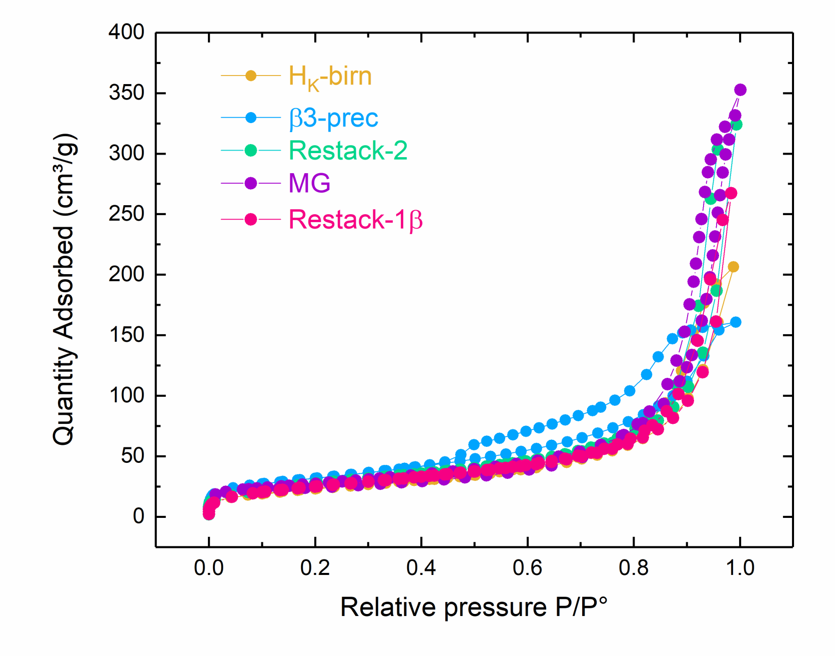

Figure 4.17.: N_2 adsorption/desorption isotherms at 77K of restacked materials composed of 50% Mn and 50% Co : mixed composite obtained by mechanical grinding of H$_K$-birn and β3-prec; Restack-1β : Restacked composite of H$_K$-birn and β3-prec obtained by method 1β; Restack-2 : Restacked composite of H$_K$-birn and β3-exNa$_{0.6}$ obtained by method 2.

The isotherms of Restack-1β, Restack-2 and mixed material obtained by mechanical grinding exhibit a similar shape, as initial H$_K$-birn. The calculated specific surfaces of Restack-2 and MG are also very close (between 95 to 100 m^2/g), and intermediate between pristine manganese oxide (85 m^2/g) and β3-prec cobalt oxyhydroxide (110 m^2/g). In the case of Restack-1β, the initial cobalt oxyhydroxide is β3-exNa$_{0.6}$ (70 m^2/g), suggesting that exfoliation did in fact increase the number of pores.

Sample	Specific surface area (m^2/g)
H_K-birn	85
β3-prec	110
β3-ex$Na_{0.6}$	70
MG	95
Restack-1β	92
Restack-2	100
Restack-1γ	2

Table 4.7.: Specific surface area of restacked materials of ratio Mn:Co obtained by different restacking techniques.

Concerning Restack-1γ, after repeated measurements, no adsorption isotherm can be obtained, leading to specific surface area lower than 2 m^2/g. Although the SEM image of Restack-1γ (see Figure 4.15.g) shows that it seems much more aggregated than Restack-1β and Restack-2, this is a very peculiar result that we have not yet managed to explain.

4.3.2.4. Influence of Mn:Co ratio

A series of restacked materials synthesized by the same method (method 2) but containing various ratios of Mn:Co has been investigated from the structural and morphology point of view, in order to determine the specific effect of the Mn and Co amounts on the structure and the morphology of the final materials.

On structure

The restacked materials obtained by the same restacking method (method 2) have been analyzed by ICP to determine the Mn:Co ratio. All the materials presented result from the restacking between colloidal suspensions of exfoliated H_K-birn and β3-prec, at different ratios. A first composite contains 33 % of Mn and 67 % of Co (ratio 1Mn:2Co), it will be denoted as *Restack-2-(Mn:2Co)*. A second material with the same amount of Mn and Co was obtained, and will be denoted as *Restack-2-(Mn:Co)*. Finally, a third material with a majority of Mn was obtained, with 75% of Mn and 25% of Co, it will be denoted as *Restack-2-(3Mn:Co)*. In this nomenclature, the restacking method is represented by the 2, and the ratio is in brackets.

The X-ray diffraction patterns of the restacked materials are presented in Figure 4.18, together with that of the pristine materials, for comparison purpose.

As shown in Figure 4.18, the X-ray diffraction patterns of the restacked materials contain the main lines that correspond to the initial H_K-birn manganese oxide and the cobalt β3-prec oxyhydroxide, with various intensities. The intensities of both lines are related to the Mn:Co ratio obtained by chemical analysis. From a general point of view, the increase of the intensity ratio between the (001) line of manganese birnessite and the

(003) line of cobalt oxyhydroxide is in full agreement with the increase of the Mn/Co atomic %. In order to have an idea of the eventual evolution of the particle thicknesses with the Mn/Co ratio, the sizes along the (00l) directions were calculated with Scherrer method, they are reported in Table 4.8.

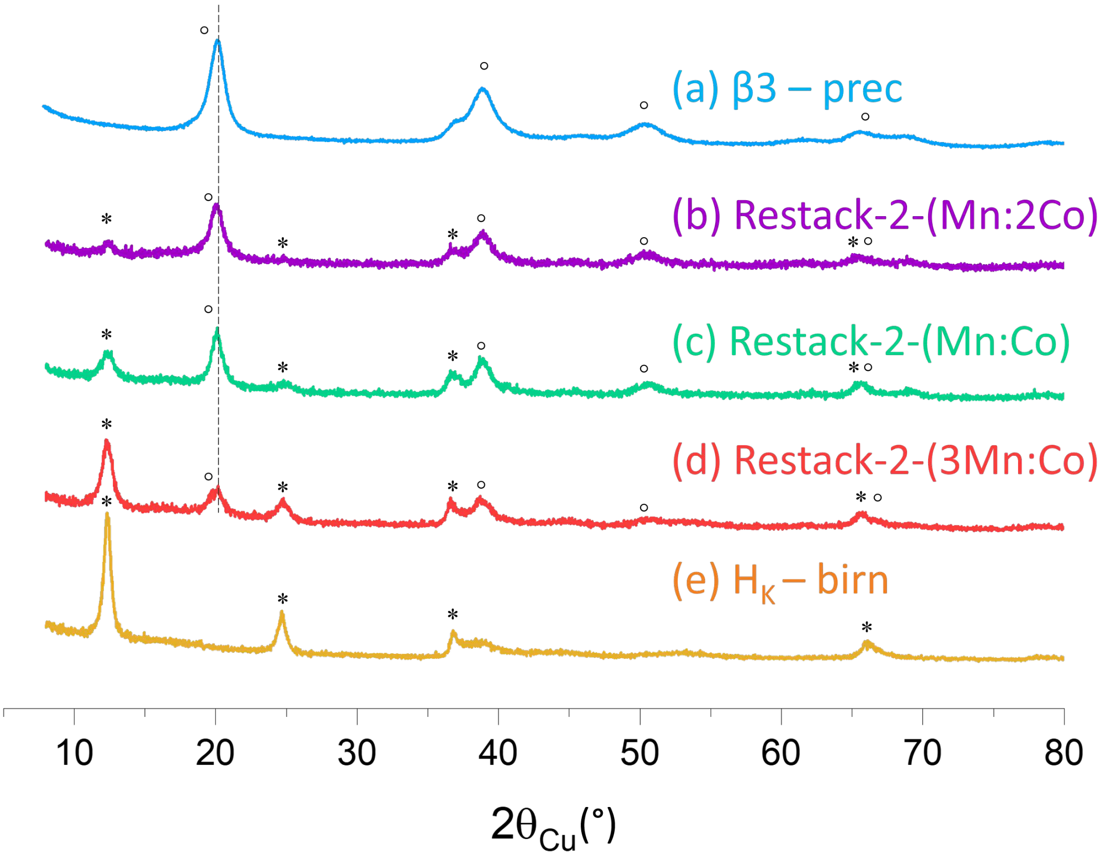

Figure 4.18.: X-Ray diffraction patterns of restacked materials from H_K-birn and $\beta 3$-prec exfoliated colloidal suspensions. (a) Initial cobalt oxyhydroxide$\beta 3 - prec$. (b) Restack-2-(Mn:2Co) : Restacked material with 33% Mn - 67% Co obtained by method 2. (c) Restack-2-(Mn:Co) : Restacked material with 50% Mn - 50% Co obtained by method 2. (d) Restack-2-(3Mn:Co) : Restacked material with 75% Mn - 25% Co obtained by method 2. (e) Initial manganese oxide H_K-birn. (*) correspond to the H_K-birn lines and (°) to the $\beta 3$ phases.

These values show that the thicknesses of manganese and cobalt nanocrystallites in the restacked samples do not vary with the Mn:Co ratio, they stay in the range 5-7 nm. Comparing these values with the particle thickness in pristine materials leads to two remarks : (i) the thickness of the coherent domains of manganese dioxide in the restacked samples is lower than in pristine manganese phase (11 nm), as expected from a classical exfoliation process (ii) the thickness of the coherent domains of cobalt oxyhydroxide in the restacked samples is the same as in pristine cobalt phase. As already claimed in section 4.3.1.1, this result can be interpreted by a delamination of the particles, constituted of a stacking of several coherent domains (crystallites), in individual nanocrystallites. In these conditions, the thickness of the coherent domains is preserved, and they are just separated one of each other to finally give thinner objects.

Sample	Size of coherent domain (nm)	
	(00l) line of H_K-birn	(003) line of β3-Cobalt
β3-prec	-	5
Restack-2-(Mn:2Co)	6	5
Restack-2-(Mn:Co)	6	6
Restack-2-(3Mn-Co)	7	5
H_K-birn	11	-

Table 4.8.: Average coherent domain sizes (nm) along the slabs stacking direction of restacked materials with different ratios determined by Scherrer method.

On morphology

The SEM-EDS images of the restacked materials with various Mn:Co ratios are presented below (Figure 4.19).

In Figure 4.19.a, the SEM image of Restack-2-(Mn:2Co) shows distinct hexagonal platelets characteristic of β3-prec. In Figure 4.19.c, these hexagonal platelets are still present although less numerous; however, no veil-like manganese particle can be observed. Finally, the SEM image of Restack-2-(3Mn:Co) in Figure 4.19.e shows even less hexagonal platelets, and veil-like particles representative of manganese oxide are observed. This is fully coherent with the ratio of Mn:Co. As the amount of Mn increases, more and more veil morphologies corresponding to Mn particles can be observed.

Although the manganese veils are difficult to observe, it is surprising that even in a Mn:Co ratio of 1:1, in sample Restack-2-(Mn:Co) no clear veil-like morphology is observed. To explain this, it is necessary to reason in terms of concentration of objects, and make an approximation on the size of Mn nanosheets sizes compared to Co hexagonal platelets. Since Mn veils are much wider ($>$ 200 nm), the smaller cobalt particles (approximately 60 nm) cover the veils. This can be visualized on Figure 4.20. If the ratio of Co is increased, Mn particles seem even more hidden by the Co particles. On the contrary, if the ratio of Co is decreased, the Mn veils become more visible.

As far as the EDS study is concerned, when one shifts from Figure 4.19.b to d and f, the images become less and less green (characteristic of Co particles) and more and more red (characteristic of Mn particles). Again, this evolution is fully in accordance with the increase of the Mn:Co ratio.

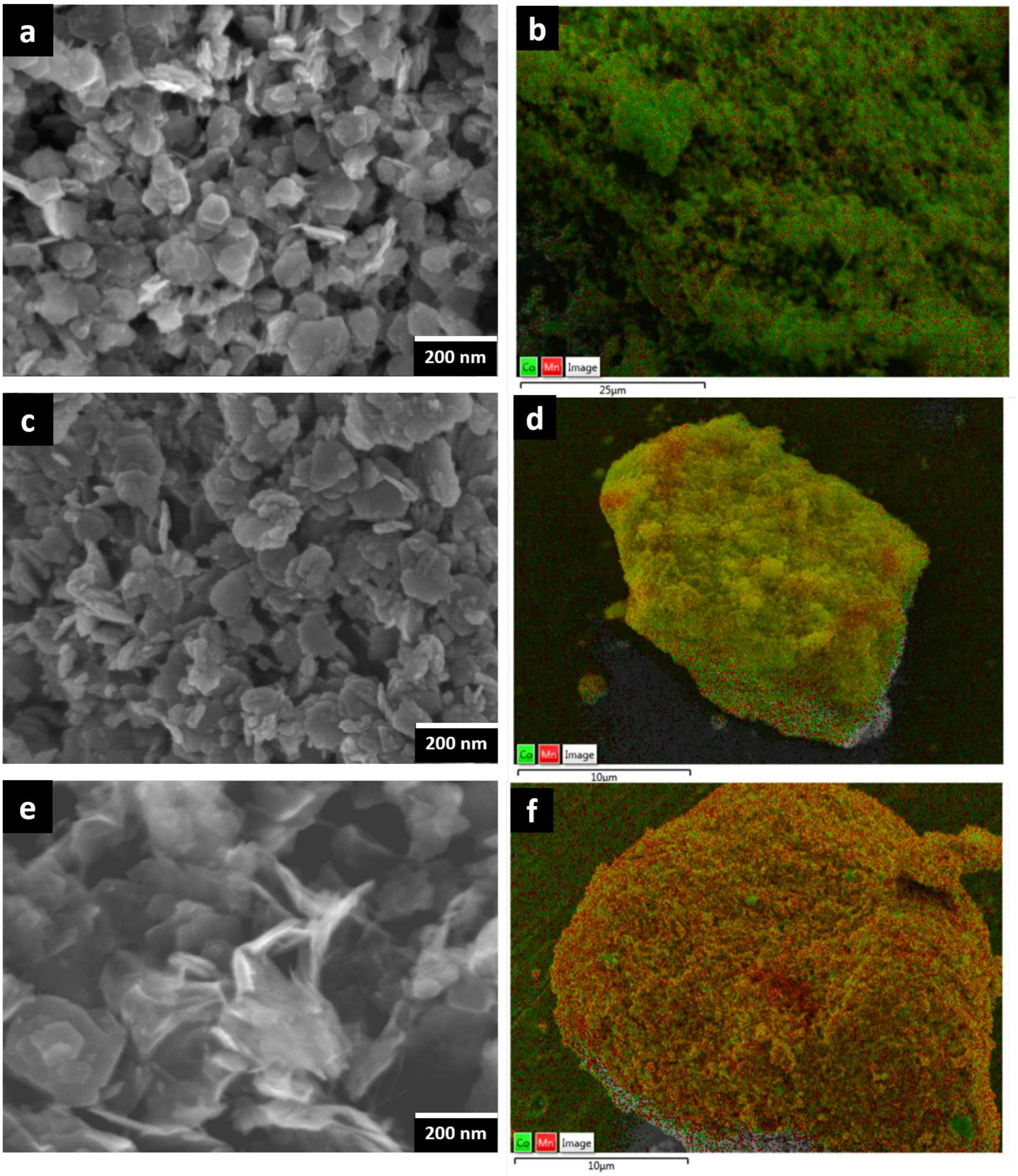

Figure 4.19.: SEM and EDS images (a) and (b) Restack-2-(Mn:2Co) : Restacked material with 33% Mn - 67% Co obtained by method 2. (c) and (d) Restack-2-(Mn:Co) : Restacked material with 50% Mn - 50% Co obtained by method 2. (e) and (f) Restack-2-(3Mn:Co) : Restacked material with 75% Mn - 25% Co obtained by method 2. Colors : red = Mn, green = Co.

It has been proved at this point by several characterization techniques that the restacked materials correspond to layered nanocomposites. As the layered structures are preserved, it is interesting, in a spirit of synergy, to verify if the good electronic properties of the cobalt oxyhydroxides, linked to the presence of Co^{4+} ions within the slab, will allow to make up the poor electronic properties of manganese oxide.

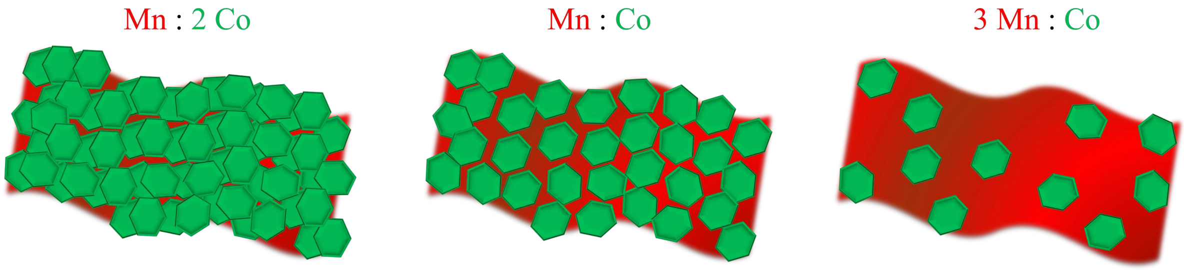

Figure 4.20.: Schematic representation of the intimate mix of Mn and Co particles depending on different ratios. H_K-birn are veil like particles (in red) and β3-prec are hexagonal platelets (green).

4.3.2.5. Conductivity properties of restacked materials in relation with the oxidation states of cobalt and manganese

Before studying the electronic conductivity, it is necessary to see if the oxidation states of the cobalt and manganese in the materials are modified by the exfoliation/restacking process. The oxidation state of each element in pristine materials are easy to determine experimentally by iodometric titration (see Annex A.2.3.1). However, restacked materials are composite materials, and a simple chemical analysis will not allow to distinguish the individual oxidation states of manganese and cobalt, but will only lead to a mean value between the two elements. In order to study the oxidation state of Mn and Co separately, other techniques are required. XANES studies were therefore performed, and their results were compared to those of XPS measurements, which can probe the surface of the samples so as to obtain the oxidation state of surfacic atoms.

Oxidation state of Mn and Co after restacking

X-ray absorption near edge structure (XANES)

XANES measurements (detailed in Annex A.2.3.2) can give access to the mean oxidation state of components of the elements of the bulk material. The information can be deduced by the pre-peak position and the position of absorption edge. All measurements were performed in collaboration with Antonella Iadecola at ROCK beam-line of synchrotron SOLEIL (France).

Mean oxidation state of Mn

The XANES spectra at Mn K-edge are shown in Figure 4.21. Mn_2O_3 and MnO_2 are used as references of Mn^{3+} and Mn^{4+} respectively.

Figure 4.21.b presents a zoom on the pre-peak region. The shape of the pre-peak corresponds to a doublet feature, due to the 3d t_{2g}-e_g splitting. In addition, no significant changes are observed in the pre-peak intensity and position for the various materials, which suggests that all the samples have Mn oxidation states in the same range.

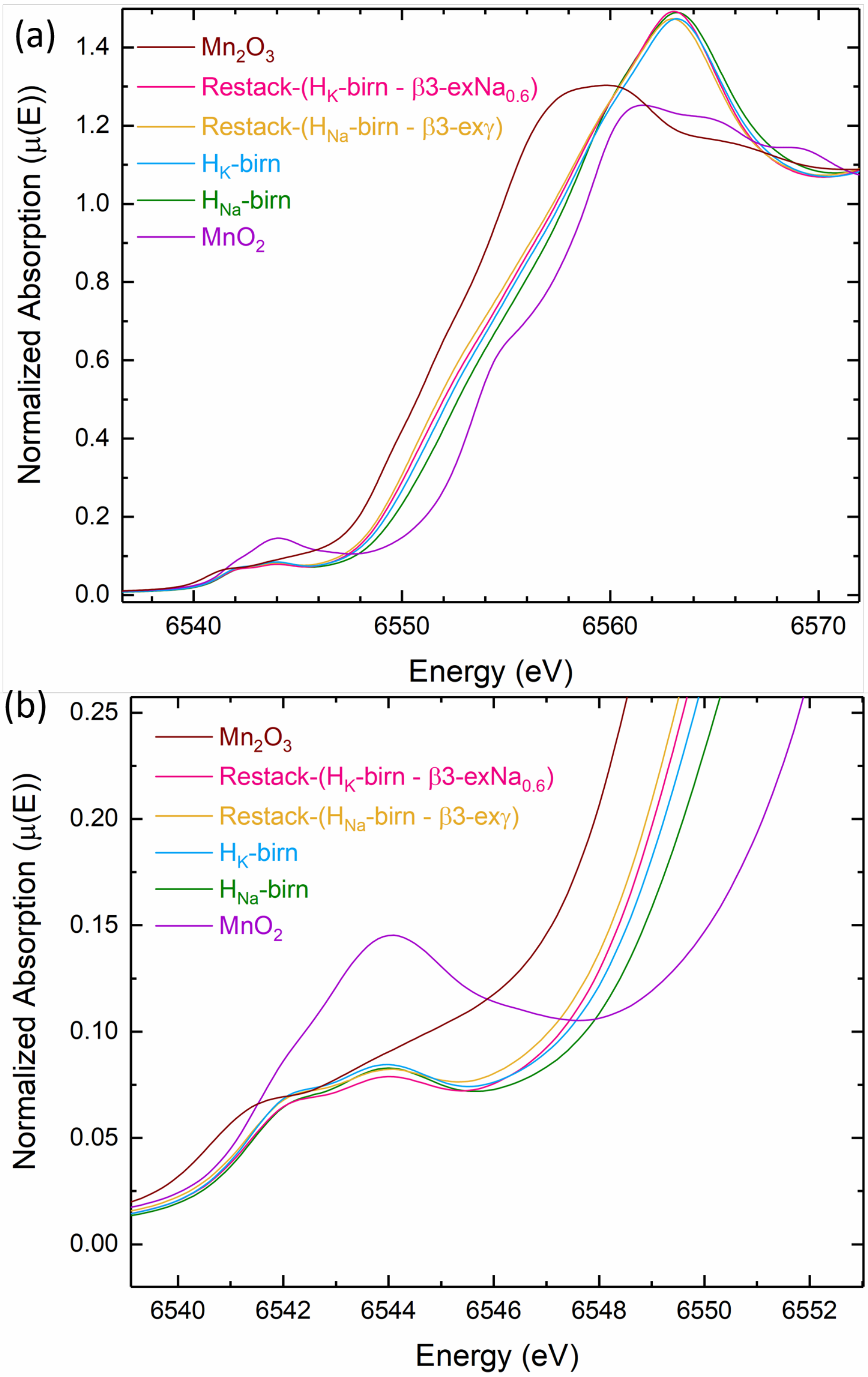

Figure 4.21.: XANES spectra of initial pristine materials and restacked materials (a) Mn K-edge. (b) Zoom on pre-peak region of Mn K-edge. Restack-(H_K-birn - β3-ex$Na_{0.6}$) is synthesized by method 1β with a Mn:Co ratio of 1:1. Restack-(H_{Na}-birn - β3-exγ) is synthesized by method 1β with a Mn:Co ratio of 4:3.

As shown in 4.21.a, Mn K-edge curves of the pristine and the restacked materials are at an intermediate position between those corresponding to Mn_2O_3 and MnO_2, which suggests that all the samples (pristine and restacked ones) contain manganese ions with an average oxidation state in the 3-4 range.

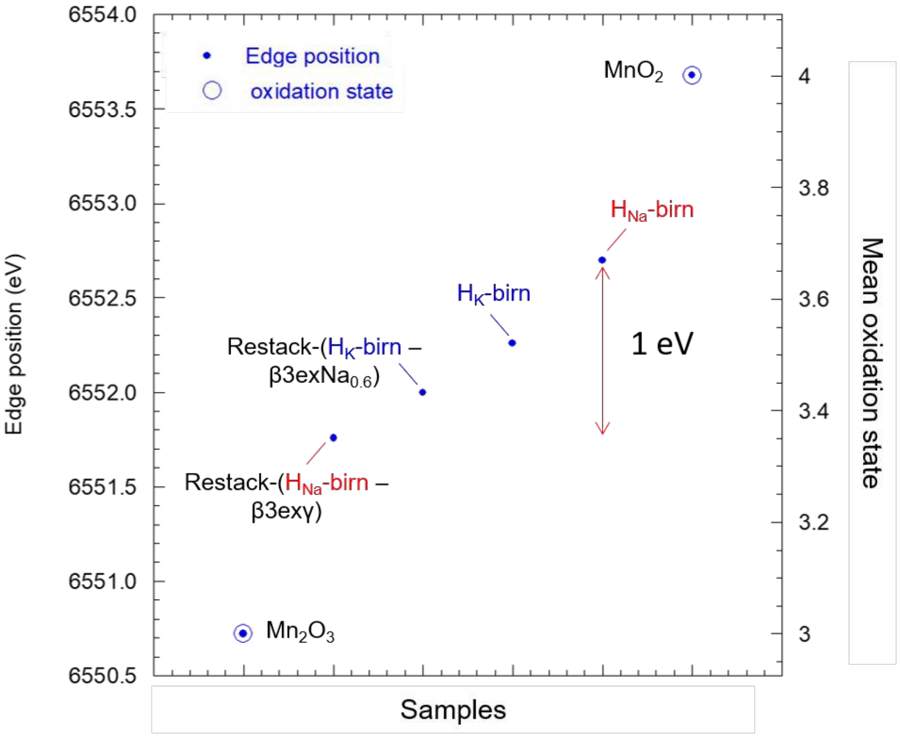

Figure 4.22.: Mn mean oxidation state plotted against Mn K-edge position of pristine samples and exfoliated/restacked ones. Mn_2O_3 and MnO_2 are used as references of Mn^{3+} and Mn^{4+}.

The Mn oxidation states in the various samples were more accurately evaluated from the edge positions for half jump, on the basis of the curve reported 4.21 and presented in Figure 4.22. In H_K-birn, the mean oxidation state of Mn shifts from 3.52 to 3.44 after restacking, and, in H_{Na}-birn, from 3.68 to 3.35 after restacking. This corresponds to a slight but significant decrease of Mn oxidation state after exfoliation/restacking, because the shifts in the edge positions are close to 1 eV.

Mean oxidation state of Co

Concerning the XANES spectra at Co K-edge (shown in Figure 4.23), Co_3O_4 ($Co^{2.67+}$) and CoOOH (Co^{+3}) are used as reference. From Figure 4.23.b featuring the pre-peak region, it can be deduced that all the samples (pristine and restacked) have a mean oxidation state between 2.67 and 3. Since there is nearly no difference in the edge positions, and the Co K-edge curves of pristine materials and restacked ones are very similar (shown in Figure 4.21.a), it can be concluded that the mean oxidation state of Co in pristine materials is not at all altered by the exfoliation/restacking process.

From these measurements, it can be concluded that manganese undergoes a slight reduction after exfoliation/restacking. However, the extent of this reduction (surface effect or global volumic reduction) can be questioned. To answer this, specific measurement of Mn surface oxidation states were performed by XPS.

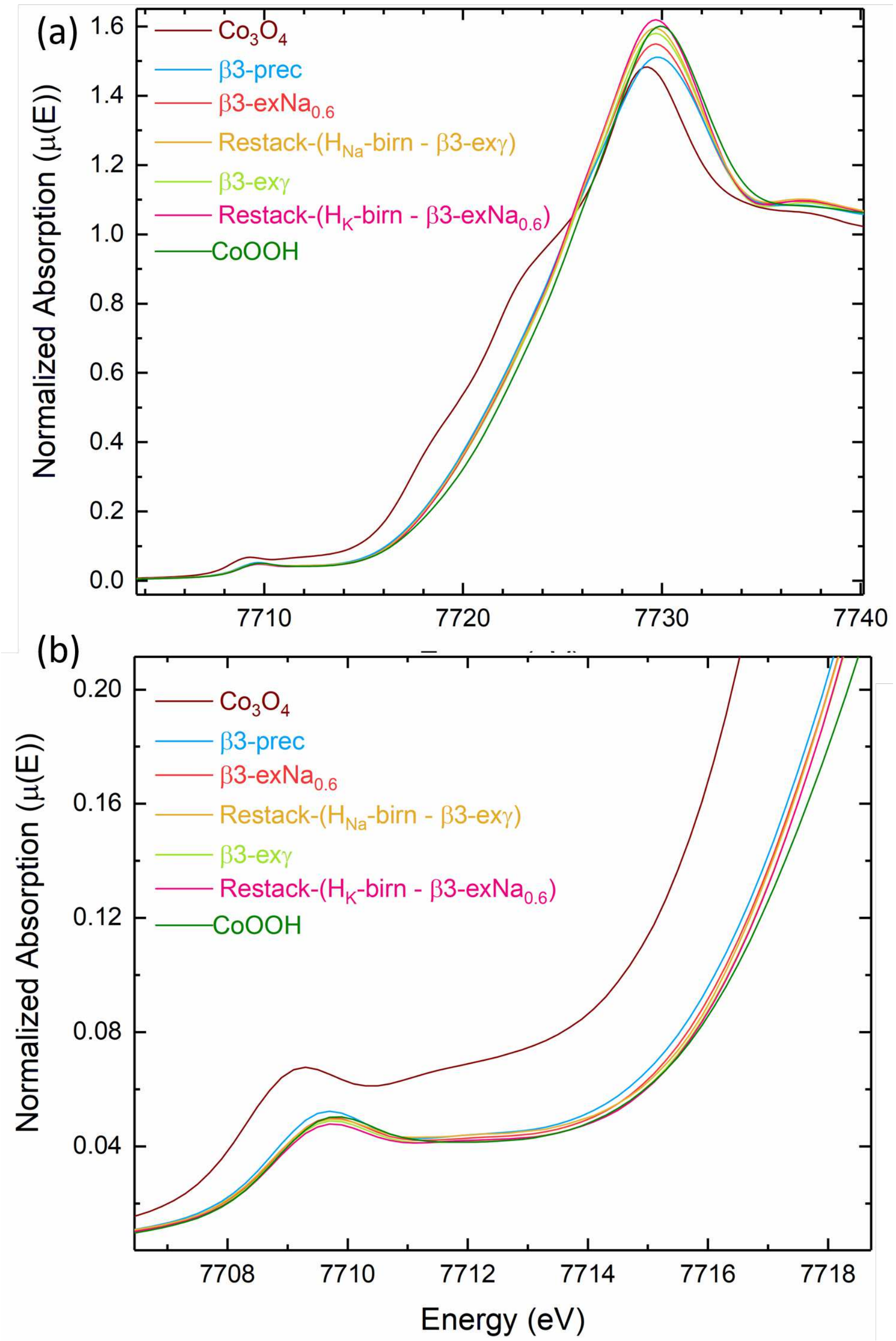

Figure 4.23.: XANES spectra of initial pristine materials and restacked materials (a) Co K-edge. (b) Zoom on pre-peak region of Co K-edge. Restack-(H_K-birn - β3-ex$Na_{0.6}$) is synthesized by method 1β and Mn:Co ratio. Restack-(H_{Na}-birn - β3-exγ) is synthesized by method 1β and Mn:Co ratio of 4:3.

X-ray photoelectron spectroscopy (XPS)

XPS is used to analyze the surface chemistry of the materials. The measurements were performed in collaboration with Christine Labrugère and are detailed in Annex A.2.3.3. Precise determination of a mean oxidation state for one element requires well-defined references. These references have to be pure and analyzed in the same conditions as the samples. Since no pure references are accessible, this precise determination of the mean oxidation state will not be possible. However, our goal is to study the impact of exfoliation/restacking process on the oxidation state of Mn and Co. A simple comparison of the XPS spectra of initial pristine materials with those of restacked materials, shown in Figure 4.24, should provide some interesting information.

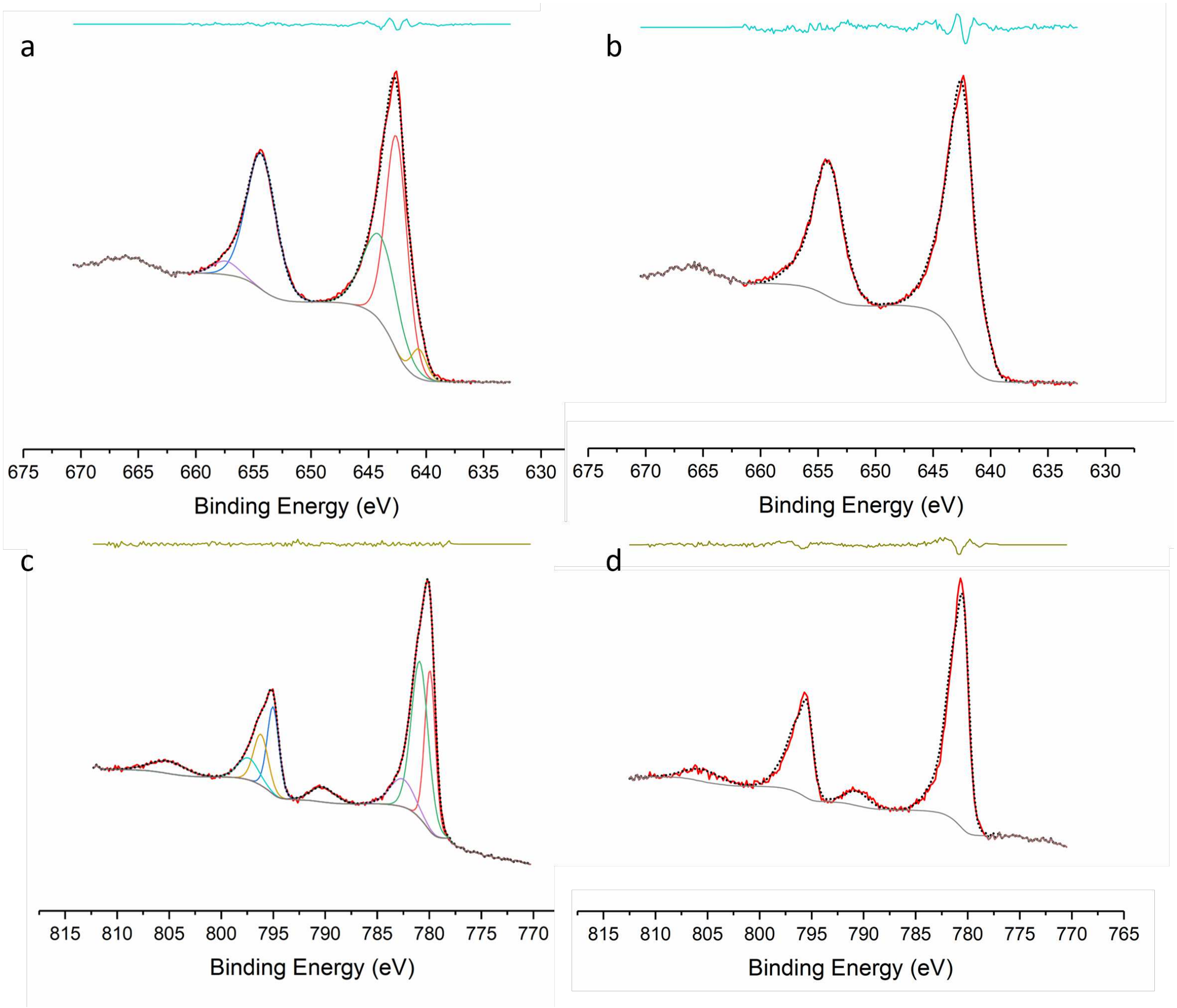

Figure 4.24.: XPS spectra for (a) Mn($2p_{3/2}$) and Mn($2p_{1/2}$) core level for pristine H_K-birn. (b) Mn($2p_{3/2}$) and Mn($2p_{1/2}$) for Restack-1β : Restacked composite of H_K-birn and β3-exNa$_{0.6}$ obtained by method 1β. (c) Co($2p_{3/2}$) and Co($2p_{1/2}$) core level for pristine β3-exNa$_{0.6}$ phase. (d) Restack-1β : Restacked composite of H_K-birn and β3-exNa$_{0.6}$ obtained by method 1β. The raw data are represented by the red lines, the baselines are represented in gray lines and the fitted envelopes are represented by black dot line. All the other lines correspond to mathematical peaks used to fit the raw data.

The Mn2p and Co2p high resolution core spectra obtained for the pristine materials are shown in Figure 4.24.a and c, respectively. The profiles are mathematically refined with a sum of several peaks, which do not have any physical signification, but are necessary to obtain the best possible fit. The resulting envelope (in black dots) corresponds to the sum of area of added peaks in order to correspond closely to the raw data (in red).

The high resolution spectra obtained for the restacked materials are shown in Figure 4.24.b and d. The fitted envelopes previously obtained are superimposed onto the core level spectra of the restacked materials. The fitted envelope for the Mn2p core level spectrum of pristine H_K-birn corresponds exactly to the raw data profile of restacked composite Restack-1β, which is obtained by restacking of H_K-birn and β3-ex$Na_{0.6}$. In a similar manner, the fitted envelope for the Co2p core level spectrum of β3-ex$Na_{0.6}$ corresponds to the experimental profile of Restack-1β. These observations lead to conclude that the local bonding environment of Mn and Co atoms in pristine materials is quasi-identical to that of the restacked materials, and therefore that the exfoliation/restacking process does not modify the mean oxidation state of Mn nor Co on the surface of the materials. This tendency is fully confirmed by further XPS measurements that were performed on one different restacked material obtained by the same restacking method 1β but with different initial materials (H_{Na}-birn and β3-exγ).

Comparison

As a summary, the XANES measurements have shown a slight decrease of mean oxidation state of Mn atom after exfoliation/restacking. Concerning the Co atoms, no change has been observed. In addition, XPS experiments have shown that there is no significant change of mean oxidation state neither of Mn nor Co atoms after exfoliation/restacking.

At first glance, this seems contradictory. However, it should be noted that XANES probes the entire bulk of samples, whereas XPS only analyzes the surface Mn and Co atoms. This behavior could be explained in the following way : in a first step, the exfoliation/restacking process could provoke Mn^{3+} disproportionation (discussed in section 3.2.3) which would decrease the average Mn oxidation state, including the Mn atoms present on the surface of the samples. However, as exfoliation/restacking ensues and the restacked samples are collected, the soluble Mn^{2+} cations on the surface atoms are eliminated, which would explain that no significant change of surface Mn oxidation state can be observed by XPS.

The impact of exfoliation/restacking on the mean oxidation states of Mn and Co atoms is particularly crucial for the cobalt element. Indeed, optimal electronic conductivity properties are subordinated to an amount of Co^{4+} as high as possible in the cobalt oxyhydroxide particles. The fact that the Co oxidation state is not altered by the exfoliation / restacking process is therefore a positive point. In the restacked composites, the presence of cobalt oxyhydroxides particles is likely to improve significantly the electronic conductivity as compared with pure manganese birnessite particles.

Electronic conductivity

Different conductivity measurements were conducted in order to verify if the restacked materials do present enhanced conductivity with regard to manganese oxides, and to understand the charge motions in the material. For that purpose, the electronic conductivities of the mixed materials were measured and compared to initial materials. Two mixed compounds with the same Mn:Co ratio of 1:1 were chosen. The first one is obtained by exfoliation/restacking (Restack-2 obtained by method 2 from H_K -birn and β3-prec) and the second one is the mixed material obtained by mechanical grinding (MG).

Since Restack-2 and MG were obtained *via* different routes, it is expected that they present different properties. The XANES and XPS measurements have shown that the Co oxidation states do not change. This means that on the surface, along the cobalt oxide layers, we can expect a good electronic conductivity. The main difference between Restack-2 and MG lies in the organization of Mn particles and Co particles. As revealed by EDS analysis, while for the mechanically ground MG sample, Mn-based area are well distinguished from the Co-based ones, they are intimately mixed in the restacked materials. The Mn:Co ratio of 1:1 should lead to the volumic percolation of cobalt oxyhydroxide in the sample after being pressed, and electronic percolation is expected, as presented in Figure 4.25 [233].

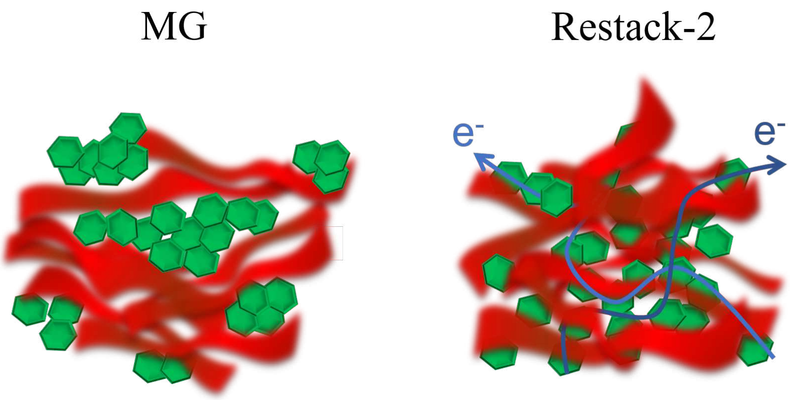

Figure 4.25.: Schematic representation of the texture of MG and Restack-2 after being pressed into pellets. Electronic pathways are schematized for Restack-2 sample.

DC 4-probe conductivity measurement

Classic 4-probe DC conductivity measurements were conducted on pellets of 8 mm diameter pressed under 1.2 GPa. The variations of the electronic conductivity versus reciprocal temperature of the pristine and protonated birnessites as well as of the β3-prec cobalt oxyhydroxide are displayed in Figure 4.26. In addition, Figure 4.26 presents the conductivity measurements of Restack-2 and MG. The values of conductivity at room temperature and activation energy associated with each sample are presented in Table 4.9.

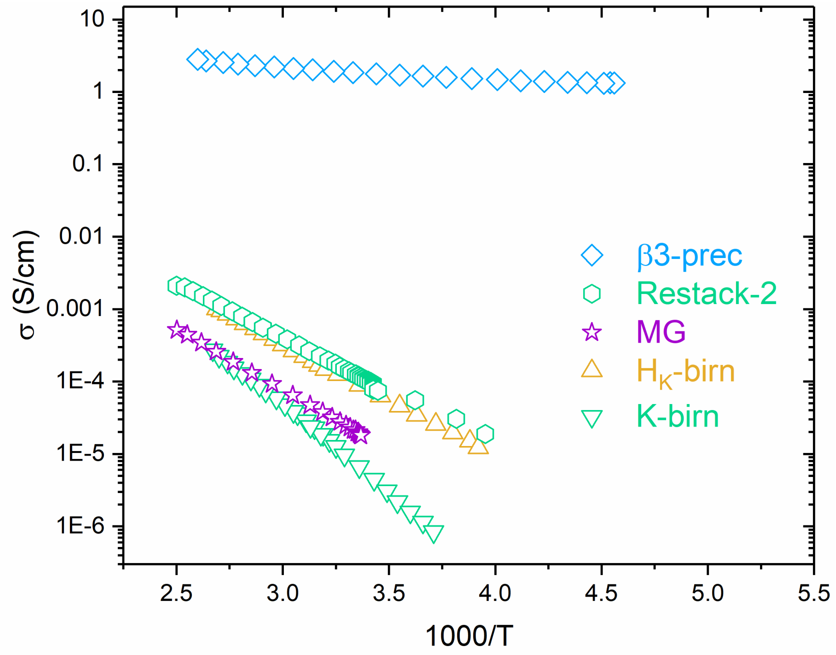

Figure 4.26.: Thermal variation of electronic conductivity for the restacked material Restack-2 (obtained by exfoliation/restacking of H_K-birn and β3-prec with 50% Mn and 50% Co using method 2) and MG sample obtained by mechanical grinding of H_K-birn and β3-prec (ratio 50% Mn and 50% Co). These are compared to the as-prepared pristine materials.

H_K-birn presents a low electronic conductivity that is activated by temperature. At room temperature, it is of 7.2·10^{-5} S/cm, while β3-prec has a metallic behavior with a good conductivity of 1.8 S/cm, which is five orders of magnitude higher.

	σ_{DC} (290 K) (S/cm)	Ea (eV)
H_K-birn	$7.2 \cdot 10^{-5}$	0.13
β3-prec	1.8	0.02
MG	$1.4 \cdot 10^{-5}$	0.17
Restack-2	$6.7 \cdot 10^{-5}$	0.14

Table 4.9.: Activation energy and conductivity at room temperature for initial H_K-birn and β3-prec compared with MG (obtained by mechanical mix of initial materials) and Restack-2 (obtained by restack of initial materials) with the same Mn:Co ratio.

For a composite made of 50% H_K-birn and 50% β3-prec, in which β3-prec particles percolate, an intermediate conductivity would be expected. When the mixing is not homogeneous, obtained by simple mechanical grinding, the conductivity of MG sample lies one order of magnitude below the initial H_K-birn, and closer to the pristine K-birn. Thus conduction pathways are inhibited in the mechanically ground sample, probably because the aggregates of Mn oxide are separated from Co oxyhydroxide aggregates. When both phases are intimately mixed, after exfoliation/restacking, the Restack-2 sample exhibits a higher electronic conductivity, meaning that the conduction pathways are favored. However, this effect is limited, as conductivity values are only similar to the initial H_K-birn. Furthermore, both activation energy associated are in the same order range as H_K-birn, Restack-2 exhibits a slightly lower activation energy than MG. We do not observe the “metallic” behavior as in pristine β3-prec. The lack of electronic conductivity enhancement for Restack-2 is not expected, as logically the cobalt oxyhydroxide should contribute to the global conductivity of the pellet, considering its geometrical percolation (see Figure 4.25). This unusual global response could be due to the technique itself, as DC conductivity measurements cannot provide any detailed information on the different contributions of the charge transport in powdered materials. In order to deeper investigate the reasons for this unexpected global response, BDS (Broadband Dielectric Spectroscopy) has been used as it is likely to provide detailed information on the different contributions of the charge transport in such powdered materials.

Broadband dielectric spectroscopy (BDS)

Charge transport in pelleted materials stems from different contributions : aggregate boundaries, grain boundaries and local motions, occurring at different scales. The use of BDS from low frequencies (few Hz) to microwaves (few GHz) allows the detection at different scales of electrical and ionic contributions.

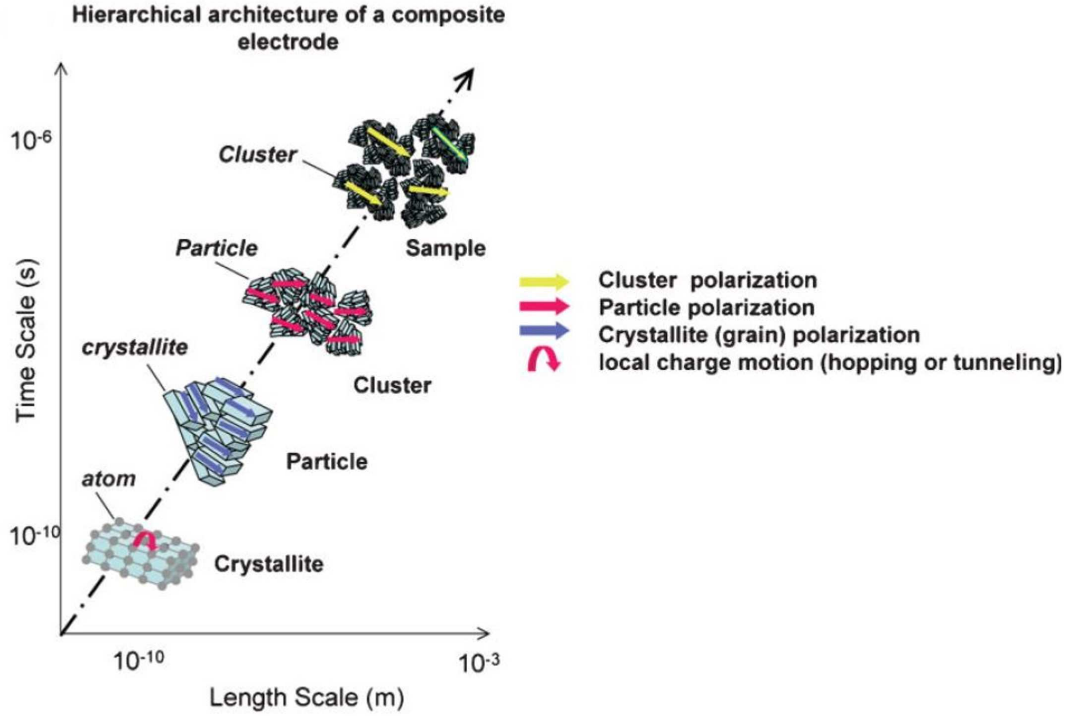

Figure 4.27.: Schematic description of hierarchical architectures within a composite material giving rise to different sources of polarization (from [234])

By measuring frequency-dependent complex permittivity and conductivity from 60 to 10^{10} Hz, it is possible to separately analyze the local motions of charges at different scales (see Figure 4.27). Since the DC measurements did not show any electronic conductivity enhancement linked with the mixing/restacking, we decided to investigate deeper the role of cobalt oxyhydroxide on electronic and ionic local motions. Also, in order to study the impact of exfoliation/restacking process, BDS measurements were also conducted on MG (composite material obtained by simple mixing) to compare the electronic contributions with Restack-2.

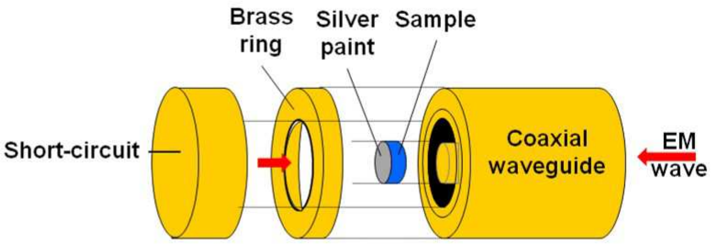

Figure 4.28.: Schematic description of the coaxial cell in which the sample (metallized powder pellet by silver paint) fills the gap between the inner conductor and a short-circuit. The brass ring ensures the electrical continuity of the outer conductor of the coaxial guide.

The experimental device consists of a coaxial cell in which the sample (metallized powder pellet) fills the gap between the inner conductor and a short-circuit [235]) as presented in Figure 4.28. The measurements are detailed in Annex A.3.2.

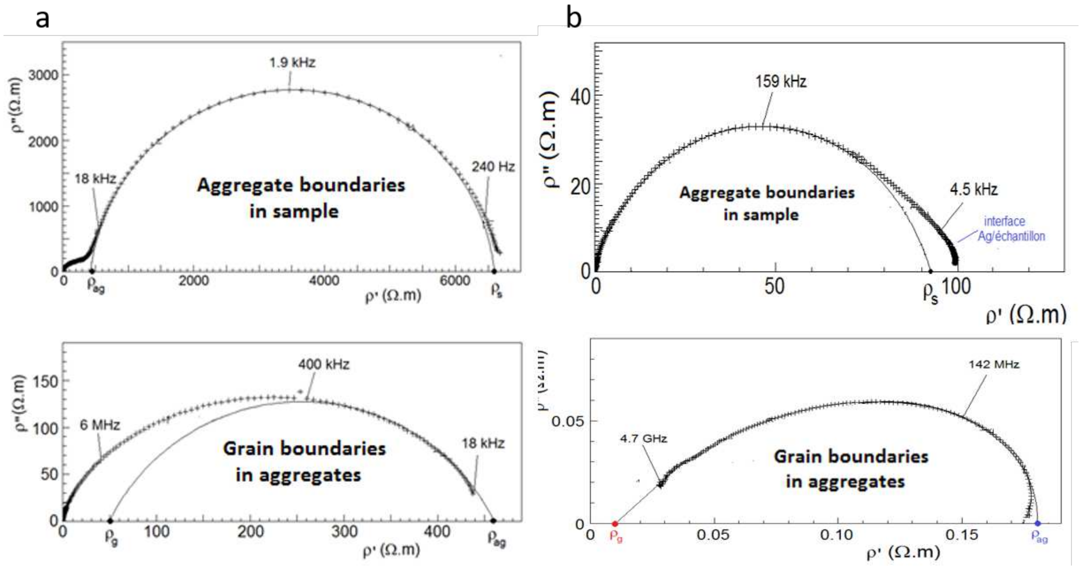

Figure 4.29.: Nyquist plot of complex resistivity of (a) H_K-birn (T=294K). (b) β3-prec. Top : Relaxation due to aggregate boundaries contribution in the sample with ρ_s and ρ_{ag} the sample and aggregate resistivities respectively. Bottom : After mathematical subtraction of the aggregate boundary relaxation, evidence of second relaxation due to grain boundaries contribution in aggregates with ρ_g and ρ_{ag} the grain and aggregate resistivities respectively.

The measurements are conducted by reflection on 3 mm diameter pellets that are pressed at 0.7 GPa and covered by conductive silver paint to ensure electronic conductivity. As the pellets used in DC measurements and BDS measurements do not have the same size nor were pressed at the same pressure, they will therefore present different compacities and different percolation thresholds. The resulting measured conductivities and activation energies determined by BDS will not be identical to the ones measured by DC.

From BDS measurements, complex admittance of the pellet is obtained, from which the conductivity of resistivity can be calculated. Figure 4.29 presents the Nyquist plots of complex resistivity that were obtained in the case of initial materials. By decomposition of these Nyquist plots, it is possible to model the relaxation of different contributions. Three relaxations in three various frequency ranges have been identified. The first one is clearly identified as the relaxation due to aggregate contact impedance, giving sample (ρ_s) and aggregate (ρ_{ag}) resistivities on the real axis of Nyquist plot. Then, mathematical subtraction of this relaxation (Figure 4.29 bottom) allows the detection of other contributions : a second relaxation can be identified as the contribution of the grain boundary in aggregates, giving aggregate grain (ρ_g) resistivity on the real axis of Nyquist plots. The sample (σ_{sample}), aggregate ($\sigma_{aggregate}$) and grain (σ_{grain}) conductivities are given by : $\sigma_{sample} = 1/\rho_s$, $\sigma_{aggregate} = 1/\rho_{ag}$ and $\sigma_{grain} = 1/\rho_g$. Note that the resistivity of the β3-prec grain in composite materials can be given by the high frequency part of the Nyquist plot (see example of MG in Figure 4.30.a).

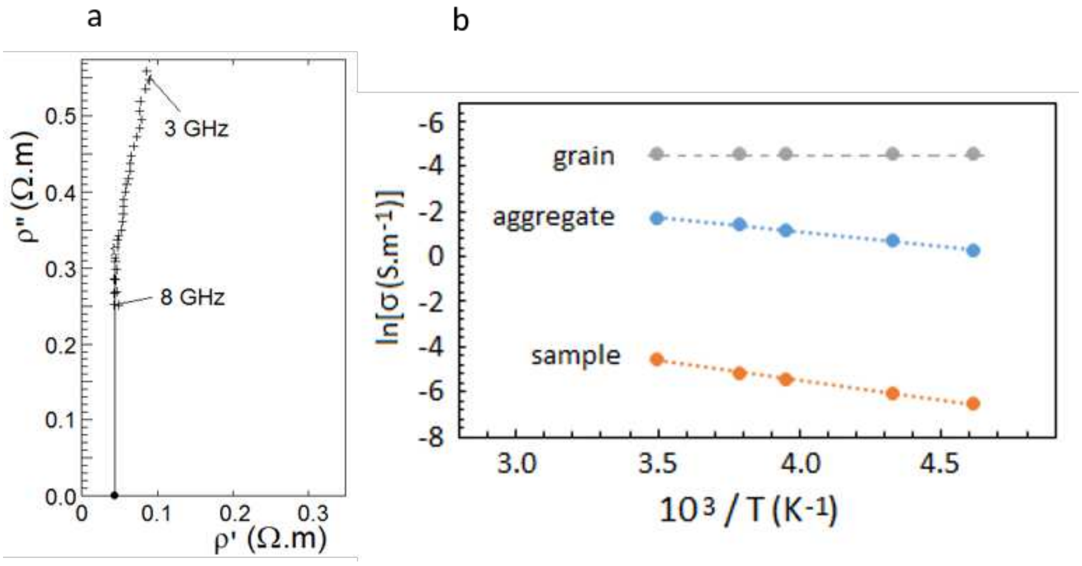

Figure 4.30.: (a) Nyquist plot of complex resistivity of MG (T=293K) : zoom of high frequency part giving the extrapolated value of β3-prec grain. (b) Electronic conductivity vs. reciprocal temperature at different scales of β3-prec (grain, aggregate and sample).

The measurements have been conducted at different temperatures, from 200 K to 295 K, so activation energies associated with each conductivity contribution can be calculated (see the example of β3-prec in Figure 4.30.b). The results for each sample are presented in Table 4.10.

	σ_{sample} (S/cm)	Ea (eV)	$\sigma_{\text{aggregate}}$ (S/cm)	Ea (eV)	σ_{grain} (S/cm)	Ea (eV)
H_K-birn	$1.5 \cdot 10^{-6}$	0.32	$2.2 \cdot 10^{-5}$	0.36	$2 \cdot 10^{-4}$	0.36
β3-prec	10^{-4}	0.15	$5 \cdot 10^{-2}$	0.11	1	0
MG	$1 \cdot 10^{-6}$	0.46	$1.1 \cdot 10^{-5}$	0.29	0.5	0
Restack-2	$1 \cdot 10^{-6}$	0.26	$3 \cdot 10^{-6}$ $2 \cdot 10^{-5}$	0.23 0.06	0.5	0

Table 4.10.: Activation energy and conductivity at room temperature for initial H_K-birn and β3-prec compared with MG (obtained by mechanical mix of initial materials) and Restack-2 (obtained by restack of initial materials) with the same Mn:Co ratio.

Manganese oxide H_K-birn

First of all, the contribution σ_{sample}=$1/\rho_s$ of H_K-birn is very low and in the same order of magnitude as the value obtained by DC measurements. As mentioned earlier, because DC pellets are pressed at higher pressure, the pellets will be more compact, strongly decreasing the resistivity of grain boundaries. The DC pellets are therefore more conductive. However, the activation energies associated with σ_{DC} (0.13 eV) and σ_{sample} (0.32 eV) are very different, revealing the fact that the detected charge carriers are not the same.

Since only the electronic conductivity is measured by DC measurements, it means that the charge carrier conductivity shown in BDS measurement is an ionic conductivity. In this case it corresponds to protonic conductivity. Furthermore, there is no difference observed in the E_a at the aggregate scale or grain scale, which means that the protonic conductivity of H_K-birn is the same at both junctions, and is the limiting factor.

Cobalt oxyhydroxide β3-prec

Concerning the cobalt β3-prec sample, the BDS-measured σ_{grain} of 1 S/cm is in the same order of magnitude as DC-measured σ_{DC}. Moreover, the E_a determined is 0 eV, in accordance with the DC measurements, revealing the metallic-type conductivity of β3-prec sample. The other activation energies associated with the sample and aggregate grain boundary are also very low, corresponding to electronic resistivity contributions.

Composite materials : Restack-2 and MG

As a reminder, Restack-2 is a composite material obtained by exfoliation/restacking of H_K-birn and β3-prec. MG is obtained by simply mixing both initial materials. Both are composed of 50% H_K-birn and 50% β3-prec.

First of all, the σ_{sample} of both materials are equal and in the same order of magnitude as the initial H_K-birn. This means that, similarly to what has been observed by DC measurement, the global conductivity is similar to that of manganese oxide. However, the activation energy associated with σ_{sample} of MG (0.46 eV) is much higher than the activation energy of Restack-2 (0.26 eV) but still characteristic of ionic conductivity. This means that the protonic charge transfer in Restack-2 is facilitated compared to MG sample, the protons have a higher mobility in Restack-2.

When looking at the grain boundaries, the mechanically ground sample MG shows a conductivity of $1.1{\cdot}10^{-5}$ S/cm which corresponds to exactly half of $\sigma_{aggregate}(H_K\text{-birn})$. As MG is composed of 50% of H_K-birn and due to the fact that the conductivity is proportional to the density of charge carriers, this value is coherent with protonic transfer from manganese oxyhydroxides. Since the protonic transfer is limitant, it is not possible to see any electronic contribution.

At this same scale, Restack-2 shows two different conductivity contributions. Therefore two types of transfer from grain to grain can be differentiated and identified thanks to the value of activation energies. High activation energy of 0.23 eV is characteristic of ionic conductivity, thus the grain boundary considered in this case can be ascribed to Mn aggregates, and the conductivity measured is of protonic diffusion. When the activation energy is much lower (0.06 eV), it means that the type of conductivity involved is electronic and can be ascribed to boundaries between Co aggregates. However, in both types of aggregates, the conductivity is very low, closer to $\sigma_{aggregates}(H_K\text{-birn})$. This point is further discussed below.

Comparison of the two mixed materials shows that the activation energies associated with $\sigma_{aggregates}(\text{Restack-2})$ are lower than $\sigma_{aggregates}(\text{MG})$. In Restack-2, there are more interfaces than in MG, due to the exfoliation/restacking process. The size of the particle certainly makes the charge transfer process easier, increasing their mobility and therefore decreasing the activation energy.

Finally, on a smaller intrinsic scale of the two composite samples, conductivity σ_{grain} is dominated by the response of the most conductive grains, i.e. Co oxyhydroxides particles. Again, it is interesting to notice that the conductivity measured corresponds to exactly half of pure $\sigma_{grain}(\beta3\text{-prec})$. This is because both composite materials are composed of 50% β3-prec.

All these measurements lead to the conclusion that the global conductivity of both composite materials is not enhanced because neither MG nor Restack-2 present electronically percolated cobalt oxyhydroxides. Overall, it is the conductivity of Mn oxides that will predominate. This is very surprising, as there are 50% Mn oxides and 50% Co oxyhydroxides, and according to the SEM images of Restack-2, it seems like all Co particles are geometrically percolated. Also, it has been shown that the mean oxidation state of Co particles has not been modified, thus meaning that the Co particles should present higher electronic conductivity.

This can be explained by an electron-trapping phenomenon, occurring at particle junctions [236, 237, 238]. The most probable hypothesis is that the electrons are blocked on the grain boundaries by the various protons present in the structure : O-H bonds or protons present in the manganese oxide's interlayer spacing. This electron-trapping would lead to lower amounts of mobile electrons, which is corroborated by the low electronic conductivity ($2{\cdot}10^{-5}$ S/cm) detected between grains, although geometric percolation is achieved. Protonic conductivity should also be affected, as observed ($3{\cdot}10^{-6}$ S/cm), but to a lower extent. Indeed, the number of electronic carriers in the cobalt oxyhydroxides (given the Co^{3+}/Co^{4+} ratio) is initially lower than the number of protons present. Thus this trapping should mainly affect the electronic conductivity, which is the case.

To conclude, Restack-2 does show an enhanced electronic conductivity compared to MG. Although geometric percolation of Co particles is achieved in Restack-2 (as shown in Figure 4.25) thanks to the exfoliation/restacking process, no electronic percolation has been achieved. Thanks to BDS, it has been understood that this is due to an increased number of grain boundaries, that induces an electron-trapping phenomenon, thus hindering the effect of Co addition.

4.4. Conclusion

The aim of this chapter was to design novel Mn-Co layered materials in a finely controlled way. A wide range of macro-scale assembling techniques can be considered : freeze-drying, spray-drying, spin-coating, dip-coating, electrophoretic deposition, spreading or casting followed by drying or annealing... However, in our case, a bottom-up strategy was chosen to finely tune nanoscale restacking. Using the exfoliated colloidal suspensions obtained in chapter 3, the nanosheets are considered as “building blocks”. It is therefore necessary to fully understand their physico-chemical state and to have a deep knowledge of their surface state.

To facilitate this, the surface of the initial particles have been modeled based on their structure, morphology and mean oxidation state of the metal ion. Then, their surface charges have been predicted by the MUSIC model leading to the determination of IEPs. The calculated values of IEP have been compared to the experimental measurements and are very close, thus validating the use of the MUSIC model. Furthermore, the MUSIC model can predict the effect of exfoliation on the surface charge of the particles. By modulating the basal surface area percentage, it predicts a slight decrease of IEP value due to exfoliation. Again, this was verified, even to a low extent, on experimental IEP of nanosheets in colloidal suspensions.

Since the IEP values of Mn oxides (3) and Co oxyhydroxides (7) are very different, it is possible to define one pH domain in which the Co oxyhydroxides particles are positively charged while the Mn oxides particles are still negatively charged. This leads to different restacking techniques that have been carried out.

To better study the impact of exfoliation on pristine materials, a first series of mono-metal restacking (simple restacking) has been conducted. No great structural difference is observed between the starting and exfoliated/restacked materials, while the morphology is modified. The most surprising result is the decrease of specific surface area, which can be linked to the restacking process. Indeed, instead of flocculation in a well-ordered manner, the nanosheets have a tendency to restack in arbitrary directions, in a more packed manner.

Mixed layered Mn-Co oxides were then obtained using various restacking methods. The structure and morphology of the obtained materials were characterized to determine the impact of the restacking techniques used as well as the influence of the Mn:Co ratio. X-ray diffraction has shown that the restacked materials correspond to nanocomposites of two phases : manganese oxide and cobalt oxyhydroxides. A microscopy comparison with mixed Mn-Co oxides obtained by mechanical grinding (used as reference) justifies the use of a bottom-up strategy which consists in exfoliating and restacking layered oxides. Indeed, whereas the EDS images of the simple mixed material show distinct Co and Mn aggregates, the images of restacked materials show a more intimate mixture of both elements.

Adding cobalt oxyhydroxides was expected to enhance the electronic conductivity of the particles. Since the electronic conductivity greatly depends on the mean oxidation state of Co in the oxide, a first step is to determine the mean oxidation state of the surfacic metal ions. This was made possible by XPS and XANES measurements, and led to the conclusion that surfacic atoms do not see their mean oxidation state modified. Finally, measurements of electronic conductivity were performed. An usual DC technique did not lead to a clear difference between restacked materials and mechanically grinded ones, so BDS was used to better understand the composites. It was shown that although geometric percolation of Co particles is achieved after exfoliation/restacking process, no electronic percolation could be observed, most probably due to an electron-trapping phenomenon at the grain boundary.

The aim of this thesis is to synthesize novel materials with enhanced electrochemical performance as supercapacitive electrodes. In the aim of obtaining a synergistic effect by combining Mn oxides and Co oxyhydroxide, although the electronic conductivity of composite materials is not greatly enhanced, it does not mean that the electrochemical performances will be the same. This leads to the following chapter, where the electrochemical performances of each restacked material will be assessed. A comparison will be made between restacked materials and pristine ones, and the best restacked material will be assembled, as positive electrode in a full device, with an activated carbon at the negative electrode.

5. Electrochemical behavior of restacked Mn-Co materials

In the previous chapter, the synthesis of mixed layered oxides by exfoliation/restacking has been detailed. Mixed multilayered composites are obtained, as proven by various characterizations techniques.

This present chapter has a double aim : select the restacked material presenting the best electrochemical behavior (capacitance, power and cycling retention) and assemble this electrode material to activated carbon in a full asymmetric cell. As mentioned in chapter 1, besides the active material, two levers allow the increase of energy density of a supercapacitor : *specific capacitance* and *voltage window.*

The *specific capacitance* is an intrinsic feature of the material, and in order to determine which restacked material will be assembled in a full cell, a first series of electrochemical tests will be compared. First, the electrode manufacturing will be optimized, by comparing various amounts of conductive carbon added. Then, different features of restacked materials will be compared in terms of electrochemical impact : difference in morphology, in Mn:Co ratio, nature of initial phases... Systematic comparison to phases obtained by mechanical grinding will be carried out.

The *voltage window* is greatly dependent on the stability window of the electrolyte. The neutral aqueous media used in this chapter (K_2SO_4) presents a stability window of 1.23 V, the real potential window can be enlarged due to over-voltage phenomena at the electrodes [16]. By combining two electrodes with different active materials and therefore different domains of electrochemical activity, asymmetric supercapacitors can see their voltage window enlarged. By associating an electrode made of restacked metal oxide with an activated carbon electrode, the final system should have a larger electrochemical activity domain. Furthermore, it can be expected that the full cell benefits from both electrodes by combining the advantages of each : higher capacitance thanks to the mixed oxide electrode and increased power density and cyclability due to the carbon-based electrode.

After choosing the best restacked material, a full cell will be built to investigate the feasibility of a hybrid assembly. Before doing so, it is necessary to balance the electrodes to get the highest efficiency for the full cell. A first part will be dedicated to the activated carbon-based electrode. Then, different ratios in both electrodes will be tested in order to determine the balanced system with the highest efficiency.

5.1. Electrochemical performance of manganese oxide and cobalt oxyhydroxide

In order to study the electrochemical properties of Mn-Co mixed materials obtained in the previous chapter, a first section will present the electrochemical properties of the initial pristine materials. The oxides powders are prepared as self-supporting films pressed on a stainless steel grid as current collector. The obtained electrodes are made of three components :

- the active material : it is the most important component, as it is the origin of energy storage. With metal oxides, high specific capacitance can be reached. However, to ensure electronic conductivity, it is often necessary to add :
- a conductive additive : in most cases, carbon additives (usually carbon black) are added. For example, in most battery electrodes, a ratio of about 30 vol% of carbon is required to allow a good conductivity [239]. This ratio is associated with the percolation of the carbon particles dispersed in the non-conducting system. The percolation threshold strongly depends on the quality of dispersion as well as on the morphology of carbon particles. However, the amount of added carbon should be minimal to maintain the largest part of active material in the system in order to achieve high specific capacitances.
- a polymer binder : PTFE or PVDF. Binders are expected to link the particles of active material together, and to ensure good cohesion with the electrode substrate, to avoid active materials falling off during the electrode working. It confers good mechanical properties to the electrode.

A detailed description of the electrode preparation as well as of the cell configuration and electrochemical techniques used can be found in Annex A.6.1 and A.6.2. In the following section, all the measurements are conducted in an aqueous electrolyte K_2SO_4 (0.5 M) in a three-cell configuration. The reference electrode is Ag/AgCl and the counter electrode is a platinum wire.

5.1.1. Influence of carbon black : how to obtain the best electrochemical performance

In order to enhance the electrochemical performance of the active material, the right ratio of carbon to active material should be added. In this study, electrodes with various ratio have been prepared. The polymer binder, PTFE, is kept at 5 wt% to ensure a good mechanical stability of the electrode film.

The ratio of carbon to material has been optimized by testing electrodes containing 0 to 55 wt% of carbon black. The obtained capacitances according to the scan rate are shown in Figure 5.1.

If there is absolutely no carbon additive in the electrode preparation, the performance of the electrode is the lowest, which justifies the use of a conductive additive. However, as only 5 wt% of carbon black is added, the capacitance rises from 30 F/g to 100

F/g at a scan rate of 0.5 mV/s, which represents a three-fold increase. This means that carbon black is an essential component to efficiently transport the electrons to the active material. As the amount of carbon black is increased, it can be observed that at all scan rates, the electrode composed of 80 wt% active manganese oxide and 15 wt% carbon black presents the best specific capacitances. As schematized in Figure 5.2, adding carbon black can efficiently increase the electrochemically active surface area. Indeed, the carbon particles induce the formation of an electronic percolation network, which is able to offer continuous electron conductive pathways. The intrinsic electronic resistivity of an electrode will directly influence its performance because it will increase the cell resistance of a supercapacitor and limit its power density and energy density.

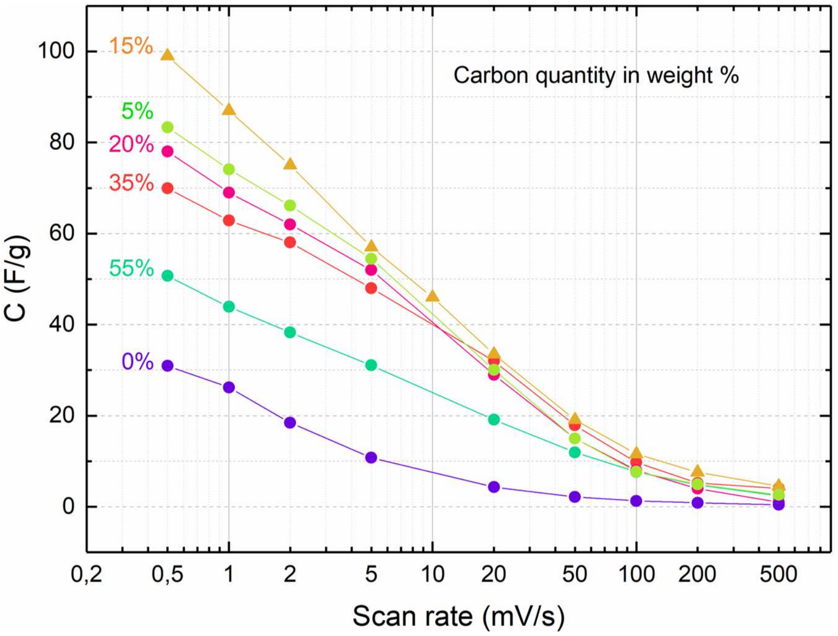

Figure 5.1.: Capacitance vs scan rate obtained for electrodes composed of H_K−birn and carbon black with ratios of carbon to active material from 0 to 55 wt%. The capacitance is normalized to the mass of active material only (m_{H_K-birn}).

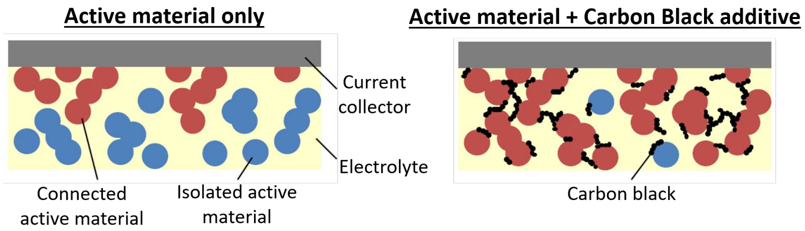

Figure 5.2.: Schematic representation of electronic percolation in an electrode when conductive carbon black is added. The active material is represented in red when electronically connected to the current collector, in blue when they are electronically insulated from the percolation network.

If the amount of carbon black is further increased to 20 wt%, a net drop of capacitance is observed. This could either be due to the low capacitance of carbon black, or to its hydrophobic nature, which will have a negative impact, higher than the percolation effect.

Finally, the best performances in terms of specific capacitance are obtained with 15 wt% of carbon black added in the electrode preparation. In the following studies, all electrodes will therefore be built with a ratio of 80 wt% active material, 15 wt% carbon black and 5 wt% PTFE, unless stated otherwise.

5.1.2. Electrochemical behavior of pristine materials

Initial manganese oxides synthesized in Chapter 3 have been studied as electrode material in a three-cell configuration. The cyclic voltammograms obtained at 5 mV/s are shown in Figure 5.3. From these voltammograms, it is possible to calculate the specific capacitance of each electrode (calculation in Annex A.6.3).

The protonated samples, H_{Na}-birn and H_K-birn, show voltammograms that have a rectangular shape typical of a pseudocapacitive behavior. The specific capacitance of H_{Na}-birn is 72 F/g, higher than the 58 F/g of H_K-birn. This can be assigned to the higher electronic conductivity of H_{Na}-birn, as shown in section 3.2.5, and by a more rectangular shape of cyclic voltammogram curve.

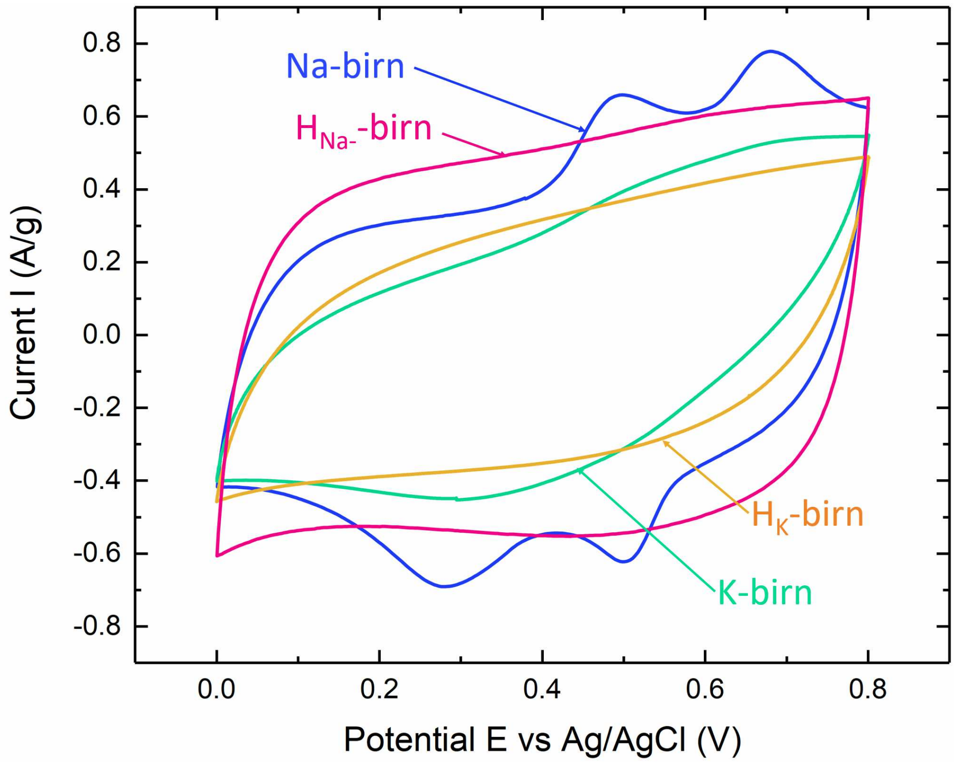

Figure 5.3.: Cyclic voltammograms at 5 mV/s of Na-birn (blue), K-birn (green) and protonated H_{Na}-birn (pink) and H_K-birn (yellow) in a three cell configuration, with Ag/AgCl reference electrode, Pt counter electrode, in 0.5 M K_2SO_4. All currents are normalized to the mass of active material.

Contrarily to the protonated samples, the voltammograms of starting materials show broad peaks superimposed on the rectangular shape of protonated version. These peaks, as reported in the literature, correspond to the Na^+ and K^+ cations insertion/deinsertion in the interlayer space [240]. Both protonated birnessites are less efficient than their starting material, as Na-birn shows a specific capacitance of 85 F/g and K-birn 60 F/g at a scan rate of 5 mV/s. It is interesting to note that Na-birn show two anodic peaks and cathodic peaks, which can be related to the presence of two sites for the cations in birnessite, one ion-exchange-type site for manganese in tetravalent state and one redox-type site for manganese in trivalent state, which cause a two-step intercalation/deintercalation process [112]. On the voltammograms of K-birn, only one very broad peak can be identified. This is probably due to the difference in morphology between Na-birn and K-birn. Indeed, K-birn is much less ordered within the slabs and in the stacking direction than Na-birn (as seen in Chapter 3). This disorder leads to the presence of a high number of different active manganese sites, thus having different oxidation and reduction potential which would result in a broadening of anodic or cathodic peak in the voltammogram.

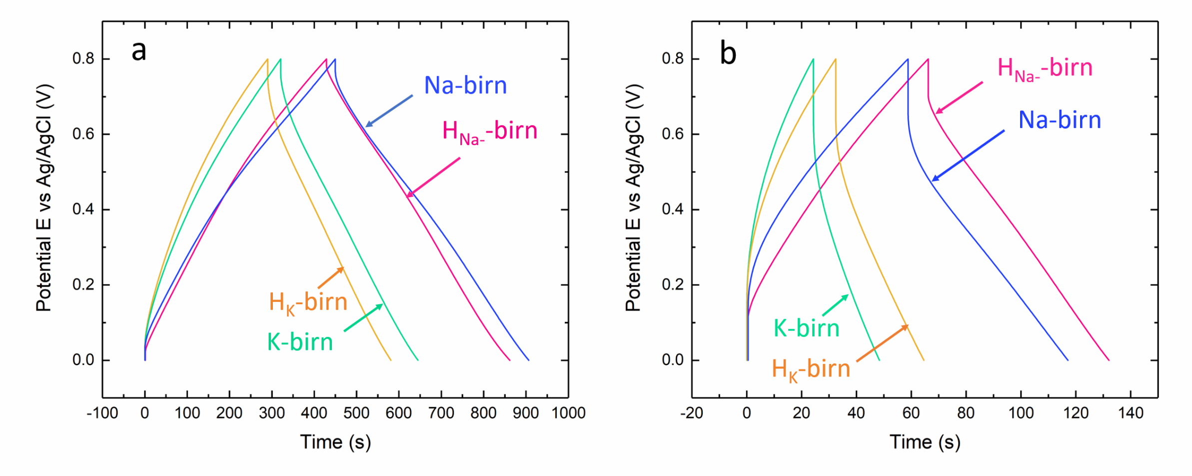

Figure 5.4.: Galvanostatic charge and discharge curves at (a) 0.2 A/g and (b) 1 A/g (right) for Na-birn (blue), K-birn (green) and protonated H_{Na}-birn (pink) and H_K-birn (yellow). All currents are normalized to the mass of active material.

It is also possible to study the electrochemical properties of the materials by galvanostatic measurements (5.4). In Figure 5.4.a, the curves obtained correspond to a current of 0.2 A/g (1 A/g in Figure 5.4.b). For an ideal supercapacitive electrode, potential evolves linearly vs time, which is not the case if faradaic reactions are implied. One cycle corresponds to one charge/discharge cycle. In reality, an ohmic drop can be observed at the very beginning of charge or discharge. The ohmic drop tends to increase with the current flow (according to $\Delta U = IR_s$ with I the current and R_s the internal resistance of the system). From the linear part of the curve, it is possible to calculate the capacitance of the electrodes in a more precise way. Here, from the slope of the curves, the capacitances obtained are : Na-birn (97 F/g), K-birn (73 F/g), H_{Na}-birn (83 F/g), H_K-birn (66 F/g) at 0.2 A/g. It is interesting to observe the tendencies of those values, and to correlate them with the values obtained by cyclic voltammogram. Indeed, in accordance with the capacitances obtained by cyclic voltammetry, the capacitances obtained at 0.2 A/g for protonated birnessites are systematically lower than those obtained for their precursors. However, the tendencies are reversed at higher rate (1 A/g) and the protonated birnessites show a higher capacitance than their precursors. This is not yet clearly understood, but could be linked to different ionic exchange processes at the surface of the protonated oxides.

Initial cobalt oxyhydroxides have also been studied and their cyclic voltammograms are shown in Figure 5.5. The results show three differently shaped voltammograms that result in different specific capacitance at 5 mV/s: β3-exNa$_{0.6}$ and β3-exγ both exhibit higher capacitances of 24 F/g (and 22 F/g respectively), whereas β3-prec exhibits a mere 7 F/g. The galvanostatic curves (shown in Figure 5.6) also show the same tendency. From the slopes, the capacitances can be calculated and the values obtained are slightly higher than the ones calculated by cyclic voltammetry :β3-exNa$_{0.6}$ (32 F/g), β3-exγ (27 F/g) and β3-prec (9 F/g).

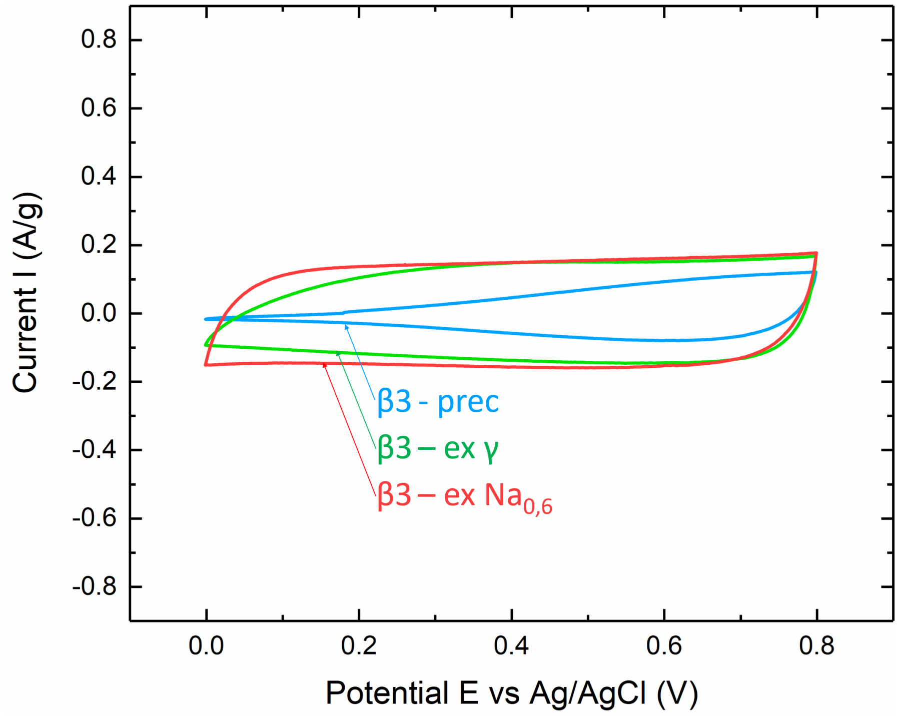

Figure 5.5.: Cyclic voltammograms at 5 mV/s of cobalt oxyhydroxides β3-exγ (green), β3-prec (blue) and β3-exNa$_{0.6}$(red) in a three cell configuration, Ag/AgCl reference electrode, Pt counter electrode in K_2SO_4 0.5M. All currents are normalized to the mass of active material.

This can be explained by the difference of morphology of the active materials. Since the β3-exNa$_{0.6}$ and β3-exγ are more divided and less crystalline, as shown in chapter 3, section 3.2.4.2, they are likely to contain more electroactive sites. The fact that β3-prec is more conducting does not seem to play a key role. Indeed the very rectangular shape of β3-exNa$_{0.6}$ reveals a low internal resistance.

The cyclic voltammograms of initial manganese oxides and cobalt oxyhydroxides shown in Figure 5.3 (and 5.5 respectively) are drawn on the same scale so as to realize their different electrochemical responses. It is clear that manganese oxides are better active materials for pseudocapacitive electrodes, even if cobalt oxyhydroxides exhibit a non-negligible pseudocapacitance. However, it is their electronic conductivity that will be put at use in the restacking. In the following, only the cyclic voltammograms are shown, as they provide a better visualization of the performance evolution. All the given capacitances are calculated on the basis of the voltammetry curves.

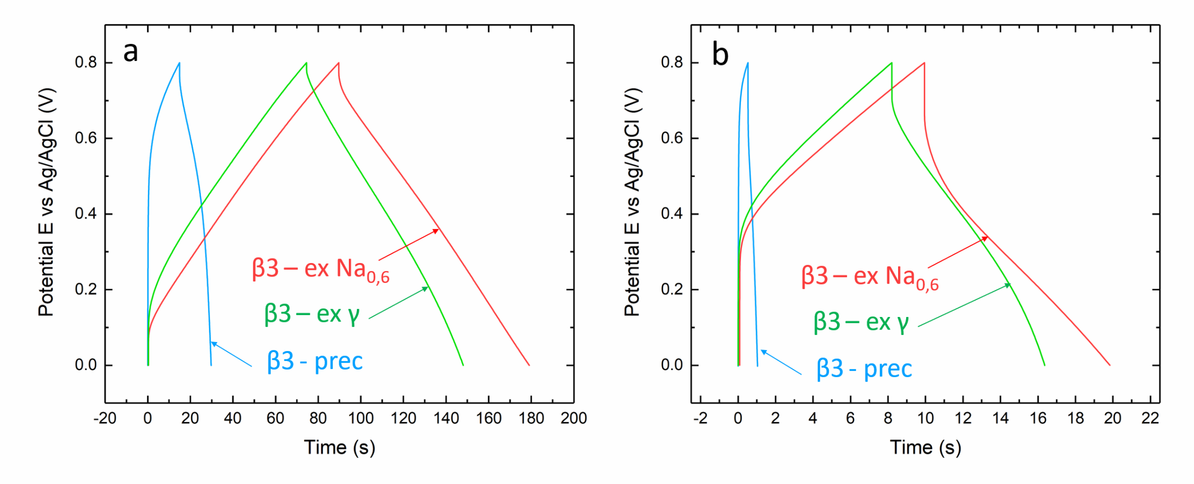

Figure 5.6.: Galvanostatic charge and discharge curves at (a) 0.2 A/g and (b) 1 A/g (right) for cobalt oxyhydroxides β3-exγ (green), β3-prec (blue) and β3-exNa$_{0.6}$(red). All currents are normalized to the mass of active material.

5.1.3. Effect of exfoliation on pristine materials

This paragraph is dedicated to the comparison between the initial materials and the exfoliated/restacked materials obtained by simple restacking (mono-element, Mn or Co) (as described in section 4.2.1.1).

The specific capacitances obtained for exfoliated/restacked materials, in comparison to the initial ones, are shown in Figure 5.7. Let us remind that the exfoliated/restacked materials are obtained by flocculation of exfoliated samples in NaCl (1 M). The curves show that in both cases, the materials obtained after exfoliation present higher specific capacitances. This has already been studied and reported for manganese oxide electrodes [205, 241], for which electrochemical activities of the exfoliated samples are enhanced. This behavior has been attributed to the fact that exfoliation leads to different microstructuration of nanosheets, and increases the active electrochemical surface in contact with the electrolyte.

However, as shown in section 4.3.1.3, the specific surface areas of exfoliated/restacked materials are significantly lower than the specific surface areas of initial materials. This is contrary to what is expected in relation with the enhanced specific capacitances. The only way to understand this is to differentiate the specific surface areas measured by N_2 adsorption/desorption and the electrochemically-active surface that will contribute to electron storage. This is because BET measures the nitrogen adsorption area while electrochemical characterizations involve electrochemically active areas. In the initial materials, the BET area is higher, but some regions may not be connected to the rest of the electrochemical active network. As seen in chapter 4 (section 4.3.1.3), the exfoliation/restacking process is supposed to change the morphology of pores, making them more connected to the rest of the electroactive particles. Furthermore, there could be a solvation effect : adsorption measurements are conducted on dried compact powder whereas electrochemical measurements are conducted on electrode films in aqueous solvent.

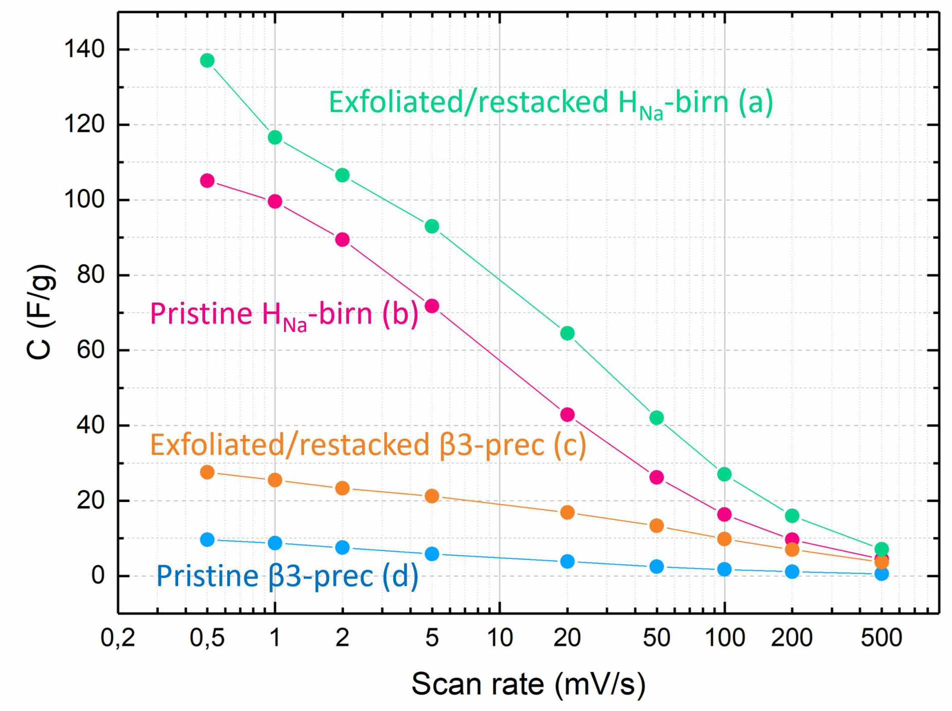

Figure 5.7.: Capacitance vs scan rate obtained for initial materials and corresponding exfoliated/restacked derived materials prepared by flocculation in NaCl (1 M). The capacitance is normalized to the mass of active material.

In conclusion, the exfoliation/restacking by flocculation process appears to improve the electrochemical performances of initial materials.

5.2. Electrochemical performance of exfoliated/restacked mixed materials

As seen in the previous section, the process of exfoliation/restacking of layered materials can efficiently enhance their electrochemical performances. In the following section, mixed Mn-Co composite layered materials, obtained by this process, will be studied to try to enhance the electronic conductivity of birnessite. First, restacked materials obtained with various restacking techniques will be compared in terms of electrochemical behavior. Then, the influence of the restacking technique along with the nature of the initial materials will be discussed. A focus will be made on the role of conductive cobalt oxyhydroxides on the electrode performances. Finally, the cyclability of the restacked composite will be examined by cyclic voltammetry over 10 000 cycles.

5.2.1. Impact of restacking method

The impact of restacking method on the structure and the morphology of the obtained compounds has been discussed in section 4.3.2.3. The materials composed of 50% Mn and 50% Co have been prepared as active material films (as described in Annex A.6.1) and their electrochemical responses are studied in this section.

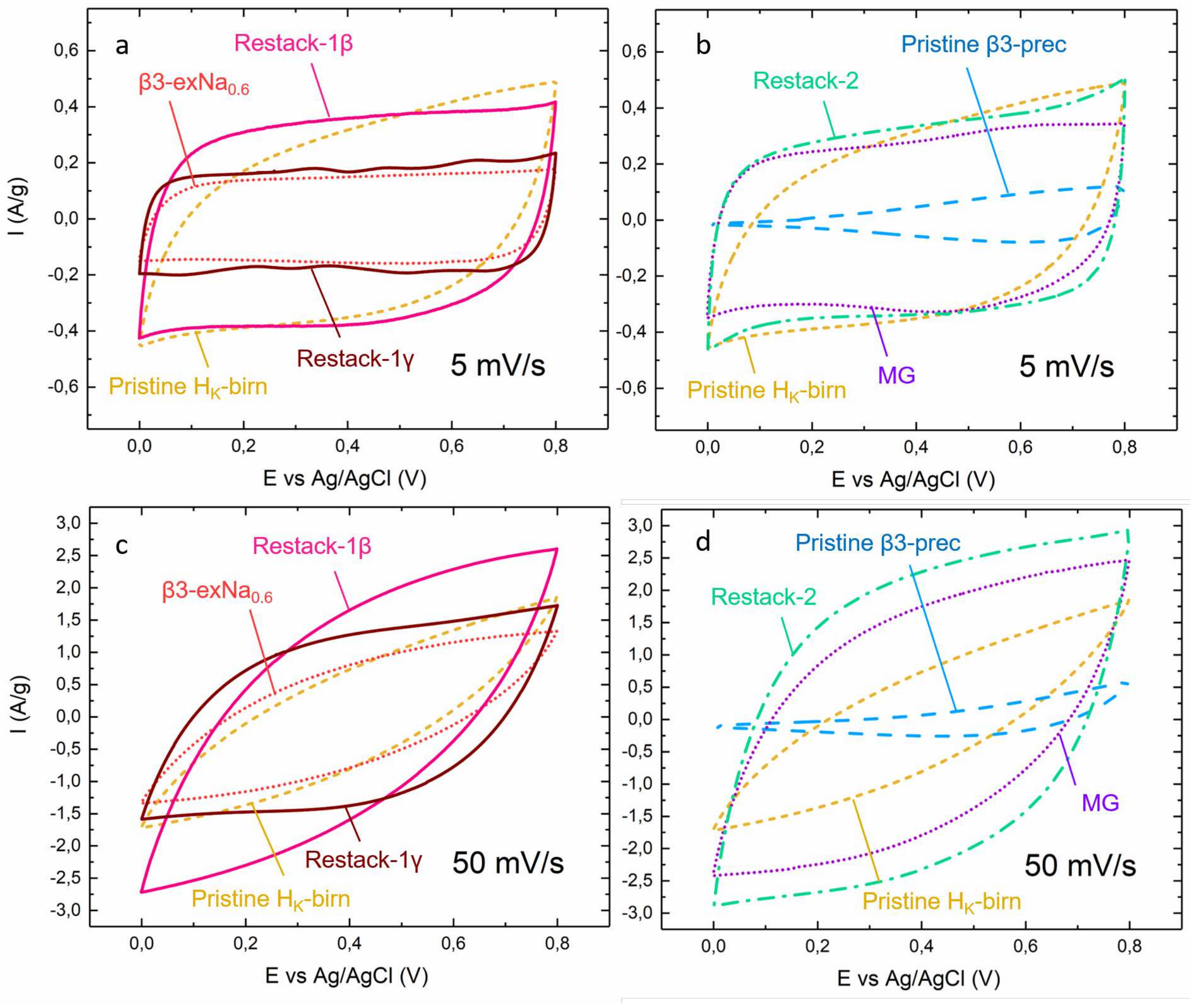

Figure 5.8.: Cyclic voltammograms of initial β3-exNa$_{0.6}$ (········) β3-prec (– –), H$_K$-birn (-----) compared to mechanically ground mixture MG (········), Restack-1β (—), Restack-2 (-·-) and Restack-1γ (—) in a three cell configuration, with Ag/AgCl reference electrode, Pt counter electrode, in 0.5 M - K$_2$SO$_4$. (a) and (b) Scan rate 5 mV/s. (c) and (d) Scan rate 50 mV/s. All currents are normalized to the mass of active material.

The cyclic voltammograms are presented in Figure 5.8 and the variations of the corresponding specific capacitances are displayed in Figure 5.9. As a reminder, all four composite compounds have a Mn:Co ratio that is kept at 1:1. Restack-1β and Restack-1γ are restacked from colloidal suspensions of H_K-birn and β3-ex$Na_{0.6}$. Whereas Restack-2 and MG (composite obtained by mechanical mixing) are based on H_K-birn and β3-prec. All four samples are obtained from different restacking methods inducing a difference in morphology. Note that for comparison sake, the scale of the graphs is kept the same for each scan rate.

The voltammograms of restacked materials at 5 mV/s have been compared to the initial materials. In Figure 5.8.a and c, Restack-1β and Restack-1γ are compared to H_K-birn and β3-ex$Na_{0.6}$. At a scan rate of 5 mV/s, the voltammograms of both restacked samples exhibit more rectangular shapes than initial materials. However, there is a clear difference between Restack-1β and Restack-1γ, as Restack-1β presents a specific capacitance of 59 F/g, which is the same as H_K-birn. Since Restack-1β contains only 50% of birnessite, it can be concluded that the enhanced diffusion pathways allow a better use of birnessite pseudocapacitance. Furthermore, the specific capacitance of Restack-1β is twice the specific capacitance of Restack-1γ with 30 F/g. As morphologies are very similar, this could be linked to the low specific surface measured for Restack-1γ (in section 4.3.2.3). It is when the scan rate is increased to 50 mV/s that the beneficial effect of adding cobalt oxyhydroxide to the active material is the most obvious. Indeed, both restacked materials present a specific capacitance higher than initial materials, clearly linked to a lower internal resistance as detected by the more rectangular shape.

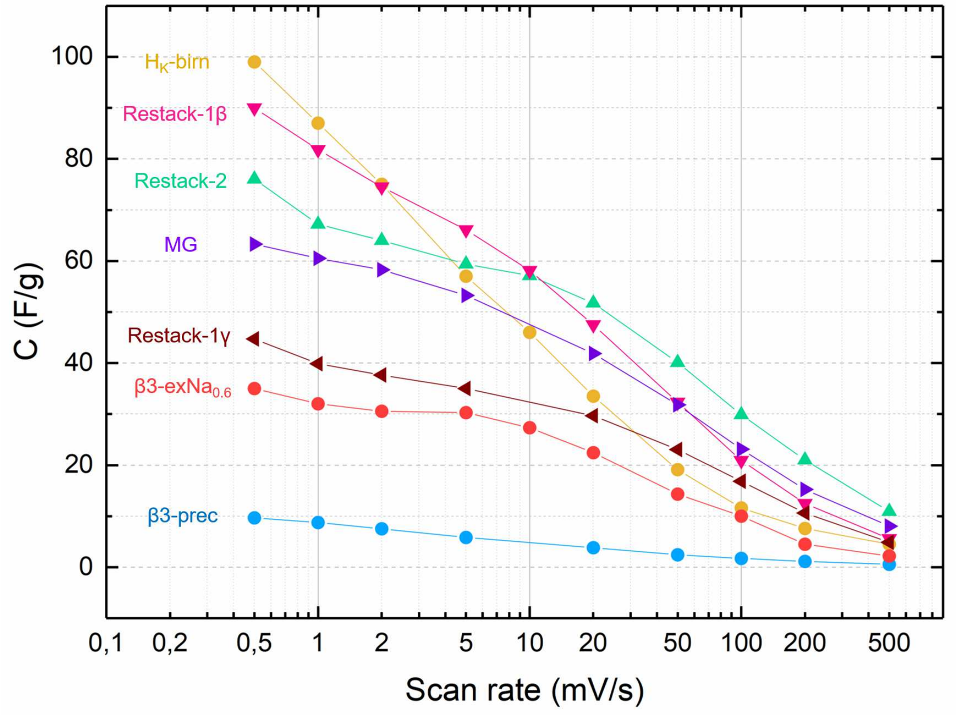

Figure 5.9.: Capacitance vs scan rate obtained for initial materials and corresponding exfoliated/restacked one. β3-ex$Na_{0.6}$ (—▲—), β3-prec (—●—), H_K-birn (—●—) compared to mechanical mix MG (—▶—), Restack-1β (—▼—), Restack-2 (—▲—) and Restack-1γ (—◀—). The capacitance is normalized to the mass of active material.

Concerning Figure 5.8.b and d, Restack-2 and the MG composite material obtained by mechanically mixing MG are compared to their initial materials H_K-birn and β3-prec. At a scan rate of 5 mV/s, both the restacked and mixed material have voltammograms with a more rectangular envelope than the initial materials. This strongly confirms the beneficial effect of conductive cobalt oxyhydroxide to the performance of the electrode independent of the mixing method employed. As the scan rate increases to 50 mV/s, the effect is emphasized, as the composite materials present specific capacitances that are twice those of the initial material. However, Restack-2 is more performant than MG. This is attributed to the microstructure of the composites. As shown in the EDS images (Figure 4.15 on page 122), the MG compound is a micro-composite in which the particles of Mn and Co are distinct. On the contrary, Restack-2 consists of a real nano-composite, showing an intimate mixture of Mn and Co oxyhydroxides.

All in all, at a scan rate of 50 mV/s, all the composite materials show better performance than initial materials. It is especially interesting to compare the voltammograms of Restack-1β and Restack-2. The materials were obtained by different restacking methods, but also with different nature of cobalt oxyhydroxides (Restack-1β is issued from β3-exNa$_{0.6}$ whereas Restack-2 from β3-prec). Although β3-exNa$_{0.6}$ presents a much better specific capacitance than β3-prec (see section 5.1.2), Restack-2 is more performant than Restack-1β, as its cyclic voltammogram is more rectangular, especially at higher scan rates. This may be due to the restacking method 2 that is used : both initial colloidal suspensions of Mn and Co are first adjusted to pH 4.5 and then mixed into one another. As the particles are already at the same pH, they tend to flocculate in a more homogeneous manner (see discussion in section 4.3.2.3 on page 121).

To sum up, restacking method 2 is the restacking method leading to the most performant material of this series (Restack-2). To deepen this study, it would have been interesting to compare Restack-2 to another restacked material, obtained by the same method 2, but from colloidal suspensions of H_K-birn and β3-exNa$_{0.6}$. This was tried many times, however, the composite materials obtained did not have the target Mn:Co molar ratio of 1:1. Again, this is due to the difficulty of evaluating the quantity of exfoliated layered objects present in the colloidal suspension.

5.2.2. Influence of Mn : Co ratio

When restacking Co oxyhydroxide with Mn oxides, electrochemical properties are strongly enhanced. Specific capacitances (normalized to the active material weight) reach higher values even if lower amount of pseudocapacitance birnessite is used. This means that the presence of CoOOH strongly boosts the pseudocapacitance of MnO_2. Optimization of such “synergistic” effect has to be done. Thus, a series of three restacked materials obtained by the same method (method 2 : two-pots-in-one strategy, both colloidal suspensions of Mn and Co are adjusted to pH 4.5 and then mixed together) are prepared as active electrode films for electrochemical characterization. The restacked materials are obtained by combining various ratios of the same initial materials : H_K-birn and β3-prec. The structural and morphological characterization of these materials are presented in chapter 4 (see section 4.3.2.4). The ratio of manganese oxide to cobalt oxyhydroxide is determined by chemical analysis. The three restacked materials are denoted as Restack-2-(Mn:2Co), Restack-2-(Mn:Co) and Restack-2-(3Mn:Co). The quantity in brackets indicate the Mn:Co ratio determined by ICP. The voltammograms obtained by the three restacked materials are shown in Figure 5.10.

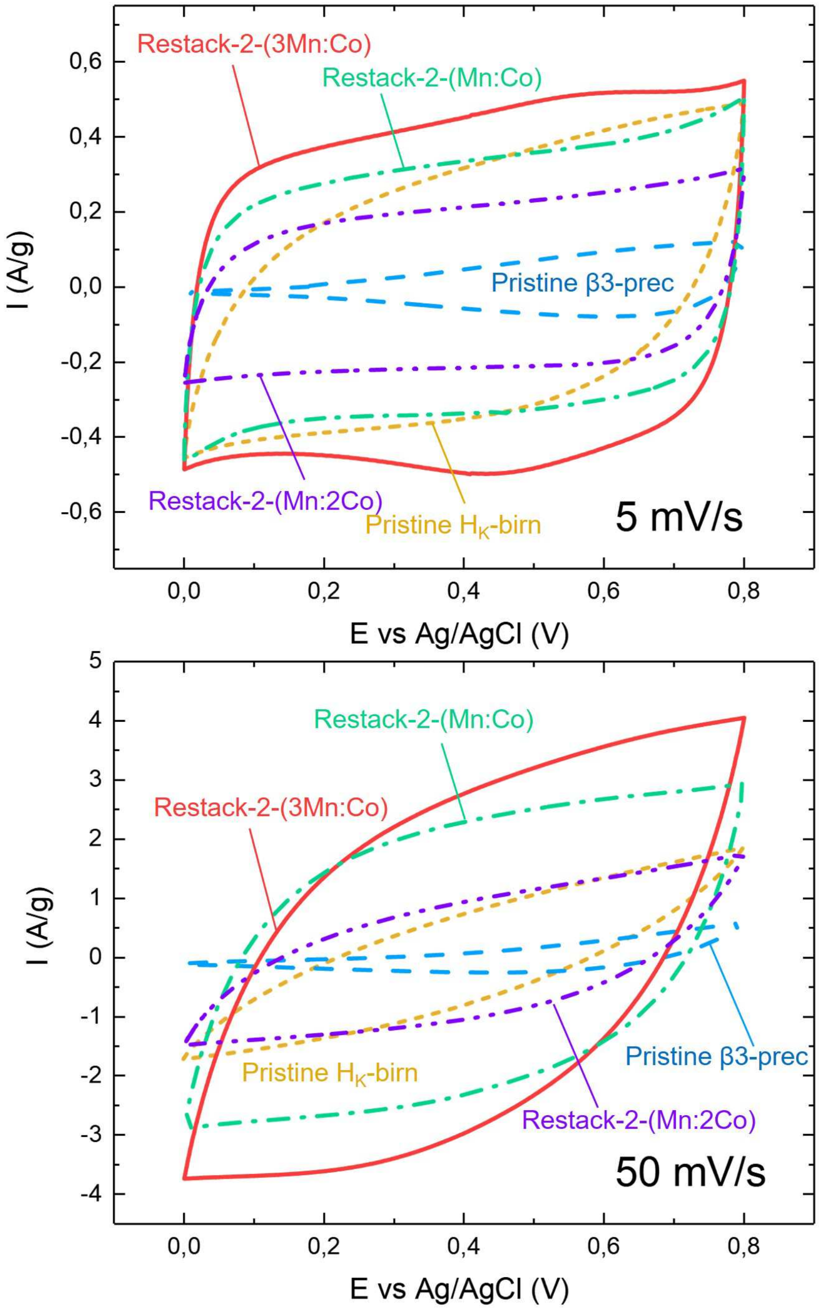

Figure 5.10.: Cyclic voltammograms of initial β3-prec (– –), H$_K$-birn (····) compared to Restack-2-(Mn:2Co) (–··–), Restack-2-(Mn:Co) (–·–) and Restack-2-(3Mn:Co) (—) in a three cell configuration, with Ag/AgCl reference electrode, Pt counter electrode, in 0.5 M - K_2SO_4. (a) Scan rate 5 mV/s. (b) Scan rate 50 mV/s. All currents are normalized to the mass of active material.

At a scan rate of 5 mV/s (Figure 5.10.a), the first observation is that whatever Mn : Co ratio, the voltammogram envelopes of the restacked materials are more rectangular shaped than the pristine materials. The initial slope of the curves at charging and discharging are more vertical for the restacked materials (in comparison, the voltammogram of pristine H_K-birn is more tilted), which means that the restacked materials have a lower internal resistivity. The specific capacitances calculated for each scan rate are displayed in Figure 5.11.

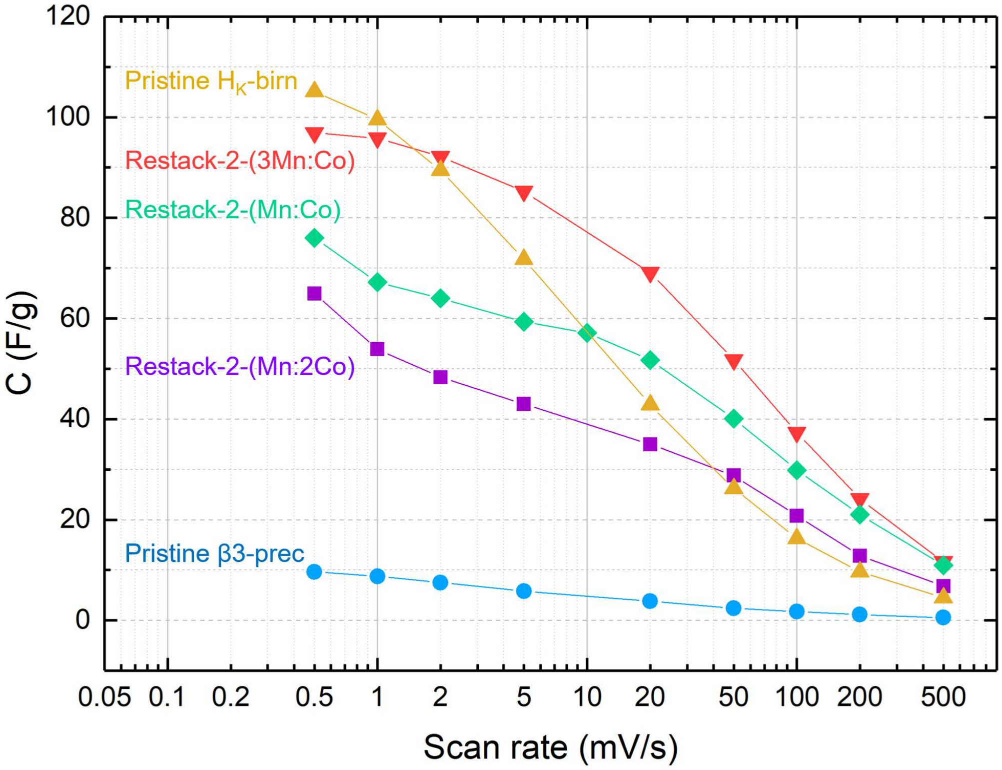

Figure 5.11.: Capacitance vs scan rate obtained for initial materials and corresponding exfoliated/restacked one. The capacitance is normalized to the mass of active material.

Restack-2-(Mn:2Co) has the lowest content of Mn, and its voltammogram is clearly more rectangular than that of pristine H_K-birn. However, the area below the curve (which is directly linked to the specific capacitance of the electrode) is smaller, meaning that although the electronic conductivity of the electrode was enhanced, the specific capacitance is not. This is because Mn is replaced by Co, so that mean pseudocapacitive contribution is decreased.

As the amount of Mn is increased, in Restack-2-(Mn:Co), the specific capacitance calculated at a scan rate of 5 mV/s is the same as initial pristine H_K-birn. However, at a scan rate of 50 mV/s, the specific capacitance is slightly higher. This means that the addition of Co oxyhydroxide in the electrode material has a clear positive effect on the power density of the electrode.

Concerning Restack-2-(3Mn:Co) that has the highest content of Mn, even at a scan rate of 5 mV/s, the voltammogram shows a much better electrochemical response. Indeed, the specific capacitance is significantly increased. This is even more obvious when comparing specific capacitances measured at 50 mV/s, as the restacked material shows a capacitance that is nearly three times higher than that of pristine material H_K-birn. Note that this is achieved with a reduced amount of Mn in the active electrode material. This emphasizes the beneficial effect of Co addition to the active material.

5.2.3. Importance of Co oxyhydroxide addition

In the previous section, it has been proved that adding cobalt oxyhydroxide, as an active material, to manganese oxide, can efficiently enhance the electrochemical performances for scan rates higher than 1 mV/s. Cobalt oxyhydroxides act as an electronic conductivity enhancer, as the cyclic voltammograms of the composite material are more rectangular than those of the initial materials.

However, as stipulated in the beginning of the chapter, it is necessary to add carbon black during the electrode making process to ensure a good percolation of particles. Therefore, it is natural to question if adding more carbon black instead of cobalt oxyhydroxide would lead to the sames performances. In other terms, does cobalt oxyhydroxide produce an added value as compared with carbon black ?

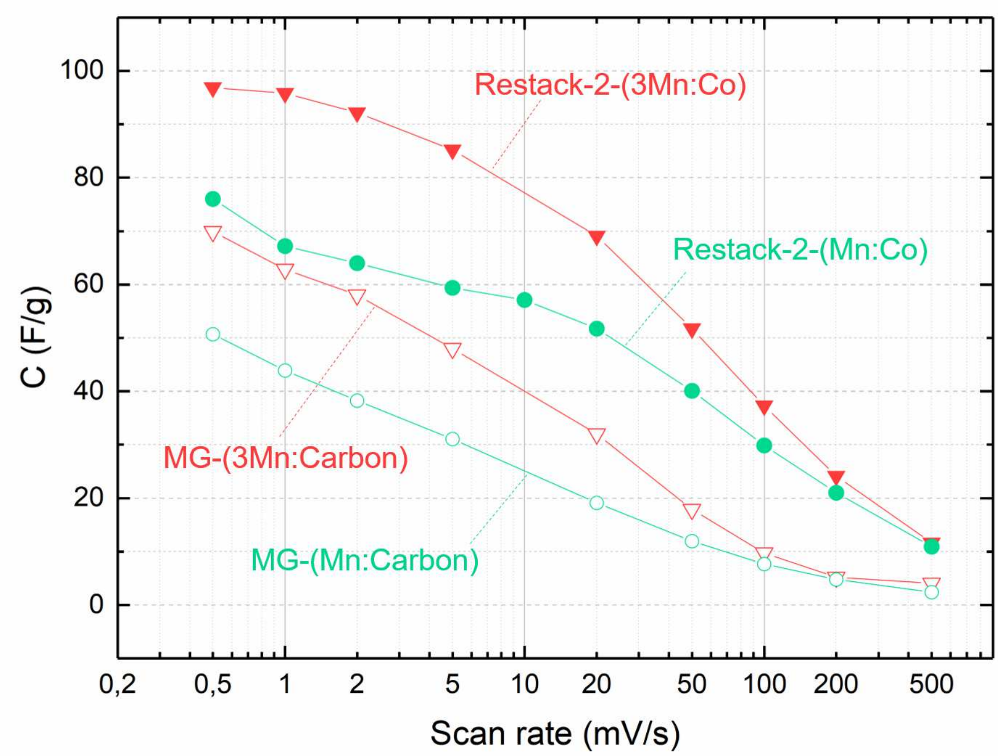

Figure 5.12.: Capacitance vs scan rate obtained for restacked materials and equivalent ones with carbon black instead of cobalt oxyhydroxides. Restack-2-(Mn:Co) —●—, MG-(Mn:Carbon) —○—, Restack-2-(3Mn:Co) —▼—, MG-(3Mn:Carbon) —▽—. The capacitance is normalized to the mass of active material.

To study this, the two most performant restacked materials, Restack-2-(Mn:Co) and Restack-2-(3Mn:Co) (pressed into electrode films containing 80% active material, 15% carbon black and 5% PTFE) are compared to electrodes containing manganese oxide and only carbon black, keeping the same percentage of Mn in the active material. These electrodes are obtained by mechanically grinding Mn oxide and carbon black. They are denoted as MG-(Mn:Carbon) and MG-(3Mn:Carbon).

The specific capacitances obtained are shown in Figure 5.12 on the facing page. At all scan rates, the mixed materials with carbon show a much lower capacitance than the restacked materials, thus emphasizing the importance of adding cobalt oxyhydroxide to the active material.

However, as seen in section 5.1.2 on page 148, initial cobalt oxyhydroxide β3-prec does not provide sufficient electroactivity to ensure such a capacitance enhancement. This leads to the conclusion that the restacked materials show a synergistic effect between initial materials, which justifies the exfoliation/restacking strategy to synthesize novel composite materials.

5.2.4. Cyclability enhancement

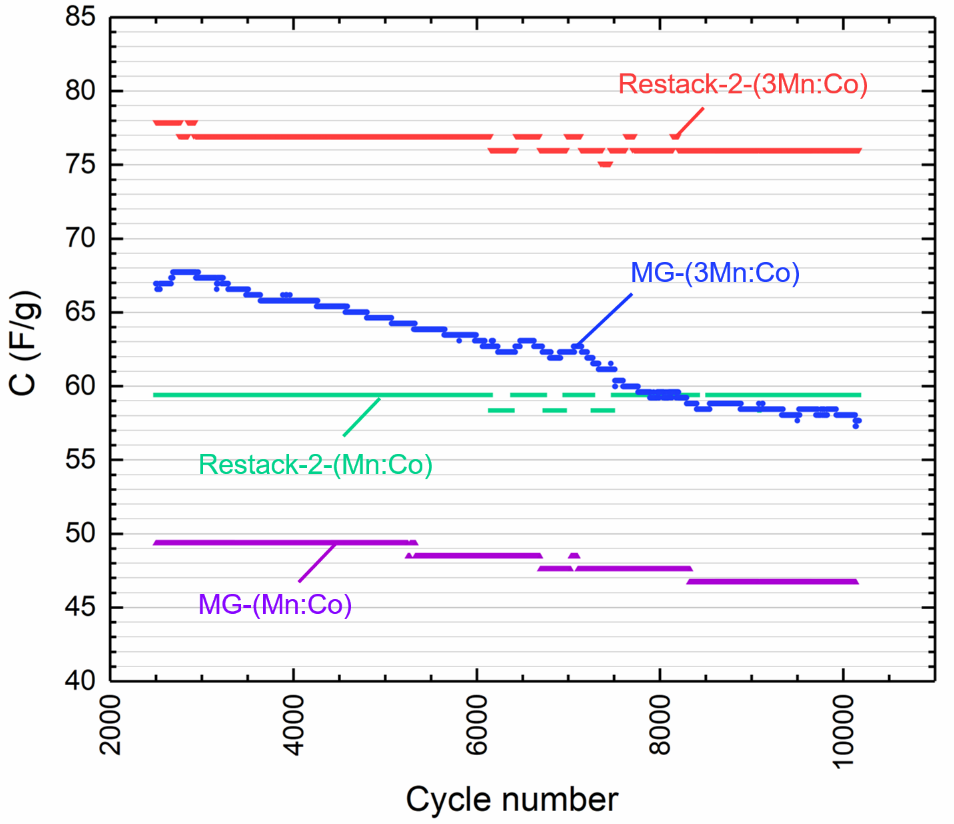

Figure 5.13.: Specific capacitance values vs scan rate obtained for restacked materials Restack-2-(Mn:Co) (green), Restack-2-(3Mn:Co) (red) and mechanically mixed composite MG-(Mn:Co) (purple) and MG-(3Mn:Co) (blue). Cycling is performed in a three-cell electrode at 10 mV/s. The capacitance is normalized to the mass of active material.

In the context of an application in supercapacitors, the cyclability of the electrodes is very important. The two best restacked materials have been chosen to be cycled up to 13 000 cycles. In addition, Restack-2-(Mn:Co) and Restack-2-(3Mn:Co) respectively, are compared to mechanically ground composites, denoted as MG-(Mn:Co) and MG-(3Mn:Co), which are obtained by mixing H_K-birn with β3-prec with the 1Mn:1Co and 3Mn:Co ratio respectively. The cycling was performed by cyclic voltammetry at a scan rate of 10 mV/s. The specific capacitances obtained are shown in Figure 5.13.

The first observation is that the restacked materials both show higher specific capacitances than the simply mixed ones, even at the very beginning of the cycling. Their capacitance is constant, up until 13 000 cycles. On the other hand, both MG-(Mn:Co) and MG-(3Mn:Co) show a non-negligible decrease of capacitance after 3000 cycles. The bad cyclability of the simply mixed composites is probably due to a progressive loss of cohesion between the manganese oxide and carbon particles during cycling, leading to higher inter-granular resistances, whereas the interfaces between the manganese and cobalt particles might be more robust in the restacked samples.

5.2.5. Conclusion

To assess the electrochemical properties of composite materials obtained by exfoliation/restacking, a first optimization study of the electrode has been carried out, especially concerning the optimal quantity of carbon black as an electronic conductivity additive. By cyclic voltammetry, it has been shown that adding 15% of carbon black is enough to percolate the active material particles.

Then, the impact of exfoliation on pristine materials has been evaluated. The electrochemical performances of exfoliated/restacked mono-element metal oxides (Mn or Co) have been compared to the performances of pristine materials. The specific capacitances obtained after exfoliation/restacking are higher, thus validating our strategy. However, the correlation between specific capacitance and the specific surface areas (BET measurement) of the previous chapter appears to be questionable : indeed there is no direct correlation between high specific area and high specific capacitance for this type of materials. This could be linked to a solvation effect.

Third, the composite Mn-Co materials obtained by exfoliation/restacking have been tested as electrode materials. A first study was conducted concerning the influence of restacking method on the performance of the material. Because it is more homogeneous, the composite material obtained by the two-pots-in-one strategy was found to be the most interesting, suggesting the important role of a more intimate mix of initial phases at the nanometric scale in this case.

A second study on the influence of Mn:Co ratio showed that the sole addition of 25% of Co can significantly enhance the specific capacitance. Furthermore, the general behavior of electrodes at high scan rates is drastically improved by the presence of cobalt. The two best restacked materials obtained were compared to materials with equivalent amount of manganese oxide but with only carbon black as additive. The restacked samples present much better performances, suggesting that there has been a synergistic effect between cobalt oxyhydroxides and manganese oxides thanks to the restacking process.

Finally, the cyclic behavior, i.e. the stability of the supercapacitors over a large number of charge–discharge cycles, is one of the most attractive aspects of the supercapacitors over rechargeable batteries. After 10 000 cycles, the restacked materials retain a high specific capacitance, indicating their excellent cycling stability. On the contrary, the composite materials obtained with equivalent Mn:Co ratio by mechanical grinding show a net decrease of specific capacitance. These overall results validate our strategy of exfoliation/restacking. The next section is devoted to the study of the feasibility of a full hybrid cell.

5.3. Hybrid assembly : study of a full supercapacitor cell

The chosen restacked materials have been assembled in a full cell in order to form an asymmetric supercapacitor. Beforehand, it is necessary to know exactly the electrochemical properties of each material (specific capacitance and stability window) in the studied electrolyte (0.5 M - K_2SO_4). The restacked materials studied in the previous section have already been characterized and Restack-2-(Mn:Co) has been chosen for being assembled in a full cell (at the positive electrode) together with activated carbon (at the negative electrode). In this section, a first part deals with the electrochemical performance of activated carbon in K_2SO_4. Then the two electrodes will be balanced to achieve a charge balance and extend the potential window to the maximum. Different weight ratios between the positive and negative electrodes will be introduced and studied.

5.3.1. Why assemble a hybrid device ?

Hybrid devices are composed of different positive and negative electrode materials and consist in the combination of electrodes with different storage mechanisms, typically, a capacitive double-layer (EDLC) electrode and a battery-type faradaic or pseudocapacitive electrode. By doing so, the overall cell potential can be increased, resulting in higher energy and power densities.

The amount of energy that a supercapacitor can store strongly depends on its maximum voltage ($\propto U^2$). This is determined by the maximum voltage that the electrolyte can hold before decomposition. A supercapacitor using an aqueous electrolyte is limited by the electrochemical stability of water (theoretical value of 1.23 V). An obvious way to improve the energy density of an aqueous supercapacitor would be to increase its operating voltage range. However, not all aqueous electrochemical devices are limited by the operating voltage of 1.23 V and many of them have a maximum voltage exceeding this. Indeed, it is possible to modulate it by electrode over-potentials due to gas evolution (oxygen or hydrogen), which can shift the potential at which the water electrolysis is supposed to happen.

By combining two electrodes based on active materials with different electrochemical activity range, the working voltage of the device can be extended. In recent years, most asymmetric supercapacitors developed have used pseudocapacitive materials as positive electrode and double layer capacitive materials at the negative electrode. By doing so, the potential range of the positive electrode is extended to the whole potential window of activated carbon. Additionally, since pseudocapacitive electrodes accumulate charge through fast faradaic electrochemical process, this can also increase the specific capacitance of the capacitor. In total, it can be expected that the asymmetric supercapacitor benefits from the nature of the two electrodes by combining their advantages : high capacitance (pseudocapacitive electrode), high power and excellent cyclability (EDLC electrode).

5.3.2. Negative electrode : activated carbon (AC)

5.3.2.1. Description of the material

The main objective of this study being the behavior of restacked materials, the activated carbon AC has not been optimized as a negative electrode material. This work has focused on one material : YP80F, denoted as AC, supplied by Kuraray (Japan). It was obtained from ground coconut shells that were pyrolyzed : low volume pores are obtained, in order to increase the specific surface area. The product obtained is activated carbon. According to the industrial specifications, it presents a large surface area (2000 m^2/g) and a pore volume of 0.7 cm^3/g.

5.3.2.2. Electrochemical properties

To characterize the electrochemical properties of YP80F, it was shaped into an electrode according to the same procedure as oxides, but without adding any carbon black. A symmetric three-cell configuration is used, with Ag/AgCl as a reference electrode. The potential window is studied by cyclic voltammetry. Since it is a symmetrical configuration, the intensity is normalized to the mean mass of the electrodes. Figure 5.14 shows the curves of the cycles between E_{max}, fixed at 0.5 V and E_{min}, varying between -0.2 to -1.6 V. It can be seen that between -1.4 and 0.5 V, the voltammogram of the activated carbon is quite rectangular, as a decrease of E_{min}leads to the reduction of the electrolyte.

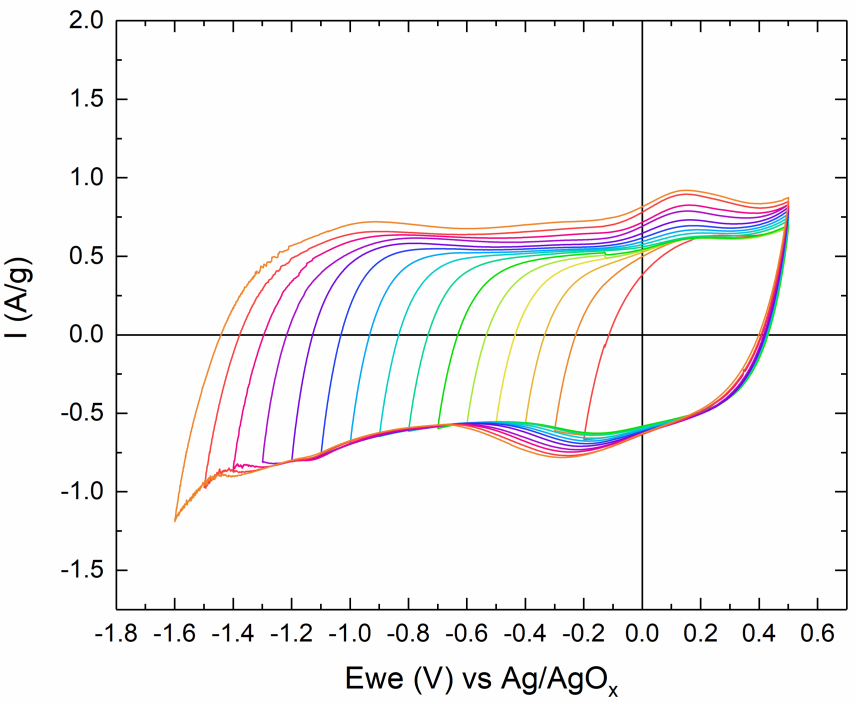

Figure 5.14.: Cyclic voltammetry of YP80F material in a three electrode symmetric cell at 5 mV/s in K_2SO_4 0.5M cycled between E_{max}=0.5 V and E_{min}= -0.2 to -1.6 V. The current is normalized to the mean of mass of active material.

An anodic peak (0.05 V) and a cathodic peak (-0.3 V) can be observed, which means that there are some faradaic reactions in addition to the double layer capacitance. This is most probably due to functional groups that were added to the activated carbon during the activation process.

As E_{min} is decreased, a cathodic peak due to the release of hydrogen (reduction of electrolyte) is observed. This is why the optimal potential window of -1.4 to 0.5 V can be defined, where the electrolysis of water is negligible. In this window, the anodic capacity can be calculated (125 F/g on 1.9 V or 65 mAh/g).

5.3.3. Balancing the electrodes

5.3.3.1. Principle

In the previous sections, it has been established that Restack-2-(Mn:Co) presents a specific capacitance of 60 F/g between 0 V and 0.8 V (14 mAh/g), whereas the activated carbon has a specific capacitance of 125 F/g between -1.4 and 0.5 V (65 mAh/g). These two capacitances have both been determined by cyclic voltammetry at 5 mV/s. The voltammograms are shown in Figure 5.15.

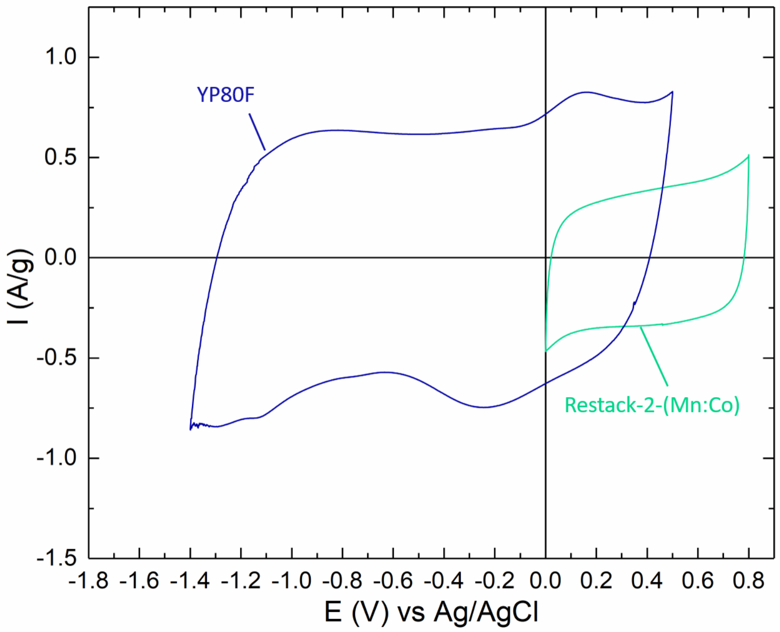

Figure 5.15.: Cyclic voltammetry at 5 mV/s in a three electrode cell in K_2SO_4 for Activated carbon YP80F (blue, symmetric assembly) and Restack-2-(Mn:Co) (green, Pt wire, Ag/AgCl counter-electrode). The current is normalized to each mass of active material.

The intensity is normalized to the mass of each electrode. The voltage window of activated carbon ranges from -1.4 to 0.5 V. For the Restack-2-(Mn:Co) sample, it ranges from 0 to 0.8 V. This means that the assembly of both could cycle over a potential range from -1.4 to 0.8 V, which would enhance the activity window and therefore the energy density achievable by a symmetric configuration. However, the cyclic voltammograms overlap, which means that each electrode will vary differently according to the potential.

Balancing an asymmetric supercapacitor consists in adjusting the masses of the positive and negative electrodes, so that the final discharge capacitance is maximal. Since the total capacitance of a supercapacitor is imposed by the electrode with lowest capacitance, the most optimized configuration is supposed to be when both electrodes possess the same capacitance, i.e. the same loading. This is true for symmetric cells, but not for hybrid configurations, as the nature of charge storage of each electrode is different.

If q_+ and q_- are the quantity of charge on each electrode (mAh) and Q_+ and Q_- their capacity (mAh/g), with m_+ and m_- their respective masses (of active material) (g), the following equations 5.1 and 5.2 link them :

$$q_+ = Q_+ \times m_+ \tag{5.1}$$

$$q_- = Q_- \times m_- \tag{5.2}$$

For balanced electrodes :

$$q_+ = q_- \tag{5.3}$$

The ratio R is defined by the following equation 5.4 :

$$R = \frac{m_+}{m_-} = \frac{Q_- \times q_+}{Q_+ \times q_-} \tag{5.4}$$

For the asymmetric supercapacitor AC/Restack-2-(Mn:Co), the theoretical R value for balanced electrodes is 4.64. In the following section, a few ratios will be considered for different devices. All the measurements are conducted in a three-electrode swagelok cell. The positive electrode is based on Restack-2-(Mn:Co), the negative electrode on AC and an Ag/AgCl reference electrode is used. When a potential is applied, it corresponds to the voltage between the positive and negative electrodes.

5.3.3.2. Description of the electrochemical system

Figure 5.16 illustrates the operation of a device. The charge is characterized by the oxidation of the active material (Restack-2-(Mn:Co)) in the positive electrode and by the adsorption of hydrogen in the micropores of the activated carbon at the negative electrode. The discharge corresponds to the opposite reactions : the reduction of the material at the positive electrode and the desorption of hydrogen at negative electrode. In these experimental curves, the intensities are normalized according to the mass of each electrode.

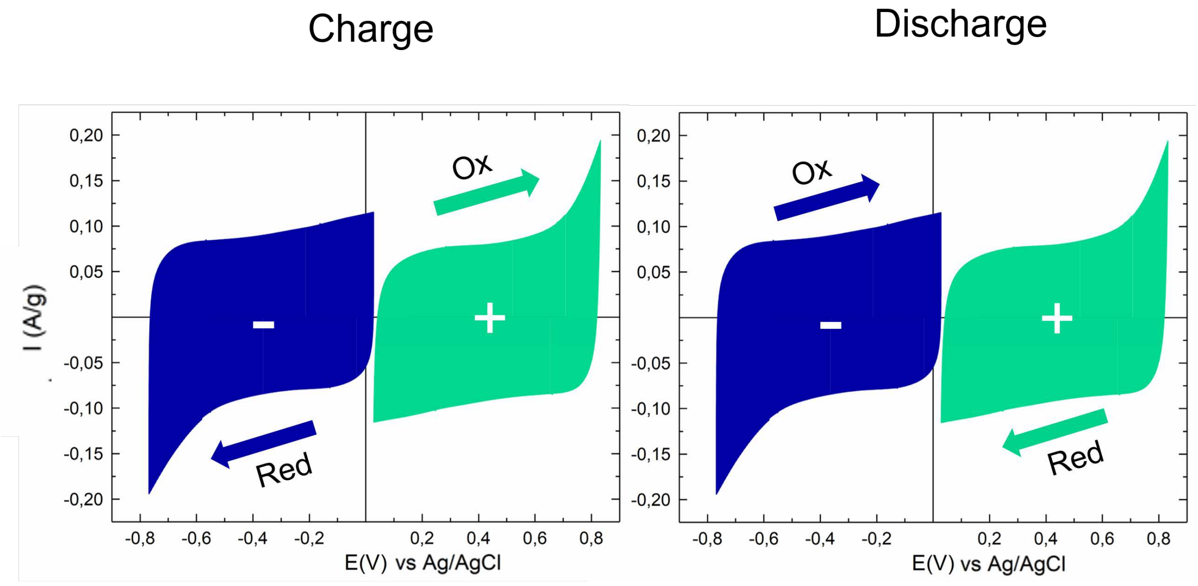

Figure 5.16.: Cyclic voltammogram of positive and negative electrode in an asymmetric supercapacitor AC/Restack-2-(Mn:Co), obtained by cyclic voltammetry in a swagelok cell (three electrode configuration) in 0.5 M - K_2SO_4 (R=1.8) between 0 and 1.6V. The intensities are reported according to the mass of each electrode.

5.3.3.3. Test of different ratios

In all the characterizations, the mass of the positive electrode is kept the same and the AC electrodes have been modified. In a classic three-electrode cell, the potential of the working electrode is well controlled. When the full device is studied, the potential of each electrode can vary independently. This is why the optimal mass ratio for a maximum energy density can differ from the one calculated above (R=4.64). Indeed, Demarconnay et al. have shown that an asymmetric AC/MnO_2 supercapacitor shows better performances when MnO_2 is over-capacitive, with an optimal ratio of 2.5 instead of a calculated ideal ratio of 2 [242]. In this case, since the Restack-2-(Mn:Co) material has a non-negligible contribution and that the electrodes have an overlapping voltage window, the optimal R could be very different from the calculated one. The intensities are normalized with the total mass of the electrodes.

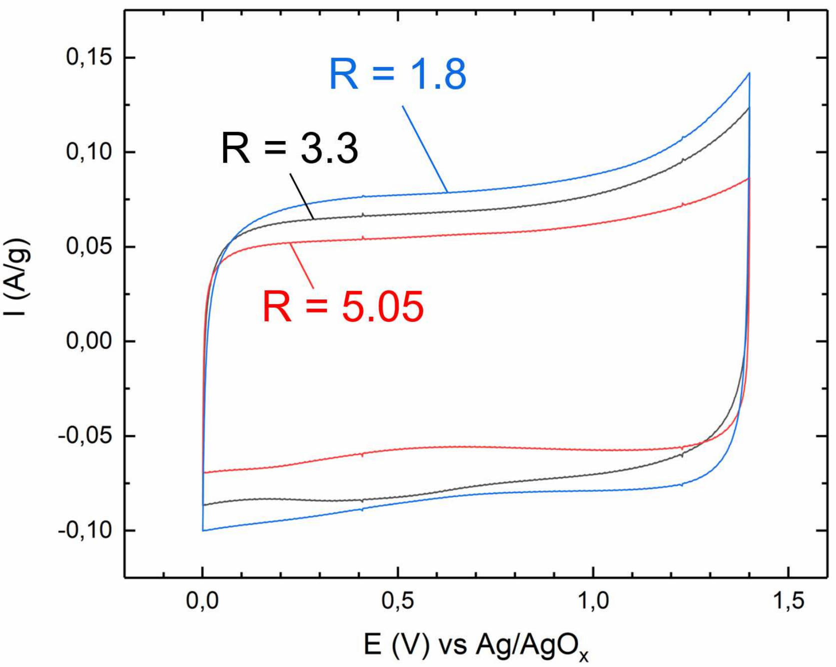

Figure 5.17.: Comparison of cyclic voltammograms obtained for various mass ratios R between positive and negative electrode. Measurements are conducted in swagelok three-cell configuration in 0.5M - K_2SO_4 at 5 mV/s between E_{min}= 0 V and E_{max}= 1.4 V. The current is normalized to the total mass of active material.

Due to difficulties in controlling the thickness of the electrode, no full device with R=4.64 was assembled. However, three different ratios have been tested : R=1.8, R=3.3 and R=5.05, which covers the two possible configurations : excess of AC or excess of Restack-2-(Mn:Co). Figure 5.17 shows the voltammograms for the three ratios in a voltage window of 0 to 1.4 V. In all three cases, the shapes of the cyclic voltammograms are rectangular, which is representative of a supercapacitive behavior. It is directly obvious that the best capacitance is obtained for a ratio of R=1.8, which underlines the importance of the AC electrode, as when the amount of AC is increased, the capacitance obtained is increased. However, this value is very low compared to the calculated R value corresponding to charge balance. This can be explained by the fact that the expected charge of the AC electrodes is exchanged in a voltage window of 1.9 V, whereas, in the present case, it only works in a maximum of a 1 V voltage window.

5.3.3.4. Defining the potential window

Figure 5.18 shows the voltammetry curves for two hybrid supercapacitors in a three-electrode configuration with different ratios : R=1.8 and R=5.05. As the voltage window is enlarged, it is possible to observe the reactions of water oxidation at the positive electrodes. In this case, the intensities are normalized to the total mass of the electrodes.

Thanks to the three-electrode configuration, it is possible to follow the potential of each electrode, as shown in Figure 5.19 for R=1.8. From the curves, it is possible to conclude that the contributions of positive and negative electrodes are equivalent. It is possible

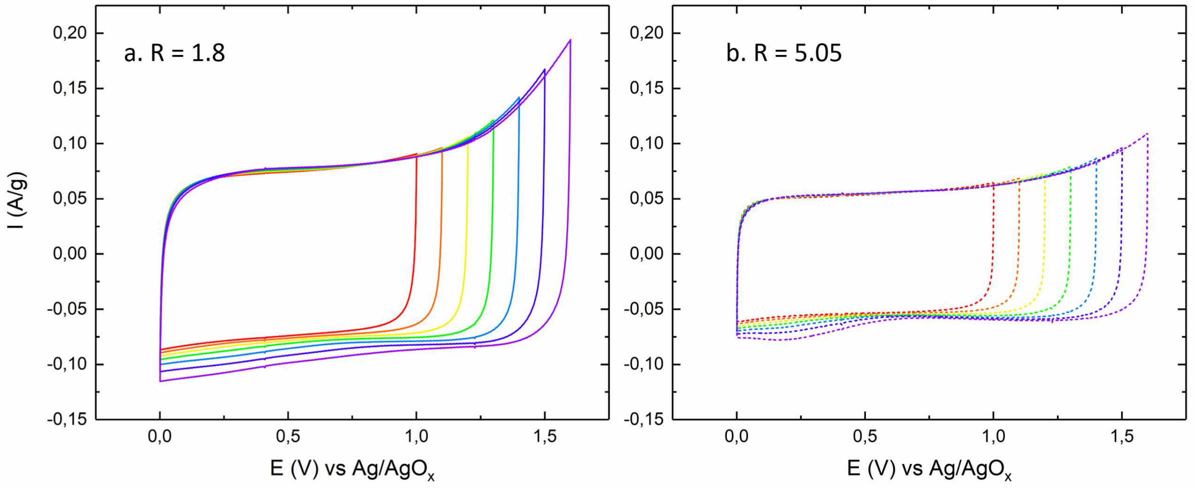

Figure 5.18.: Window potential of an asymmetric AC/Restack-2 in a swagelok three-cell configuration in K_2SO_4 0.5M at 5 mV/s between E_{min}=0 V to E_{max} from 1 to 1.6 V. (a) R=1.8 (b) R=5.05. All currents are normalized to the total mass of electrodes.

to identify the limits of the electrolyte : at 0.8 V an anodic peak corresponding to O_2 release can be observed. Note that the AC electrode cycles within the potential window of 0.1 - 0.8 V (0.9 V), which is a much narrower range than in symmetrical cell (1.9 V). This will most probably lead to a lower energy than expected.

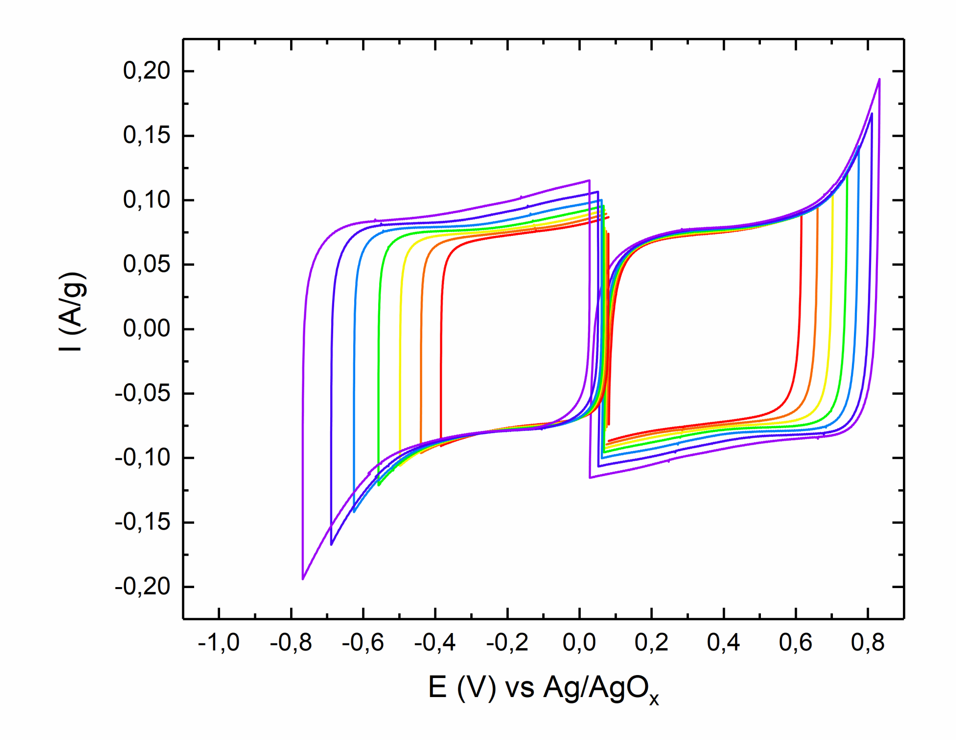

Figure 5.19.: Cyclic voltammogram of positive and negative electrode in an asymmetric supercapacitor AC/Restack-2-(Mn:Co), R=1.8, obtained by cyclic voltammetry in a swagelok cell (three electrode configuration) in K_2SO_4 0.5M (device 3) between 1 V and 1.6 V. The intensities are reported according to the total mass.

The coulombic efficiency shown in Figure 5.20 is higher to 99% and drops to 98% as the voltage window is expanded to 1.6 V. This is due to the contribution of the electrolyte oxidation while cycling. To take this into account, the optimal window potential for best performance will be limited to V_{max} = 1.4 V. (V_{max} is defined as the maximum voltage window).

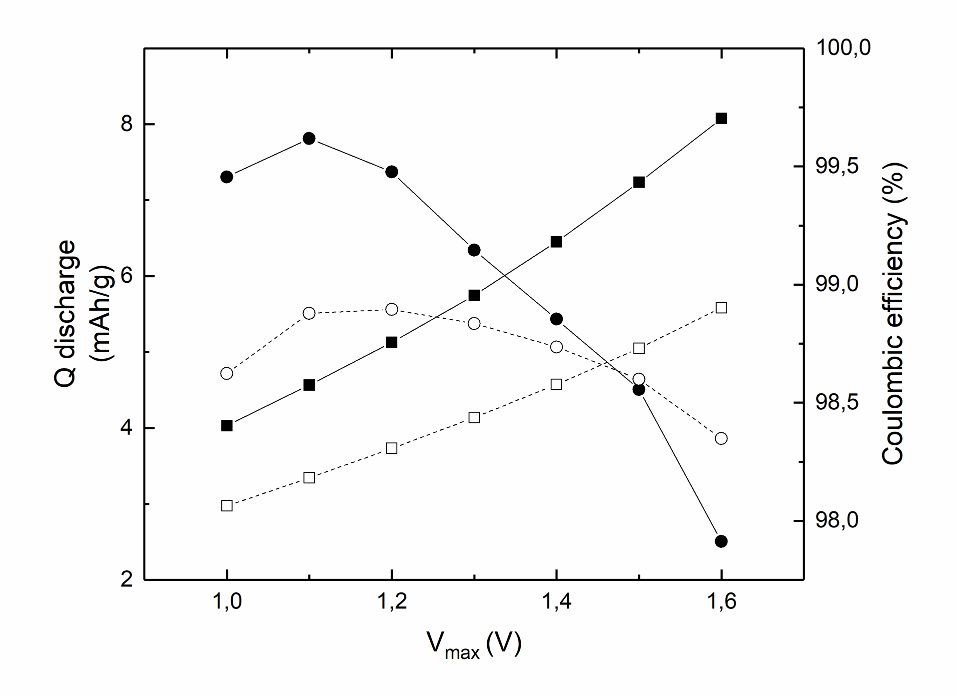

Figure 5.20.: Discharge capacity normalized to the total mass of electrodes : (●) for R=1.8, (○) for R=5.05. Coulombic efficiency : (■) for R=1.8, (□) R=5.05.

5.3.4. Conclusion

Following the electrochemical performance of restacked materials, Restack-2 was chosen to be assembled in a full cell to evaluate its properties. First, activated carbon YP80F was studied as material for the negative electrode. This step is fundamental to balance the electrodes to be assembled in a full cell. In theory, the balanced mass ratio between positive and negative electrode was evaluated to be 4.64. Following this, the voltage window in which the cell is stable was fixed between 0 - 1.4 V.

Then, three different cells with three different weight ratios have been tested. Surprisingly, the cyclic voltammetry showed that the best performance was recorded for R = 1.8, which underlines the importance of AC electrode. Indeed, as the mass of carbon electrode is increased, the specific capacitance of the full cell is enhanced.

This study proved the feasibility of a full cell composed of our restacked material as positive electrode and activated carbon as negative electrode. To further complete this study, more measurements at different scan rates can be conducted. This way, it is possible to calculate power density and energy density in order to compare the cell to other commercial ones on a Ragone plot.

Although not complete, this study paves the way for further investigation of restacked materials. A performance enhancement is observed, mainly due to the addition of cobalt oxyhydroxide. The understanding of charge storage mechanism in restacked materials is the next step to further improve their performance. Indeed, as observed by BDS (seen in section A.3.2), the addition of cobalt oxyhydroxides by exfoliation/restacking process might add too many interfaces and not increase the conductivity nor capacitance as much as expected. Controlling the size of Co and Mn grains in restacked materials is vital for the next studies.

Conclusion

The objective of this work was to design novel transition-oxide materials for supercapacitor electrodes and devices. The strategy envisaged consisted in a rational design of mixed 2D layered materials with enhanced performances.

Starting from the 2D layered birnessite, which presents excellent pseudocapacitive properties, but low conductivity, we tried to address this issue with the help of cobalt oxyhydroxide, known for its high electronic conductivity. In order to preserve the properties of each initial material while creating a synergistic effect, an original synthesis strategy was proposed. First, the synthesis involved delamination of “building blocks” which were restacked in order to obtain a novel composite material. After structural and morphological characterizations of composite materials, their conduction and electrochemical performances were evaluated to determine if a synergistic effect between Mn oxides and Co oxyhydroxides was achieved.

After having synthesized the initial layered Mn and Co oxides, an intercalation/exfoliation reaction was carried out to obtain them as “building blocks”. The exfoliation process of layered manganese oxides has already been extensively reported, however, the obtention of cobalt oxyhydroxide “building blocks” was less trivial. Nonetheless, after laborious optimization of experimental conditions, stable colloidal suspensions of Mn and Co oxides were successfully recovered. Because the exfoliation process was complex, time-consuming and tedious, and although the colloidal suspensions were stable, the objects obtained were very polydisperse. It was then necessary to conduct a thorough size-selection process, in order to isolate mono-layered nanosheets. The efficiency of the exfoliation and size-selection process was proven by microscopy characterizations, as mono-layered objects were successfully obtained. Complete exfoliation was scarce, as the quantity of mono-layered objects produced is very low, and a majority of oligolayers were obtained. Nevertheless, for the intended applications oligo-layered nanosheets could be even more interesting as the pseudocapacitance of manganese oxides relies on ion mobility in the interlayer space.

As the "building blocks" created are extremely thin, their surface chemistry and reactivity could be strongly modified, thus affecting the restacking process. The main focus of this work was to rationalize the restacking process by using the MUSIC model to predict the surface charge of the particles. We particularly focused on two points: (i) influence of the basal surface area percentage ; (ii) effect of the nature and oxidation state of the metal ions. Comparison with experimental values allowed to validate the use of MUSIC model and enabled a better understanding of the exfoliated materials. This greatly facilitated the restacking process as optimal conditions were defined. Mn oxide particles present a low IEP of 3, whereas Co oxyhydroxide particles have a higher IEP of 7. Therefore, an optimal pH of 4.5 could be determined for a well controlled restacking, where Mn and Co (oxyhydr)oxide particles are oppositely charged.

From this, multiple restacking techniques were conducted, and in all cases, the obtained mixed compounds were identified as Mn-Co composites. The morphologies of restacked materials were compared to mixed materials obtained by mechanical grinding, and have proven the efficiency of exfoliation/restacking process. On one hand, mechanical grinding led to micro-composites as a clear distinction could be observed between Mn and Co aggregates. On the other hand, a nano-composite showing an intimate mixture at the nanometric scale of Mn and Co particles was achieved through the exfoliation/restacking process. Furthermore, by varying the initial pH and restacking strategies, more homogeneous restacked composites could be obtained.

A focus was made on the electronic conductivity of restacked materials as a conductivity enhancement was observed compared to pristine manganese oxides. This could directly be linked to the intermediate protonated birnessites that already showed higher conductivity than their precursors. However, no synergistic effect linked to the addition of Co oxyhydroxide was observed. To understand this, further investigation was conducted by Broadband Dielectric Spectroscopy, which provided detailed information on the different contributions of the charge transport occurring at different scales. Results showed that even if the exfoliation/restacking process has enabled an intimate mixture of Co and Mn particles, thus increasing the number of interfaces between Co particles and Mn particles, the electronic pathways were not percolated in the global sample. Our hypothesis is that the intimate restacking gives rise to an electron-trapping phenomenon at the particle interfaces thus hindering the beneficial effect of Co oxyhydroxide addition.

Finally, the electrochemical performances of the restacked materials were evaluated. Composite restacked materials have been pressed into active material films and assessed as electrode material. A clear impact of restacking method has been observed, greatly influencing the morphology of restacked materials and therefore their electrochemical activity. In all cases, the cyclic voltammograms of restacked materials are more rectangular than initial pristine materials, thus showing that the internal resistances of electrodes based on restacked materials are lower. Also, a clear enhancement of specific capacitance was observed for restacked materials, especially at higher scan rates. This proves the beneficial effect of Co oxyhydroxide addition for high power densities.

Furthermore, adding Co oxyhydroxide to Mn oxide has proven to be effective in performance enhancement. Indeed, the restacked materials have been compared to electrodes made with the equivalent amount of Mn oxide, but replacing Co additive by classic carbon additive. The results show that at all scan rates, restacked materials show higher specific capacitance, thus proving a synergistic effect between Mn oxides and Co oxyhydroxides.

Moreover, the composite materials obtained by exfoliation/restacking show much higher cyclability stability than mechanically mixed materials, as stability over 10 000 cycles was observed. This is enabled thanks to intimate and robust mixture of “building blocks” achieved by exfoliation/restacking.

To complete the study, a hybrid supercapacitor composed of the best restacked material at positive electrode with an activated carbon at the negative electrode was assembled in order to increase the energy density and power density. This allowed the access to a larger voltage window (1.4 V aqueous electrolyte) which in turn, increases the energy density. After having chosen the most appropriate material, full cells with different weight ratios were assembled. The promising results showed the good feasibility of these systems, even if further optimization is required.

This entire study paves the way to further investigation on the exfoliation-restacking process. Indeed, after having achieved intimate mixing with nanoparticles, the increase in number of interfaces has proven to limit the electronic conductivity enhancement. This might be linked to the limited size of Co oxyhydroxides. It would be interesting to continue the study by modulating the size of Mn and Co particles through exfoliation and compare the conductivity enhancement of restacked materials.

Furthermore, to complete the understanding of electrochemical performances, it would be interesting to establish a link between restacking technique, morphology and charge storage mechanism. Indeed, these complex composite materials are difficult to comprehend, as various phenomena could be occurring (double layer, pseudocapacitance, faradaic...). In situ XRD and XANES studies are planned, so as to de-correlate and investigate the role of each material.

A logical continuation of the study is to pursue the exfoliation/restacking process with other types of layered objects. For example, exfoliated layered double hydroxides bearing a positive charge could facilitate the restacking with negatively charged nanolayers of Mn oxides. The nature of LDH is highly adjustable, and cobalt-nickel mixed LDH could be a good candidate for exfoliation/restacking. This approach is currently carried out through the PhD work of by Alberto Adan Mas at ICMCB.

Another material interesting to insert to those studies would be reduced graphene oxide. This kind of material would fit the philosophy of this work for their high electronic conductivity and easy exfoliation. However, synthesis challenges are expected for such a restacking and another restacking strategy has to be found. Indeed, RGO tends to flocculate very easily in aqueous media, so that restacking in organic solvents would be a solution. This would however totally change the restacking reasoning based on surface charge behind this work.

A. Annexes

A.1. Structural characterization

A.1.1. X-Ray diffraction spectra

The X-Ray powder diffraction analyses were carried out on a Philips Panalytical X'Pert Pro diffractometer with a Bragg-Brentano θ-θ geometry. In the case of manganese oxides, a copper Kα radiation was used ($\lambda_{K_{\alpha_2}}$= 0.1544 nm, $\lambda_{K_{\alpha_1}}$= 0.1540 nm). The powder diffraction patterns were recorded for about 2h in the 8°-80° (2θ) angular range, with a 0.0167° (2θ) step size and a 2.122° (2θ) active width in the detector. In the case of cobalt oxyhydroxides, a cobalt Kα radiation ($\lambda_{K_{\alpha_2}}$= 0.1793 nm, $\lambda_{K_{\alpha_1}}$= 0.1789 nm) was used. The powder diffraction patterns were recorded for about 10h in the 10°-110° (2θ) angular range, with a 0.0167° (2θ) step size and a 2.122° (2θ) active width in the detector.

A.1.2. Scherrer Method

The crystallite size of nanoparticles were calculated from the integral width of diffraction peak (hkl) using the Scherrer formula :

$$D_{hkl} = \frac{\lambda}{\beta_{meas} \cos\theta} \tag{A.1}$$

With D = average crystallite size, λ = the wavelength of the Kα radiation used, β_{meas} = integral width (ratio of peak area to height) in radians and θ = the angle of diffraction.

Note that β_{meas} is the sum of the contribution of the material observed β_{mat} and the instrumental contribution β_{inst} :

$$\beta_{meas} = \beta_{mat} + \beta_{inst} \tag{A.2}$$

The β_{inst} is experimentally determined but is negligible when nanometric materials are observed.

A.2. Chemical analysis

The chemical formula of the obtained powders have been determined by ICP and CHNS. The mean oxidation states of Co and Mn have been determined by iodometric titration.

A.2.1. ICP

ICP-OES (Inductive Coupled Plasma-Optical Emission Spectroscopy) is an analytical technique used for the detection of trace metals and alkaline ions (except hydrogen).

The analysis requires multiple steps. First, the samples are prepared by dissolving 10 - 20 mg of powder into boiling HCl. Then the obtained solutions are diluted in order to obtain concentrations varying from 1 to 200 mg/L. The solution is then introduced in a nebulisation chamber along with an argon flow to create an aerosol.

The ionization of an argon flow creates a hot plasma (6000 K – 10000 K) that vaporizes the dissolved sample into unbound atoms and excited ions. While coming back to their fundamental state, these atoms and ions emit ultraviolet and visible photons. A photomultiplier counts the photons and the comparison to a series of reference samples will allow the quantification. In our materials, only the Co, Mn, K and Na cations could be quantified.

Five measures were realized for each sample on a Varian 720ES apparatus by Laetitia Etienne, Engineer at ICMCB.

A.2.2. CHNS

Elemental analysis or CHNS analysis is accomplished by a combustion analysis to determine the mass fractions of carbon, hydrogen, nitrogen and sulfur of a sample. The sample is burned at 920 °C in a tin foil in an excess of oxygen. The combustion products are collected (H_2O, CO_2, N_2 et SO_2) and quantified. From this, it is possible to obtain the composition of C, H, N and S in the material.

All measurements are conducted on a Thermo Flash EA 111E Series. Since the mass of the sample has to be very precise, it is measured with a very precise scale (µg precision). Exactly 1.5 mg of powder is placed in the tin foil. To reduce the experimental errors, two measurements are conducted for each sample.

A.2.3. Mean oxidation state determination

A.2.3.1. Iodometry

Mean oxidation states x (of Mn and Co) have been determined by iodometric titration. It involved indirect titration of iodine liberated by redox reaction.

Titration principle :

- Mn or Co oxides are dissolved in acidic medium

- A KI solution is added and I^- ions will reduce all the transition metals that have a mean oxidation state superior to 2. This reaction will lead to the oxidation of I^- ions and form I_2 :

$$(x-2)I^- + Me^{x+} \rightarrow Me^{2+} + \frac{x-2}{2}I_2 \tag{A.3}$$

- The I $_2$ molecules are then titrated by sodium thiosulfate ($Na_2S_2O_3$, 0.1 M)

$$2(S_2O_3)^{2-} + I_2 \rightarrow S_4O_6^{2-} + 2I^- \tag{A.4}$$

To calculate the mean oxidation state (x), the quantity of I_2 formed can be expressed as :

$$n_{I_2} = \frac{x-2}{2} n_{Me^{x+}} = \frac{1}{2}[S_2O_3^{2-}] \times V_{eq} \tag{A.5}$$

where V_{eq} is the volume of sodium thiosulfate added at the equivalence. It is therefore possible to determine x :

$$x = \frac{[S_2O_3^{2-}] \times V_{eq}}{n_{Me^{x+}}} + 2 \tag{A.6}$$

Experimentally, the procedure is as follows :

- Around 30 mg of powder are dissolved in 5mL distilled water, 10 mL KI solution at 10 g/L and 5 mL HCl solution at 12M (37%)
- Then the solution is heated for total dissolution of powder (yellow color)
- Immediately after, the solution is titrated by sodium thiosulfate in order to obtain V_{eq} when the solution turns for yellow to transparent (slightly pink if cobalt oxyhydroxide)

It is important to stress out that Cl^- ions are likely to reduce Me^{x+} ions ($x > 2$). To minimize this effect, HCl solution is added last very carefully, so the metal ions are first reduced by KI. The titration is conducted rapidly after dissolution, in order to reduce the uncertainties induced by this technique. This is why the whole procedure is repeated three times for each sample.

A.2.3.2. XAS

XAS measurements at the Mn and Co K-edges were performed in transmission mode at the ROCK beam-line (financed by the ANR-10-EQPX-45) [243] of synchrotron SOLEIL (France) by Antonella Iadecola.

X-ray absorption spectroscopy or XAS is a commonly used technique which allows the determination of local structures and oxidation state. It is based on the excitation of the core-level electrons of an atom (K, L or M shells) when it is exposed to X-rays of specific energy (edge) equal to the energy difference between the excited and fundamental electronic states. This phenomenon is the basis of photoelectric absorption. The absorption A of the X-ray beam through a slab is proportional to the ratio between the intensities of the incident and transmitted X-ray beams.

About 4 mg of powder sample are mixed uniformly in cellulose matrix and pressed into a pellet of 10 mm, ensuring the Mn and Co K-edge step to be ~1. Measurements are performed in transmission mode provide bulk information averaged over many particles that are situated in the beam spot size of ~2 mm^2. A Si (111) channel-cut quick-XAS monochromator with an energy resolution of 0.7 eV at 7 keV was used. The intensity of the monochromatic X-ray beam was measured with three consecutive ionization detectors. The samples were placed between the first and the second ionization chambers. For each measurement, the spectra were collected at a rate of 2 Hz and averaged out over periods of 10 minutes. The energy calibration was established with simultaneous absorption measurements on a Mn or Co foil used as reference and placed between the second and the third ionization chambers. The data was treated using the Demeter package [244] for energy calibration and normalization. The energy was calibrated by adjusting using the first maximum of the first derivate of the Mn or Co foil spectrum to 6540 eV and 7709 eV, respectively. Then the spectra were background corrected and normalized using the flattening algorithm used by Athena. The E_0 value used to extract the EXAFS oscillations was fixed at 6557 eV (for Mn) and 7725.5 eV (for Co) after some trials. The EXAFS oscillations were weighted by k^2 and extracted using a Sine window in the k range [3.8, 14.8] Å^{-1} for both K-edges. It is noteworthy that Fourier transforms (FT) presented in this study are not phase corrected. Then the distances of the main FT contributions which are discussed in the text are shifted compared to the real crystallographic distances.

A.2.3.3. XPS

All the measurements were carried out by C. Labrugère at the PLACAMAT platform. Five points are measured per sample to determine homogeneity. As it was ensures, one point was randomly chosen for the fitting. All the data analysis was conducted by Lénaïc Madec from IPREM (Pau) using CasaXPS.

X-ray photoelectron spectroscopy (XPS) is a technique for analyzing the surface chemistry of a material. XPS can measure the elemental composition, empirical formula, chemical state and electronic state of the elements within a material. XPS spectra are obtained by irradiating a solid surface with a beam of X-rays while simultaneously measuring the kinetic energy and electrons that are emitted from the top 1-10 nm of the material being analyzed. A photoelectron spectrum is recorded by counting ejected electrons over a range of electron kinetic energies. Peaks appear in the spectrum from atoms emitting electrons of a particular characteristic energy. The energies and intensities of the photoelectron peaks enable identification and quantification of all surface elements (except hydrogen).

A K-Alpha spectrometer (ThermoFisher Scientific) was used for surface analysis of the powders pressed onto indium foil. The monochromatized Al Kα source (h_ν = 1486.6

eV) was activated with a spot size 200 µm in diameter. The full spectra (0-1350 eV) were obtained with a constant pass energy of 200 eV and high resolution spectra with a constant pass energy of 40 eV. Depth profiles were obtained through Ar^+ sputtering. Mn2p and Co2p spectra were fitted and quantified using the CasaXPS software.

A.2.4. Determination of chemical formulae

From ICP, CHNS and iodometric titration, it is possible to determine the chemical formulae of synthesized powders.

The materials have a general formula of :

$$H_w^+ Na_y^+ K_z^+ Me^{x+} O_2 (H_2O)_t \tag{A.7}$$

- Electroneutrality gives :

$$w + y + z + x = 4 \tag{A.8}$$

- $y = \frac{Na}{Me}$ and $z = \frac{K}{Me}$ determined by ICP; x is determined by iodometric titration
- By electroneutrality, w can be calculated
- $\frac{H}{Me}$ is determined by CHNS and therefore, t $= \frac{H}{Me} - w$

A.3. Electrical conductivity

A.3.1. DC measurement

The electric conductivity measurements have been performed with the four-probe technique, using direct current in the 230-400 K temperature range. Because of their instability beyond 400 K, these materials could not be sintered. Therefore, the pellets (8mm) in diameter are obtained by compacting 200 mg of powder at 1.2 GPa. All the measurements were conducted by Rodolphe Decourt from ICMCB.

A.3.2. BDS

All experiments are conducted with the help of Jean-Claude Badot (Chimie ParisTech) and Olivier Dubrunfaut (GEEPS, Supélec) at the GEEPS, Saclay. All the data was analyzed by Jean-Claude Badot.

The broadband dielectric spectroscopy requires some devices and instruments (network and impedance analyzers) for complete coverage of the frequency range. Complex resistivity and permittivity spectra are recorded over abroad frequency range of 40 Hz to 10 GHz, using simultaneously impedance and network analyzers Agilent 4294 (40 Hz–110 MHz), 4291 (1 MHz–1.8 GHz), PNA E8364B (10 MHz–10 GHz). The experimental devices are fully described in the literature [235, 245].

The experimental devices consist of a coaxial cell (APC7 standard) in which the cylindrical sample fills the gap between the inner conductor and a short circuit. The measurements are conducted by reflection on 3 mm diameter pellets that are pressed at 0.7 GPa. To ensure good contacts (junctions) between the sample/inner conductor and sample/short-circuit, its front faces are covered with silver paint.

After a relevant calibration of the analyzers, the sample admittance is computed from measurements of the complex reflection coefficient of the device. The knowledge of the admittance allows the determination the complex (relative) permittivity of the sample. Complete dielectric spectra are made from about 600 measurements with an accuracy of approximately 3 to 5% in the whole frequency range. The knowledge of the complex permittivity allows the calculation of complex resistivity and conductivity.

The measurements are recorded in the range of 200 to 300 K under dry N_2 flux. Since all the polarizations at different scales are generally additive, their contributions can be thus evidenced by the decomposition of the different dielectric spectra using Nyquist plots (imaginary part vs. real part of the permittivity, the conductivity and the resistivity). Spectra analyses are recorded by home-made software [235, 245].

A.4. Particle morphology

A.4.1. SEM

This technique, based on the interaction between the electrons from the microscope beam and the sample enables to observe the microstructure and homogeneity of ceramics in terms of grains size, composition and porosity. This is possible through different types of electron – material interactions: Secondary electrons providing information concerning the material morphology. Backscattered electrons, giving a chemical contrast which enables to observe the ceramics homogeneity in term of composition. Indeed, the lighter elements providing less backscattered electrons, appear darker. Photon X, with characteristic energies for each element, enables also to see the homogeneity within the ceramic. This analysis is known as energy dispersive spectrometry (EDS).

- JEOL JSM 6700F which is a high resolution one with an accelerating voltage from 0.5 to 30 kV and magnification up to 650000 at PLACAMAT and operated by P. Legros
- JEOL JSM 7800F Prime which is a high resolution one with an accelerating voltage from 1 to 30 kV and magnification up to 1000000 operated by S. Le Blond Duplouy at the Toulouse center of micro characterization (UMS Raimond Castaing)

A.4.2. TEM

A JEOL 2200FS with an accelerating voltage of 200 kV and equipped with a high resolution camera. In this case, the resolution is 0.23 nm. The Digital Micrograph (GATAN) software was used to acquire the images. All experiments were conducted with the help of François Weill and Marion Gayot.

This technique, based on the interaction between the electrons from the microscope beam going through the sample and the ones from the sample itself to create an image, enables to observe the nanoparticles in terms of size (to determine their size distribution) and morphology. It is also possible, in high resolution mode (HRTEM) to observe the atomic arrangement. This enables to discuss the crystallite size calculated from the XRD measurements and see if the nanoparticles are mono-crystalline. Finally, such analysis gives information concerning the homogeneity of the powder

For colloidal suspensions :

To perform this measurement, the dispersion is drop-casted onto a copper grid. It is important to use dilute dispersions to avoid reaggregation of the nanosheets during the deposition. When drop-casting, the best results are obtained when the grid is placed on a filter paper to wick away access solvent. During the image acquisition, it is important to adjust the field of view according to the nanosheet size.

In order to conduct the TEM characterizations, all supernatants were collected after ultracentrifugation speed of 50000 rpm and diluted by ten fold.

A.4.3. AFM

For AFM analysis, it is particularly critical to avoid reaggregation of nanosheets on the wafer during solvent evaporation. For this, very dilute dispersions are used and drop-casted onto a microscope slide. The slide is pre-treated with freshly cleaved mica surface in order to obtain an atomically flat surface.

AFM images were recorded by the tapping-mode phase imaging using a standard silicon cantilever (approx 20 N/m, 150 kHz) on a commercial ICON AFM (Bruker). The experiments were conducted in collaboration with Hassan Saadaoui (CRPP). The software used to analyze the images is Nanoscope Analysis.

A.5. Surface analysis

A.5.1. BET

All the specific surfaces and characterization of mesoporosity of materials were conducted by N_2 adsorption at 77K. The measurements were performed by Marie-Anne Dourges from ISM on ASAP2010 (Micromeritics Corp., Norcross, GA, USA). Each sample is degassed at 100°C under vacuum during the necessary time to obtain a constant pressure of 10 µm Hg (approximately 12 - 15 hours). The BET model was applied for relative pressures (P/P^0) between 0.01 and 0.3 to calculate the specific surface S_{BET} [246]. Pore distribution is determined using the BJH model [247]. The pore dimensions are calculated from the desorption isotherms.

A.5.2. Zetametry measurements

The zeta potential of dispersions were measures with a Malvern Zetasizer Nano series. The Zetasizer Nano series calculates the zeta potential by determining the Electrophoretic Mobility and then applying the Henry equation. The electrophoretic mobility is obtained by performing an electrophoresis experiment on the sample and measuring the velocity of the particles using Laser Doppler Velocimetry (LDV).

The measure takes place in a cell with electrodes at either end to which a potential is applied (as shown in Figure A.1). The cell is illuminated by a laser used to provide a light source. The light source is split to provide an incident and reference beam. When an electric filed is applied to the cell, any particles moving through the measurement volume will cause the intensity of light detected to fluctuate with a frequency proportional to the particle speed.

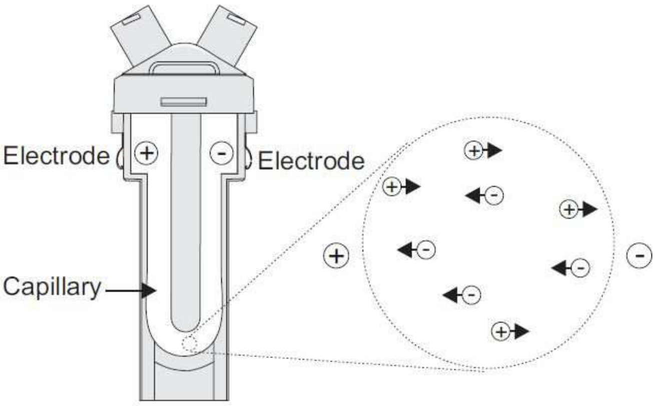

Figure A.1.: Cell for zeta measurements

A.6. Electrochemistry

A.6.1. Electrode preparation

To study the electrochemical performances of Mn and Co oxides, the materials synthesized are prepared into electrodes, i.e. as films pressed on a current collector. The films are composed of active material (either metal oxide or activated carbon) and a binder (PTFE). This composition produce films with good mechanic stability and low resistance while preserving powder porosity. If metal oxides are used as active material, carbon black is added to enhance the electrochemical conductivity of the active material. In this study, acetylene black (AB) was used and the optimal amount is fixed at 15% (weight percentage vs active material).

The current collector is a stainless steel grid for its chemical stability and because it is inert in a neutral aqueous electrolyte. The procedure to make electrodes is :

1. Precise weight of active material
2. If carbon additive needed, precise weight of activated carbon
3. Intimate mix of both
4. Addition of PTFE (60 wt% suspension in water)
5. Addition of ethanol to obtain a suspension, mixing and evaporation in order to obtain a slurry
6. Mixing the slurry until obtention of a homogeneous film with good mechanic stability
7. Drying the obtained film at 60°C for 12 hours
8. Cutting electrodes in the film (6 or 8 mm diameter) : measurement of mass and thickness
9. If needed, press the electrode onto the stainless steel grid at 6 ton/cm^2

A.6.2. Electrochemical cell

A.6.2.1. Three-electrode cell

The three-electrode cell is mostly use to study positive electrodes. It is composed of a working electrode (studied cell), a counter electrode (Platinum wire) and a reference electrode (Ag/AgCl).

The three-electrode configuration allows the fine control of the working electrode's potential. Furthermore, the size of the cell enables the use of a large volume of electrolyte (approximately 300 mL), which can make the gaseous release due to oxidation and reduction of electrolyte negligible.

A.6.2.2. Swagelok

The Swagelok™-type cells are named after the Swagelok™ Company, specialized in the manufacturing of tube, valves … for gas and fluid systems. The positive and negative electrodes are pressed against platinum current collectors. Two layers of polymer separators provide a support for the liquid electrolyte absorption and prevent any short circuit between the positive and negative electrodes.

A two-electrode configuration was used when the behavior of activated carbon YP80F was studied. Concerning the full asymmetric device study, the three-electrode configuration was used : the reference electrode Ag/AgO$_x$ was used. Their schematic representations are shown in Figure A.2.

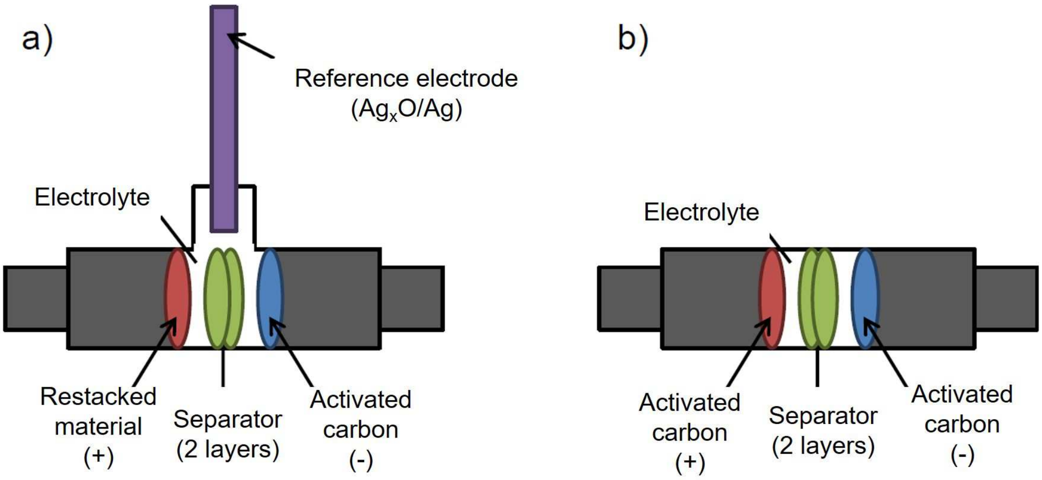

Figure A.2.: Schematic representation of swagelok cells. a) Three-electrode configuration allowing the monitoring of each electrode's potential. b) Two-electrode symmetrical configuration.

A.6.3. Measurements

The electrochemical characterization of electrodes was carried out using an EC-Lab potentiostat.

A.6.3.1. Cyclic Voltammetry

Cyclic voltammetry is a widely used electrochemical technique to investigate the role of thermodynamics and electron transfer kinetics at the interface of the electrode and electrolyte for supercapacitor and Li-ion battery application. In cyclic voltammetry, the electrochemical cell is cycled in a particular potential window, where the potential is applied to the working electrode and measured for different scan rates. Scan rate is defined as the change in potential versus time. The electrochemical performance of material can be evaluated by observing the current change in a cathodic and anodic scan. the applied potential varies linearly with time :

$$U = U_0 + vt \tag{A.9}$$

where U_0 is the open circuit voltage, v the scan rate (V/s) and t time (s).

For an ideal supercapacitor, the current response is rectangular. Non-rectangular shapes can be ascribed to resistivities in the cell (contact resistance between electrode and electrolytes...). It is also possible to observe faradaic reactions with the presence of oxidation/reduction peaks.

The current intensity is linked to the capacity and scan rate by this equation :

$$i = Cv \tag{A.10}$$

It is therefore possible to calculate the capacity of an electrode by integrating the area under the curve :

$$Q[mAh/g] = \frac{area\,under\,curve\,[A/gV]}{v\,[V/s]} \tag{A.11}$$

From the capacity (in mAh/g) it is possible to determine the capacitance C (F/g) :

$$C[F/g] = \frac{3.6 \times Q[mAh/g]}{\Delta E[V]} \tag{A.12}$$

where ΔE is the potential window.

A.6.3.2. Galvanostatic charge-discharge

These characterizations are performed under a constant current. The evolution of the voltage U is plotted as a function of time.

If I is the current applied to the cell, the potential measured is give by this equation :

$$U = RI \tag{A.13}$$

Where R is the sum of the resistances present in the cell (current collector, contact between current collector and active material, separator...)

For an ideal supercapacitor, the potential response is linear with time, which is not the case if faradaic reactions occur. This technique is the most precise way to determine the capacity of an electrode as

$$Q = It \tag{A.14}$$

where t represents the charge or discharge time.

B. Résumé en français

Introduction

La forte progression démographique mondiale, associée au développement économique des pays émergents ne cesse d'accroitre la demande en énergie. En considérant les réserves limitées en combustible, la remise en question du nucléaire et la réduction des émissions de gaz carboniques à l'origine du réchauffement climatique, il est désormais primordial de considérer des sources d'énergies propres et renouvelables. Cependant, ces nouvelles sources d'énergies étant de nature intermittente (alternance jour/nuit, force du vent. . .), il s'avère nécessaire de maitriser le transport et stockage de l'énergie générée, afin de pouvoir la restituer sur demande et optimiser son utilisation. Parallèlement au développement de nouvelles énergies, une attention particulière est donc accordée aux dispositifs de stockage de l'énergie électrique.

L'une des meilleures façons de stocker de l'énergie afin de la restituer est de convertir de l'énergie chimique en énergie électrique puisque toutes deux partagent le même vecteur qu'est l'électron. Il existe deux types de dispositifs rechargeables capables d'effectuer une telle conversion. Les accumulateurs électrochimiques peuvent délivrer et stocker de l'énergie électrique sur la base de réactions d'oxydo-réduction réversibles des matériaux d'électrode. C'est un mécanisme de stockage faradique qui conduit à des énergies spécifiques importantes car tout le volume du matériau actif participe au stockage de charges. En effet, la quantité de charges stockées est conditionnée par la quantité de matière électrochimiquement active. Cependant, la densité de puissance est limitée car les cinétiques des processus faradiques sont intrinsèquement liées au transfert de charges et de masses, augmentant les temps de réponses des accumulateurs. De même, leur cyclabilité est restreinte en raison des modifications de composition et de structure des électrodes lors du cyclage.

D'une autre part, les supercondensateurs sont basés sur les propriétés capacitives d'une double couche d'électrons-ions aux interfaces électrolyte-électrode, atteignant une capacité par unité de surface jusqu'à des millions de fois plus grande qu'un condensateur diélectrique classique. Le stockage est dit capacitif et repose sur l'accumulation de charges électrostatique à la surface des électrodes. Ainsi, la densité de puissance qui en résulte est de 10 à 100 fois plus élevée que dans le cas des accumulateurs. Cependant, la quantité de charges stockées dépend de la tension appliquée et, la surface spécifique des électrodes étant limitée, l'énergie massique reste inférieure à celle des accumulateurs.

Pour y pallier, de nombreuses études ont porté sur des matériaux dits pseudocapacitifs, qui ont une réponse électrochimique similaire à celle des matériaux capacitifs classiques, mais associé à un mécanisme de stockage de charges faradique à la surface. Ainsi, des propriétés intermédiaires aux accumulateurs et supercondensateurs classiques peuvent être atteintes avec ce type de matériaux.

Historiquement, la pseudocapacité est une notion qui a été définie par Conway suite à ses recherches sur l'oxyde de ruthénium [34]. Cependant, le ruthénium étant toxique et onéreux, une alternative a été trouvé grâce à un candidat prometteur : l'oxyde de manganèse.

L'oxyde de Mn cristallise sous différentes structures qui présentent des propriétés physicochimiques (notamment la surface spécifique) menant à des propriétés électrochimiques différentes. Cependant, ceux-ci présentent des conductivités électroniques faibles conduisant à des densités de puissances limitées, notamment à haut régime. Pour y remédier, plusieurs stratégies sont envisageables : l'augmentation de la surface spécifique, notamment par nanostructuration, ou l'amélioration de la conductivité électronique.

Pour réaliser cela, nous nous proposons de développer une stratégie de synthèse originale visant à améliorer la conductivité électronique de l'oxyde de manganèse lamellaire, la birnessite, qui présente les meilleures capacités. L'objectif est de combiner la pseudocapacité de la birnessite avec un autre oxyde lamellaire plus conducteur : l'oxyhydroxyde de cobalt. La stratégie envisagée vise à conserver l'intégrité des feuillets afin de préserver au mieux les propriétés des matériaux initiaux. C'est une approche "nano-architecturale" des matériaux, considérant les feuillets d'oxydes comme des briques élémentaires qui sont assemblées entre elles.

Une représentation schématique de la stratégie est représentée dans la Figure B.1. La première étape consiste en la synthèse des matériaux lamellaires initiaux. S'ensuit une étape d'exfoliation, afin d'obtenir des nanofeuillets correspondant à des briques élémentaires. Puis intervient l'étape cruciale de réempilement, durant laquelle la physicochimie des feuillets sera étudiée afin de réaliser un empilement alterné et statistique. Enfin, les matériaux obtenus sont caractérisés puis assemblés en électrode afin d'en évaluer les performances électrochimiques.

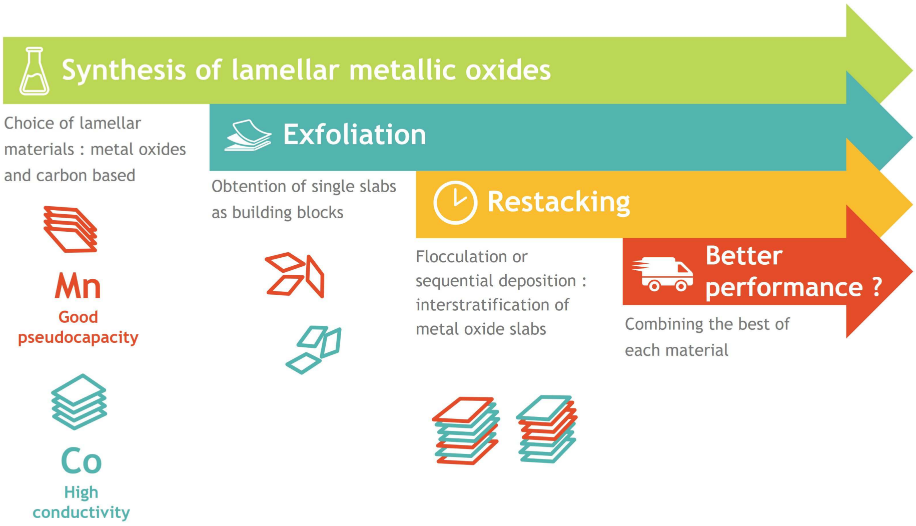

Figure B.1. : Représentation schématique de la stratégie de synthèse présentée dans ce travail.

B.1. Synthèse d'oxydes lamellaires de Mn et Co

La structure des oxydes lamellaires A_xMO_2 (A = H, K, Na, Li, H et M = métal de transition) consiste en un empilement de feuillets MO_2 constitués d'octaèdres MO_6 partageant des arêtes. Les feuillets MO_2, dans lesquels les liaisons M–O sont fortes, forment la structure hôte rigide. Les ions alcalins ou protons A sont intercalés entre les feuillets, permettant ainsi de stabiliser thermodynamiquement la structure en minimisant les répulsions électrostatiques entre les couches d'oxygène adjacentes. Une nomenclature proposée par Delmas et al [164] permet de différencier les empilements qui peuvent être rencontrés. La structure est alors décrite par l'association d'une lettre (P, T ou O), qui décrit l'environnement respectivement prismatique, tétraédrique ou octaédrique de l'ion alcalin, et d'un chiffre (1, 2 ou 3), qui indique le nombre de feuillets nécessaires à la construction de la maille élémentaire.

B.1.1. L'oxyde lamellaire de Mn : la birnessite

La birnessite est un oxyde de manganèse lamellaire hydraté dont les feuillets sont composés d'octaèdres [MnO_6] partageant des arêtes, ainsi que représenté sur la Figure B.2. La distance entre deux feuillets successifs est de 7 Å environ. L'écart à la stœchiométrie, dû à la présence de cations Mn hétérovalents (Mn^{2+}, Mn^{3+}, Mn^{4+}) et/ou de lacunes foliaires engendre un déficit de charge qui est compensé par la présence, dans l'espace interfeuillet, de cations hydratés, principalement alcalins ou alcalino-terreux.

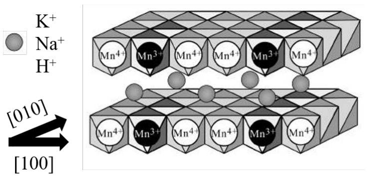

Figure B.2. : Structure de la birnessite.

La birnessite peut être obtenue par de nombreuses voies de synthèse qui vont influencer le taux de lacunes, leur organisation ainsi que la microstructure des feuillets et leur turbostraticité [186]. Dans ce travail, une voie de synthèse "classique" à température ambiante a été choisie pour son aspect pratique, sa facilité de mise en œuvre, et son rendement élevé [188].

La synthèse se réalise en dissolvant du sulfate de manganèse $MnSO_4$ en milieu acide (NaOH ou KOH 6M). Un précipité marron apparait spontanément, correspondant à la phase $Mn(OH)_2$. Puis un oxydant fort est ajouté ($K_2S_2O_8$) afin d'obtenir la birnessite sodiée (notée Na-birn) ou potassée (K-birn). Le mélange réactionnel est agité pendant 30 minutes supplémentaires avant d'être centrifugé puis séché à 60°C pendant une nuit.

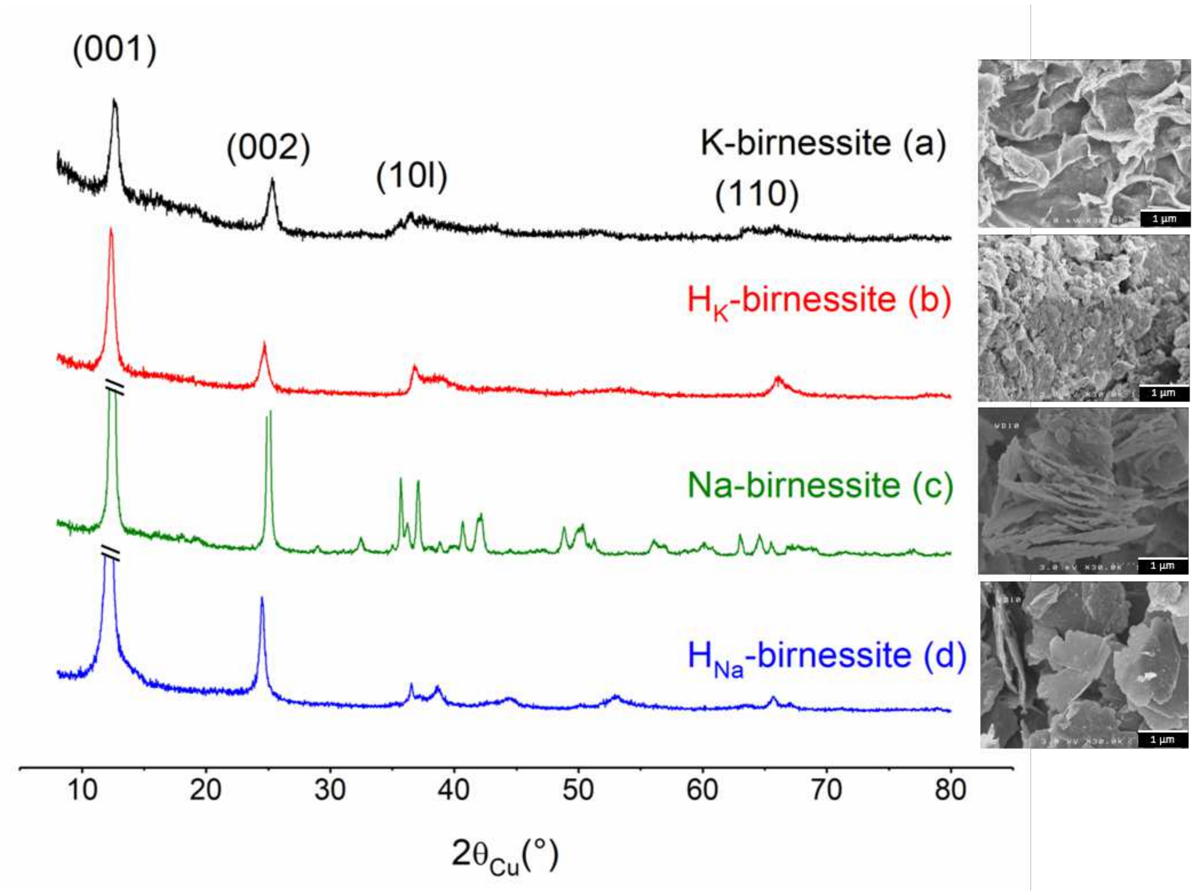

Figure B.3. : Diffractogrammes et microscopie électronique à balayage des oxydes lamellaires de manganèse synthétisés. (a) K-birnessite. (b) H_K-birnessite. (c) Na-birnessite. (d) H_{Na}-birnessite.

Afin de préparer l'étape suivante d'exfoliation, il est nécessaire de procéder à une réaction d'échange ionique, qui correspond à une réaction de protonation durant laquelle les cations alcalins sont échangés par des protons. Pour cela, le solide obtenu est introduit en milieu acide pendant plusieurs jours. Après ce traitement acide, le mélange réactionnel est centrifugé puis séché afin d'obtenir les birnessites protonées (H_{Na}-birn ou H_K-birn).

Une première caractérisation par diffraction des rayons X permet de confirmer la préservation de la structure lamellaire suite à la protonation (Figure B.3). L'évolution de la distance inter-lamellaire, qui peut être déduite de la raie (001), permet de constater une modification de l'espace inter-lamellaire. De même, la microscopie électronique à balayage et à transmission permettent d'observer des morphologies voilaires plus ou moins rigides, en fonction de la nature du cation alcalin. La protonation permet de conserver ces morphologies. Les analyses chimiques (ICP, CHNS, mesure du degré d'oxydation) permettent de confirmer l'échange inter-lamellaire.

B.1.2. L'oxyhydroxyde lamellaire de Co : la phase β3-cobalt

Différentes voies de synthèse ont été mises en œuvre pour obtenir la phase β3-cobalt. Celles-ci permettent de moduler le degré d'oxydation moyen de l'ion cobalt et ainsi d'améliorer la conductivité électronique de l'oxyhydroxyde [18]. Une première voie correspond à une précipitation à température ambiante du nitrate de cobalt en milieu NaClO/KOH afin d'obtenir la phase β3-prec. L'autre voie de synthèse correspond à une succession de réactions topotactiques à partir de la phase lamellaires de $Na_{0.6}CoO_2$ synthétisée à haute température. Celle-ci est soit directement hydrolysée en milieu basique et oxydant pour obtenir β3-ex$Na_{0.6}$, soit hydrolysée en milieu acide afin d'obtenir une phase intermédiaire (la phase γ-Cobalt) qui est ensuite oxydée en phase β3-exγ.

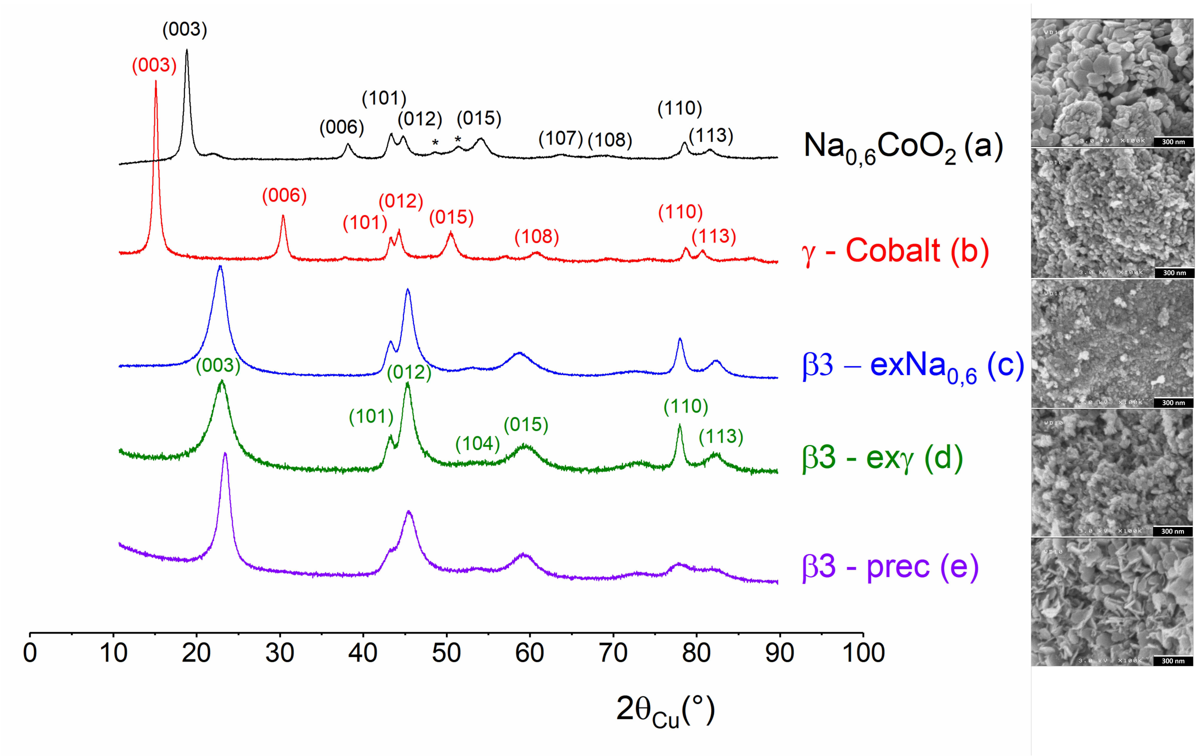

Figure B.4. : Diffractogrammes et microscopie électronique à balayage des oxydes lamellaires de cobalt synthétisés. (a) $Na_{0.6}CoO_2$. (b) γ-Co, synthétisé par échange ionique à partir de $Na_{0.6}CoO_2$. (c) β3-exγ, obtenu par hydrolyse acide de γ-Co. (d) β3-ex$Na_{0.6}$, obtenue par hydrolyse acide de $Na_{0.6}CoO_2$. (e) β3-prec, synthétisé par précipitation du sel de cobalt en milieu basiqueet oxydant.

La diffraction des rayons X (présentée sur la Figure B.4) montre que les trois voies de synthèses mises en œuvre permettent d'obtenir des phases avec des structures similaires et une légère modification dans l'espace interfeuillet (raie 110). La microscopie électronique à balayage permet de constater que la voie de synthèse influe directement sur la morphologie des particules. En effet, les particules de β3-prec sont des plaquettes hexagonales rigides, tandis que les particules de β3-ex$Na_{0.6}$ ou β3-exγ sont plus finement divisées. Ceci est lié à la morphologie des particules initiales qui ont subi une réaction topotactique.

B.1.3. Comparaison des conductivités électroniques

Les conductivités électroniques des matériaux synthétisés sont représentées sont forme graphique et tabulées dans la Figure B.5.

Les phases $Na_{0.6}CoO_2$ ainsi que γ-Co se distinguent avec une énergie d'activation quasi-nulle, caractéristique d'un comportement pseudo-métallique. Les autres phases synthétisées, notamment les phases β3-cobalt et les oxydes de Mn présentent tous un comportement semi-conducteur.

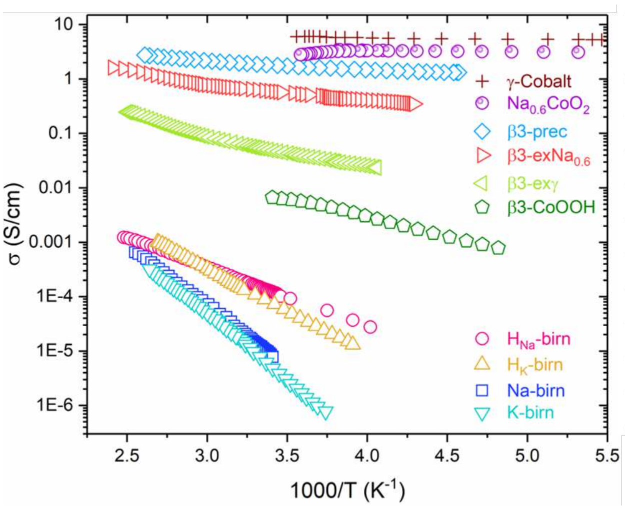

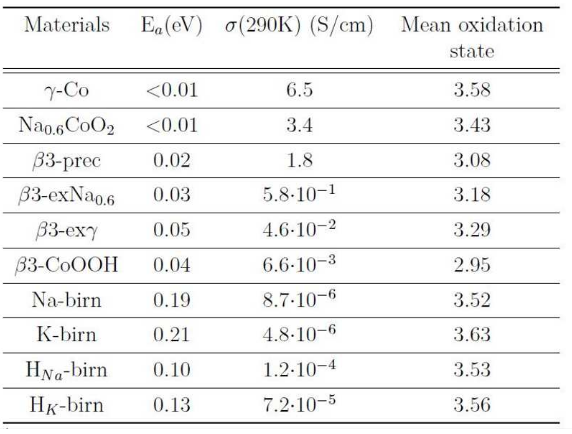

Materials	E_a(eV)	σ(290K) (S/cm)	Mean oxidation state
γ-Co	<0.01	6.5	3.58
$Na_{0.6}CoO_2$	<0.01	3.4	3.43
β3-prec	0.02	1.8	3.08
β3-exNa$_{0.6}$	0.03	$5.8 \cdot 10^{-1}$	3.18
β3-exγ	0.05	$4.6 \cdot 10^{-2}$	3.29
β3-CoOOH	0.04	$6.6 \cdot 10^{-3}$	2.95
Na-birn	0.19	$8.7 \cdot 10^{-6}$	3.52
K-birn	0.21	$4.8 \cdot 10^{-6}$	3.63
H_{Na}-birn	0.10	$1.2 \cdot 10^{-4}$	3.53
H_K-birn	0.13	$7.2 \cdot 10^{-5}$	3.56

Figure B.5. : Variation des conductivités électroniques des matériaux synthétisés et énergies d'activation associées

Les oxydes de manganèse présentent des conductivités électroniques à température ambiante d'environ 10^{-6} S/cm et des énergies d'activations relativement élevées. Il est intéressant de noter que les birnessites protonées sont légèrement plus conductrices que les phases initiales. En comparaison, les oxyhydroxydes de cobalt β3 présentent des conductivités électroniques plus élevées (de l'ordre de 1 S/cm), ainsi que des énergies d'activation plus faibles. Ceci justifie le choix porté sur les oxyhydroxydes de Co pour améliorer la conductivité électronique des oxydes de Mn.

B.2. Exfoliation

B.2.1. Principe

Après avoir obtenu les phases lamellaires de départ, nous procédons à une étape d'exfoliation (représentée dans la Figure B.6). Celle-ci correspond à l'intercalation d'un agent exfoliant (l'ion tétrabutylammonium noté TBA^+) avec les protons présents dans l'interfeuillet. Puis le matériau est exfolié en milieu liquide sous ultrasonication, afin de diminuer les interactions d'attraction électrostatique entre les feuillets. Une suspension colloïdale stable est obtenue, correspondant à la délamination des feuillets.

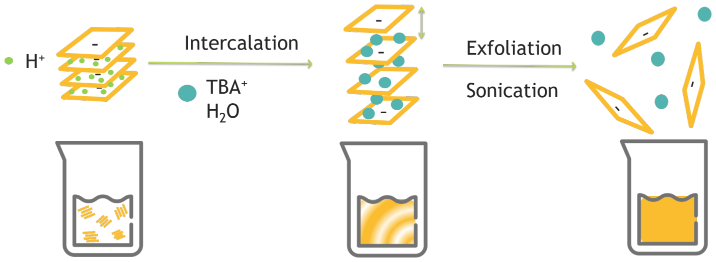

Figure B.6. : Schéma du procédé d'exfoliation

L'étape d'exfoliation est délicate car difficile, lente et non-totale. Les suspensions colloïdales obtenues sont polydisperses, il est alors nécessaire d'effectuer des cycles de centrifugations successifs afin de pouvoir séparer les feuillets de différentes taille pour mieux les caractériser. Une première centrifugation à 4000 tours/minute est réalisée pour éliminer les particules non-exfoliées. Puis les surnageants sont récupérés et centrifugés à vitesse croissante afin d'isoler, après 50 000 tours/minute, les feuillets les plus fins.

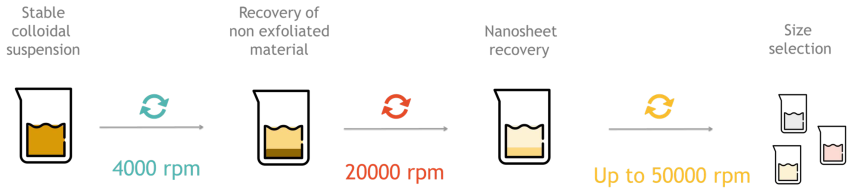

Z (d.nm)	745	260	130	66
PdI	0.68	0.53	0.38	0.35

Figure B.7. : Taille moyenne des particules et indice de polydispersité (PdI) des surnageants après chaque cycle de centrifugation suite à l'exfoliation de la phase H_K-birn.

B.2.2. Caractérisation des oligo-feuillets

Les surnageants obtenus à l'issue d'une centrifugation à 50 000 tours/minute permettent de mettre en évidence des oligofeuillets fins. Ceux-ci peuvent être observés par microscopie électronique à transmission et leur épaisseur peut être évaluée par microscopie à force atomique. Ainsi, la Figure B.8.a permet de visualiser l'aspect des feuillets obtenus après exfoliation de H_{Na}-birn. Sur l'image de microscopie à transmission électronique, il est possible de distinguer un empilement d'oligo-feuillets sous forme de voiles très fins. On constate la préservation de l'intégrité du feuillet ainsi que son exfoliation partielle. La microscopie à force atomique permet de mettre en évidence des feuillets ayant une épaisseur de 2 à 4 nm, ce qui représente, en considérant les données cristallographiques, à un empilement de 3 à 5 lamelles. Les suspensions colloïdales obtenues après exfoliation de l'oxyhydroxyde de cobalt β3-prec ont aussi été caractérisées et les images sont montrées dans la Figure B.8.b. On observe des particules exfoliées plus épaisses que les feuillets exfoliés de Mn, correspondant à des nano-morceaux de feuillets hexagonaux, caractéristiques des β3-prec. Ceci est confirmé par microscopie à force atomique, l'épaisseur minimale mesurée est d'environ 4-6 nm, ce qui correspond à un empilement de 4 à 6 feuillets.

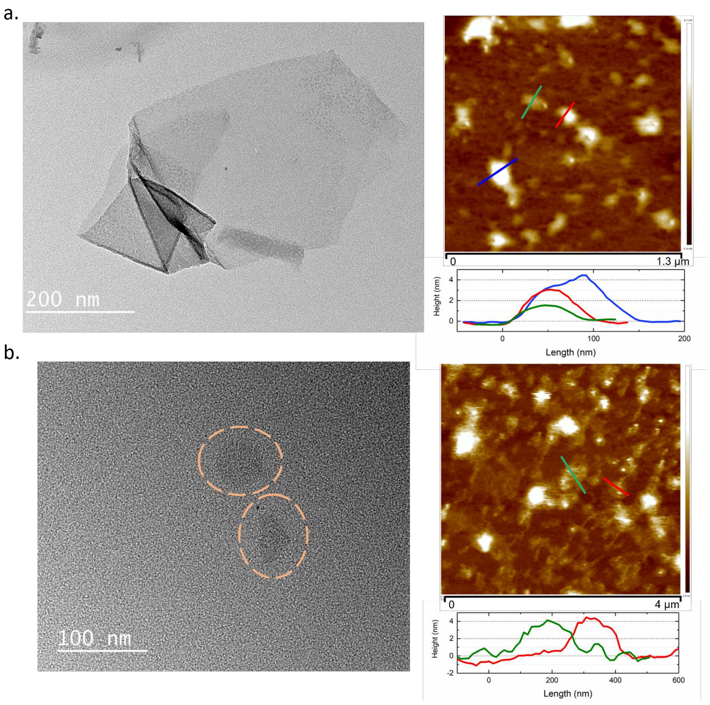

Figure B.8. : Images obtenues par microscopie électronique à transmission d'une particule exfoliée présente dans le surnageant après une centrifugation à 50 000 rpm (gauche). Les épaisseurs de feuillets sont évaluées par microscopie à force atomique (droite). a. Suspension colloïdale de H_{Na}-birn. b. Suspension colloïdale de β3-prec.

Cette étude permet de conclure sur l'exfoliation partielle des particules initiales. Cependant, le rendement à haute vitesse de centrifugation est faible, si bien que la suite des travaux a été réalisée sur des suspensions colloïdales obtenues après faible vitesse de centrifugation.

B.3. Réempilement

Réempiler les oxydes de manganèse et oxyhydroxydes de cobalt exfolié de façon contrôlée et statistique nécessite une connaissance précise de leur état de surface. Pour l'évaluer, il est nécessaire de déterminer leur point isoélectrique (PIE). En effet, les particules exfoliées correspondent à des nanofeuillets, ou des "briques élémentaires" qui sont chargées en suspension. Le point isoélectrique correspond au pH pour lequel toutes les charges de la surface d'un oxyde en suspension sont compensées.

B.3.1. Détermination du PIE

Le point isoélectrique peut être déterminé expérimentalement par zétamétrie. En raison de la polydispersité des matériaux ainsi que de la faible quantité de matière exfoliée obtenue, il a été jugé intéressant de modéliser le PIE grâce au modèle MUSIC tant sur un plan fondamental que pratique.

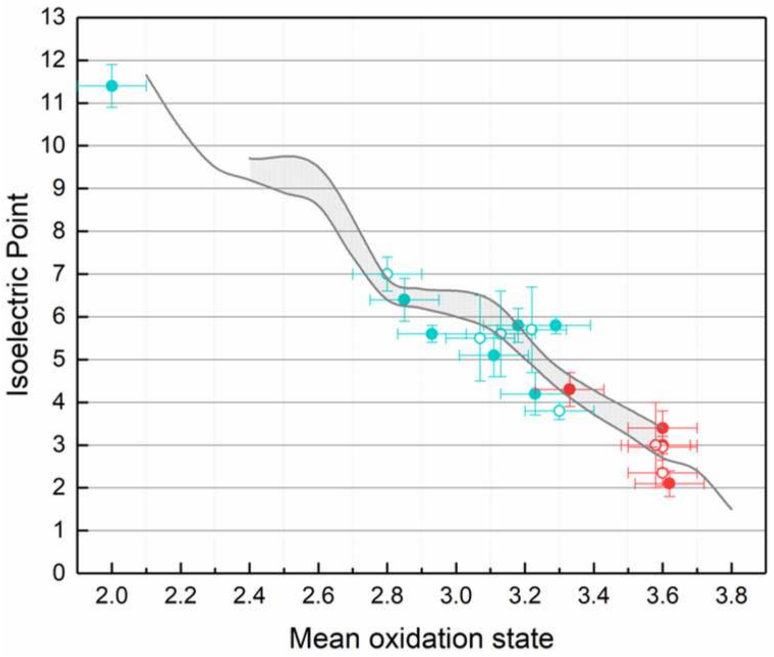

Figure B.9. : Valeurs expérimentales de PIE selon le degré d'oxydation moyen des cations métalliques du matériau initial (oxydes de manganèse (●), oxyhydroxydes de cobalt (●)) et des matériaux exfoliés (oxydes de manganèse (○), oxyhydroxydes de cobalt (○)). Celles-ci sont comparées avec les courbes de PIE modélisées : la courbe inférieure représente une surface basale de 100%, la courbe supérieure une surface basale sur latérale de 85%, ce qui correspond à la réalité des matériaux.

La Figure B.9 présente la comparaison entre les courbes de PIE modélisées et les points expérimentaux déterminés par zétamétrie. Grâce à ces mesures, il est possible d'étudier avec précision l'influence du degré d'oxydation moyen des matériaux sur leur charge de surface ainsi que l'impact de l'exfoliation sur la valeur du PIE.

Les mesures expérimentales permettent l'obtention de courbes de potentiel zéta en fonction du pH, qui rendent possibles la détermination de trois domaines de pH. Dans les domaines de pH I ou III, les suspensions colloïdales d'oxydes de manganèse ou d'oxydroxydes de cobalt sont chargées de façon identique. Tandis que dans le domaine de pH II, les suspensions colloïdales sont chargées de façon opposée.

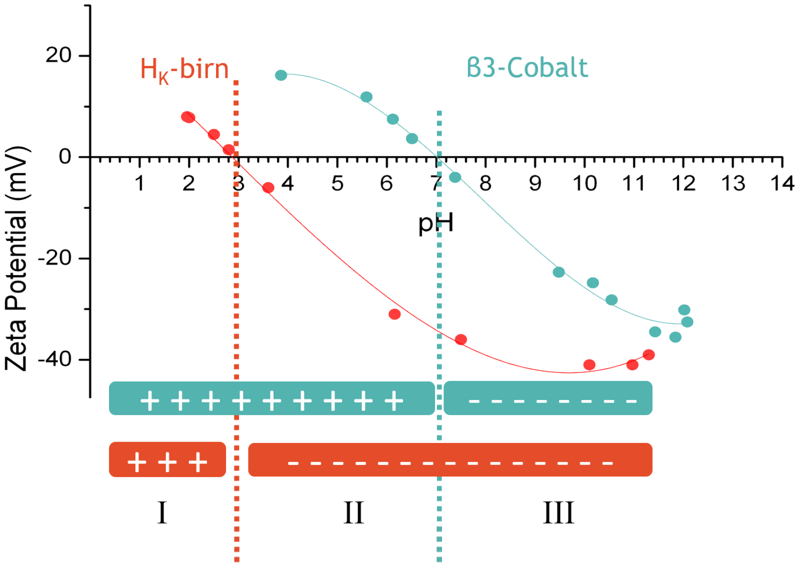

Figure B.10. : Courbes expérimentales de potentiel zéta-pH obtenues pour la birnessite initiale H_K-birn (rouge) et les oxyhydroxydes de cobaltβ3-prec (bleu). La charge de surface des particules est représentée par (+) et (-). Si pH<3, les particules de H_K-birn et β3-prec sont chargées positivement. Si pH>7, elles sont chargées négativement. Si 3<pH<7, les particules de H_K-birn sont chargées négativement et les particules deβ3-prec sont chargées positivement.

Grâce à la connaissance de ces pH, il est possible de procéder aux réempilements des particules : tout d'abord nous avons procédé au réempilement simple pour juste étudier l'effet de l'exfoliation, avant d'enchainer sur le réempilement mixte.

B.3.2. Stratégies de réempilement

Pour induire un réempilement entre les briques élémentaires, trois stratégies peuvent être adoptées, celles-ci sont schématisées sur la Figure B.11. A l'issue de l'exfoliation, toutes les suspensions colloïdales sont basiques à un pH 12.

Une première consiste à d'abord mélanger les suspensions d'oxyde de Mn et d'oxyhydroxyde de Co entre elles, puis de provoquer une flocculation entre celles-ci avec l'ajout d'un contre-ion.

Afin d'obtenir un réempilement alterné entre les briques élémentaires de Mn et Co, une seconde stratégie vise à atteindre le domaine de pH II. Après avoir mélangé les deux suspensions colloïdales entre elles, le mélange est porté à un pH optimal de 4.5. Ainsi, les particules de Mn sont chargées négativement tandis que les particules de Co sont chargées positivement. Une attraction électrostatique entre les lamelles peut s'opérer. Un contrôle encore plus fin de l'alternance des feuillets peut être obtenu si les suspensions colloïdales sont portées à pH 4.5 séparément puis ensuite mélangées entre elles.

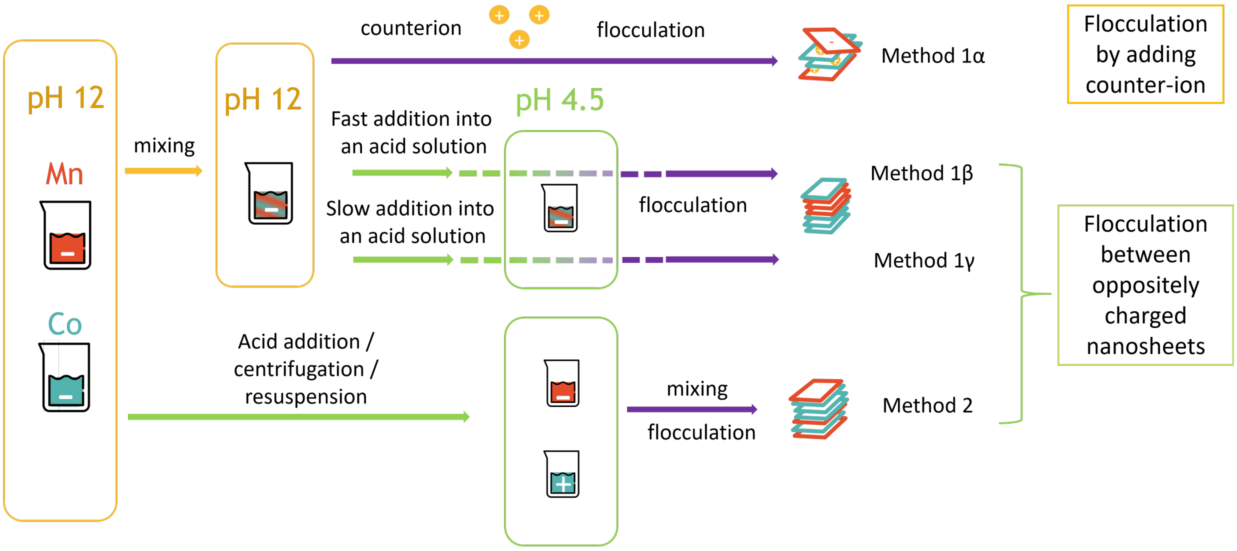

Figure B.11. : Représentation schématique des méthodes de réempilement employées

Grâce à toutes ces techniques de réempilement, il est possible d'étudier d'une part l'influence du ratio molaire Mn :Co sur les matériaux obtenus, d'autre part l'influence de la méthode de réempilement sur la finesse de l'organisation des feuillets entre eux. Les matériaux mixtes obtenus sont systématiquement comparés à un mélange obtenu par simple broyage au mortier des particules initiales entre elles.

B.3.3. Propriétés des matériaux réempilés

B.3.3.1. Influence du ratio molaire

En modifiant les quantités de matériaux à ajouter, nous avons d'abord étudié l'influence du ratio Mn :Co. Tous les matériaux sont obtenus à partir de la même méthode de réempilement, qui consiste à amener les suspensions colloïdales à un pH optimal de 4.5 avant de les mélanger entre elles.

La Figure B.12 présente les diffractogrammes des poudres obtenues ainsi que des images de MEB-EDS associées. Tous les matériaux réempilés présentent les mêmes raies caractéristiques des matériaux de départ, ce qui permet de conclure que les matériaux réempilés correspondent à des mélanges composites. Ceci est vérifié par les images MEB-EDS où le Mn est représenté en rouge tandis que le Co est représenté en vert. Lorsque le ratio de Co augmente, les raies correspondant à l'oxyhydroxyde de cobalt ont une intensité plus importante, ce qui est en parfaite corrélation avec un aspect plus "vert" des particules. Pour un matériau réempilé comportant 50% de Co et 50% de Mn, on observe des particules à l'aspect "jaune" ce qui permet de conclure sur la bonne homogénéité du matériau composite.

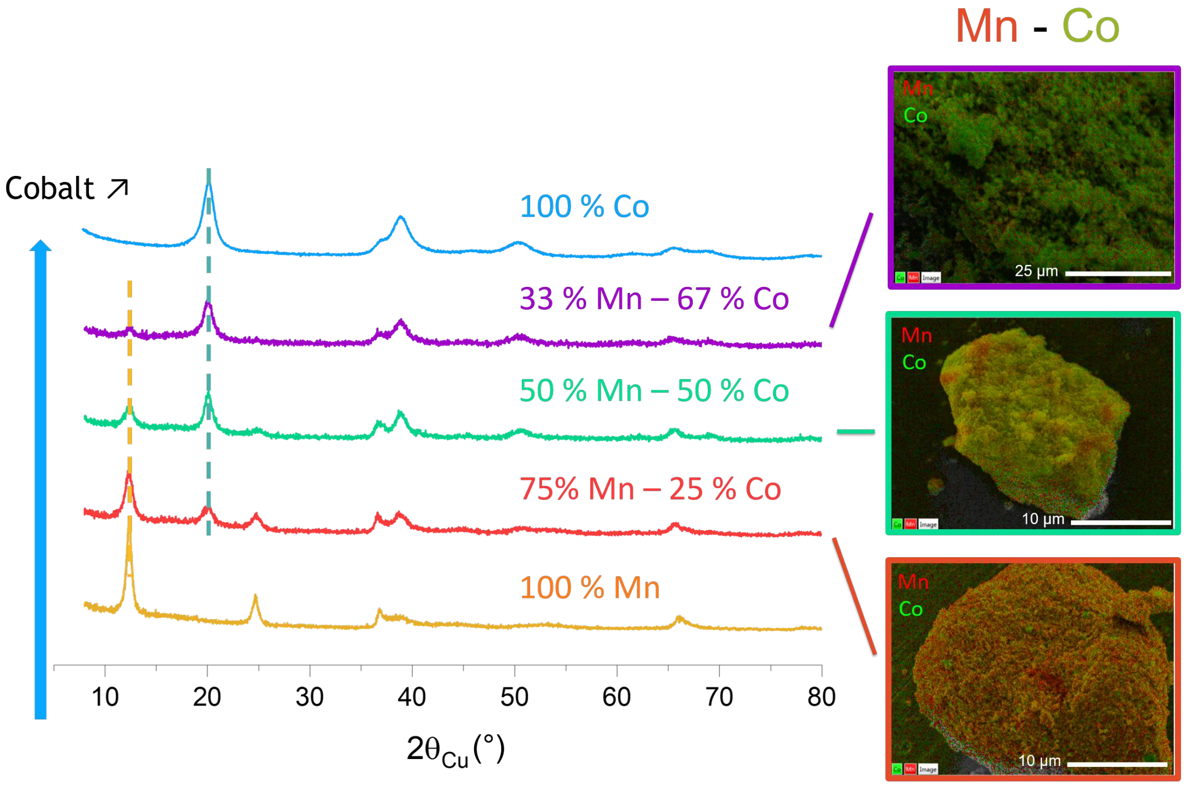

Figure B.12. : Diffractogrammes des rayons X et images MEB-EDS associées aux matériaux obtenus par exfoliation et réempilement de H_K-birn et $\beta 3$-prec. En haut : oxyhydroxyde de cobalt initial$\beta 3-prec$, puis dans l'ordre décroissant (de haut en bas) : matériau réempilé Restack-2-(Mn :2Co) avec 33% Mn - 67% Co ; matériau réempilé Restack-2-(Mn :Co) avec 50% Mn - 50% Co ; matériau réempilé Restack-2-(3Mn :Co) avec 75% Mn - 25% Co ; en bas, oxyde de manganèse initial H_K-birn. (*) correspondent aux raies caractéristiques de H_K-birn lines et (°) aux raies des phases$\beta 3$

B.3.3.2. Influence de la méthode de réempilement

L'influence de la méthode de réempilement a été étudiée en fixant le ratio Mn :Co à 50 :50. Ainsi, les matériaux réempilés sont comparés à un matériau obtenu par simple broyage mécanique des phases initiales. Les diffractogrammes des rayons X (Figure B.13) des trois matériaux montrent une superposition des raies caractéristiques des matériaux initiaux. Ceci permet de conclure que le broyage et les processus d'exfoliation/réempilement donnent lieu à des matériaux composites. Cependant, les images de MEB-EDS associées permettent de les différencier. Le matériau obtenu par simple broyage correspond à un microcomposite : il y a une claire distinction entre les particules à base de Mn (en rouge) et les particules à base de Co (en vert). Le réempilement après mélange des suspensions colloïdales puis acidification permet d'accéder à un nanocomposite, avec un mélange intime des deux phases initiales. Enfin, il est possible de conclure que le matériau réempilé obtenu après acidification des suspensions colloïdales puis mélange est encore plus homogène, avec des zones de “jaune” où il y a réelle superposition des deux phases. Cette technique de réempilement permet d'accéder à un nanocomposite homogène d'oxyde de

Mn et d'oxyhydroxyde de Co.

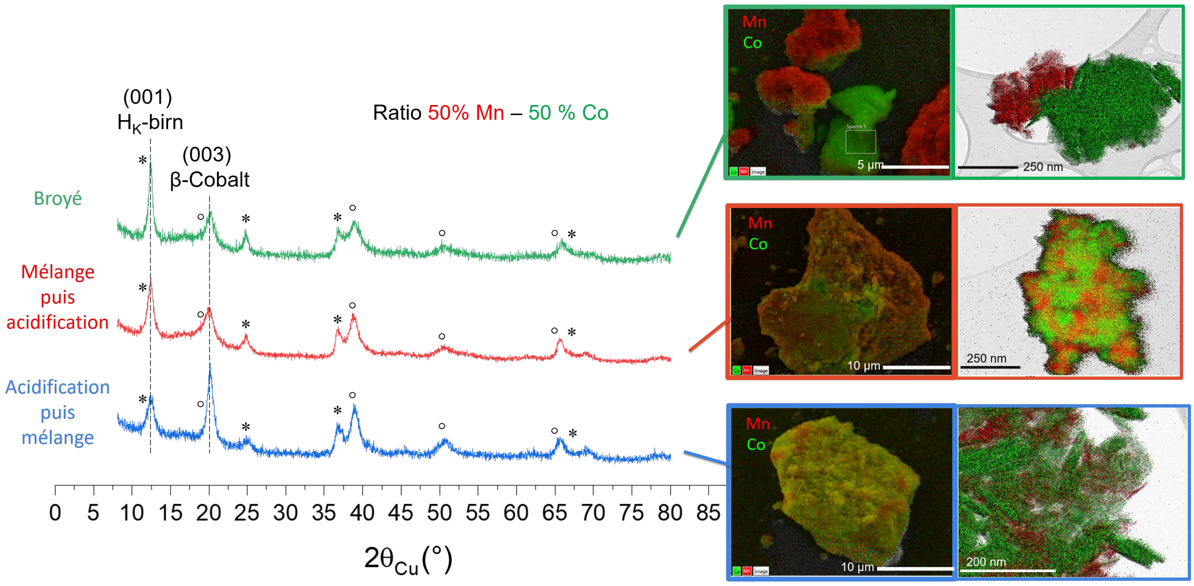

Figure B.13. : Diffractogrammes de rayons X et images MEB-EDS associées aux matériaux obtenus par exfoliation/réempilement de H_K-birn et β3-prec selon différentes méthodes. De haut en bas : simple broyage mécanique des poudres initiales, mélange des suspensions colloïdales puis acidification à un pH optimal de 4.5, acidification des suspensions colloïdales puis mélange. (*) correspond à la phase H_K-birn et (°) aux oxyhydroxydes de β3-cobalt.

B.3.3.3. Propriétés électrochimiques

Les composites obtenus par exfoliation/réempilement ont été étudiés en matériaux d'électrodes afin d'en déterminer les performances électrochimiques. La Figure B.14 montre les courbes de voltamétrie cyclique ainsi que les capacités des matériaux obtenus en fonction de la vitesse de balayage. D'emblée, nous observons que les matériaux réempilés ont une signature électrochimique plus rectangulaire. Ceci indique une diminution de la résistance intrinsèque à l'électrode. De plus, cette amélioration est d'autant plus visible lorsque la vitesse de balayage est augmentée.

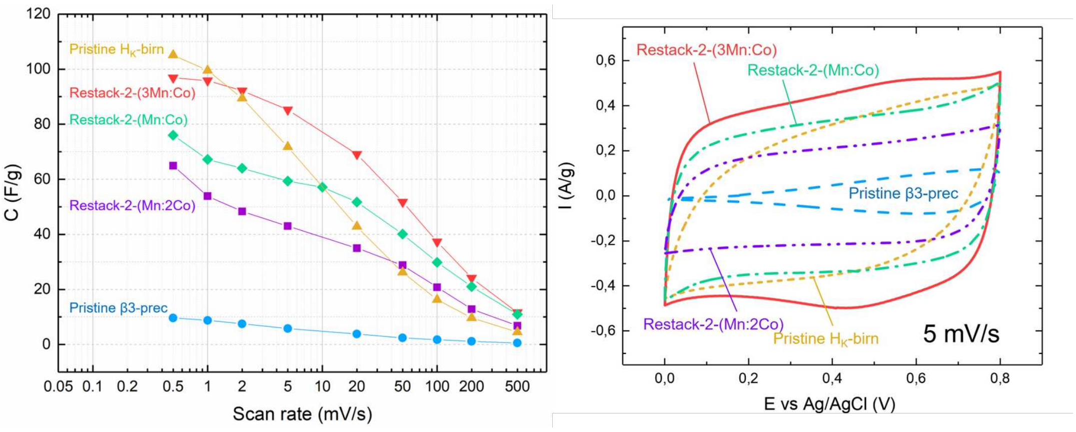

Figure B.14. : Gauche : capacités spécifiques (normalisées à la masse de matière active) en fonction de la vitesse de balayage, obtenues pour les matériaux réempilés Restack-2-(Mn :Co), Restack-2-(3Mn :Co), Restack-2-(Mn-2Co) comparés aux matériaux initiaux H$_K$-birn et β3-prec. Droite : courbes de voltamétrie cyclique obtenues pour les mêmes matériaux à 5 mV/s.

De même, il est possible de constater, sur la Figure B.15, que selon la méthode de réempilement, les performances électrochimiques vont différer. Pour un même ratio molaire, le matériau réempilé obtenu après acidification puis mélange des suspensions colloïdales, de par sa grande homogénéité, affiche les meilleures capacités à haute vitesse de balayage.

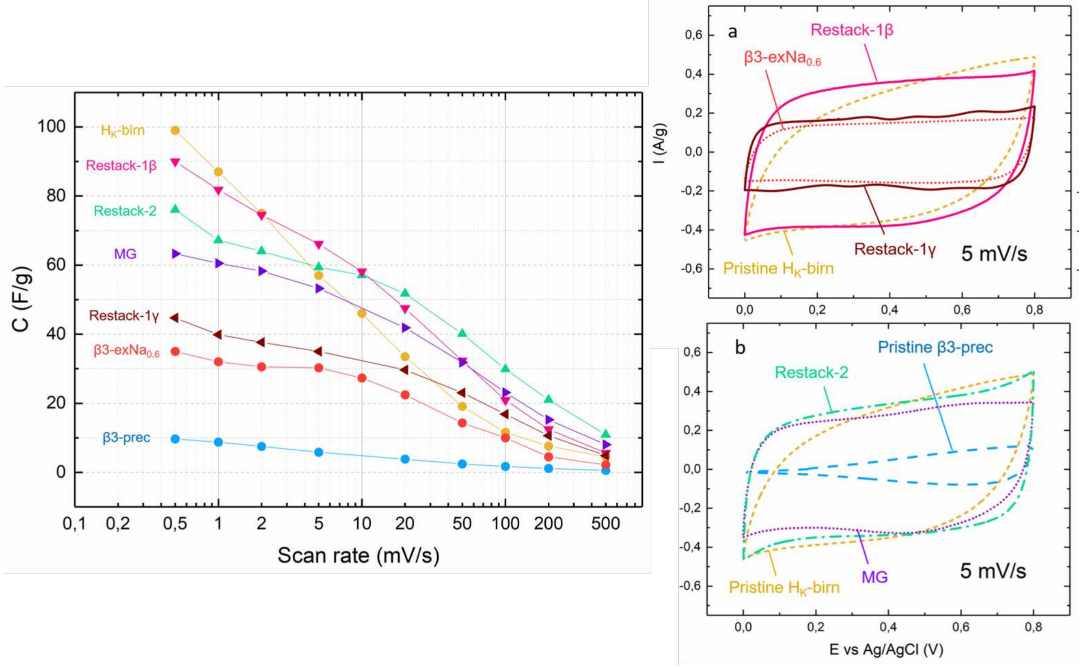

Figure B.15. : Gauche : capacités spécifiques (normalisées à la masse de matière active) en fonction de la vitesse de balayage, obtenues pour les matériaux réempilés Restack-1β, Restack-2, Restack-1γ, le composite obtenu par broyage MG comparés aux matériaux initiaux H$_K$-birn et β3-prec et β3-exNa$_{0.6}$. Droite : courbes de voltamétrie cyclique obtenues pour les mêmes matériaux à 5 mV/s.

La synthèse de matériaux par exfoliation/réempilement est d'autant plus intéressante que les matériaux obtenus présentent des capacités plus élevées, mais aussi une meilleure cyclabilité. Ceci est illustré dans la Figure B.16. On constate que les nanocomposites obtenus vont avoir une capacité quasi-constante sur plus de 10 000 cycles, ce qui est exceptionnel pour des oxydes lamellaires.

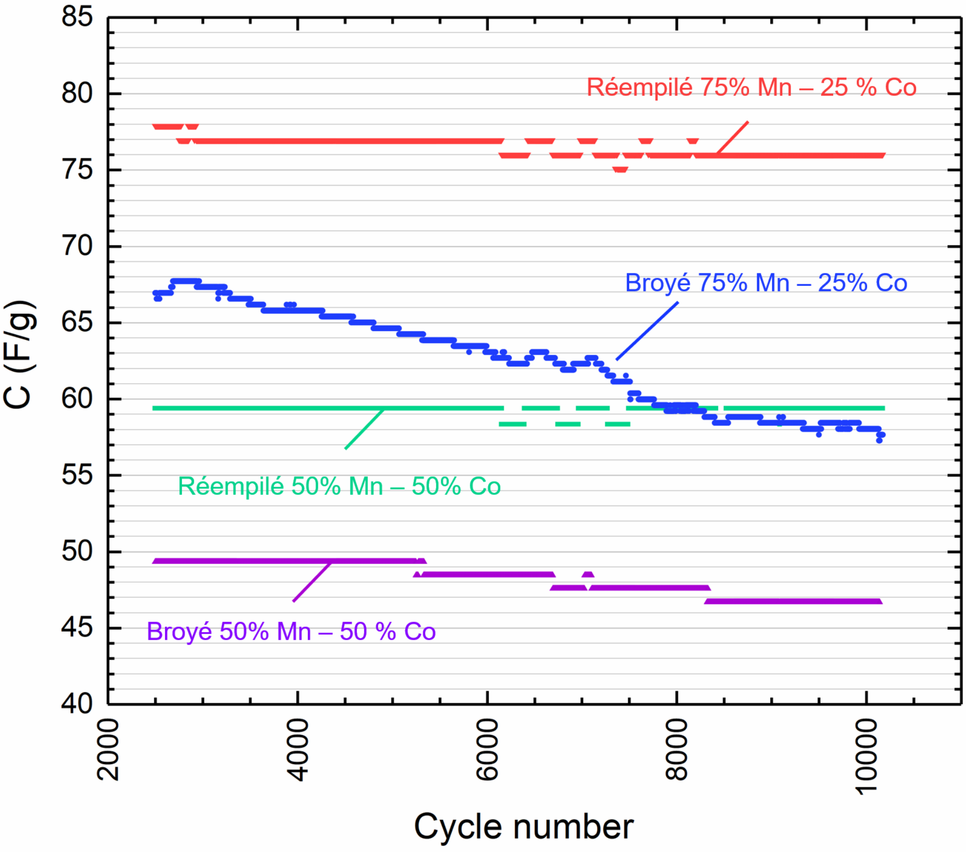

Figure B.16. : Capacités spécifiques en fonction du nombre de cycles, obtenues pour le matériau réempilé Restack-2-(Mn :Co) avec 50% Mn - 50% Co (vert) ; le matériau réempilé Restack-2-(3Mn :Co) avec 75% Mn - 25% Co (rouge) ; le composite obtenu par broyage MG-(Mn :Co) avec 50% Mn - 50% Co (violet) ; et le composite obtenu par broyage MG-(3Mn :Co) avec 75% Mn - 25% Co (bleu). Le cyclage a été réalisé en cellule à 3 électrodes à 10 mV/s. La capacité est normalisée à la masse de matière active.

Conclusion

L'objectif de ce travail est de synthétiser de nouveaux matériaux d'électrodes à base d'oxyde lamellaires de Mn pour des applications en tant qu'électrode de supercondensateurs. En effet, les oxydes de manganèse sont d'excellents matériaux pseudocapacitifs mais assez peu conducteurs électroniques. Pour y pallier, on cherche à améliorer cette conductivité en les associant avec des oxydes de cobalt conducteurs. Pour cela, une approche « architecturale » de synthèse de matériaux a été choisie. En partant d'oxydes de Mn et de Co lamellaires, ceux-ci sont exfoliés pour obtenir des nanofeuillets de nature différente. S'ensuit une étape de réempilement pour aboutir à un matériau lamellaire alterné. L'analyse structurale et morphologique des matériaux prouve que des nanocomposites très finement divisés sont obtenus. Les propriétés électrochimiques obtenues pour ces nanocomposites s'avèrent meilleures que celles des matériaux initiaux, tant en densité d'énergie qu'en puissance. Cette stratégie originale est prometteuse et ouvre la voie à des réempilements de différente nature, impliquant notamment le graphène.

Bibliography

[1] T. Kousksou, P. Bruel, A. Jamil, T. El Rhafiki, and Y. Zeraouli. Energy storage: Applications and challenges. *Solar Energy Materials and Solar Cells*, 120:59–80, January 2014.

[2] Martin Winter and Ralph J. Brodd. What Are Batteries, Fuel Cells, and Supercapacitors? *Chemical Reviews*, 104(10):4245–4270, October 2004.

[3] J.-M. Tarascon and M. Armand. Issues and challenges facing rechargeable lithium batteries. *Nature*, 414(6861):359–367, November 2001.

[4] Patrice Simon, Yury Gogotsi, and Bruce Dunn. Where Do Batteries End and Supercapacitors Begin? *Science*, 343(6176):1210–1211, March 2014.

[5] Andrew Burke. R&D considerations for the performance and application of electrochemical capacitors. *Electrochimica Acta*, 53(3):1083–1091, December 2007.

[6] Patrice Simon and Yury Gogotsi. Materials for electrochemical capacitors. *Nature Materials*, 7(11):845–854, November 2008.

[7] Jintao Zhang and X. S. Zhao. On the Configuration of Supercapacitors for Maximizing Electrochemical Performance. *ChemSusChem*, 5(5):818–841, May 2012.

[8] V. Subramanian, C. Luo, A.M. Stephan, K.S. Nahm, S. Thomas, and B. Wei. Supercapacitors from Activated Carbon Derived from Banana Fibers. *Journal of Physical Chemistry C*, 111(20):7527–7531, May 2007.

[9] A. G. Pandolfo and A. F. Hollenkamp. Carbon properties and their role in supercapacitors. *Journal of Power Sources*, 157(1):11–27, June 2006.

[10] Mingjia Zhi, Chengcheng Xiang, Jiangtian Li, Ming Li, and Nianqiang Wu. Nanostructured carbon–metal oxide composite electrodes for supercapacitors: a review. *Nanoscale*, 5(1):72–88, December 2012.

[11] Veronica Augustyn, Patrice Simon, and Bruce Dunn. Pseudocapacitive oxide materials for high-rate electrochemical energy storage. *Energy & Environmental Science*, 7(5):1597–1614, April 2014.

[12] Deepak P. Dubal and Rudolf Holze. Synthesis, properties, and performance of nanostructured metal oxides for supercapacitors. *Pure and Applied Chemistry*, 86(5), January 2014.

[13] J. P. Cheng, J. Zhang, and F. Liu. Recent development of metal hydroxides as electrode material of electrochemical capacitors. *RSC Advances*, 4(73):38893–38917, August 2014.

[14] Ming Huang, Fei Li, Fan Dong, Yu Xin Zhang, and Li Li Zhang. MnO 2-based nanostructures for high-performance supercapacitors. *Journal of Materials Chemistry A*, 3(43):21380–21423, 2015.

[15] T. Brousse, M. Toupin, and D. Bélanger. A Hybrid Activated Carbon-Manganese Dioxide Capacitor using a Mild Aqueous Electrolyte. *Journal of the Electrochemical Society*, 151(4):A614–A622, 2004.

[16] V. Khomenko, E. Raymundo-Piñero, and F. Béguin. Optimisation of an asymmetric manganese oxide/activated carbon capacitor working at 2 V in aqueous medium. *Journal of Power Sources*, 153(1):183–190, January 2006.

[17] F. Wang, S. Xiao, Y. Hou, C. Hu, L. Liu, and Y. Wu. Electrode materials for aqueous asymmetric supercapacitors. *RSC Advances*, 3(32):13059–13084, 2013.

[18] M. Butel, L. Gautier, and C. Delmas. Cobalt oxyhydroxides obtained by 'chimie douce' reactions: structure and electronic conductivity properties. *Solid State Ionics*, 122(1–4):271–284, July 1999.

[19] G. Godillot, L. Guerlou-Demourgues, P.-L. Taberna, P. Simon, and C. Delmas. Original Conductive Nano-Co3o4 Investigated as Electrode Material for Hybrid Supercapacitors. *Electrochemical and Solid-State Letters*, 14(10):A139–A142, October 2011.

[20] Joseph V. Stewart. *Intermediate Electromagnetic Theory*. World Scientific, 2001. Google-Books-ID: mwLI4nQ0thQC.

[21] Gordon Keith Chalmers. The Lodestone and the Understanding of Matter in Seventeenth Century England. *Philosophy of Science*, 4(1):75–95, January 1937.

[22] Letter IV: Benjamin Franklin to Peter Collinson, (Bigelow vol II p. 237-253), April 1749.

[23] Richard Shelton Kirby. *Engineering in History*. Dover Civil and Mechanical Engineering.

[24] Professor Helmholtz. XLII.—On the modern development of Faraday's conception of electricity. 39(0):277–304, January 1881.

[25] Low voltage electrolytic capacitor. Classification aux États-Unis 361/508, 429/212; Classification internationale H01G9/00, H01G9/155; Classification coopérative H01G9/155; Classification européenne H01G9/155.

[26] Electrical energy storage apparatus. Classification aux {É}tats-Unis 429/200, 429/222, 429/219, 361/434, 429/206, 429/231.8, 429/204; Classification internationale H01G9/00, H01M10/36; Classification coopérative H01M10/36, H01G9/0029, Y02E60/12; Classification européenne H01M10/36, H01G9/00M.

[27] Augustin Privat-Deschanel. *Elementary Treatise on Natural Philosophy*, volume Part 3 : Electricity and Magnetism. D. Appleton and Company, 1878. Google-Books-ID: jasLAAAAYAAJ.

[28] B. E. Conway. *Electrochemical supercapacitors: scientific fundamentals and technological applications*. Plenum Press, New York, 1999. OCLC: 245751293.

[29] M. Mallouki, F. Tran-Van, C. Sarrazin, C. Chevrot, and J. F. Fauvarque. Electrochemical storage of polypyrrole–Fe2o3 nanocomposites in ionic liquids. *Electrochimica Acta*, 54(11):2992–2997, April 2009.

[30] Linpo Yu and George Z. Chen. High energy supercapattery with an ionic liquid solution of LiClO4. *Faraday Discussions*, 190(0):231–240, August 2016.

[31] Girum Ayalneh Tiruye, David Muñoz-Torrero, Jesus Palma, Marc Anderson, and Rebeca Marcilla. Performance of solid state supercapacitors based on polymer electrolytes containing different ionic liquids. *Journal of Power Sources*, 2016.

[32] A. Balducci. Electrolytes for high voltage electrochemical double layer capacitors: A perspective article. *Journal of Power Sources*, 2016.

[33] Yinyu Xiang, Junsheng Li, Jiaheng Lei, Dan Liu, Zhizhong Xie, Deyu Qu, Ke Li, Tengfei Deng, and Haolin Tang. Advanced Separators for Lithium-Ion and Lithium–Sulfur Batteries: A Review of Recent Progress. *ChemSusChem*, 9(21):3023–3039, November 2016.

[34] B. E. Conway, V. Birss, and J. Wojtowicz. The role and utilization of pseudocapacitance for energy storage by supercapacitors. *Journal of Power Sources*, 66(1–2):1–14, May 1997.

[35] J.P. Zheng, P.J. Cygan, and T.R. Jow. Hydrous ruthenium oxide as an electrode material for electrochemical capacitors. *Journal of the Electrochemical Society*, 142(8):2699–2703, 1995.

[36] Nokia 3310, July 2017. Page Version ID: 792088214.

[37] Albert N. Link, Alan C. O'Connor, and Troy J. Scott. *Battery Technology for Electric Vehicles: Public Science and Private Innovation*. Routledge, April 2015. Google-Books-ID: OpYGCAAAQBAJ.

[38] Mouad Dahbi, Fouad Ghamouss, François Tran-Van, Daniel Lemordant, and Mérièm Anouti. Comparative study of EC/DMC LiTFSI and LiPF6 electrolytes for electrochemical storage. *Journal of Power Sources*, 196(22):9743–9750, November 2011.

[39] H. Sato, D. Takahashi, T. Nishina, and I. Uchida. Electrochemical characterization of thin-film LiCoO2 electrodes in propylene carbonate solutions. *Journal of Power Sources*, 68(2):540–544, 1997.

[40] H. Helmholtz. Studien über electrische Grenzschichten. *Annalen der Physik*, 243:337–382, 1879.

[41] David C. Grahame. The Electrical Double Layer and the Theory of Electrocapillarity. *Chemical Reviews*, 41(3):441–501, December 1947.

[42] A. K. Geim. Graphene: Status and Prospects. *Science*, 324(5934):1530–1534, June 2009.

[43] K. Jurewicz, K. Babeł, A. Źiółkowski, and H. Wachowska. Ammoxidation of active carbons for improvement of supercapacitor characteristics. *Electrochimica Acta*, 48(11):1491–1498, 2003.

[44] Andrzej Lewandowski, Angelika Olejniczak, Maciej Galinski, and Izabela Stepniak. Performance of carbon–carbon supercapacitors based on organic, aqueous and ionic liquid electrolytes. *Journal of Power Sources*, 195(17):5814–5819, September 2010.

[45] Juan Mi, Xiao-Rong Wang, Rui-Jun Fan, Wen-Hui Qu, and Wen-Cui Li. Coconut-Shell-Based Porous Carbons with a Tunable Micro/Mesopore Ratio for High-Performance Supercapacitors. *Energy & Fuels*, 26(8):5321–5329, August 2012.

[46] Erman Taer, Mohamad Deraman, Ibrahim Abu Talib, Akrajas Ali Umar, Munetaka Oyama, and Rozan Mohamad Yunus. Physical, electrochemical and supercapacitive properties of activated carbon pellets from pre-carbonized rubber wood sawdust by CO2 activation. *Current Applied Physics*, 10(4):1071–1075, July 2010.

[47] S. T. Mayer, R. W. Pekala, and J. L. Kaschmitter. The Aerocapacitor: An Electrochemical Double-Layer Energy-Storage Device. *Journal of The Electrochemical Society*, 140(2):446–451, February 1993.

[48] Dingshan Yu and Liming Dai. Self-Assembled Graphene/Carbon Nanotube Hybrid Films for Supercapacitors. *The Journal of Physical Chemistry Letters*, 1(2):467–470, January 2010.

[49] Martti Kaempgen, Candace K. Chan, J. Ma, Yi Cui, and George Gruner. Printable Thin Film Supercapacitors Using Single-Walled Carbon Nanotubes. *Nano Letters*, 9(5):1872–1876, May 2009.

[50] Rahul R. Salunkhe, Ying-Hui Lee, Kuo-Hsin Chang, Jing-Mei Li, Patrice Simon, Jing Tang, Nagy L. Torad, Chi-Chang Hu, and Yusuke Yamauchi. Nanoarchitectured Graphene-Based Supercapacitors for Next-Generation Energy-Storage Applications. *Chemistry – A European Journal*, 20(43):13838–13852, 2014.

[51] S. R. C. Vivekchand, Chandra Sekhar Rout, K. S. Subrahmanyam, A. Govindaraj, and C. N. R. Rao. Graphene-based electrochemical supercapacitors. *Journal of Chemical Sciences*, 120(1):9–13, January 2008.

[52] Xian Du, Peng Guo, Huaihe Song, and Xiaohong Chen. Graphene nanosheets as electrode material for electric double-layer capacitors. *Electrochimica Acta*, 55(16):4812–4819, June 2010.

[53] A.K. Geim and K.S. Novoselov. The rise of graphene. In *Nanoscience and Technology: A Collection of Reviews from Nature Journals*, pages 11–19. 2009. DOI: 10.1142/9789814287005_0002.

[54] Qing-Yu Li, Ze-Sheng Li, Lin Lin, X. Y. Wang, Yan-Fang Wang, Chu-Hua Zhang, and Hong-Qiang Wang. Facile synthesis of activated carbon/carbon nanotubes compound for supercapacitor application. *Chemical Engineering Journal*, 156(2):500–504, January 2010.

[55] Kwang Sun Ryu, Kwang Man Kim, Nam-Gyu Park, Yong Joon Park, and Soon Ho Chang. Symmetric redox supercapacitor with conducting polyaniline electrodes. *Journal of Power Sources*, 103(2):305–309, January 2002.

[56] Zi-Hang Huang, Yu Song, Xin-Xin Xu, and Xiao-Xia Liu. Ordered Polypyrrole Nanowire Arrays Grown on a Carbon Cloth Substrate for a High-Performance Pseudocapacitor Electrode. *ACS Applied Materials & Interfaces*, 7(45):25506–25513, November 2015.

[57] Yadi Zhang, Zhongai Hu, Yufeng An, Bingshu Guo, Ning An, Yarong Liang, and Hongying Wu. High-performance symmetric supercapacitor based on manganese

oxyhydroxide nanosheets on carbon cloth as binder-free electrodes. *Journal of Power Sources*, 311:121–129, 2016.

[58] R. Holze and Y.P. Wu. Intrinsically conducting polymers in electrochemical energy technology: Trends and progress. *Electrochimica Acta*, 122:93–107, March 2014.

[59] Rudolf Holze. Copolymers—A refined way to tailor intrinsically conducting polymers. *Electrochimica Acta*, 56(28):10479–10492, December 2011.

[60] Graeme A. Snook, Pon Kao, and Adam S. Best. Conducting-polymer-based supercapacitor devices and electrodes. *Journal of Power Sources*, 196(1):1–12, January 2011.

[61] Tat'yana Vladimirovna Vernitskaya and Oleg Nikolaevich Efimov. Polypyrrole: a conducting polymer; its synthesis, properties and applications. *Russian Chemical Reviews*, 66(5):443–457, 1997.

[62] Kwang Sun Ryu, Soon Ho Chang, Seong-Gu Kang, Eung Ju Oh, and Chul Hyun Yo. Physicochemical and electrical characterization of polyaniline induced by crosslinking, stretching and doping. *Bull. Korean Chem. Soc*, 20(3):333, 1999.

[63] A. Laforgue, P. Simon, C. Sarrazin, and J.-F. Fauvarque. Polythiophene-based supercapacitors. *Journal of Power Sources*, 80(1):142–148, 1999.

[64] A. Laforgue, P. Simon, and J.-F. Fauvarque. Chemical synthesis and characterization of fluorinated polyphenylthiophenes: Application to energy storage. *Synthetic Metals*, 123(2):311–319, 2001.

[65] A. Rudge, J. Davey, I. Raistrick, S. Gottesfeld, and J.P. Ferraris. Conducting polymers as active materials in electrochemical capacitors. *Journal of Power Sources*, 47(1-2):89–107, 1994.

[66] H. Talbi, P.-E. Just, and L. H. Dao. Electropolymerization of aniline on carbonized polyacrylonitrile aerogel electrodes: applications for supercapacitors. *Journal of Applied Electrochemistry*, 33(6):465–473, June 2003.

[67] Hee Y. Lee and J. B. Goodenough. Supercapacitor Behavior with KCl Electrolyte. *Journal of Solid State Chemistry*, 144(1):220–223, April 1999.

[68] C. P. De Pauli and S. Trasatti. Electrochemical surface characterization of IrO$_2$ + SnO2 mixed oxide electrocatalysts. *Journal of Electroanalytical Chemistry*, 396(1–2):161–168, October 1995.

[69] Kuo-Chuan Liu and Marc A. Anderson. Porous nickel oxide/nickel films for electrochemical capacitors. *Journal of the Electrochemical Society*, 143(1):124–130, 1996.

[70] C. Arbizzani, M.C. Gallazzi, M. Mastragostino, M. Rossi, and F. Soavi. Capacitance and cycling stability of poly(alkoxythiophene) derivative electrodes. *Electrochemistry Communications*, 3(1):16–19, 2001.

[71] M. Mastragostino, C. Arbizzani, and F. Soavi. Conducting polymers as electrode materials in supercapacitors. *Solid State Ionics*, 148(3-4):493–498, 2002.

[72] A. Laforgue, P. Simon, J. F. Fauvarque, J. F. Sarrau, and P. Lailler. Hybrid Supercapacitors Based on Activated Carbons and Conducting Polymers. *Journal of The Electrochemical Society*, 148(10):A1130–A1134, October 2001.

[73] Thierry Brousse, Pierre-Louis Taberna, Olivier Crosnier, Romain Dugas, Philippe Guillemet, Yves Scudeller, Yingke Zhou, Frédéric Favier, Daniel Bélanger, and Patrice Simon. Long-term cycling behavior of asymmetric activated carbon/MnO2 aqueous electrochemical supercapacitor. *Journal of Power Sources*, 173(1):633–641, November 2007.

[74] V. Khomenko, E. Raymundo-Piñero, E. Frackowiak, and F. Béguin. High-voltage asymmetric supercapacitors operating in aqueous electrolyte. *Applied Physics A*, 82(4):567–573, November 2005.

[75] Encarnación Raymundo-Piñero, Martin Cadek, and François Béguin. Tuning Carbon Materials for Supercapacitors by Direct Pyrolysis of Seaweeds. *Advanced Functional Materials*, 19(7):1032–1039, April 2009.

[76] Zhibin Lei, Nikolay Christov, Li Li Zhang, and X. S. Zhao. Mesoporous carbon nanospheres with an excellent electrocapacitive performance. *Journal of Materials Chemistry*, 21(7):2274–2281, February 2011.

[77] Ali Izadi-Najafabadi, Satoshi Yasuda, Kazufumi Kobashi, Takeo Yamada, Don N. Futaba, Hiroaki Hatori, Motoo Yumura, Sumio Iijima, and Kenji Hata. Extracting the Full Potential of Single-Walled Carbon Nanotubes as Durable Supercapacitor Electrodes Operable at 4 V with High Power and Energy Density. *Advanced Materials*, 22(35):E235–E241, September 2010.

[78] Y. Zhu, S. Murali, M. D. Stoller, K. J. Ganesh, W. Cai, P. J. Ferreira, A. Pirkle, R. M. Wallace, K. A. Cychosz, M. Thommes, D. Su, E. A. Stach, and R. S. Ruoff. Carbon-Based Supercapacitors Produced by Activation of Graphene. *Science*, 332(6037):1537–1541, June 2011.

[79] Zhong-Shuai Wu, Da-Wei Wang, Wencai Ren, Jinping Zhao, Guangmin Zhou, Feng Li, and Hui-Ming Cheng. Anchoring Hydrous RuO2 on Graphene Sheets for High-Performance Electrochemical Capacitors. *Advanced Functional Materials*, 20(20):3595–3602, October 2010.

[80] T. Cottineau, M. Toupin, T. Delahaye, T. Brousse, and D. Bélanger. Nanostructured transition metal oxides for aqueous hybrid electrochemical supercapacitors. *Applied Physics A*, 82(4):599–606, March 2006.

[81] Wendy G. Pell and Brian E. Conway. Peculiarities and requirements of asymmetric capacitor devices based on combination of capacitor and battery-type electrodes. *Journal of Power Sources*, 136(2):334–345, October 2004.

[82] C. Decaux, G. Lota, E. Raymundo-Piñero, E. Frackowiak, and F. Béguin. Electrochemical performance of a hybrid lithium-ion capacitor with a graphite anode preloaded from lithium bis(trifluoromethane)sulfonimide-based electrolyte. *Electrochimica Acta*, 86:282–286, December 2012.

[83] X. Wang and J. P. Zheng. The Optimal Energy Density of Electrochemical Capacitors Using Two Different Electrodes. *Journal of The Electrochemical Society*, 151(10):A1683–A1689, October 2004.

[84] Linpo Yu and George Z. Chen. Redox electrode materials for supercapatteries. *Journal of Power Sources*, 2016.

[85] Fan Zhang, Tengfei Zhang, Xi Yang, Long Zhang, Kai Leng, Yi Huang, and Yongsheng Chen. A high-performance supercapacitor-battery hybrid energy storage device based on graphene-enhanced electrode materials with ultrahigh energy density. *Energy & Environmental Science*, 6(5):1623–1632, April 2013.

[86] Steven A. Klankowski, Gaind P. Pandey, Gary A. Malek, Judy Wu, Ronald A. Rojeski, and Jun Li. A Novel High-Power Battery-Pseudocapacitor Hybrid Based on Fast Lithium Reactions in Silicon Anode and Titanium Dioxide Cathode Coated on Vertically Aligned Carbon Nanofibers. *Electrochimica Acta*, 178:797–805, October 2015.

[87] Sho Makino, Yuto Shinohara, Takayuki Ban, Wataru Shimizu, Keita Takahashi, Nobuyuki Imanishi, and Wataru Sugimoto. 4 V class aqueous hybrid electrochemical capacitor with battery-like capacity. *RSC Advances*, 2(32):12144–12147, November 2012.

[88] Sho Makino, Rie Yamamoto, Shigeyuki Sugimoto, and Wataru Sugimoto. Room temperature performance of 4 V aqueous hybrid supercapacitor using multi-layered lithium-doped carbon negative electrode. *Journal of Power Sources*, 2016.

[89] Gyoung Hwa Jeong, Seungmin Baek, Seungyeol Lee, and Sang-Wook Kim. Metal Oxide/Graphene Composites for Supercapacitive Electrode Materials. *Chemistry - An Asian Journal*, 11(7):949–964, April 2016.

[90] Wei Wei, Yongcheng Wang, Hao Wu, Abdullah M. Al-Enizi, Lijuan Zhang, and Gengfeng Zheng. Transition metal oxide hierarchical nanotubes for energy applications. *Nanotechnology*, 27(2):02LT01, 2016.

[91] Z.-S. Wu, G. Zhou, L.-C. Yin, W. Ren, F. Li, and H.-M. Cheng. Graphene/metal oxide composite electrode materials for energy storage. *Nano Energy*, 1(1):107–131, 2012.

[92] Guihua Yu, Xing Xie, Lijia Pan, Zhenan Bao, and Yi Cui. Hybrid nanostructured materials for high-performance electrochemical capacitors. *Nano Energy*, 2(2):213–234, March 2013.

[93] Suzana Sopčić, Marijana Kraljić Roković, Zoran Mandić, and György Inzelt. Preparation and characterization of RuO2/polyaniline composite electrodes. *Journal of Solid State Electrochemistry*, 14(11):2021–2026, November 2010.

[94] M. Mallouki, F. Tran-Van, C. Sarrazin, P. Simon, B. Daffos, A. De, C. Chevrot, and J. F. Fauvarque. Polypyrrole-Fe2o3 nanohybrid materials for electrochemical storage. *Journal of Solid State Electrochemistry*, 11(3):398–406, May 2006.

[95] X. Qin, S. Durbach, and G. T. Wu. Electrochemical characterization on RuO2 · xH2o/carbon nanotubes composite electrodes for high energy density supercapacitors. *Carbon*, 42(2):451–453, 2004.

[96] A. Ghosh, E.J. Ra, M. Jin, H.-K. Jeong, T.H. Kim, C. Biswas, and Y.H. Lee. High pseudocapacitance from ultrathin V2o5 films electrodeposited on self-standing carbon-nanofiber paper. *Advanced Functional Materials*, 21(13):2541–2547, 2011.

[97] Y. Liang, M.G. Schwab, L. Zhi, E. Mugnaioli, U. Kolb, X. Feng, and K. Müllen. Direct access to metal or metal oxide nanocrystals integrated with one-dimensional

nanoporous carbons for electrochemical energy storage. *Journal of the American Chemical Society*, 132(42):15030–15037, 2010.

[98] Dan Luo, Cameron J. Wallar, Kaiyuan Shi, and Igor Zhitomirsky. Enhanced capacitive performance of MnO2- multiwalled carbon nanotube electrodes, prepared using lauryl gallate dispersant. *Colloids and Surfaces A: Physicochemical and Engineering Aspects*, 509:504–511, November 2016.

[99] Thomas M. Higgins, David McAteer, Joao Carlos Mesquita Coelho, Beatriz Mendoza Sanchez, Zahra Gholamvand, Greg Moriarty, Niall McEvoy, Nina Christina Berner, Georg Stefan Duesberg, Valeria Nicolosi, and others. Effect of percolation on the capacitance of supercapacitor electrodes prepared from composites of manganese dioxide nanoplatelets and carbon nanotubes. *ACS nano*, 8(9):9567–9579, 2014.

[100] Guoxiang Xin, Yanhui Wang, Jinhui Zhang, Shaopei Jia, Jianbing Zang, and Yafei Wang. A self-supporting graphene/MnO2 composite for high-performance supercapacitors. *International Journal of Hydrogen Energy*, 40(32):10176–10184, 2015.

[101] Y. Su and I. Zhitomirsky. Influence of Dopants on Performance of Polypyrrole Coated Carbon Nanotube Electrodes and Devices. *Journal of The Electrochemical Society*, 162(5):A5013–A5019, January 2015.

[102] M. Toupin, T. Brousse, and D. Bélanger. Charge storage mechanism of MnO2 electrode used in aqueous electrochemical capacitor. *Chemistry of Materials*, 16(16):3184–3190, 2004.

[103] Chi-Chang Hu and Ta-Wang Tsou. Ideal capacitive behavior of hydrous manganese oxide prepared by anodic deposition. *Electrochemistry Communications*, 4(2):105–109, February 2002.

[104] Thierry Brousse, Mathieu Toupin, Romain Dugas, Laurence Athouël, Olivier Crosnier, and Daniel Bélanger. Crystalline MnO2 as Possible Alternatives to Amorphous Compounds in Electrochemical Supercapacitors. *Journal of The Electrochemical Society*, 153(12):A2171–A2180, December 2006.

[105] David Portehault. *Synthèse par chimie douce en milieu aqueux d'oxydes de manganèse nano-structurés. Des matériaux pour batteries au lithium ?* PhD thesis, Université Pierre et Marie Curie, 2008.

[106] S. W. Donne, A. F. Hollenkamp, and B. C. Jones. Structure, morphology and electrochemical behaviour of manganese oxides prepared by controlled decomposition of permanganate. *Journal of Power Sources*, 195(1):367–373, January 2010.

[107] S. Devaraj and N. Munichandraiah. Effect of Crystallographic Structure of MnO2 on Its Electrochemical Capacitance Properties. *The Journal of Physical Chemistry C*, 112(11):4406–4417, March 2008.

[108] Suh-Cem Pang, Marc A. Anderson, and Thomas W. Chapman. Novel Electrode Materials for Thin-Film Ultracapacitors: Comparison of Electrochemical Properties of Sol-Gel-Derived and Electrodeposited Manganese Dioxide. *Journal of The Electrochemical Society*, 147(2):444–450, February 2000.

[109] Sun Wen, Joon-Woo Lee, In-Hyeong Yeo, Jongman Park, and Sun-il Mho. The role of cations of the electrolyte for the pseudocapacitive behavior of metal oxide electrodes, MnO2 and RuO2. *Electrochimica Acta*, 50(2):849–855, November 2004.

[110] Mathieu Toupin, Thierry Brousse, and Daniel Bélanger. Influence of Microstucture on the Charge Storage Properties of Chemically Synthesized Manganese Dioxide. *Chemistry of Materials*, 14(9):3946–3952, September 2002.

[111] Shin-Liang Kuo and Nae-Lih Wu. Investigation of Pseudocapacitive Charge-Storage Reaction of MnO2 nH2o Supercapacitors in Aqueous Electrolytes. *Journal of The Electrochemical Society*, 153(7):A1317–A1324, July 2006.

[112] Laurence Athouël, François Moser, Romain Dugas, Olivier Crosnier, Daniel Bélanger, and Thierry Brousse. Variation of the MnO2 Birnessite Structure upon Charge/Discharge in an Electrochemical Supercapacitor Electrode in Aqueous Na2so4 Electrolyte. *The Journal of Physical Chemistry C*, 112(18):7270–7277, May 2008.

[113] Ouassim Ghodbane, Fatemeh Ataherian, Nae-Lih Wu, and Frédéric Favier. In situ crystallographic investigations of charge storage mechanisms in MnO2-based electrochemical capacitors. *Journal of Power Sources*, 206:454–462, May 2012.

[114] Laura Coustan, Pierre Lannelongue, Paul Arcidiacono, and Frédéric Favier. Faradaic contributions in the supercapacitive charge storage mechanisms of manganese dioxides. *Electrochimica Acta*, 206:479–489, July 2016.

[115] Huajun Zheng, Fengqiu Tang, Melvin Lim, Aniruddh Mukherji, Xiaoxia Yan, Lianzhou Wang, and Gao Qing (Max) Lu. Multilayered films of cobalt oxyhydroxide nanowires/manganese oxide nanosheets for electrochemical capacitor. *Journal of Power Sources*, 195(2):680–683, January 2010.

[116] En-Hui Liu, Wen Li, Jian Li, Xiang-Yun Meng, Rui Ding, and Song-Ting Tan. Preparation and characterization of nanostructured NiO/MnO2 composite electrode for electrochemical supercapacitors. *Materials Research Bulletin*, 44(5):1122–1126, May 2009.

[117] J. Duay, E. Gillette, R. Liu, and S.B. Lee. Highly flexible pseudocapacitor based on freestanding heterogeneous MnO 2/conductive polymer nanowire arrays. *Physical Chemistry Chemical Physics*, 14(10):3329–3337, 2012.

[118] Michael P. Clark, Wei Qu, and Douglas G. Ivey. Nanostructured manganese oxide and manganese oxide/polyethylenedioxythiophene rods electrodeposited onto nickel foam for supercapacitor applications. *Journal of Applied Electrochemistry*, pages 1–11.

[119] Wenbin Ni, Dengchao Wang, Zhongjie Huang, Jianwei Zhao, and Guoeng Cui. Fabrication of nanocomposite electrode with MnO2 nanoparticles distributed in polyaniline for electrochemical capacitors. *Materials Chemistry and Physics*, 124(2–3):1151–1154, December 2010.

[120] Jianwei Liu, Jeremy Essner, and Jun Li. Hybrid Supercapacitor Based on Coaxially Coated Manganese Oxide on Vertically Aligned Carbon Nanofiber Arrays. *Chemistry of Materials*, 22(17):5022–5030, September 2010.

[121] Myeongjin Kim, Yongseon Hwang, and Jooheon Kim. Super-capacitive performance depending on different crystal structures of MnO2 in graphene/MnO2 composites for supercapacitors. *Journal of Materials Science*, 48(21):7652–7663, November 2013.

[122] Sheng Chen, Junwu Zhu, Xiaodong Wu, Qiaofeng Han, and Xin Wang. Graphene OxideMnO2 Nanocomposites for Supercapacitors. *ACS Nano*, 4(5):2822–2830, 2010.

[123] Hao Jiang, Chunzhong Li, Ting Sun, and Jan Ma. High-performance supercapacitor material based on Ni (OH) 2 nanowire-MnO 2 nanoflakes core–shell nanostructures. *Chemical Communications*, 48(20):2606–2608, 2012.

[124] Chuanjun Yuan, Haibo Lin, Haiyan Lu, Endong Xing, Yusi Zhang, and Bingyao Xie. Anodic preparation and supercapacitive performance of nano-Co3o4/MnO2 composites. *RSC Advances*, 4(110):64675–64682, 2014.

[125] Yun-Bo He, Gao-Ren Li, Zi-Long Wang, Cheng-Yong Su, and Ye-Xiang Tong. Single-crystal ZnO nanorod/amorphous and nanoporous metal oxide shell composites: Controllable electrochemical synthesis and enhanced supercapacitor performances. *Energy & Environmental Science*, 4(4):1288–1292, 2011.

[126] Myriam Douin, Liliane Guerlou-Demourgues, Michel Ménétrier, Emilie Bekaert, Lionel Goubault, Patrick Bernard, and Claude Delmas. Effect of Thermal Treatment on the Electronic Conductivity Properties of Cobalt Spinel Phases Synthesized by Electro-Oxidation in Ternary Alkaline Electrolyte (KOH, LiOH, NaOH). *Chemistry of Materials*, 20(21):6880–6888, November 2008.

[127] Kian Keat Lee, Wee Shong Chin, and Chorng Haur Sow. Cobalt-based compounds and composites as electrode materials for high-performance electrochemical capacitors. *J. Mater. Chem. A*, 2(41):17212–17248, August 2014.

[128] Wishvender K. Behl and Jorge E. Toni. Anodic oxidation of cobalt in potassium hydroxide electrolytes. *Journal of Electroanalytical Chemistry and Interfacial Electrochemistry*, 31(1):63–75, June 1971.

[129] Frédéric Tronel, Liliane Guerlou-Demourgues, Michel Ménétrier, Laurence Croguennec, Lionel Goubault, Patrick Bernard, and Claude Delmas. New Spinel Cobalt Oxides, Potential Conductive Additives for the Positive Electrode of NiMH Batteries. *Chemistry of Materials*, 18(25):5840–5851, December 2006.

[130] Sumanta Kumar Meher and G. Ranga Rao. Effect of Microwave on the Nanowire Morphology, Optical, Magnetic, and Pseudocapacitance Behavior of Co3o4. *The Journal of Physical Chemistry C*, 115(51):25543–25556, December 2011.

[131] Gérôme Godillot. *Electrodes pour supercondensateurs à base d'oxydes de cobalt conducteurs.* PhD thesis, Université Sciences et Technologies-Bordeaux I, 2012.

[132] Prasant Kumar Nayak and N. Munichandraiah. Cobalt Hydroxide as a Capacitor Material: Tuning Its Potential Window. *Journal of The Electrochemical Society*, 155(11):A855–A861, November 2008.

[133] Fedor S. Fedorov, Julia Linnemann, Kristina Tschulik, Lars Giebeler, Margitta Uhlemann, and Annett Gebert. Capacitance performance of cobalt hydroxide-

based capacitors with utilization of near-neutral electrolytes. *Electrochimica Acta*, 90:166–170, February 2013.

[134] Eiji Hosono, Shinobu Fujihara, Iraru Honma, Masaki Ichihara, and Haoshen Zhou. Synthesis of the CoOOH fine nanoflake film with the high rate capacitance property. *Journal of Power Sources*, 158(1):779–783, July 2006.

[135] A. D. Jagadale, D. P. Dubal, and C. D. Lokhande. Electrochemical behavior of potentiodynamically deposited cobalt oxyhydroxide (CoOOH) thin films for supercapacitor application. *Materials Research Bulletin*, 47(3):672–676, March 2012.

[136] Kai Zhang, Xiaopeng Han, Zhe Hu, Xiaolong Zhang, Zhanliang Tao, and Jun Chen. Nanostructured Mn-based oxides for electrochemical energy storage and conversion. *Chemical Society Reviews*, 44(3):699–728, 2015.

[137] Xiuhua Tang, Zong-huai Liu, Chengxiao Zhang, Zupei Yang, and Zenglin Wang. Synthesis and capacitive property of hierarchical hollow manganese oxide nanospheres with large specific surface area. *Journal of Power Sources*, 193(2):939–943, September 2009.

[138] Ping Wang, Yu-Jing Zhao, Li-Xiong Wen, Jian-Feng Chen, and Zhi-Gang Lei. Ultrasound–Microwave-Assisted Synthesis of MnO2 Supercapacitor Electrode Materials. *Industrial & Engineering Chemistry Research*, 53(52):20116–20123, December 2014.

[139] Ming Huang, Rui Mi, Hao Liu, Fei Li, Xiao Li Zhao, Wei Zhang, Shi Xuan He, and Yu Xin Zhang. Layered manganese oxides-decorated and nickel foam-supported carbon nanotubes as advanced binder-free supercapacitor electrodes. *Journal of Power Sources*, 269:760–767, December 2014.

[140] Bingcao Guo, Yibo Zhao, Wei Wu, Hong Meng, Haikui Zou, Jianfeng Chen, and Guangwen Chu. Research on the preparation technology of polyaniline nanofiber based on high gravity chemical oxidative polymerization. *Chemical Engineering and Processing: Process Intensification*, 70:1–8, August 2013.

[141] Xingyou Lang, Akihiko Hirata, Takeshi Fujita, and Mingwei Chen. Nanoporous metal/oxide hybrid electrodes for electrochemical supercapacitors. *Nature Nanotechnology*, 6(4):232–236, April 2011.

[142] Yonghe Li, Haoyu Fu, Yuefei Zhang, Zhenyu Wang, and Xiaodong Li. Kirkendall Effect Induced One-Step Fabrication of Tubular Ag/MnOx Nanocomposites for Supercapacitor Application. *The Journal of Physical Chemistry C*, 118(13):6604–6611, April 2014.

[143] Junjiao Chen, Ying Huang, Chao Li, Xuefang Chen, and Xiang Zhang. Synthesis of NiO@MnO2 core/shell nanocomposites for supercapacitor application. *Applied Surface Science*, 360:534–539, January 2016.

[144] Ziya Wang, Fengping Wang, Jianhai Tu, Dong Cao, Xixi An, and Yaping Ye. Nickel foam supported hierarchical mesoporous MnO 2/Ni (OH) 2 nanosheet networks for high performance supercapacitor electrode. *Materials Letters*, 171:10–13, 2016.

[145] Jai Bhagwan, V. Sivasankaran, K. L. Yadav, and Yogesh Sharma. Porous, one-dimensional and high aspect ratio nanofibric network of cobalt manganese oxide

as a high performance material for aqueous and solid-state supercapacitor (2 V). *Journal of Power Sources*, 327:29–37, September 2016.

[146] Byung Chul Kim, C. Justin Raj, Won-Je Cho, Won-Gil Lee, Hyeon Taek Jeong, and Kook Hyun Yu. Enhanced electrochemical properties of cobalt doped manganese dioxide nanowires. *Journal of Alloys and Compounds*, 617:491–497, December 2014.

[147] Guowei Zhang, Fei Ding, Lin Sang, Guiling Wang, Mengya Feng, Zhipeng Ma, and Guangjie Shao. Two-dimensional cobalt–manganese binary metal oxide porous nanosheets for high-performance supercapacitors. *Journal of Solid State Electrochemistry*, pages 1–8, 2016.

[148] Wen Lei, Ping He, Yuhao Wang, Xingquan Zhang, An Xia, and Faqin Dong. Solvothermal preparation of microspherical shaped cobalt–manganese oxide as electrode materials for supercapacitors. *Composites Science and Technology*, 102:82–86, October 2014.

[149] Hongwei Che, Yamei Lv, Aifeng Liu, Jingbo Mu, Xiaoliang Zhang, and Yongmei Bai. Facile synthesis of three dimensional flower-like Co3o4@MnO2 core-shell microspheres as high-performance electrode materials for supercapacitors. *Ceramics International*, 43(8):6054–6062, June 2017.

[150] Dezhi Kong, Jingshan Luo, Yanlong Wang, Weina Ren, Ting Yu, Yongsong Luo, Yaping Yang, and Chuanwei Cheng. Three-Dimensional Co3o4@MnO2 Hierarchical Nanoneedle Arrays: Morphology Control and Electrochemical Energy Storage. *Advanced Functional Materials*, 24(24):3815–3826, June 2014.

[151] Jinping Liu, Jian Jiang, Chuanwei Cheng, Hongxing Li, Jixuan Zhang, Hao Gong, and Hong Jin Fan. Co3o4 Nanowire@MnO2 Ultrathin Nanosheet Core/Shell Arrays: A New Class of High-Performance Pseudocapacitive Materials. *Advanced Materials*, 23(18):2076–2081, May 2011.

[152] Rusi, P. Y. Chan, and S. R. Majid. Layer by Layer Ex-Situ Deposited Cobalt-Manganese Oxide as Composite Electrode Material for Electrochemical Capacitor. *PLoS ONE*, 10(7):e0129780.

[153] Jeng-Kuei Chang, Ming-Tsung Lee, Chiung-Hui Huang, and Wen-Ta Tsai. Physicochemical properties and electrochemical behavior of binary manganese–cobalt oxide electrodes for supercapacitor applications. *Materials Chemistry and Physics*, 108(1):124–131, March 2008.

[154] Xuezhao Wang, Yuanhua Xiao, Dangcheng Su, Shengang Xu, Liming Zhou, Shide Wu, Lifeng Han, Shaoming Fang, and Shaokui Cao. Hierarchical porous cobalt monoxide nanosheet@ultrathin manganese dioxide nanosheet core-shell arrays for high-performance asymmetric supercapacitor. *International Journal of Hydrogen Energy*, 41(31):13540–13548, August 2016.

[155] Fereydoon Gobal and Sanaz Jafarzadeh. A comparative study of sequentially layer-deposited and co-deposited Co–Mn oxides as potential redox capacitors. *Journal of Solid State Electrochemistry*, 16(4):1561–1569, April 2012.

[156] Xuezhao Wang, Yuanhua Xiao, Dangcheng Su, Liming Zhou, Shide Wu, Lifeng Han, Shaoming Fang, and Shaokui Cao. High-quality Porous Cobalt Monoxide

Nanowires @ Ultrathin Manganese dioxide Sheets Core-Shell Nanowire Arrays on Ni Foam for High-Performance Supercapacitor. *Electrochimica Acta*, 194:377–384, March 2016.

[157] Nasser A. M. Barakat, Myung Seob Khil, Faheem A. Sheikh, and Hak Yong Kim. Synthesis and Optical Properties of Two Cobalt Oxides (CoO and Co $_3$ O $_4$) Nanofibers Produced by Electrospinning Process. *The Journal of Physical Chemistry C*, 112(32):12225–12233, August 2008.

[158] M. Oshitani, H. Yufu, K. Takashima, S. Tsuji, and Y. Matsumaru. Development of a Pasted Nickel Electrode with High Active Material Utilization. *Journal of The Electrochemical Society*, 136(6):1590–1593, June 1989.

[159] Q. S. Song, G. K. Aravindaraj, H. Sultana, and S. L. I. Chan. Performance improvement of pasted nickel electrodes with multi-wall carbon nanotubes for rechargeable nickel batteries. *Electrochimica Acta*, 53(4):1890–1896, December 2007.

[160] Gérôme Godillot, Hua Huo, Michel Ménétrier, Lydie Bourgeois, Liliane Guerlou-Demourgues, and Claude Delmas. Promising Nanometric Spinel Cobalt Oxides for Electrochemical Energy Storage: Investigation of Li and H Environments by NMR. *The Journal of Physical Chemistry C*, 116(50):26598–26607, December 2012.

[161] G. Binotto, D. Larcher, A. S. Prakash, R. Herrera Urbina, M. S. Hegde, and J-M. Tarascon. Synthesis, Characterization, and Li-Electrochemical Performance of Highly Porous Co3o4 Powders. *Chemistry of Materials*, 19(12):3032–3040, June 2007.

[162] Jonathan N. Coleman, Mustafa Lotya, Arlene O'Neill, Shane D. Bergin, Paul J. King, Umar Khan, Karen Young, Alexandre Gaucher, Sukanta De, Ronan J. Smith, Igor V. Shvets, Sunil K. Arora, George Stanton, Hye-Young Kim, Kangho Lee, Gyu Tae Kim, Georg S. Duesberg, Toby Hallam, John J. Boland, Jing Jing Wang, John F. Donegan, Jaime C. Grunlan, Gregory Moriarty, Aleksey Shmeliov, Rebecca J. Nicholls, James M. Perkins, Eleanor M. Grieveson, Koenraad Theuwissen, David W. McComb, Peter D. Nellist, and Valeria Nicolosi. Two-Dimensional Nanosheets Produced by Liquid Exfoliation of Layered Materials. *Science*, 331(6017):568–571, February 2011.

[163] Valeria Nicolosi, Manish Chhowalla, Mercouri G. Kanatzidis, Michael S. Strano, and Jonathan N. Coleman. Liquid Exfoliation of Layered Materials. *Science*, 340(6139):1226419, June 2013.

[164] C. Delmas, C. Fouassier, and P. Hagenmuller. Structural classification and properties of the layered oxides. *Physica B+C*, 99(1–4):81–85, January 1980.

[165] O. Prieto, M. Del Arco, and V. Rives. Characterisation of K, Na, and Li birnessites prepared by oxidation with H2o2 in a basic medium. Ion exchange properties and study of the calcined products. *Journal of Materials Science*, 38(13):2815–2824, July 2003.

[166] Jeffrey E. Post and David R. Veblen. Crystal structure determinations of synthetic sodium, magnesium, and potassium birnessite using TEM and the Rietveld method. *American Mineralogist*, 75(5-6):477–489, 1990.

[167] Qi Feng, Hirofumi Kanoh, Yoshitaka Miyai, and Kenta Ooi. Hydrothermal Synthesis of Lithium and Sodium Manganese Oxides and Their Metal Ion Extraction/Insertion Reactions. *Chemistry of Materials*, 7(6):1226–1232, June 1995.

[168] Zong-huai Liu, Kenta Ooi, Hirofumi Kanoh, Wei-ping Tang, and Tahei Tomida. Swelling and Delamination Behaviors of Birnessite-Type Manganese Oxide by Intercalation of Tetraalkylammonium Ions. *Langmuir*, 16(9):4154–4164, May 2000.

[169] Yoshitomo Omomo, Takayoshi Sasaki, Wang, and Mamoru Watanabe. Redoxable Nanosheet Crystallites of MnO2 Derived via Delamination of a Layered Manganese Oxide. *Journal of the American Chemical Society*, 125(12):3568–3575, March 2003.

[170] Katsutoshi Fukuda, Izumi Nakai, Yasuo Ebina, Masahiko Tanaka, Takeharu Mori, and Takayoshi Sasaki. Structure Analysis of Exfoliated Unilamellar Crystallites of Manganese Oxide Nanosheets. *The Journal of Physical Chemistry B*, 110(34):17070–17075, August 2006.

[171] Biehou Ma, Wenyan Hou, Yinfeng Han, Runguang Sun, and Zong-Huai Liu. Exfoliation reaction of birnessite-type manganese oxide by a host–guest electrostatic repulsion in aqueous solution. *Solid State Sciences*, 10(2):141–147, February 2008.

[172] Anne-Claire Gaillot, Victor A. Drits, Alain Plançon, and Bruno Lanson. Structure of Synthetic K-Rich Birnessites Obtained by High-Temperature Decomposition of KMnO4. 2. Phase and Structural Heterogeneities. *Chemistry of Materials*, 16(10):1890–1905, May 2004.

[173] Rongji Chen. New manganese oxides by hydrothermal reaction of permanganates. volume 453, pages 653–658. Materials Research Society, 1997.

[174] R. Giovanoli, E. Stähli, and W. Feitknecht. Über Oxidhydroxide des vierwertigen Mangans mit Schichtengitter 2. Mitteilung: Mangan (III)-manganat (IV). *Helvetica Chimica Acta*, 53(3):453–464, January 1970.

[175] Sa Heum Kim, Sung Jin Kim, and Seung M. Oh. Preparation of Layered MnO2 via Thermal Decomposition of KMnO4 and Its Electrochemical Characterizations. *Chemistry of Materials*, 11(3):557–563, March 1999.

[176] Stanton Ching, Jennifer A. Landrigan, and Matthew L. Jorgensen. Sol-gel synthesis of birnessite from KMnO4 and simple sugars. *Chemistry of Materials*, 7(9):1604–1606, September 1995.

[177] P. Le Goff, N. Baffier, S. Bach, and J. P. Pereira-Ramos. Synthesis, ion exchange and electrochemical properties of lamellar phyllomanganates of the birnessite group. *Materials Research Bulletin*, 31(1):63–75, January 1996.

[178] B. Lanson. Structure of H-exchanged hexagonal birnessite and its mechanism of formation from Na-rich monoclinic buserite at low pH. *The American mineralogist*, 85(5-6):826–838, 2000.

[179] B. Lanson. Structure of synthetic Na-birnessite: Evidence for a triclinic one-layer unit cell. *The American mineralogist*, 87(11-12):1662–1671, 2002.

[180] Jian Luo, Qiuhua Zhang, and Steven L. Suib. Mechanistic and Kinetic Studies of Crystallization of Birnessite. *Inorganic Chemistry*, 39(4):741–747, February 2000.

[181] J. Luo. Preparative parameters, magnesium effects, and anion effects in the crystallization of birnessites. *Journal of Physical Chemistry B*, 101(49):10403–10413, 1997.

[182] Rongji Chen, Tom Chirayil, Peter Zavalij, and M. Stanley Whittingham. The hydrothermal synthesis of sodium manganese oxide and a lithium vanadium oxide. *Solid State Ionics*, 86:1–7, July 1996.

[183] Shin-ichi Hirano, Ryoichi Narita, and Shigeharu Naka. Hydrothermal synthesis and properties of Na0.70mno2.25 layer crystal. *Materials Research Bulletin*, 19(9):1229–1235, September 1984.

[184] Stanton Ching, Diana J. Petrovay, Matthew L. Jorgensen, and Steven L. Suib. Sol-Gel Synthesis of Layered Birnessite-Type Manganese Oxides. *Inorganic Chemistry*, 36(5):883–890, February 1997.

[185] Jian Luo, Aimin Huang, Ssang Hyun Park, Steven L. Suib, and Chi-Lin O'Young. Crystallization of SodiumBirnessite and Accompanied Phase Transformation. *Chemistry of Materials*, 10(6):1561–1568, June 1998.

[186] Anne-Claire Gaillot. *Caractérisation structurale de la birnessite: Influence du protocole de synthese.* PhD thesis, Université Joseph-Fourier-Grenoble I, 2002.

[187] Myriam Douin. *Etude de phases spinelle cobaltée et d'oxydes lamellaires dérivés de Na 0, 6 CoO 2 employés comme additifs conducteurs dans les accumulateurs Ni-MH.* PhD thesis, Université Sciences et Technologies-Bordeaux I, 2008.

[188] Stanton Ching, Ram P. Neupane, and Timothy P. Gray. Synthesis and Characterization of a Layered Manganese Oxide: Materials Chemistry for the Inorganic or Instrumental Methods Lab. *Journal of Chemical Education*, 83(11):1674, November 2006.

[189] Maurice Butel. *Etude de nouveaux oxyhydroxydes de cobalt pouvant être utilisés comme additif conducteur électronique ajoutés à l'hydroxydes de nickel dans les accumulateurs nickel/cadmium et nickel/métal hydrure.* PhD thesis, Bordeaux I, 1998.

[190] RD t Shannon. Revised effective ionic radii and systematic studies of interatomic distances in halides and chalcogenides. *Acta crystallographica section A: crystal physics, diffraction, theoretical and general crystallography*, 32(5):751–767, 1976.

[191] Victor A. Drits, Ewen Silvester, Anatoli I. Gorshkov, and Alain Manceau. Structure of synthetic monoclinic Na-rich birnessite and hexagonal birnessite: I. Results from X-ray diffraction and selected-area electron diffraction. *American Mineralogist*, 82(9-10):946–961, 1997.

[192] Ewen Silvester, Alain Manceau, and Victor A. Drits. Structure of synthetic monoclinic Na-rich birnessite and hexagonal birnessite: II. Results from chemical studies and EXAFS spectroscopy. *American Mineralogist*, 82(9-10):962–978, 1997.

[193] Sing K. S. W. Reporting physisorption data for gas/solid systems with special reference to the determination of surface area and porosity (Recommendations 1984). *Pure and Applied Chemistry*, 57(4):603, 2009.

[194] V. Pralong, A. Delahaye-Vidal, B. Beaudoin, B. Gérand, and J.-M. Tarascon. Oxidation mechanism of cobalt hydroxide to cobalt oxyhydroxide. *Journal of Materials Chemistry*, 9(4):955–960, January 1999.

[195] R. Ma and T. Sasaki. Two-dimensional oxide and hydroxide nanosheets: Controllable high-quality exfoliation, molecular assembly, and exploration of functionality. *Accounts of Chemical Research*, 48(1):136–143, 2015.

[196] Guillaume A. Muller, John B. Cook, Hyung-Seok Kim, Sarah H. Tolbert, and Bruce Dunn. High Performance Pseudocapacitor Based on 2d Layered Metal Chalcogenide Nanocrystals. *Nano Letters*, 15(3):1911–1917, March 2015.

[197] K. S. Novoselov, V. I. Falko, L. Colombo, P. R. Gellert, M. G. Schwab, and K. Kim. A roadmap for graphene. *Nature*, 490(7419):192–200, October 2012.

[198] Qing Hua Wang, Kourosh Kalantar-Zadeh, Andras Kis, Jonathan N. Coleman, and Michael S. Strano. Electronics and optoelectronics of two-dimensional transition metal dichalcogenides. *Nature Nanotechnology*, 7(11):699–712, November 2012.

[199] Minoru Osada and Takayoshi Sasaki. Exfoliated oxide nanosheets: new solution to nanoelectronics. *Journal of Materials Chemistry*, 19(17):2503–2511, April 2009.

[200] Alfonso Reina, Xiaoting Jia, John Ho, Daniel Nezich, Hyungbin Son, Vladimir Bulovic, Mildred S. Dresselhaus, and Jing Kong. Large Area, Few-Layer Graphene Films on Arbitrary Substrates by Chemical Vapor Deposition. *Nano Letters*, 9(1):30–35, January 2009.

[201] Goki Eda, Hisato Yamaguchi, Damien Voiry, Takeshi Fujita, Mingwei Chen, and Manish Chhowalla. Photoluminescence from Chemically Exfoliated MoS2. *Nano Letters*, 11(12):5111–5116, December 2011.

[202] Paul F Luckham and Sylvia Rossi. The colloidal and rheological properties of bentonite suspensions. *Advances in Colloid and Interface Science*, 82(1–3):43–92, October 1999.

[203] Tomohiro Tanaka, Yasuo Ebina, Kazunori Takada, Keiji Kurashima, and Takayoshi Sasaki. Oversized Titania Nanosheet Crystallites Derived from Flux-Grown Layered Titanate Single Crystals. *Chemistry of Materials*, 15(18):3564–3568, September 2003.

[204] Mustafa Lotya, Yenny Hernandez, Paul J. King, Ronan J. Smith, Valeria Nicolosi, Lisa S. Karlsson, Fiona M. Blighe, Sukanta De, Zhiming Wang, I. T. McGovern, Georg S. Duesberg, and Jonathan N. Coleman. Liquid Phase Production of Graphene by Exfoliation of Graphite in Surfactant/Water Solutions. *Journal of the American Chemical Society*, 131(10):3611–3620, March 2009.

[205] Wang, Kazunori Takada, Akihisa Kajiyama, Mitsuko Onoda, Yuichi Michiue, Zhang, Mamoru Watanabe, and Takayoshi Sasaki. Synthesis of a LiMn-oxide with Disordered Layer Stacking through Flocculation of Exfoliated MnO2 Nanosheets, and Its Electrochemical Properties. *Chemistry of Materials*, 15(23):4508–4514, November 2003.

[206] Xiaojing Yang, Yoji Makita, Zong-huai Liu, Kohji Sakane, and Kenta Ooi. Structural Characterization of Self-Assembled MnO2 Nanosheets from Birnessite Man-

ganese Oxide Single Crystals. *Chemistry of Materials*, 16(26):5581–5588, December 2004.

[207] Zhaoping Liu, Renzhi Ma, Yasuo Ebina, Kazunori Takada, and Takayoshi Sasaki. Synthesis and Delamination of Layered Manganese Oxide Nanobelts. *Chemistry of Materials*, 19(26):6504–6512, December 2007.

[208] Min-Sun Song, Kyung Min Lee, Yu Ri Lee, In Young Kim, Tae Woo Kim, Jayavant Laxman Gunjakar, and Seong-Ju Hwang. Porously Assembled 2d Nanosheets of Alkali Metal Manganese Oxides with Highly Reversible Pseudocapacitance Behaviors. *The Journal of Physical Chemistry C*, 114(50):22134–22140, December 2010.

[209] Zhaoping Liu, Renzhi Ma, Minoru Osada, Nobuo Iyi, Yasuo Ebina, Kazunori Takada, and Takayoshi Sasaki. Synthesis, Anion Exchange, and Delamination of CoAl Layered Double Hydroxide: Assembly of the Exfoliated Nanosheet/Polyanion Composite Films and Magneto-Optical Studies. *Journal of the American Chemical Society*, 128(14):4872–4880, April 2006.

[210] Qiuming Gao, Oscar Giraldo, Wei Tong, and Steven L. Suib. Preparation of Nanometer-Sized Manganese Oxides by Intercalation of Organic Ammonium Ions in Synthetic Birnessite OL-1. *Chemistry of Materials*, 13(3):778–786, March 2001.

[211] Yanhua Cui, Zong-Huai Liu, Mingzhen Wang, and Kenta Ooi. New approach to the delamination of layered manganese oxide. *Chemistry Letters*, 35(7):740–741, 2006.

[212] Renzhi Ma, Minoru Osada, Linfeng Hu, and Takayoshi Sasaki. Self-Assembled Nanofilm of Monodisperse Cobalt Hydroxide Hexagonal Platelets: Topotactic Conversion into Oxide and Resistive Switching. *Chemistry of Materials*, 22(23):6341–6346, December 2010.

[213] Renzhi Ma, Kazunori Takada, Katsutoshi Fukuda, Nobuo Iyi, Yoshio Bando, and Takayoshi Sasaki. Topochemical Synthesis of Monometallic (Co2+–Co3+) Layered Double Hydroxide and Its Exfoliation into Positively Charged Co(OH)2 Nanosheets. *Angewandte Chemie International Edition*, 47(1):86–89, January 2008.

[214] Zhaoping Liu, Renzhi Ma, Minoru Osada, Kazunori Takada, and Takayoshi Sasaki. Selective and Controlled Synthesis of - and -Cobalt Hydroxides in Highly Developed Hexagonal Platelets. *Journal of the American Chemical Society*, 127(40):13869–13874, October 2005.

[215] B. Schneiderová, J. Demel, J. Pleštil, H. Tarábková, J. Bohuslav, and K. Lang. Electrochemical performance of cobalt hydroxide nanosheets formed by the delamination of layered cobalt hydroxide in water. *Dalton Transactions*, 43(27):10484–10491, June 2014.

[216] TaeWoo Kim, Eun-Jin Oh, Ah-Young Jee, SeungTae Lim, DaeHoon Park, Minyung Lee, Sang-Hoon Hyun, Jin-Ho Choy, and Seong-Ju Hwang. Soft-Chemical Exfoliation Route to Layered Cobalt Oxide Monolayers and Its Application for Film Deposition and Nanoparticle Synthesis. *Chemistry – A European Journal*, 15(41):10752–10761, October 2009.

[217] Owen C. Compton, Ali Abouimrane, Zhi An, Marc J. Palmeri, L. Catherine Brinson, Khalil Amine, and SonBinh T. Nguyen. Exfoliation and Reassembly of Cobalt Oxide Nanosheets into a Reversible Lithium-Ion Battery Cathode. *Small*, 8(7):1110–1116, April 2012.

[218] Jong-Young Kim, Jin-Il Kim, Soon-Mok Choi, Young Soo Lim, Won-Seon Seo, and Hae Jin Hwang. Nanostructured thermoelectric cobalt oxide by exfoliation/restacking route. *Journal of Applied Physics*, 112(11):113705, December 2012.

[219] Renzhi Ma and Takayoshi Sasaki. Nanosheets of Oxides and Hydroxides: Ultimate 2d Charge-Bearing Functional Crystallites. *Advanced Materials*, 22(45):5082–5104, December 2010.

[220] Liang Li, Renzhi Ma, Yasuo Ebina, Katsutoshi Fukuda, Kazunori Takada, and Takayoshi Sasaki. Layer-by-Layer Assembly and Spontaneous Flocculation of Oppositely Charged Oxide and Hydroxide Nanosheets into Inorganic Sandwich Layered Materials. *Journal of the American Chemical Society*, 129(25):8000–8007, June 2007.

[221] George A. Parks. The Isoelectric Points of Solid Oxides, Solid Hydroxides, and Aqueous Hydroxo Complex Systems. *Chemical Reviews*, 65(2):177–198, April 1965.

[222] Linus Pauling. The principles determining the structure of complex ionic crystals. *Journal of the american chemical society*, 51(4):1010–1026, 1929.

[223] Marek Kosmulski. *Chemical Properties of Material Surfaces*, volume 102 of *Surfactants Surface Series*. CRC Press, July 2001.

[224] Dimitri A. Sverjensky and Nita Sahai. Theoretical prediction of single-site enthalpies of surface protonation for oxides and silicates in water. *Geochimica et cosmochimica acta*, 62(23):3703–3716, 1998.

[225] Tjisse Hiemstra, Peter Venema, and Willem H. Van Riemsdijk. Intrinsic proton affinity of reactive surface groups of metal (hydr) oxides: The bond valence principle. *Journal of colloid and interface science*, 184(2):680–692, 1996.

[226] T Hiemstra, J.C.M De Wit, and W.H Van Riemsdijk. Multisite proton adsorption modeling at the solid/solution interface of (hydr)oxides: A new approach. *Journal of Colloid and Interface Science*, 133(1):105–117, November 1989.

[227] T. Hiemstra and W. H. Van Riemsdijk. A Surface Structural Approach to Ion Adsorption: The Charge Distribution (CD) Model. *Journal of Colloid and Interface Science*, 179(2):488–508, May 1996.

[228] I. D. Brown and D. Altermatt. Bond-valence parameters obtained from a systematic analysis of the Inorganic Crystal Structure Database. *Acta Crystallographica Section B*, 41(4):244–247, August 1985.

[229] John Westall and Herbert Hohl. A comparison of electrostatic models for the oxide/solution interface. *Advances in Colloid and Interface Science*, 12(4):265–294, March 1980.

[230] Marek Kosmulski. Isoelectric points and points of zero charge of metal (hydr)oxides: 50 years after Parks' review. *Advances in Colloid and Interface Science*, 238:1–61, December 2016.

[231] Robert J. Hunter. *Zeta Potential in Colloid Science: Principles and Applications.* Academic Press, September 2013.

[232] Xiao-feng Yang, Geng-chao Wang, Rui-yu Wang, and Xing-wei Li. A novel layered manganese oxide/poly(aniline-co-o-anisidine) nanocomposite and its application for electrochemical supercapacitor. *Electrochimica Acta*, 55(19):5414–5419, July 2010.

[233] Annick Lesne and Michel Laguës. *Invariance d'échelle. Des changements d'états à la turbulence: Des changements d'états à la turbulence.* Humensis, July 2015. Google-Books-ID: vhGWDgAAQBAJ.

[234] Jean-Claude Badot, Éc Ligneel, Olivier Dubrunfaut, Dominigve Guyomard, and Bernard Lestriez. A Multiscale Description of the Electronic Transport within the Hierarchical Architecture of a Composite Electrode for Lithium Batteries. *Advanced Functional Materials*, 19(17):2749–2758, September 2009.

[235] S. Berthumeyrie, J.-C. Badot, J.-P. Pereira-Ramos, O. Dubrunfaut, S. Bach, and P.H. Vermaut. Influence of lithium insertion on the electronic transport in electroactive MoO3 nanobelts and classical powders: Morphological and particle size effects. *Journal of Physical Chemistry C*, 114(46):19803–19814, 2010.

[236] Keith P. McKenna and Alexander L. Shluger. Electron-trapping polycrystalline materials with negative electron affinity. *Nature Materials*, 7(11):859–862, November 2008.

[237] Keith P. McKenna and Alexander L. Shluger. Electron and hole trapping in polycrystalline metal oxide materials. *Proceedings of the Royal Society of London A: Mathematical, Physical and Engineering Sciences*, page rspa20100518, February 2011.

[238] Suzanne K. Wallace and Keith P. McKenna. Grain Boundary Controlled Electron Mobility in Polycrystalline Titanium Dioxide. *Advanced Materials Interfaces*, 1(5):n/a–n/a, August 2014.

[239] Y.-H. Chen, C.-W. Wang, G. Liu, X.-Y. Song, V. S. Battaglia, and A. M. Sastry. Selection of Conductive Additives in Li-Ion Battery Cathodes. *Journal of The Electrochemical Society*, 154(10):A978, 2007.

[240] Laurence Athouël, Paul Arcidiacono, Claudia Ramirez-Castro, Olivier Crosnier, Daniel Guay, Daniel Bélanger, and Thierry Brousse. Outer and Inner Surface Contribution of Manganese Dioxides Energy Storage Characterization by Cavity Microelectrode Technique. *ECS Transactions*, 58(27):53–59, February 2014.

[241] L. Yu, Y. X. Yan, Q. Liu, J. Wang, B. Yang, B. Wang, X. Y. Jing, and L. H. Liu. Exfoliation at Room Temperature for Improving Electrochemical Performance for Supercapacitors of Layered MnO2. *Journal of The Electrochemical Society*, 161(1):E1–E5, January 2014.

[242] L. Demarconnay, E. Raymundo-Piñero, and F. Béguin. Adjustment of electrodes potential window in an asymmetric carbon/MnO2 supercapacitor. *Journal of Power Sources*, 196(1):580–586, January 2011.

[243] V. Briois, C. La Fontaine, S. Belin, L. Barthe, Th Moreno, V. Pinty, A. Carcy, R. Girardot, and E. Fonda. ROCK: the new Quick-EXAFS beamline at SOLEIL. *Journal of Physics: Conference Series*, 712(1):012149, 2016.

[244] B. Ravel and M. Newville. XAFS Data Interchange: A single spectrum XAFS data file format. *Journal of Physics: Conference Series*, 712(1):012148, 2016.

[245] Jean-Claude Badot, Bernard Lestriez, and Olivier Dubrunfaut. Interest in broadband dielectric spectroscopy to study the electronic transport in materials for lithium batteries. *Materials Science and Engineering: B*, 213(Supplement C):190–198, November 2016.

[246] Stephen Brunauer, P. H. Emmett, and Edward Teller. Adsorption of Gases in Multimolecular Layers. *Journal of the American Chemical Society*, 60(2):309–319, February 1938.

[247] Elliott P. Barrett, Leslie G. Joyner, and Paul P. Halenda. The Determination of Pore Volume and Area Distributions in Porous Substances. I. Computations from Nitrogen Isotherms. *Journal of the American Chemical Society*, 73(1):373–380, January 1951.